F I N A L R E P O R T

DOE Experimental Program to Stimulate Competitive Research (EPSCoR)
Implementation Award
DE-SC0002470

Nanostructure-enhanced Phase Change Materials (NePCM)

Project Director: Dr. John W. Steadman, Alabama DOE EPSCoR Agency Director, University of South Alabama, 150 Jaquar Drive, Shelby Hall Room 2114, Mobile, AL 36688; (T) 251-460-6140; Email: jsteadman@usouthal.edu.
Administrative Point of Contact: Charlotte Nix, The University of Alabama, Box 870164, Tuscaloosa, AL 35487 (T) 205-348-7079; Email: cnix@aalan.ua.edu.
Principal Investigator: Dr. Jay M. Khodadadi, Alumni Professor, Department of Mechanical Engineering, 1418 Wiggins Hall, Auburn University, AL 36849-5341; (T) 334-844-3333, (F) 334-844-3307; Email: khodajm@auburn.edu.

Collaborating Institutions/PIs:
Dr. German Mills, Associate Professor, Department of Chemistry and Biochemistry, 179 Chemistry Building, Auburn University, AL 36849, (T) 334-844-6974, (F) 334-844-6959; millsge@auburn.edu.
Dr. Muhammad Ali Rob Sharif, Assoc. Professor, Aero. Eng. and Mechanics Dept., The University of Alabama, Box 870280, Tuscaloosa, AL 35487; (T) 205-348-8052, (F) 205-348-7240;msharif@eng.ua.edu
Dr. Tamara Floyd-Smith, Associate Professor and 3M Scholar, Department of Chemical Engineering, Tuskegee University, Tuskegee, AL 36088; (T) 334-727-8975, (F) 334-727-8996; tamara.floyd@tuskegee.edu
Dr. Luis A. Cueva-Parra, Associate Professor, Dept. of Mathematics, 310A Goodwyn Hall, Auburn Univ. Montgomery, Montgomery, AL 36124; (T) 334-244-3321, (F) 334-244-3826; lcuevapa@aum.edu
Dr. Robert L. Jackson, Associate Professor, Department of Mechanical Engineering, 1418 Wiggins Hall, Auburn University, AL 36849-5341; (T) 334-844-3340, (F) 334-844-3307; Email: jacksr7@auburn.edu.
Dr. Kuang-Ting Hsiao, Associate Professor, Department of Mechanical Engineering, University of South Alabama, 150 Jaguar Drive, SHEC 3130, Mobile, AL 36688-0002; (T) 251-460-7889, (F) 251-460-6549; KTHsiao@SouthAlabama.edu.

Submitted to

DOE/Office of Science Program Technical Contact: Dr. Tim Fitzsimmons
Tel: 301-903-9830; Fax: 301-903-9513; Tim.Fitzsimmons@science.doe.gov

Table of Contents

Introduction 3

Alabama DOE EPSCoR Management and Human Resource Development 3

NEPCM Research Cluster Summary 21

Background on the NePCM Project..... 23

1. NePCM Development and Characterization..... 25

2. NePCM Modeling and Testing 44

3. Nanoparticle Separation/Reclamation 66

4. NePCM in Thermal Management of Electronics..... 106

5. Multi-Scale, Multi-Physics Non-Continuum Modeling 111

6. Nanoparticle-Enhanced Lubricating Tribology..... 144

7. Thermal Conductivity and Dispersion Effects 194

Introduction

The Alabama DOE EPSCoR Project includes two components: the Research Cluster entitled, *Nanostructure-Enhanced Phase Change Materials (NEPCM) Tailored for Energy Efficiency, High-Power Electronics, Thermal Storage/Comfort and Building Materials Applications,* and a Management and Human Resource Development component.

Alabama DOE EPSCoR Management and Human Resource Development

The Alabama DOE EPSCoR program is one of the five EPSCoR programs (EPA, NSF, NASA, USDA, DOE) for which the State of Alabama is eligible to compete for Federal support. The State of Alabama has an established EPSCoR Steering Committee that consists of Vice Presidents for Research from the seven Ph.D. granting institutions in the state. The statewide EPSCoR structure allows the members of the Alabama EPSCoR Steering Committee to focus institutional resources at their disposal (state appropriated special funds and institutionally appropriated funds for research) on those programs aligned with the State's strategic plan for economic growth and development.

The Alabama EPSCoR Steering Committee appoints agency directors for each of the federal EPSCoR programs for which Alabama is eligible. Dr. John Steadman serves as the Alabama DOE EPSCoR Agency Director and Project Director of the DOE Implementation Grant DE-SC0002470, NEPCM and HRD Coordination, which began August 15, 2009. Dr. Steadman is the Dean of Engineering at the University of South Alabama in Mobile, Alabama.

The mission of the Alabama DOE EPSCoR HRD program is to build relationships between Alabama researchers and DOE National Laboratories, provide stimulating experiences in science, technology, engineering and mathematics (STEM) education, and develop a diverse and skilled workforce of scientists, technicians, engineers, mathematicians and educators for Alabama's evolving high-tech industry and increase energy-related research in our state. The project has great potential to improve the quality, distribution, and effectiveness of the state's human resources in STEM disciplines.

The HRD program has a successful history of placing undergraduates, graduate students, faculty, postdoctoral students and researchers in programs with DOE Federal Laboratories. The program philosophy is illustrated below. The Travel Grant Program assists with costs incurred by Alabama researchers to visit a federal laboratory and/or apply for one of the several DOE program awards designed to stimulate collaborative research. A particular focus of our efforts is to lay the foundation for science and engineering faculty to build successful DOE lab partnership research programs. The HRD funding supports transportation and lodging costs for brief visits (2-5 days/up to a total of $1,500) or for extended periods of time (up to one semester/up to a total of $5,000). Travel requests require a 50% match from the participating institution.

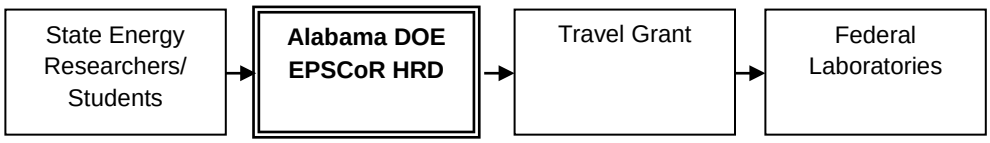

The Human Resource Development component concentrated its efforts again in Year 4 to distribute information regarding the availability of travel support through an e-mail distribution list that included the Vice Presidents of Research, Deans of Engineering and Deans of Arts and Sciences at the seven Ph.D. granting institutions including Alabama A&M University (AAMU), Auburn University (AU), Tuskegee University (TU), The University of Alabama (UA), University of Alabama at Birmingham (UAB), University of Alabama in Huntsville (UAH), and the University of South Alabama (USA). A similar list was made with appropriate contacts at Athens State University, Alabama State University, Jacksonville State University, University of Montevallo, University of North Alabama and the University of West Alabama.

In Year 4, Alabama DOE EPSCoR continued to support HRD travel to energy related domestic travel for presentations at national conferences and visits to national laboratories. Attendance at energy related national conferences encourages networking of investigators, exposure to current research, challenging new ideas, and potential collaborations. Alabama DOE Human Resource Development travel has faced the challenge of foreign students not being permitted access to DOE National labs and some universities not having resources to provide matching funds. Below are five tables describing Alabama DOE EPSCoR NEPCM Human Resource Development travel starting with a short synopsis for the entire project to date followed by details for Year 4. Table 1 shows the yearly request, approval and denial rate of HRD travel for the entire project to date. Clearly, Year 4 experienced more travel than the three previous years combined. Table 2 outlines travel requests, approvals and denials specifically for Year 4. Tables 3, 4 and 5 outline details of the travel that was approved, approved but not completed, and travel that was denied, respectively.

Alabama DOE EPSCoR has had two requests for travel thus far during the 2013-2015 extension period. We will continue to encourage energy related travel until resources are depleted. A description of each of the requests for travel can be found following the tables.

HRD Table 1: NEPCM HRD Project Travel (2009-November 2013)						
	Yr 1	Yr 2	Yr 3	Yr 4	2013-2015 Extension	Total
Requests for HRD funding	2	13	11	35	2	61
Trips Approved and funded		9	5	28	1	42
Trips Approved, but not funded			3	4		7
Trips Denied	2	4	3	4		13
Universities requesting support	UA	AAMU, UA, UAB, UAH	AU, TU, UA,	AAMU, AU, UA, UAH, USA		

HRD Table 2: Alabama DOE EPSCoR NEPCM HRD Travel - Year 4									
	AAMU	AU	TU	UA	UAB	UAH	USA	Other	Total
Requests for HRD funding mid-May 2012 to mid-August 2013	1	12	0	19	0	1	2		35
Trips Approved and funded mid-May 2012 to mid-August 2013		12		15			1		28
Trips Approved, but not funded mid-May 2012 to mid-August 2013	1			1		1	1		4
Trips Denied mid-May 2012 to mid-August 2013				4					4
Trips Requested during 2013-2015 extension to date				1			1		2

November-13

HRD Table 3 - Year 4 DOE EPSCoR NEPCM HRD Travel - Approved							
Name	Title	Dept	Inst	Destination	Dates	Research/ Plan	Status
Hamed Ghaednia	Ph.D. student	Mech Eng	AU	Society of Tribologist and Lubrication Engineers (STLE) 2012	May 2012	Present the effect of nanoparticle research on the tribological properties of lubricants	Completed (description provided in previous report)
Susan Burkett	Alabama Power Foundation Endowed Professor	Elect/ Comp Eng	UA	Dr. Anirudha Sumant, Materials Scientist at Argonne Nat'l Lab	July/Aug 2012	Matthew will perform extended collaborative research on 3D integration (2 trips)	Completed (description provided in previous report)
Matthew Jordan	grad student						
Jay Khodadadi	Professor	Mechanical Engineering	AU	American Association of Mechanical Engineers, Heat Transfer Conference, Puerto Rico	July 8-12, 2012	Dr. Khodadadi presented two papers, Mr. Sedeh co-presented with Dr. Khodadadi	completed
Mahmoud Sedeh	grad student						

Heath Turner	Associate Prof.	Bio/Chem Engineering	UA	AICHE Conference	Oct/Nov 2012	present "Simulatioin and Experimental Benchmarking of the Thermopysical Properties of *N*-Funcionalized Alkylimidozoles"	completed
Sushma Kotru	Associate Prof.	Elect/ Comp Eng	UA	present paper in Thin Films for Energy Applications Section of the Americal Vacuum Society (AVS) 59th International Symposium and Exhibition	Oct/Nov 2012	paper entitled "Effect of Top Electrodes on the Photovoltaic Properties of Ferroelectric PLZT Thin Film Capacitors"	completed
Yousef M.F. Hasadi	Ph.D. student	Mech Eng	AU	present research at the 49th Annual Technical Meeting of Society of Engineering Science, Atlanta, GA	Oct 2012	NePCM	completed
Hasan Babaei	Ph.D. student	Mech Eng	AU			molecular dynamic simulations	completed
Mahmoud Sedeh	Ph.D. student	Mech Eng	AU			NePCM	completed
Mahdi Nabil	Ph.D. student	Mech Eng	AU			NePCM	completed
Kevin Chou	Professor	Mech Eng	UA	visit with Dr. Ryan Dehoff at Oakridge National Lab	June/July 2013	initiate an initial meeting on additive manufacturing technology	completed
Mohammad Hossain	Ph.D. student	Chemistry	AU	present at poster at the Southwestern Regional American Chemical Society, Baton Rouge, LA	Nov 2012	"Synthesis of concentrated Ag colloids"	completed

				with Dr. German Mills			
Jason Bara	Asst. Prof	Chem/Bio Engineering	UA	gave several presentations at the 2012 American Institute of Chemical Engineering Meeting, Pittsburg PA and met with NETL personnel	Oct 2012	clean energy processes and carbon capture	completed, with Dr. Bara's complimentary registration, Michelle was able to attend.
Matthew Shannon	grad student						
Michelle Hindman	grad student						
Melanie Beazley	post doc	Biological sciences	UA	attend training session at the Institute for Genome Sciences, University of Maryland	Nov 2012	bioremediation of uranium	completed
Margaret Liu	Asst. Prof	Chem/Bio Engineering	UA	present paper at 245th ACS National Meeting and Exposition, New Orleans	April 2013	"Biobutanol Production Improvement by Combining Metabolic Engineering of *C. tyrobutyricum* and Production Process Development	completed
Chao Ma	grad student						
Jason Bara	Asst Prof	Chem/Bio Engineering	UA	present at the Carbon Capture Utilization and Sequestration Conference, Pittsburg	May 2013	clean energy processes and carbon capture	completed
Jason Darvin	undergraduate student	Chem/ Biochem	AU	present a paper at the 245th American	Apr 2013	NEPCM getting travel funds for an undergrad was	completed

				Chemical Society Meeting in New Orleans		difficult	
Robert Barletta		Chemistry	USA	Brookhaven National Lab	July 2013	conduct proof-of-concept test on the use of the infrared microscope of the U2B beam line on the NSLS	completed
Dustin Heaton	grad student	Computer Science	UA	ORNL visit	June and July 2013	Working with Markis Eisenbach and ORNL LSMS (Locally-Self-Consistent Multiple Scattering Code) team to assess their use of software engineering practices to ensure development of maintainable software and augment practices where lacking	completed
Dr. Jeffrey Carver	Associate Prof.				two short visits during June and July 2013		
Hannah Neuffer	undergraduate student	Mechanical Engineering	AU	Society of Tribologist and Lubrication Engineering Conf	May 5-9, 2013	present group's findings, get helpful feedback, meet with Dr. Przesmitzki, Fuels and Lubricants Technology Mgr at US DOE	completed
Hamed Ghaednia	grad student						
Dr. Robert Jackson	Assoc. Professor						
Zhang O'Neill	Asst. Prof	Mechanical Engineering	UA	American Society of Heating, Refrigerating and Air Conditioning	June 23-26, 2013	present a paper	completed

				Engineering Meeting, Denver, CO			

HRD Table 4 - Year 4 DOE EPSCoR HRD Travel - Approved but not completed							
Name	Title	Dept	Inst	Destination	Dates	Research/ Plan	Status
Xin Zhong	Ph.D. student	Physics	UA	Oakridge National Lab	October 2012	conduct experiment, "Layer-Specific Magnetization and Magnetic Anisotrophy of Fe/Co Superlattices" for studying the depth dependent magnetization and anisotrophy	postponed due to consistency inspection
Waleed D., Al-Assadi	Ph.D. student	Elect/ Comp Eng	USA	visit to ORNL to participate in the 3rd Annual Bridging the Gap Forum	March 5-6-2013	intended to explore new innovations in energy and advanced materials, as well as possible research collaborations	approved, but registration for workshop was closed, trip cancelled
Junpeng Guo	Associate Prof.	Elect/ Comp Eng	UAH	International Society for Optics and Photonics (SPIE)	April 29-May 3, 2013	present paper on energy and chemical sensors	did not travel

HRD Table 5 - Year 4 DOE EPSCoR NEPCM HRD Travel - Denied							
Name	Title	Dept	Inst	Destination	Dates	Research/ Plan	Status
Conor Henderson	Asst. Prof.	Physics/Astronomy	UA	LHC Physics Center at Fermilab	Fall 2012	LPC working group at UA	denied, no confirmation from contact at Fermilab
Jeff Gray	Assoc. Prof	Computer Science	UA	attend a software engineering	Fall 2012	describes work done at PNNL	no formal request, not DOE focused

				conference			
Nicholas De Leon	Graduate Student	Metall and Materials Engineering	UA	Extended stay at Sandia National Lab	Fall 2012		no formal proposal submitted
Erick Ellis	Assist. Prof	Chem	AAMU	Advanced Biofuels Leadership Conference, Wash., D.C.	Apr. 2013	attend conference	no formal proposal submitted
Cemen Ibrahim	Chair and Professor	Geology	UA	attend AAPG Conf in Pittsburg, PA	May-13	present at the conference	extremely late request, no formal proposal

Jay M. Khodadadi, Ph.D. American Assoc. of Mechanical Engineers
Mahmoud Sedeh, Mechanical Engineering Graduate Student

The results of the ongoing research projects of the NePCM cluster are generally presented at national heat transfer/energy conferences and then integrated into journal submissions. The research group of Dr. Khodadadi has three (3) papers that will be presented at the ASME 2012 Heat Transfer Conference, July 8-12. Since one of these papers will be presented by one of the graduate students (Mr. Moeini Sedeh), Dr. Khodadadi will present the remaining 2 papers, i.e.

1. EXPERIMENTAL DETERMINATION OF TEMPERATURE-DEPENDENT THERMAL CONDUCTIVITY OF SOLID EICOSANE-BASED NANOSTRUCTURE-ENHANCED PHASE CHANGE MATERIALS. This offering is co-authored with Mr. M. Nabil and outlines the thermal conductivity measurement of eicosane-CuO solid colloids that were obtained following two different solidification methods. Whereas measurements of the thermal conductivity of liquid colloids are straightforward, similar measurements in the solid phase are plagued with set-up difficulties and anomalous observations. The results presented in this paper are meant to highlight these issues and pave the way for more accurate measurements in the near future.

2. NUMERICAL SIMULATION OF THE EFFECT OF THE SIZE OF NANOPARTICLES ON THE SOLIDIFICATION PROCESS OF NANOPARTICLE-ENHANCEND PHASE CHANGE MATERIALS. This paper is co-authored with Mr. Y. El Hasadi and concerns continuum modeling of heat and mass transfer during freezing of a column of nanoparticle-laden colloid. The presence of the solid nanoparticles was modeled as a “mixture” and rejection of particles at the liquid-solid interface is accounted for. Through incorporation of a modified model for transport of nanoparticles, the results exhibit breakdown of a planar interface to a wavy structure similar to dendiritic growth of micron-sized colloidal systems. Moreover, the notion of expediting of freezing is refined to take account of mass transfer and particle rejection issues.

Plans/Expected Benefits for attending this conference**:**

- Present results of two (2) research projects to the greater energy community and interaction with other researchers engaged in thermal energy storage.
- Learn about results of thermal energy storage research of others at the presentations.

Heath Turner, Ph.D. 2012 American Institute of Chemical Engineering Annual Meeting

I plan to deliver a presentation at the Annual AIChE Conference in Pittsburgh, PA (October 28th – November 1, 2012). The title of my presentation is "Simulation and Experimental Benchmarking of the Thermophysical Properties of *N*-Functionalized Alkylimidazoles", and we are using these imidazole compounds to facilitate CO2 capture from coal-fired power plants. Our primary goal is to develop low cost and energy-efficient technologies for post-combustion CO2 capture, and we have assembled a nice team of computational and experimental experts to advance membrane-based technologies for these applications. Since the majority of our domestic energy originates from coal-fired power plants, the topic of CO2 capture and sequestration is a high-priority focus for the Department of Energy. In particular, the proximity of the AIChE Annual Meeting this year to NETL should attract a larger than normal number of DOE staff to the meeting. This should provide an excellent opportunity for me to develop strategic interactions with some of the program managers at DOE.

Sushma Kotru, PhD Amer. Vacuum Society International Symposium and Exhibition

The purpose of the travel is to attend the AVS 59th International Symposium and Exhibition at Tampa, FL. The symposium is scheduled Oct.28th – Nov 2, 2012. AVS is a very well recognized meeting where researches, scientists and faculty from various areas come together to present their latest scientific findings. This meeting provides an opportunity to interact not only with fellow faculties from other Universities but also with scientists and researchers for many national labs including DoE labs. I would like to attend this meeting for following reasons/benefits:

(i) Present a paper at the meeting. Our paper entitled, "Effect of Top Electrodes on the Photovoltaic Properties of Ferroelectric PLZT Thin Film Capacitors" has been accepted as an oral presentation in *Thin Films for Energy Applications* session.

(iii) Work presented at AVS meeting can be submitted for publication in the Journal of vacuum science and technology (JVST).

(ii) Make contact with scientists from national labs for potential future collaborations.

(iii) I am a member of the technical committee for the AVS MEMS/NEMS. Attending this conference will provide me an opportunity to attend the annual meeting of the MEMS/NEMS group. Interaction and acquaintance with Committee members also could lead to fruit full collaborations.

(iv) I would like to initiate collaboration with Argonne National Lab for a future research project. I intend to submit a grant to visit a DOE National Laboratory for conducting research in near future. Generally there is a good participation from ARL scientists in AVS meetings, so it will provide me an excellent opportunity to initiate collaboration with DoE scientists.

Yousef M. F. El Hasadi, PhD Candidate, Technical Meeting of Society of Eng. Science

Nanoparticle-enhanced phase change materials (NEPCM) were proposed recently as alternatives to traditional phase change materials due to their enhanced thermophysical properties. In this study, the effect of using nanoparticles with different properties, on the morphology of the solid-liquid interface and the evolving concentration, during solidification has been reported numerically. The numerical method that has been used was based on the one-fluid-mixture model. The model takes into account the thermal as well as the solutal convection effects. A square cavity was used in the simulation. Three different NEPCM suspensions were used for the current study, and those are copper (Cu)-water, alumina oxide (Al2O3)-water, and copper oxide (CuO)-water. The suspensions with the nanoparticle sizes of 5nm and 2nmwere solidified from bottom. The temperature difference between the hot and cold sides was 5 degrees centigrade and the loading of the nanoparticles that have been used in the simulation was 10% by mass. The results obtained from the model were compared with those existing in the literature, and the comparison was fair. The solid-liquid interface for the case of NEPCM with 5 nm particle size was planar throughout the solidification process for the three suspensions used in the study as shown in Figure 1. However, for the case of the NEPCM with particle size of 2 nm, the solid-liquid interface evolved from planar stable shape to unstable dendritic structure, as the solidification process proceeds with time as it is illustrated in Figure 2. This was attributed to the constitutional supercooling effect. The shape and the distribution of the dendrites are different depending on the nanoparticle type that was used as shown in Figure 3. The thermo-solutal convection cells are clearly seen for the case of aluminum oxide (Al2O3) NEPCM. This can be attributed to the lower density if it is compared to that of copper (Cu), and copper oxide (CuO) nanoparticles. It was also found that the concentration of the copper (Cu) nanoparticles on the liquid side of the interface was higher if it is compared with other two nanoparticles used in the study.

Plans for attending this conference:

- Present the outcomes of the recent research and receive feedback, suggestions and constructive criticism from other experts in this field.
- Observe the results of similar work of other researchers in this field.
- Meet other researchers in this field and networking.

Hasan Babaei, PhD Candidate SES 49th Annual Technical Meeting

By utilizing molecular dynamics (MD) simulations, we investigate the relationship between the crystalline structure of paraffins (n-octadecane as specific material) and its thermal conductivity and the thermal conductivity enhancement achieved by increasing the alignment of paraffin molecules in a particular direction by introducing cylindrical carbon nanotubes (CNT) and planar grapheme sheets into the paraffin. We observed that the thermal conductivity of a perfect crystalline structure in the direction of molecular axis is nearly one order of magnitude greater than the thermal conductivity value for the regular paraffin solid. Our results indicate that introducing CNT and graphene into paraffin leads to a considerable enhancement in thermal conductivity along the direction parallel to the CNT's symmetry axis or graphene plane. This happens due to the fact that these nanofillers increase the alignment of molecules along a particular direction. An alignment parameter was defined to quantitatively study the

relationship between the thermal conductivity and the alignment of molecules along a particular direction. The calculations show that, generally, the thermal conductivity increases with the alignment parameter.

Plans for attending this Society of Engineering Sciences conference:

- Present the outcomes of the recent research and receive feedback, suggestions and constructive criticism from other experts in this field.
- Observe the results of similar work of other researchers in this field.
- Meet other researchers in this field and networking.

Mahmoud Moeini Sedeh, PhD Candidate SES 49th Annual Technical Meeting

This part of our research is focused on the numerical investigation of solidification and melting of phase change materials, infiltrated in a porous structure, under the presence of voids. This is a fundamental process during the utilization (i.e. charge/discharge cycles) of PCM/NePCM in thermal energy storage (TES) systems. Initial void formation occurs in TES systems in infiltration process, during which PCM/NePCM is impregnated into highly-porous, highly-conductive structures. Presence of such voids affects the solidification and melting processes due to different thermophysical properties of void (usually air) with infiltrated PCM/NePCM. Using a pore level modeling approach, this research covers the numerical investigation of solidification and melting processes of PCM/NePCM infiltrated into graphite foams. Moreover, formation of another void, known as shrinkage void happens occurs during the solidification due to the difference between densities of liquid and solid PCM/NePCM. A numerical approach was employed based on the combination of Volume-of-Fluid (VOF) and enthalpy methods to cover the phase change processes. The proposed method takes into account the effects of surface tension and pressure gradient (e.g. major driving forces in pore level) and is able to predict phase change details as well as the amount and distribution of shrinkage void during the solidification. Simulation results indicate that the amount of shrinkage void during the Solidification is in agreement with theoretical volume change of the PCM/NePCM. The shrinkage void fades out during the melting process and after melting the void content is equal to the initial void content, i.e. infiltration void. The amount of predicted shrinkage void is in agreement with theoretical volume change of PCM during phase change. Solidification and melting patterns were identified via transient numerical results during the solidification and melting processes. Furthermore, the simulation and verification of infiltration voids were performed prior to this research and is currently in the process of journal publication.

Plans for attending this Technical Meeting of the Society of Engineering Sciences:

- Present the outcomes of the recent research and receive feedback, suggestions and constructive criticism from other experts in this field.
- Observe the results of similar works by other researchers in this field.
- Meet other researchers in this field and networking.

Mr. Mahdi Nabil, PhD Student SES 49th Annual Technical Meeting

Copper oxide (CuO) nanoparticles, stabilized by sodium oleate acid (SOA), were used to enhance the thermal conductivity of eicosane (C20H42) as the base PCM (phase change material). Thermal conductivity measurements of NePCM (nano-

structure enhanced phase change material) samples were performed using transient plane source (TPS) technique. The dependence of thermal conductivity on temperature, method of solidification and the loading of CuO nanoparticles were investigated. At first, liquid samples (0, 1, 2, 5 and 10 wt%) were poured into small diameter molds and were degased within a vacuum oven. The molds were then subjected to either ambient solidification or ice-water bath freezing method. With the aid of a controllable temperature bath, measurements were conducted at various temperatures between 10 and 35°C for the solid samples. At each temperature, three different runs were performed and the standard deviation of data was less than 5%. Measured thermal conductivity data of the composites were found to be nearly independent of the measurement temperature for a given loading of CuO nanoparticles regardless of the solidification scheme. Irrespective of the solidification method, as the melting temperature was approached, thermal conductivity data of the solid disks rose sharply for both sets of experiments. The composites prepared using the ice-water bath solidification scheme consistently exhibited lower values of thermal conductivity when compared to the samples which prepared under ambient solidification method. XRD analysis for solid samples was performed as well to explain the phenomenon from the crystal structure point of view.

Plans for attending this Technical Meeting Society of Engineering Science conference:

- Present the outcomes of the recent research and receiving feedbacks, suggestions and constructive criticism from other experts in this field.
- Observe the results of similar work of other researchers in this field.

Kevin Chou, PhD Oak Ridge National Laboratory

I plan to visit with Dr. Ryan Dehoff, Materials Processing & Manufacturing Group, Materials Science & Technology Division at Oak Ridge National Laboratory (ORNL).

The purpose of the proposed visits to DOE's ORNL is to initiate a meeting on a research subject: additive manufacturing (AM) technology. I currently direct a project, entitled "Electron Beam Additive Fabrication (EBAF) Technology for Rapid Manufacturing of Space Vehicle Hardware," funded by NASA EPSCoR. On the other hand, Dr. Ryan Dehoff and his colleagues at ORNL have also been working on the EBAF technology for energy-efficient manufacturing. I have talked with Dr. Dehoff regarding this research and we decided I should visit their facility and give a seminar to their group in this field. The anticipated benefits of this visit are (1) increased visibility of our AM research, (2) better familiarity with the AM interest/expertise at ORNL, and (3) increased potential in collaboration with ORNL researchers.

Mohammad Hossain, PhD Student American Chemical Society Meeting

I am a student of Dr. German Mills at Auburn University. I request travel funds to attend and present a poster in SouthWestern Regional ACS meeting at Hilton Baton Rouge Capitol Center, Baton Rouge, LA.

Jason Bara, PhD AIChE National Convention

Matthew Shannon and Michelle Hindman, Graduate Students

I plan to attend the AIChE National Convention in Pittsburgh, PA from 10/28/12 – 11/2/12. I will give several presentations at this conference on my energy-focused

research in the areas of clean energy processes and carbon capture. This request is highly relevant to the DOE EPSCoR funding as Pittsburgh is the home to the DOE National Energy Technology Laboratory (NETL). I expect DOE program managers, especially from NETL, to be in attendance. Specifically, I will plan to meet with several NETL program managers including Andy Aurelio and Lynn Brickett during my time at the conference. I have developed a good relationship with Mr. Aurelio and Mrs. Brickett over the past several years and this is an excellent opportunity to discuss new funding announcements and other ways that my research group can interact with DOE through NETL. I will also plan to bring my graduate student, Mr. Matthew Shannon with me to this conference, and am also requesting funds for him to attend the conference, where he will give a presentation and also interact with DOE/NETL program managers. With Dr. Bara's complimentary registration, another graduate student, Michelle Hindman was able to attend.

Melanie Beazley, Post Doc Institute for Genome Sciences

I plan to attend a training conference at the Institute for Genome Sciences at the University Of Maryland School Of Medicine on November 12-16, 2012 in Baltimore, Maryland.

Margaret Liu, PhD National Conference of the American Chemical Society
Chao Ma, Graduate Student

I request travel support to present my bioenergy-related research presentation at a National Conference of American Chemical Society (ACS). I plan to attend the 245th Annual ACS Conference in New Orleans, Louisiana (April 7-11, 2013). The title of my presentation is "Metabolically engineer *C. tyrobutyricum* to improve the productivity and tolerance of biobutanol production". Biobutanol can be used as a substitute for gasoline, and converted to bio-jet (JP8) and biodiesel fuels. The goal of this research is to construct a novel engineered microorganism to meet the requirement of high biofuel production in fuel market. Considering the similar energy content of butanol to that of gasoline and the environment friendly advantage of biofuel production, the construction of an efficient biobutanol producing stain is a promising research topic for the Department of Energy. The Program Theme of the 245th ACS is Chemistry of Energy & Food, so a large number of DOE staff and researchers are expected to attend the conference. This would provide me a valuable opportunity to communicate with other biofuel researchers and interact with some DOE program managers.

Jason Bara, PhD Carbon Capture Utilization and Sequestration Conference

I wish to attend the Carbon Capture Utilization and Sequestration Conference in Pittsburgh, PA from May 13-16, 2013. I will give two presentations at this conference on my energy-focused research in the areas of clean energy processes and carbon capture. This request is highly relevant to the DOE EPSCoR funding as Pittsburgh is the home to the DOE National Energy Technology Laboratory (NETL). I expect a number of DOE program managers, especially from NETL, to be in attendance. Specifically, I will plan to meet with several NETL program managers including Andy Aurelio and Lynn Brickett during my time at the conference. I have developed a good relationship with Mr. Aurelio and Mrs. Brickett over the past several years and this is an excellent opportunity

to discuss new funding announcements and other ways that my research group can interact with DOE through NETL. Furthermore, this conference is well-attended by other DOE agencies including the Office of Science, ARPA-E and presents opportunities to network with additional program managers and DOE staff.

Jason R. Darvin, Undergraduate Student American Chemical Society Meeting

Synthesis of nanometer-sized Ag particles dispersed in hydrocarbons is of current interest due to potential applications of the colloids as agents for efficient heat transfer. Earlier studies showed that only dilute Ag colloids were accessible via photochemical reactions. Presented here is a simple technique that can yield stable Ag colloids with concentrations as high as 1% by weight. Ag nanoparticles were achieved by reduction of Ag(I) ions in dodecane, which acted as solvent and also as a reducing agent, whereas oleoyl sarcosine served as a particle stabilizer. The colloids were characterized by UV-Vis spectroscopy, optical microscopy, X-Ray diffraction, and transmission electron microscopy. The particles consist of fcc silver and are nearly spherical in shape with an average diameter of 6.4 nm. Optical microscopy has shown that 450 nm particle aggregates coexist with the nanometer-sized Ag particles in solution.

Plans for Attending the Conference:

- Give an oral presentation on the synthesis of concentrated silver nanoparticles in dodecane (NePCM).
- Attend presentations on related systems.
- Meet with other chemist/engineers studying similar problems.

Robert Barletta, PhD Brookhaven National Laboratory

I request travel support to visit Brookhaven National Laboratory in Upton New York to conduct a proof-of-concept test on the use of the infrared microscope of the U2B beam line of the NSLS. The proposed date of the travel is the week of July 7, 2013. It is anticipated that 5 days will be necessary to perform these experiments. The U2B beam line is required because it possesses an infrared (FTIR) microscope capable of measuring spectra on biological materials with high infrared intensity down to energy of ~500 cm^{-1}.

The specific biological material to be studied in these experiments is marine phytoplankton such as Phaeocystis which are known to produce biogenic sulfur compounds of critical importance to the global sulfur cycle. These compounds include dimethyl sulfoxide (DMSO) and dimethylsulfoniopropionate (DMSP). Both DMSP and DMSO have been speculated to provide osmoregulation within phytoplankton so that the ability to detect their presence directly through spectroscopic means would advance an understanding of their role in the environment from both a global and species-specific perspective. Estimates of their intracellular concentrations of these chemicals in certain marine algae range into the 100's of mM, making them attractive candidates for analysis with techniques involving vibrational spectroscopy such as infrared. Critical for such a technique is the ability to access the characteristic carbon-sulfur stretching mode of these molecules, which occur at < 700 cm^{-1}. Because of the anticipated intensity of these modes as well as their low frequency the high brightness of the facility at the NSLS is of critical importance. It is anticipated that scoping test will be conducted

on both the freeze-dried and hydrated plankton. If possible mapping of presence of these compounds on a cell specific basis will also be investigated. Successful completion of these tests will demonstrate the usefulness of characterizing biogenic sulfur in phytoplankton and will serve as the basis for a follow-on proposal to characterize other species as well as the effects of environmental conditions on the production of intracellular biogenic sulfur.

Representatives of the U2B user group have been contacted concerning these experiments and have indicated a willingness to allocate beam time for them during the late spring and early summer. A proposed travel budget is given in the table below. One third of total travel cost ($504.40) will be provided by the University Of South Alabama College Of Arts and Sciences' Support and Development Award. An email of interest and pending BNL approval for this work is attached. We are currently discussions with L. Miller of BNL concerning the timing and requirements for these experiments. Travel has been approved by the University of South Alabama contingent upon a final BNL approval being received. This BNL approval will be forwarded as soon as it is available.

Jeffrey Carver, PhD Oakridge National Laboratory
Dustin Heaton, Graduate Student

We are requesting travel support for Mr. Dustin Heaton to spend 2 months (June and July 2013) at Oak Ridge National Laboratory. We have reached an agreement with Markus Eisenbach who leads the Locally-Self-Consistent Multiple-Scattering Code (LSMS) team at Oak Ridge to host Dustin for this time period. The LSMS code solves the Schrodinger equation at zero temperature using linear scaling first principles electronic structure calculations and statistical physics of magnetic systems. The code was awarded the Gordon-Bell prize in 1998 and 2009. The LSMS team is currently rewriting the code and is interested in revising the code architecture to bring it closer to current software engineering best practices and ensure its future viability. One key software engineering best practice is ensuring the maintainability of the software, i.e. making sure that the software is easily changeable over time. Our main focus will be working with the LSMS team to assess their use of software engineering practices to ensure the development of maintainable software and augment those practices where they appear to be lacking.

To perform this work, we will begin with surveys and interviews with team members to determine their current approach to developing maintainable software. We will also survey the team members regarding their knowledge of software engineering techniques that industrial software engineers use to create maintainable software. Using the results of the surveys and interviews, we will identify any relevant software engineering techniques with which the team is not familiar. We will train the team members on the use of those techniques and then help the team implement them into their design process. In particular, if the team leader says that he is trying to enforce the use of some specific software engineering practices, but the surveys show that the team members do not possess the knowledge required to implement the practice, we will focus on those techniques. Some specific techniques upon which we will focus include: code reviews, refactoring, automated testing, and iterative development. Software engineers have shown these techniques help produce maintainable software in

industrial software development and we expect they will have similar results in scientific software development.

This extended visit to Oak Ridge National Laboratory should be beneficial in deepening an existing relationship that Dr. Carver has with other researchers at Oak Ridge. Specifically, it will also help Mr. Dustin Heaton begin building relationships that will be beneficial as he continues his dissertation work, based at least partially upon the results from this visit. We also anticipate that the results of the work conducted during this visit will be publishable within the software engineering and computational science literature. Finally, we expect this visit to have a positive impact on the LSMS team by helping them create more maintainable software and by increasing their knowledge of useful software engineering practices.

Robert Jackson, PhD Society of Tribologists and Lubrication Eng Conference
Hamed Ghaednia, Graduate Student and Hannah Neuffer, Undergraduate Student

We are currently working on characterizing "enhanced lubricants using nano particle additives (nano-lubricants)" the goal of which is to detect and quantify the effect of nanoparticles on the tribological properties of lubricants. Nano-lubricants have proven to possess great tribological benefits, especially in terms of friction enhancement. Full understanding of the mechanisms governing a nano-lubricants' performance would result in the design and employment of optimal nano-lubricants. A carefully designed and prepared nano-lubricant could reduce friction and wear which is the main source of energy and maintenance losses in industry and even consumer products such as automobiles. This would bring about substantial energy savings and capital savings in virtually all lubrication systems.

Our ongoing research includes the analytical and experimental analysis of nano-lubricants in contact between rough surfaces and measuring the friction and wear coefficients of the nano-lubricants in different lubrication regimes. Mechanisms which help nanoparticles improve the tribological behavior of lubricants is one of the most complicated and least characterized territories in the field of tribology. Our experimental findings suggest that multiple mechanisms are governing the tribological properties of nano-lubricants. The concentration of nanoparticles and the working conditions specify how much each mechanism contributes. This may result in drawbacks such as improving the friction coefficient at the cost of having an excessive wear rate. Therefore, a clear understanding of the mechanisms behind the effect of nanoparticles on lubricants seems to be a key aspect in this field of research.

The goal of the paper we are presenting at this conference is to investigate the effect of silver nanoparticle additives on the friction, wear and tribological properties of polyethylene glycol lubricants (PEG 600). Experimental investigations have been carried out using a pin-on-disk test setup. Wear is measured using surface profilometry which reports the worn volume of the surface. The tested samples are submerged in a small reservoir of the nano-lubricant while the test is running. Different studies explored the effect of normal force and particle concentration on friction and wear. The nanoparticle/surface interaction has also been investigated using x-ray photoelectron spectroscopy (XPS) and auger electron spectroscopy (AES). Results show that particles are effective in reducing the friction. Moreover, based on the results, different

enhancing mechanisms of nanoparticles have been discussed and the possible mechanisms have been elucidated.

Through attending this conference I plan to:

- Present our group's recent findings and receive helpful feedback, suggestions and constructive criticism from other experts in this field, in addition to observing the results of their recent work.
- Present results of energy-related research.
- Meet with Dr. Steve Przesmitzki, Fuels and Lubricants Technology Manager at the US DOE. He is an invited speaker at this conference.
- Meet and network with other researchers in the nano-lubrication field.

Zhang O'Neill, PhD ASHRAE Annual Meeting

I wish to attend the 2013 ASHRAE (American Society of Heating, Refrigerating and Air Conditioning Engineers) Annual Meeting at Denver, CO from June 23rd to June 26th. I will be presenting a paper, entitled "Development of Control-Oriented Models for Model Predictive Control in Buildings", in the conference.

Purpose

- Present results of energy-related research. This paper is from a research project sponsored by DOE Energy Efficient Building (EEB) HUB.
- During this meeting, I will meet with program managers and researchers from DOE Building Technology Office (BTO) and national labs (i.e., LBNL and PNNL) to discuss potential collaborations in the area of energy efficient buildings.

Financial Report

The University of Alabama submitted the SF425 financial report through 9/30/13 to DOE in late October 2013. The University of Alabama recently received two large invoices from the Research Cluster led at Auburn University and will process those xpeditiously. Approximately $ 150K remains in Research Cluster funds while approximately $ 35K is available for HRD travel.

FEDERAL FINANCIAL REPORT

(Follow form instructions)

1. Federal Agency and Organizational Element to Which Report is Submitted	2. Federal Grant or Other Identifying Number Assigned by Federal Agency (To report multiple grants, use FFR Attachment)	Page	of
DOE	DE-SC0002470	1	pages

3. Recipient Organization (Name and complete address including Zip code)
The University of Alabama, Contract & Grant Accounting
Box 870135
Tuscaloosa, AL 35487 - 0135

4a. DUNS Number	4b. EIN	5. Recipient Account Number or Identifying Number (To report multiple grants, use FFR Attachment)	6. Report Type	7. Basis of Accounting
045632635	1-63-6001138-AL	GR22820	X Quarterly ☐ Semi-Annual ☐ Annual Final	X Cash ☐ Accrual

8. Project/Grant Period From: (Month, Day, Year)	To: (Month, Day, Year)	9. Reporting Period End Date (Month, Day, Year)
8/15/2009	8/14/2015	9/30/2013

10. Transactions	Cumulative
(Use lines a-c for single or multiple grant reporting)	
Federal Cash (To report multiple grants, also use FFR Attachment):	
a. Cash Receipts	$1,561,270.95
b. Cash Disbursements	$1,561,270.95
c. Cash on Hand (line a minus b)	$0.00
(Use lines d-o for single grant reporting)	
Federal Expenditures and Unobligated Balance:	
d. Total Federal funds authorized	$2,199,000.00
e. Federal share of expenditures	1,561,270.95
f. Federal share of unliquidated obligations	308,655.20
g. Total Federal share (sum of lines e and f)	$1,869,926.15
h. Unobligated balance of Federal funds (line d minus g)	$329,073.85
Recipient Share:	
i. Total recipient share required	$1,006,859.00
j. Recipient share of expenditures	822,984.84
k. Remaining recipient share to be provided (line i minus j)	$183,874.16
Program Income:	
l. Total Federal program income earned	$0.00
m. Program income expended in accordance with the deduction alternative	-
n. Program income expended in accordance with the addition alternative	-
o. Unexpended program income (line l minus line m or line n)	$0.00

	a. Type	b. Rate	c. Period From	Period To	d. Base	e. Amount Charged	f. Federal Share
11. Indirect Expense		44.50%			180,246.47	80,209.68	71,960.41
				g. Totals:	180,246.47	80,209.68	71,960.41

12. Remarks: *Attach any explanations deemed necessary or information required by Federal sponsoring agency in compliance with governing legislation:*
Cash balance is for charges in process that have not hit the GL. For questions plese contact Alaina Peoples at 205-348-8118 or apeoples@fa.ua.edu

13. Certification: **By signing this report, I certify that it is true, complete, and accurate to the best of my knowledge. I am aware that any false, fictitious, or fraudulent information may subject me to criminal, civil, or administrative penalities. (U.S. Code, Title 218, Section 1001)**

a. Typed or Printed Name and Title of Authorized Certifying Official	c. Telephone (Area code, number and extension)
Tammy Hudson, Associate Director, Contract & Grant Accounting	205-348-8117
	d. Email address thudson@fa.ua.edu
b. Signature of Authorized Certifying Official Tammy Hudson	e. Date Report Submitted (Month, Day, Year) 10/30/2013
	14. Agency use only:

Standard Form 425
OMB Approval Number: 0348-0061
Expiration Date: 10/31/2011

Paperwork Burden Statement
According to the Paperwork Reduction Act, as amended, no persons are required to respond to a collection of information unless it displays a valid OMB Control Number. The valid OMB control number for this information collection is 0348-0061. Public reporting burden for this collection of information is estimated to average 1.5 hours per response, including time for reviewing instructions, searching existing data sources, gathering and maintaining the data needed, and completing and reviewing the collection of information. Send comments regarding the burden estimate or any other aspect of this collection of information, including suggestions for reducing this burden, to the Office of Management and Budget, Paperwork Reduction Project (0348-0061), Washington, DC 20503.

TM 10/30/13

NEPCM Research Cluster Summary

A stepwise procedure was developed to produce surface-coated spherical CuO nanoparticles useful for the preparation of colloids with concentrations of up to 20 wt% in a variety of hydrocarbons. Long-term stability against particle precipitation was observed for concentrations ≤ 5 wt%. Copper colloids stable in air-free octane were prepared via a simple photochemical method in which the solvent acted as the agent that reduced Cu(II) ions. Detailed mechanistic information about the generation of this novel colloid enabled utilization of the photosynthetic method to achieve stable colloids of Ag, Pd and Pt in alkanes. The photochemical studies provided knowledge about the key role played by oleoyl saecosine as a particle stabilizer. Utilization of this knowledge enabled optimization of reaction parameters (choice of solvent and amount of stabilizer) that ultimately resulted in a very straightforward thermal procedure for the synthesis of concentrated Ag colloids in alkanes. Despite their seemingly ideal properties, only modest enhancements in thermal conductivity were exhibited by the Ag colloids.

Thermal conductivity of the developed colloids were measured in both liquid and solid states using the transient planar source technique. No anomalous improvement of thermal conductivity beyond those predicted by the effective media theory was observed. Molecular dynamics-based non-continuum simulations of freezing of hydrocarbons in presence of nanoparticles, nanotubes and graphene were conducted. Nanotubes and graphene structures provided templates that promote crystallization of the phase change material leading to improved thermal conductivity. Infiltration of phase change materials into pores of carbon foam and subsequent freezing and melting of the system were investigated both computationally and experimentally. Presence of a gas void formed during infiltration was shown to affect the melting/freezing times and the improved thermal conductivity values. Continuum modeling of colloids using a two-fluid model that accounted for rejection of the suspended particles enabled to capture growth of dendritic structures during freezing of colloids.

Many approaches to separate the nanoparticles already suspended in hydrocarbons were studied. The specific colloidal mixture of dodecane ($C_{12}H_{26}$) and CuO nanoparticles (1% - 5% mass fraction and 5-15 nm size distribution) was considered. The identified methods include (i) distillation under atmospheric and reduced pressure, (ii) high speed centrifugation, (iii) destabilization of the nanoparticles by adding chemical agents thereby inducing gravitational precipitation, (iv) silica-column chromatography, (v) silica adsorption and (vi) nanofiltration. Performance of these separation methods was analyzed in relation to their effectiveness.

Utilization of colloids in conjunction with microfluidics for microelectronics cooling applications was investigated. A platform for studying microelectronics cooling methods was fabricated and characterized. Both conventional cooling methods and novel cooling methods using microchannels and NePCM were investigated. Further increases of cooling were achieved by switching from PCM to NePCM. A fundamental investigation of NePCM thermal conductivity using non-spherical particles synthesized using stop flow lithography, a microfluidics-based method, was also studied.

A group of undergraduate students concentrated their efforts on development of Molecular Dynamics, Monte Carlo, and Lattice Boltzmann modeling and simulation techniques, and the associated Visualization and Computer Graphics tools. The computational tools were applied to simple fluids for determination of thermophysical properties and thermal transport colloidal systems with some success.

Tribological effect of nanoparticle colloidal lubricants was investigated. Tribological properties of a nano-lubricant that consists of CuO nanoparticles (9 nm average diameter) suspended in mineral base oil using sodium oleate (SOA) as a surfactant are investigated. Nano-lubricants with concentrations of 0.5, 1 and 2 %wt were investigated using a disk-on-disk friction and wear test in the boundary lubrication regime. The CuO/SOA nanoparticle additives reduce the friction between the lubricated. Wear analysis based on profilometry suggest that the wear increases with concentration up to a 1 %wt and then decreases for a 2 %wt nano-lubricant. SEM/EDS results suggest that nanoparticles are present on the surfaces after the tests. Different possible mechanisms for nanoparticles at the boundary lubrication were evaluated and reduction in the real area of contact was suggested as the possible mechanism. Modeling of nanoparticles in contact between surfaces uses two sub-models to handle different scales of contact, namely the nano-sized particles and micron-sized roughness features. The results suggest that particles would reduce the real area of contact and therefore decrease the friction force. Also, particles could induce abrasive wear by scratching the surfaces. Friction tests for a nano-lubricant in the elasto-hydrodynamic lubrication regime show that the presence of nanoparticles reduces friction. Through surface analyses and molecular dynamics simulation, effectiveness of different interactions in the system was studied. A novel friction reduction mechanism has been deduced, that is the nanoparticles can induce an obstructed flow in the thin film between lubricated surfaces.

Synthesis and thermal conductivity characterization of colloids of CNF/paraffin wax and HHTCNF/$ZnCl_2$ were studied. The paraffin matrix shows that the thermal conductivity enhancements due to 8 wt% HHTCNF doping were 126.3 and 210.8% in the liquid and solid phases, respectively. The LHT grade CNF provided much less thermal conductivity enhancement. Therefore, it has been concluded the thermal conductivity enhancement of a CNF/paraffin NEPCM substantially depends on the phase of the PCM, the loading of CNF and the type of CNF used. For the high temperature HHTCNF/$ZnCl_2$ system, the 8 wt% HHTCNF/$ZnCl_2$ colloid improved the thermal conductivity by almost 200%. Compared with the base paraffin wax PCM, the 8 wt% HHTCNF/paraffin system significantly accelerated the discharging speed and the charging speed to 3 times (340%) and 2 times (200%), respectively. A numerical study of heat dispersion of the liquid-phase NEPCM was performed. Through the unit cell non-isothermal computational fluid dynamics (CFD) simulations, it was concluded that the heat dispersion effect can be approximated as a function of the Peclet number, Reynolds number, and nanoparticle volume fraction. For a simulated micro-channel flow study of a liquid-phase NEPCM consisting of 5% volume-fraction CuO-paraffin, heat dispersion was found to increase the total heat transfer by about 8%.

Background on the NePCM Project

Among the various energy-related nanotechnology opportunities, improvement of the thermal properties of phase change materials (PCM) through introduction of nanostructures was only addressed very recently. Development, characterization, determination of properties and testing of these materials that are widely known as nanostructure-enhanced PCM (NePCM) have progressed dramatically since 2005. Building on the early work of the PI on NePCM, research on the development, characterization, testing, reclamation and utilization of NePCM through dispersion of nanosize particles in alkanes was initiated in August 2009 through the DOE grant DE-SC0002470 (http://www.eng.auburn.edu/nepcm). Original focus was on copper-based nanoparticles dispersed in alkanes. A summary of the major findings of the project are given in this Final Report.

Starting in August 2009, research was initiated on five campuses in Alabama to investigate various topics in relation to the development of stable NePCM as functionality-proven suspensions that can perform over long periods for thermal energy storage. The investigators:

- Dr. Jay M. Khodadadi, Alumni Prof., Mech. Eng., Auburn University,
- Dr. German Mills, Assoc. Professor, Chemistry, Auburn University,
- Dr. Muhammad A.R. Sharif, Assoc. Prof., Aero. Eng. & Mech., The Univ. of Alabama,
- Dr. Tamara Floyd-Smith, Assoc. Prof., Chem. Eng., Tuskegee University,
- Dr. Luis A. Cueva-Parra, Assoc. Prof., Mathematics, Auburn Univ. Montgomery,
- Dr. Robert L. Jackson, Assoc. Prof., Mech. Eng., Auburn University,
- Dr. Kuang-Ting Hsiao, Assoc. Prof., Mechanical Eng. Dept., Univ. of South Alabama,

continued and/or initiated NePCM studies summarized below:

	JMK	*GM*	*MS*	*TFS*	*LCP*	*RLJ*	*KTH*
Preparation/Characterization of Suspensions		X					
Property Measurements	X	X					
Continuum and non-Continuum Modeling	X				X		
Freeze-Thaw Cycling Experiments	X	X					
Tribological Testing of Parrafinic Colloids	X	X				X	
Separation/Reclamation of NePCM	X	X	X				
NePCM in High Flux Electronics	X			X			
Effective Thermal Cond. / Heat Dispersion		X					X

The greatest involvement and responsibility rested with Profs. Khodadadi and Mills of Auburn University who have worked together on the development of NePCM since 2005. Dr. Mills has more than 25 years of experience with colloids and was the ideal person to develop these materials with their desired properties. Dr. Khodadadi has

worked on phase change for 25 years focusing on computational work and testing of thermal storage systems. Other investigators have expertise in filtration/separation of multi-component systems (Prof. Sharif), microfluidic systems (Prof. Floyd-Smith), non-continuum modeling (Prof. Cueva-Parra), paraffinic oils for tribology (Prof. Jackson) and composite materials (Prof. Hsiao). The specific objectives of the NePCM research projects as stated in the original proposal are reproduced here:

1. Prepare suspensions of Cu-based NePCM with desired functionalities of enhanced thermal conductivity and proven long-term stability. Compatibility of hydrocarbon paraffins with both Cu and CuO nanoparticles will be manipulated in preparation of these suspensions. The main challenge is the long-term stability and low sensitivity of these suspensions when subjected to repeated freeze-thaw cycles.

2. Collect the relevant thermophysical properties using the existing and to-be-acquired state-of-the-art instrumentation. The insensitivity of these properties over time and upon successive freeze/thaw cycles will serve as the main success criterion. Moreover, these properties will be used to develop mathematical models for the expedited charge/discharge rates of practical systems that will utilize NePCM. A continuum-Brownian/thermophoretic-diffusion-based mathematical model for simulating the process of melting, ensuing convection and solidification of NePCM will be developed, tested and thoroughly investigated.

3. Study various techniques for eventual separation/reclamation of nanostructures after their useful service life in a given application. A collaborative link between UA and AU's work on development of NePCM will be formed.

4. Investigate utilization of NePCM in high-flux electronics and thermal management of the next generation of microprocessors. This project at Tuskegee will be directly linked to AU's work on the development of NePCM.

5. Development of multi-scale, multi-physics non-continuum modeling tools for NePCM as a science-based initiative that relies on advanced mathematical and computational techniques. Non-continuum numerical tools will be used to predict the thermophysical property enhancement/modifications of NePCM, thus complementing the materials characterization studies at AU.

6. Investigate the enhanced tribological properties of paraffinic oils due to addition of nanoparticles. This project will take advantage of the development of stable nanoparticle-laden paraffinic oils at AU and will investigate the improved lubrication properties of these suspensions.

7. Study the effective thermal conductivity of NePCM (both solid and liquid states) and heat dispersion effect of liquid NePCM.

The following seven (7) sections are prepared by the individual investigators to highlight the essential findings of the various groups as of late 2013.

1. NePCM Development and Characterization
(Dr. German Mills, Chemistry and Biochemistry Department, Auburn University)

During the course of the EPSCoR/DOE implementation grant No. DE-SC0002470 the chemistry group, led by co-PI Mills, committed to achieving basic goals needed to spear head the NEPCM research project. In order to provide materials to fellow members of the research cluster as a basis for the study of thermophysical and tribological properties, the duty of the chemistry group was to prepare and characterize colloids consisting of particles with nanometer dimensions. The main function of these colloids was to serve as nanofluids, which are liquid dispersions of metallic and metal oxide particles that have been claimed to exhibit enhanced thermal conduction.[1] Significant goals of this research was to synthesize concentrated colloids in solvents relevant to PCM that also exhibited long-term stability against precipitation. Preparation of concentrated yet stable colloids is a difficult task that, until the present investigation, had been achieved only for TiO_2 and ZnO systems in polar solvents.[2,3] The higher instability of concentrated colloids is due to the fact that the frequency of inter-particle collisions increases with rising concentration, leading to particle growth and precipitation. Interactions of ionic or polymeric materials with the surface of the particles enhance their stability via decreasing the frequency of reactive collisions. Thus, such materials are used as stabilizers of colloidal suspensions.

Heavy alkanes are considered promising PCM candidates since they are chemically inert, possess large values of the enthalpy of fusion (ΔH_{fus}), and the melting temperature (T_m) of hydrocarbons is a function of their chain length, allowing a wide range of T_m values to be available.[4] Hence, NEPCM systems were envisioned to use long chain alkanes as solvents for the colloidal nanofluids.[5] The requirement of hydrocarbon materials imposed additional hurdles in the synthesis of stable colloidal particles given limited range of chemical precursors that dissolve in alkanes, and also because most ionic and polymeric stabilizers are incompatible with these solvents. For these reasons, methods for the preparation of stable yet concentrated colloids in alkanes existed only in the case of liquid toners relevant to digital printing.[6] However, preparation methods remain proprietary and the toners are based on micron-sized carbon black particles that employ inverse micelles as stabilizing agents. Not only are these very complex systems but they also exhibit limited long-term stability that can be severely compromised when undergoing freezing-melting cycles.
The central task of the chemistry group consisted of preparing Cu-based nanometer-sized particles suspended as concentrated colloids in hydrocarbon liquids. After such goal was accomplished, other metal systems were also successfully explored.

1.1 Synthesis of Cu-based colloids in alkanes

1.1a) CuO colloids: Initial experiments were based on a literature procedure for the preparation of concentrated colloidal rods of CuO in hydrocarbons that employed oleate ions as particle stabilizers.[7] Although the described method was straightforward, the resulting μm-sized rods were only partially stable and the results were not always reproducible. This method also yielded a substantial amount of spherical CuO crystallites exhibiting long-term stability against precipitation. A new approach was,

therefore, developed that used oleate groups for the stabilization of spherical CuO particles. Two main preparation strategies are usually employed to achieve colloids containing nanometer-sized particles: the step-wise method and the direct procedure. In the first approach the particles are synthesized separately, followed by coating of their surfaces with a stabilizer and then dispersion in an appropriate solvent. However, this multistep procedure is laborious, complex and verification that final success has been achieved requires lengthy periods of time. The direct approach is faster as the particles are made directly in the solvent of choice. However, reaction of metal complexes with hydroxides inevitable leads to salts of the spectator ions as exemplified in the case of CuO:

$$CuX_2 + 2MOH \rightarrow CuO + 2MX + H_2O \qquad (1.1)$$

Given that the presence of MX salts invariably compromises the long-term stability of colloids, the multistep procedure seemed most reasonable for the synthesis of oxide particles.

Our procedure involved hydrolysis of Cu(II) ions in basic solutions which also contained sodium oleate (SOA), the Na^+ salt of oleic acid. In this strategy, oleate ions were expected to serve as “capping” agents able to bind to the surface of the growing CuO particles. If surface bonding occurred, the oleate ions were anticipated to regulate particle growth and also inhibit particle aggregation and precipitation. Furthermore, the long hydrocarbon chains present in SOA were expected to facilitate dispersion of the “capped” CuO crystallites in liquid alkanes. The specific chemical steps involved neutralization of oleic acid to form SOA with NaOH, followed by hydrolysis of $Cu(NO_3)_2$ in the presence SOA at 100 °C. Subsequent extensive purification of the resulting material enabled dispersion of the product in numerous hydrocarbons, the exact details of the synthetic procedure have been published.[8] The resulting CuO particles were easily dispersed in numerous hydrocarbons such as hexane (C_6H_{14}), octane (C_8H_{18}), dodecane ($C_{12}H_{26}$) and eicosane ($C_{20}H_{42}$) as well as in other solvents up to concentrations of 20 wt%. Figure 1.1 is an image of a CuO colloid together with a representation of an oxide particle containing bound oleate groups.

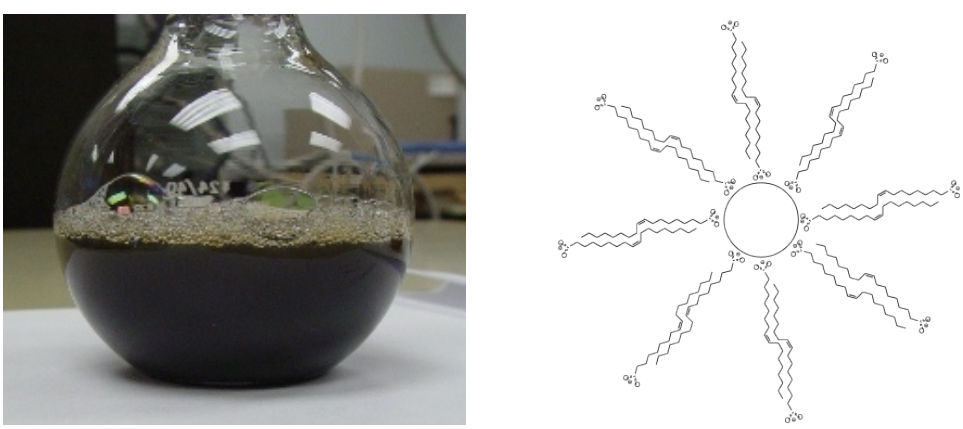

Figure 1.1. Left panel: image of a CuO colloid in octane. Right panel: schematic representation of a CuO particle with bonded oleate groups.

Figure 1.2 shows an X-ray diffraction (XRD) pattern from the particulate material exhibiting signals that match the characteristic reflections of CuO listed in JCPDS card # 41-0254. Reproducible preparation of cupric oxide particulate was achieved with the

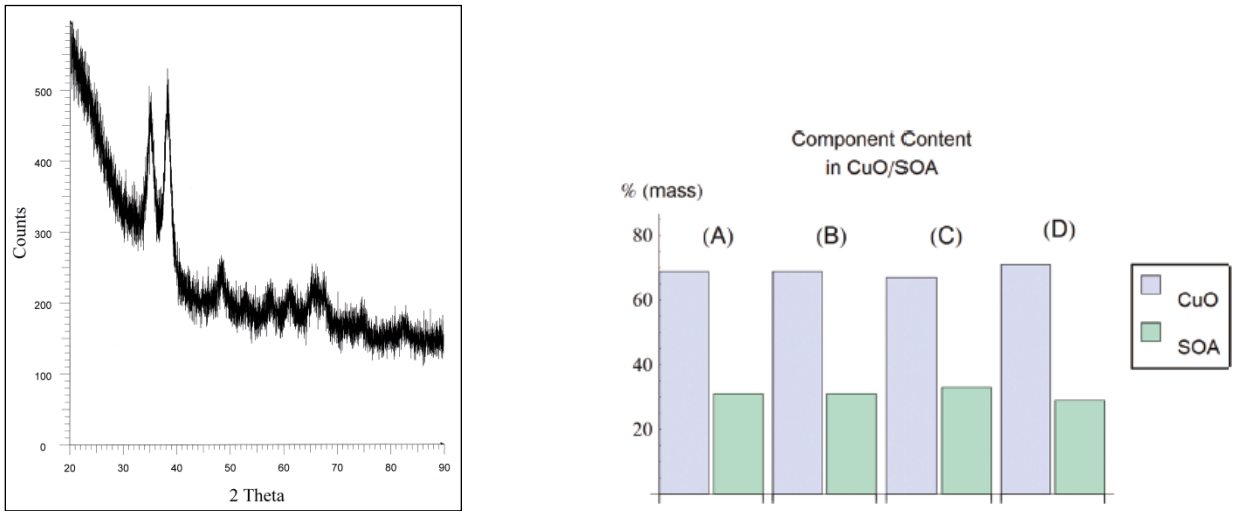

Figure 1.2. Left panel: XRD pattern of CuO particles coated with sodium oleate. Right panel: elementary analysis from four different preparations of CuO/oleate particulates.

employed strategy; included in Figure 1.2 are results from the elementary analysis of 4 different batches of the oleate-coated CuO particulates demonstrating the constant composition of the product. Displayed in Figure 1.3 is a typical image obtained from transmission electron microscopy (TEM) measurements performed on an octane colloid. Similar images resulted when the oxide particles were dispersed in other hydrocarbons, or from colloids aged in the dark for extended times.

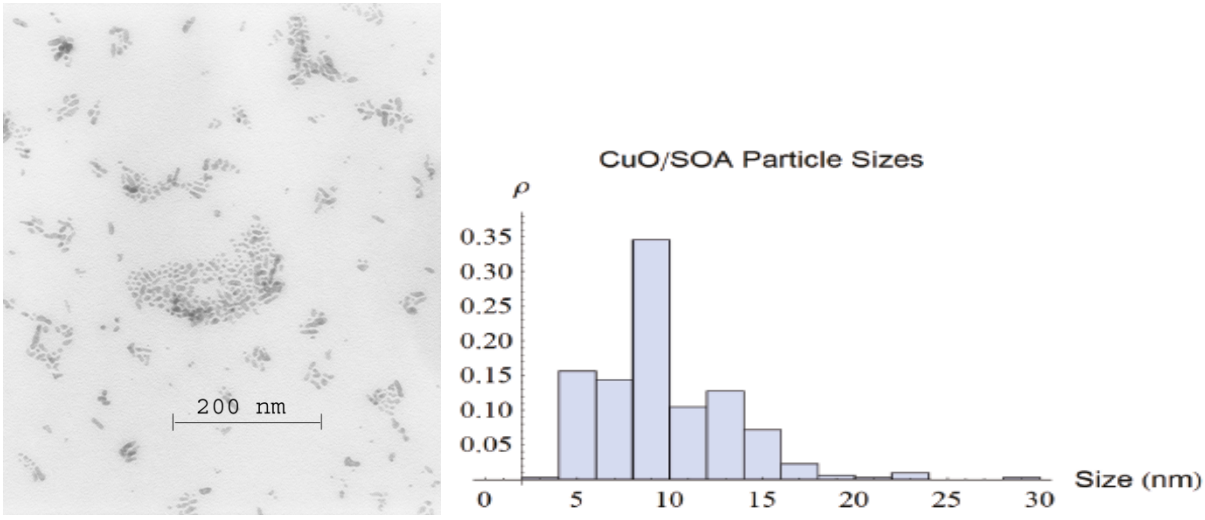

Figure 1.3. Left panel: TEM image obtained from a CuO colloid in octane, scale bar = 200 nm. Right panel: size histogram of the CuO crystallites derived from TEM images.

Included in Figure 1.3 is a histogram of particle diameters that resulted from analysis of over 250 particles. Most of the particles sizes were within 2 to 18 nm and the average diameter (d_{av}) amounted to 9 nm.

Spectrophotometric measurements indicated that the optical spectra of the colloids between 250-600 nm were characterized by a steady increase in absorbance with decreasing wavelength until a maximum was reached at 282 nm. A typical optical spectrum of the CuO particles obtained by dilution of an octane colloid in hexane is presented in Figure 1.4. Systematic studies showed that optical measurements enabled analytical determination of the oxide amount present in the hydrocarbon solvents for CuO concentrations up to 100 ppm. For simplicity, concentrations of dispersed particles were determined from absorbance measurements at 282 nm in hexane (extinction coefficient (ε) = 2010 M^{-1} cm^{-1}) since particle growth or precipitation was not detected upon dilution with C_6H_{14} of CuO colloids prepared in any of the alkane solvents tested.

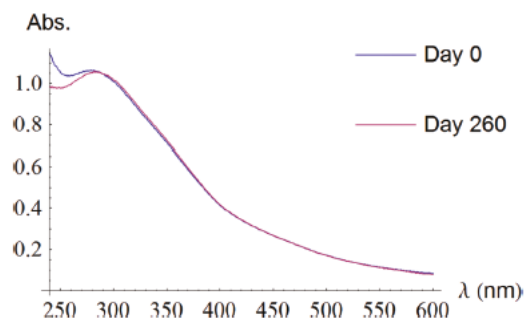

	ΔH_{fus} ($\frac{J}{g}$)	M.P. (°C)
0% CuO/SOA	249.1	35.3 ±0.1
1% CuO/SOA	240.6	35.6 ±0.1
5% CuO/SOA	226.6	35.4 ±0.1
10% CuO/SOA	218.4	35.3 ±0.1
20% CuO/SOA	181.7	35.3 ±0.1

Figure 1.4. Left panel: typical optical spectra of a 1 wt% CuO colloid in octane immediately and after 260 days of preparation. Right panel: table of enthalpies of fusion and melting points (M.P.) of eicosane colloids with increasing CuO concentration.

The spectrophotometric procedure constituted a simple and efficient method for the determination of particle stability at room temperature as a function of time. In this procedure, aged colloids containing high particle concentrations were diluted with hexane to a nominal concentration of about 60 ppm. Colloids containing 20 wt% CuO were stable for periods longer than 2 weeks, and particle stability increased with decreasing oxide concentration. As illustrated in Figure 1.4, an octane colloid containing 1 wt% CuO remained stable after 260 days. In fact, particle precipitation was not detected over a year for colloids with concentrations < 5 wt% irrespective of the hydrocarbon fluid used as a dispersion medium. Such observations are significant given that preparation of stable colloidal CuO dispersions of high concentrations has not been previously realized. Furthermore, colloids that were stable against particle precipitation for extended times were achieved in a variety of solvents including long chain hydrocarbons such as $C_{12}H_{26}$ and $C_{20}H_{42}$. These findings demonstrate the accomplishment of important goals in terms of realizing long-term colloidal stability.

The stability of the resulting CuO colloids enabled determination of some of their thermodynamic properties at different temperatures. Melting temperatures, heats of

fusion and specific heat capacities were determined by means of differential scanning calorimetry (DSC). Figure 1.4 includes a table that summarizes ΔH_{fus} values (latent heats) for CuO colloids in eicosane containing particle concentrations between 1 and 20%. Eicosane was selected as a solvent given that the thermodynamic properties (T_m and ΔH_{fus}) of this hydrocarbon are well suited for NEPCM applications.[5] Also shown in the table are T_m values for eicosane mixtures as a function of CuO concentration. Steady decreases in the enthalpy of fusion result in increasing particle concentration because ΔH_{fus} is a partial molar quantity that depends on the amount of eicosane present in the sample.[9] Increasing the concentration of CuO inevitably decreases the amount of solvent present. The data indicate that a tolerably small decrease (≈ 10%) in ΔH_{fus} of the eicosane mixtures results after introduction of CuO with particle concentrations ≤ 5 wt%.

Interestingly, the data of the table included in Figure 1.4 demonstrates that no change in the melting temperature of eicosane occurred in the presence of oleate-coated CuO. Simple solution properties, such as melting point dependence on solute concentration, are well described within the framework of colligative properties.[9] Because of the presence of SOA in the eicosane colloids, a lowering in M.P. of the hydrocarbon was anticipated on the basis of the colligative behavior of this liquid. From the experimental ΔH_{fus} value, a substantial melting point decrease of 0.78 ºC was calculated for the colloid with 20% CuO, which also contained the largest amount of SOA. The fact that no such change in M.P. was detected implies that the oleate groups were not freely dissolved in the hydrocarbon. Obviously, the oleate species interact strongly with the CuO particles, probably as a result of their attachment to the surface of the oxide material via sturdy covalent/ionic bonds. Achievement of particles exhibiting strong bonding to stabilizers was another goal of this project.

Measurements of heat capacities were carried out on colloids prepared in dodecane and eicosane with CuO concentrations of 1, 5, 10 and 20 wt%. These alkanes were selected since dodecane remains as a liquid in the temperature range of 0-100 ºC whereas $C_{20}H_{42}$ undergoes a solid to liquid phase transition at 35.3 ºC. Preliminary experiments showed that negligible particle precipitation occurred upon exposing the colloids to heating and cooling between 0-100 ºC. Figure 1.5 depicts the evolution of the specific heat capacity at constant pressure (C_p) as a function of temperature for SOA, CuO particles coated with SOA, bare CuO particles and the oxide colloids. The experimental C_p values of bare CuO and of the hydrocarbon solvents match, within 20%, of the published data.[10] As anticipated, C_p increases linearly with temperature for all the systems tested. Also, in agreement with Kirchhoff's law,[9] the presence of CuO decreases the C_p value of the systems because the oxide exhibits the smallest specific heat capacity of all components. However, the decrease in C_p is only minor (≤ 20%) for nanofluids containing particle concentrations equal or lower than 5%, particularly when eicosane was the dispersing medium. Additional tests were completed to assess the heat transport properties of the colloids in which they were exposed to heating and cooling cycles (Newton Law experiments) between 0-100 ºC. The oxide material appeared to affect in a detrimental fashion the ability of the hydrocarbon molecules to transport heat via convection. This effect was particularly noticeable when

CuO particles were present at concentrations > 5 wt% in dodecane, and > 1 wt% in eicosane.

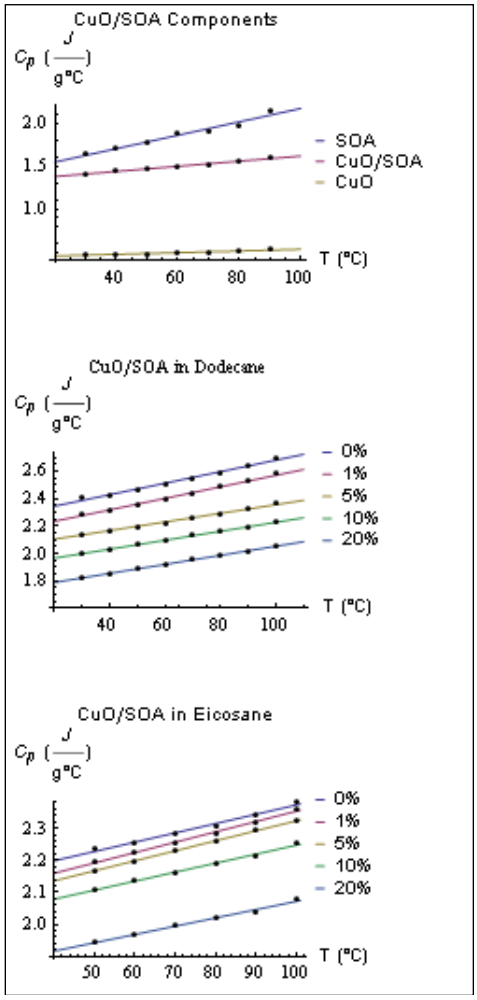

Figure 1.5. Specific heat capacity vs. temperature plots for the CuO/SOA components (A), CuO/SOA in dodecane (B), and CuO/SOA in eicosane (C).

Another interesting outcome is our strategy of preparing CuO particles containing oleate groups strongly bonded to the oxide surface enabled direct dispersion of the crystallites in a variety of hydrocarbons. Hence, transfer of the particles between different solvents was not required, which obviated the need of adapting the CuO material in order to obtain colloids in different hydrocarbons.

Training sessions on the synthesis of the CuO particulate, held in the laboratory of co-PI Mills under the supervision of his graduate student Dan Clary, were made available to graduate students from groups of the NEPCM cluster. However, the most expedient way to ensure timely availability of the desired CuO quantities involved training a chemistry undergraduate student (Jason Darvin) and then hiring him to prepare the material in order to cover the needs of the different groups from the NEPCM cluster.

The data obtained from our thermodynamic measurements indicated that CuO colloids with particle concentrations ≤ 5 wt% were best suited to function as nanofluids. Based on such results, the group of PI Khodadadi performed thermal conductivity (TC) experiments utilizing colloids in cyclohexane with 4 wt% CuO.[5] Thermal conductivity enhancements of about 6% were obtained for both the solid and liquid phases. Despite all the seemingly ideal properties exhibited by the copper oxide colloids, further experiments using eicosane containing up to 10 wt% of the CuO material yielded only a maximum TC enhancement of 7%. In view of these results, our subsequent efforts were devoted to the preparation of Cu and Ag colloids as these metals exhibit more favorable thermal properties than those of CuO.[11]

1.1b) Cu colloids: Establishment of a synthetic path to obtain metallic Cu particles in hydrocarbons exhibiting stability against growth and precipitation was a significantly more challenging goal. The synthesis usually involves reduction of Cu(II) ions by a strong reducing agent, which can be accomplished in water since ionic or polar compounds dissolve easily in this solvent. However, chemical preparation of Cu colloids in low dielectric media has relied on complex procedures that failed to generate stable crystallites mostly due to the incompatibility of the required polar solutes with the non-polar solvent. The strategy selected in the present study used oleoyl sarcosine (OS) as a particle stabilizer since this chemical is soluble in hydrocarbons and is effective at stabilizing Cu and Ag nanoparticle in such solvents.[12] Our approach was based on a direct procedure involving *in situ* generation of highly reducing radicals via photochemical excitation of benzophenone (BP). Excitation of this sensitizer with 350 nm photons results in H-atom abstraction from molecules that function as donors (such as hydrocarbons), generating strongly reduced radicals of BP and of the solvent.[13] In this approach, the alkane solvent also fulfills the role of reducing agent, and is oxidized by the sensitizer utilizing electromagnetic radiation as the driving force. The resulting BP and solvent radicals were expected to reduce Cu(II) ions to metal particles since such transformation is driven in water by a polymeric benzophenone as the sensitizer and a macromolecular H-atom donor.[14]

Numerous long-chain chemicals soluble in hydrocarbons were tested as particle stabilizers, only OS yielded acceptable results. One of the few cupric complexes soluble in alkanes is the Cu(II) dimer containing oleate anions as ligands, $Cu(oleate)_2$; shown in Figure 1.6 is the structure of this compound.[15] Extensive modification of the method described in the literature yielded a reproducible procedure for the synthesis of the dimer. Photolysis of air-free octane solutions containing $Cu(oleate)_2$ and OS with 350 nm photons induced fast fading of the green color from the dimer, forming a colorless Cu(I) solution. The fast discoloration step was followed by a reaction lasting about 20 minutes that yielded a red color, see scheme shown in Figure 1.6. Obviously, metal particles formed since Cu colloids exhibit a red coloration.[14] Confirmation that this was the case resulted from TEM measurements. The top image of Figure 1.7 is a representative TEM image showing the presence of fairly spherical particles. Depicted on the bottom left of Figure 1.7 is a histogram of particle diameters obtained by analysis of about 400 particles; the distribution of sizes ranged from 1.7 to 14 nm with d_{av} = 11

nm. Selected area electron diffraction experiments (SAED) yielded ring patterns characteristic of fcc metallic Cu; the bottom right image of Figure 1.7 was obtained from such

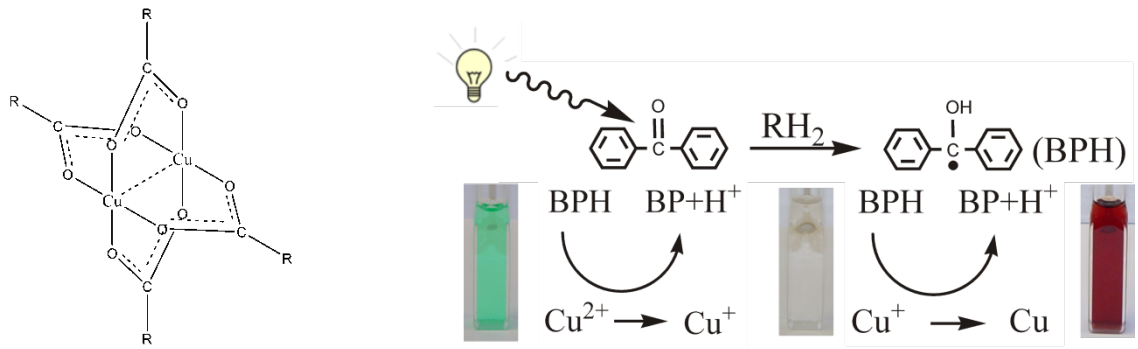

Figure 1.6. Left panel: structure of the Cu(oleate)$_2$ complex. Right panel: schematic representation of the photochemical steps involved in the generation of Cu particles.

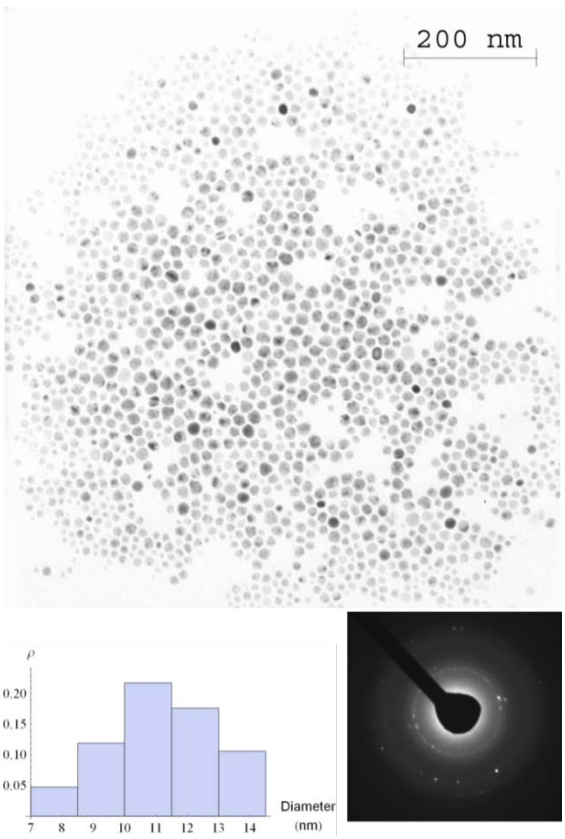

Figure 1.7. Top image: TEM photo from a Cu colloid prepared photochemically, scale bar = 200 nm. Bottom left: corresponding size histogram. Bottom right: SAED image showing a ring diffraction pattern characteristic of Cu crystallites (JCPDS card 4-0836).

experiments. Colloid concentrations of up to 0.02 wt% (3.1 mM) were made with this method. Successful transfer of the colloidal particles from C_8H_{18} to several dry alkanes (including hexane and toluene) was achieved without the need of adapting the Cu crystallites.

Figure 1.8A shows optical spectra collected during illumination of an air-free octane solution of Cu(oleate)$_2$ and OS. Reduction of the Cu(II) oleate complex was followed from the decay of the optical signal of this compound centered at 720 nm. The resulting Cu(I) ions exhibited no distinctive absorbance but their subsequent reduction by the photogenerated BP radicals yielded an absorbance with a wavelength of maximum absorption (λ_{max}) located at 565 nm. This optical signal is a characteristic feature of

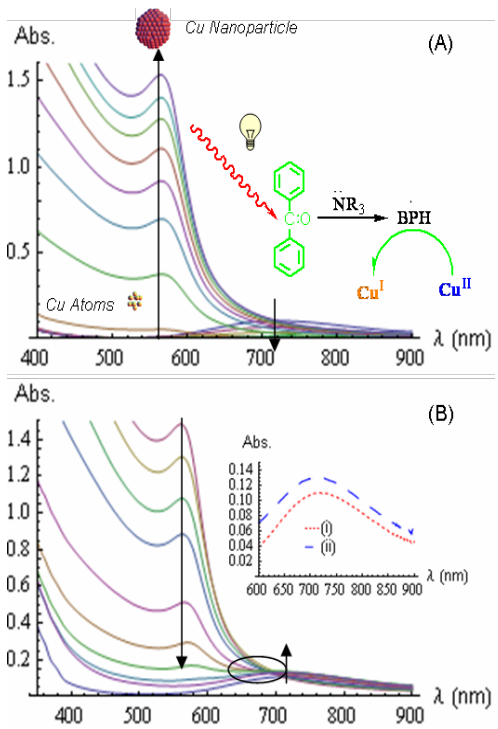

Figure 1.8. (A) Spectra obtained during the photogeneration of Cu particles in C_8H_{18}. (B) Optical changes during the decay of the Cu plasmon upon exposure to O_2 and simultaneous emergence of the Cu(II) signal. The inset shows the initial (i) and final (ii) spectra of the Cu(II) complex after a cycle of particle formation and oxidation.

of colloidal Cu particles also known as a plasmon resonance.[14] The linear dependence of the absorbance at 565 nm on particle concentration (ε_{565} = 2 x 10^3 M^{-1} cm^{-1}) enabled quantitative determination of the amounts of copper crystallites present in the alkane. Shown in Figure 1.8A is the evolution of both optical signals under illumination. Quantum yields (φ) for the reduction of the copper (II) oleate complex ranged from 1.5 to 2 and for metal formation φ was between 0.2 and 0.5. These values are, at least, 50 times higher than those determined in aqueous polymer solutions.[14] A complete study on the mechanism of the particle formation process has been

published.[16] The strong plasmon of the Cu crystallites made possible to determine the stability of the colloids as a function of aging time. Particle precipitation was detected after two months of aging the colloids in the absence of O_2 at room temperature.

Introduction of oxygen into Cu colloids in octane induced a very sluggish oxidation of the metal particles depicted in Figure 1.8B. Complete decay of the metal crystallites occurred in about 12 hours, which contrasts with the instantaneous oxidation of Cu particles noticed in aqueous solutions.[14] Also, an isosbestic point at 697 nm, highlighted in Figure 1.8B, was noticed during the particle decay process. Hence, particle oxidation by O_2 occurred via a two-electron process transforming Cu atoms present on the particle surface directly into the Cu(II) dimer. Indeed, the optical data presented in the inset of Figure 1.8B demonstrates that initial Cu(II) (oleate) species were quantitatively reformed, indicating that formation of Cu particles in octane is a reversible process.

This research achieved preparation of fairly stable Cu crystallites with nm dimensions in alkanes. A significant advantage of the direct photochemical method is that the solvent acted as a reducing agent. Thus, utilization of a reductant is avoided, elimination problems associated with the oxidation products derived from this chemical can affect the stability of the colloidal particles. However, the slow particle oxidation process hampered attempts to determine the TC values of the Cu colloids. Efforts to stabilize the copper crystallites via galvanic displacement of surface Cu atoms by silver ions were unsuccessful. Also, the presence of trace amounts of water induced formation of oxides intermediates, which affected significantly the reproducibility of the method. For these reasons, efforts were made to use this very simple and successful photochemical method for the generation of colloids from metals that are impervious to oxidation by air.

1.2 Photochemical synthesis of Ag, Pd and Pt colloids in alkanes

Successful preparation of colloids via direct reduction of metal ions was constrained by the availability of suitable metal complexes soluble in alkanes. The complexes silver neodecanoate (AgOOR), $Pd(acac)_2$ and $Pt(acac)_2$ (where acac = acetylacetonate ion) were suitable precursors given their reasonable solubility in hydrocarbons.

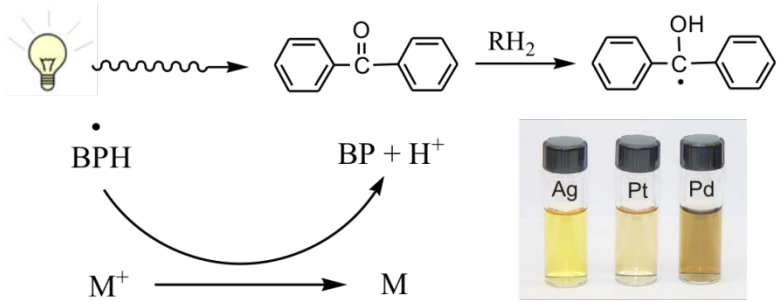

Figure 1.9. Scheme of the photoreduction of the Ag, Pd and Pt complexes initiated by BP; BPH• represents the BP radical formed in the top reaction. Included is an image showing samples of the colloids.

Photochemical illumination of air-free octane solutions containing BP, OS and any of the metal complexes with 350 nm photons induced a fast coloration of the liquid. The initial colorless solutions turned yellow, dark brown and light brown after formation of Ag, Pd and Pt colloids, respectively. Figure 1.9 depicts a scheme representing the mechanism of the reduction process and an image showing samples of the three colloids. The

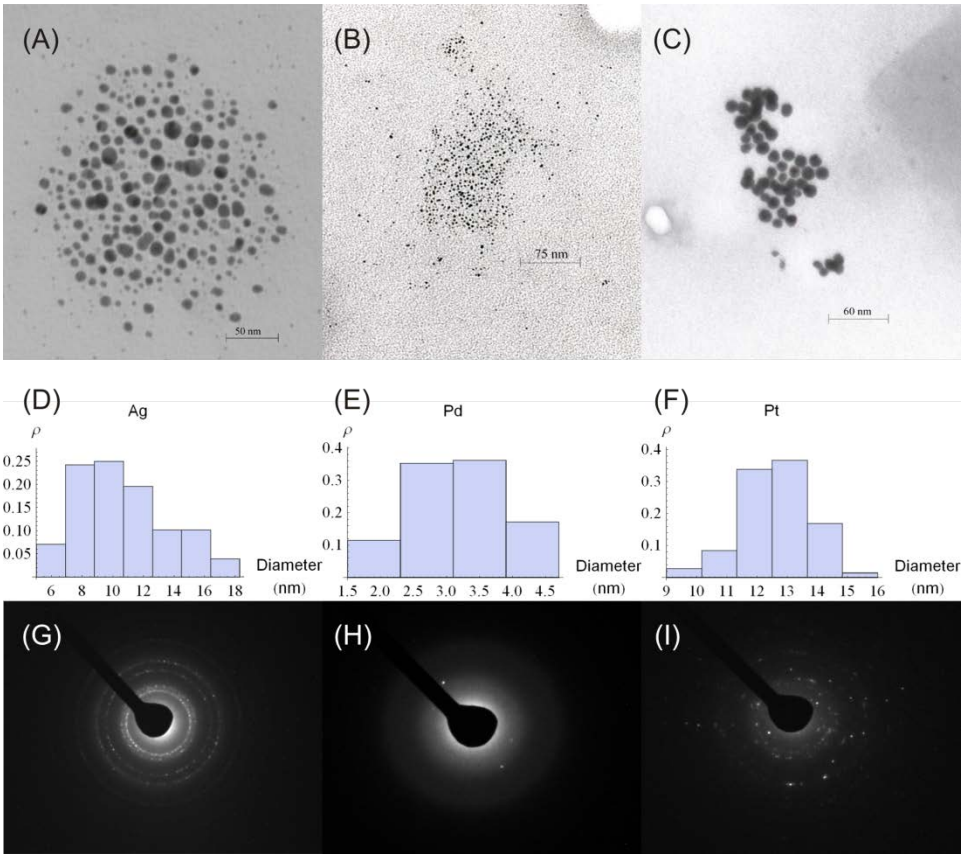

Figure 1.10. TEM images of Ag (A), Pd (B), and Pt (C) particles revealing spherical morphology; histograms of particle sizes with mean diameters of 11, 3, and 12.5 nm, respectively (D-F); and corresponding SAED patterns verifying particle crystallinity (G-I).

quantum yields for reduction of Pd(II) and Pt(II) ions amounted to 0.007 and 0.0045, at least 2 times higher than the values determined without BP. In contrast, φ = 1.2 for the photoreduction of AgOOR, which is 20 times the yield of the aqueous polymeric system.[14] A detailed report of the kinetic data has been recently published.[17]

Figures 1.10A-1.10C present electron micrographs of the metal colloids illustrating that the particles possessed fairly spherical morphology. The histograms shown in Figures 1.10D-1.10F provide corresponding size distributions with d_{av} values of 11, 3, and 12.5 nm for Ag, Pd, and Pt, respectively. SAED data verified the crystallinity of each colloid. The Debye rings shown in Figures 1.10G-1.10I are in good agreement with the reflections of fcc Ag, Pd and Pt listed in JCPDS cards 4-0783, 46-1043 and 4-0802.

Colloids with metal concentrations ≤ 5 mM (0.065 wt% for Ag 0.036 wt% for Pt) showed no evidence of flocculation after 4 months according to visible inspection, except that 0.065 wt% Pd sols suffered from particle precipitate within 1 week of preparation.

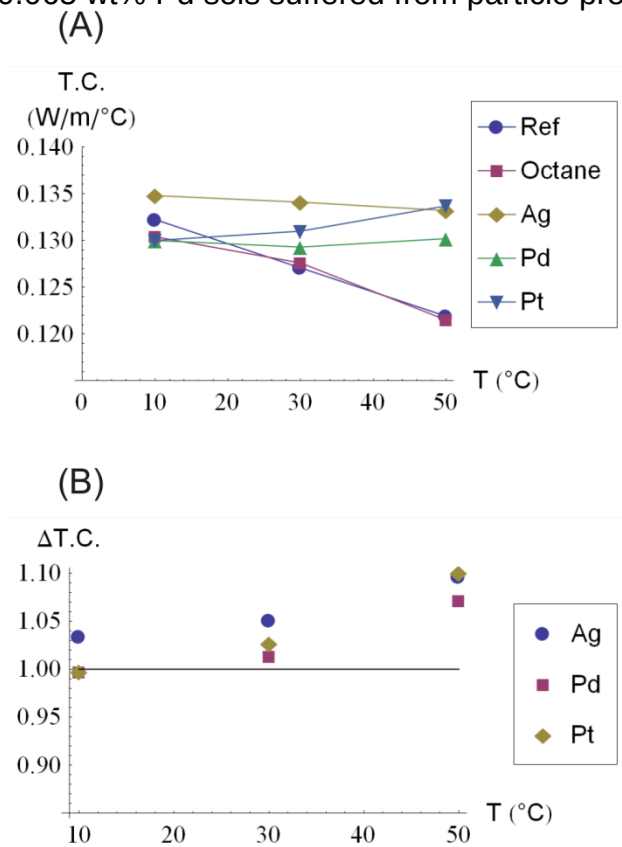

Figure 1.11. Plots of absolute TC (A), and relative TC (B); colloids with 5 mM of metal, 20 mM BP, and 40 mM OS. The experimental values for octane are in good agreement with reference data.[11]

Thermal conductivities were evaluated between 10 and 50 °C on colloids containing 5 mM of Ag, Pd, or Pt, 20 mM BP and 40 mM OS. Absolute TC values are plotted in Figure 1.11A, which also includes experimental and literature data for pure octane.[11] As shown in the plot, TC of the solvent decreased with increasing temperature and the experimental results were in agreement with the published values. The opposite trend was noticed for Pd and Pt colloids with TC rising modestly when T increased. Ag colloids exhibited the highest thermal conductivity at the lowest temperatures but TC decreased slightly when T increased. The TC values followed the trend Ag > Pt > Pd in the range of 10 °C ≤ T ≤ 30 °C, agreeing qualitatively with the differences in thermal conductivities of the bulk metals.[11] The efficacy of nanofluids is typically evaluated in terms of the relative thermal conductivity or TC enhancement, (ΔTC), where ΔTC = TC of the colloid / TC of octane. Presented in Figure 1.11B is a plot of ΔTC vs. temperature for each colloid; in all cases the relative thermal conductivity increased smoothly with rising T. Maximum enhancements were noticed at 50 °C with values of ~10% for both Ag and Pt systems, and 7% for the Pd colloid. These low TC enhancements were not

surprising given that the photochemical method yielded colloids with rather small particle concentrations. An important issue was the apparent inability of producing concentrated colloids with this procedure. One plausible explanation was that the BP sensitizer affected negatively particle stability. Another issue was that rigorously dry reagents were needed to obtain reproducible results. Thus, further efforts utilized a direct reduction approach driven by thermal energy instead of light.

1.3 Thermal generation of Ag colloids

1.3a Colloidal synthesis in alkanes

Ag was selected as this metal is stable against oxidation and exhibits the highest TC value of all metals and metallic oxides.[11] Dodecane was the solvent of choice since we discovered that OS is significantly more soluble in $C_{12}H_{26}$, which was anticipated to enable stabilization of colloids with larger concentrations. Also, the high boiling point of dodecane (216 ºC) enables access to a wider range of temperatures, and $C_{12}H_{26}$ remains a liquid at room temperature, allowing to circumvent experimental limitations imposed by the high T_m of the heavier alkanes best suited for PCM applications. The standard procedure that enabled preparation of 0.1 M (1.3 wt%) Ag colloids involved fast addition of silver neodecanoate powder to a solution containing 0.125 M OS in docecane preheated to 150 °C in an oil bath under vigorous stirring. After dissolution of AgOOR, the temperature was quickly increased to 180°C and maintained at that value until the reaction was completed. High temperatures were preferred to accomplish the reduction of Ag^+ ions in the shortest possible time. Keeping the reduction times short was anticipated to yield smaller Ag particles and also diminish the probability of colloid precipitation. An important advantage of the thermal procedure is that no purification of the reagents was required in order to obtain reproducible results.

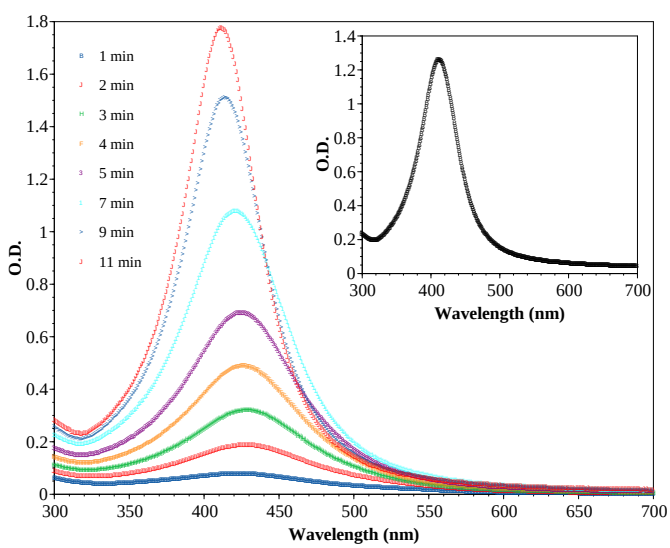

Figure 1.12. Evolution of the optical spectra during the thermal reduction of a dodecane solution containing 0.1 M Ag and 0.125 M OS, $T_{initial}$ = 150 °C and T_{final} = 180 °C; samples were diluted to 1.2 x 10^{-4} M silver with $C_{12}H_{26}$, ℓ = 1 cm. The inset displays an optical spectra of a 0.1 M sol diluted 1/1 with decanol, ℓ = 10 µm.

A fast and continuous darkening of the solution ensued after dissolution of the AgOOR powder in $C_{12}H_{26}$. Ag colloids with concentrations of up to 0.1 M (1.3 wt%) were achieved; the concentrated sols exhibited a dark color that turned yellow upon dilution. The yellow color of Ag colloids originates from the strong surface plasmon, centered between 400-420 nm, exhibited by nanometer sized spherical silver crystallites.[14] Shown in Figure 1.12 is the evolution of the plasmon as a function of the reaction time. The blue shifts originate from slight changes in strength and λ_{max} of the plasmon when the particle size increases. Considering that large dilutions of the colloids were needed to obtain quantitative spectral data, confirmation of the results of Figure 11 was attempted using concentrated sols and an optical quartz cell with a shorter path length (ℓ) of only 10 μm. Presented in the inset of Figure 1.12 is the absorption spectrum obtained with such a cell. The typical plasmon with λ_{max} = 414 nm was detected irrespective of dilution demonstrating that spherical Ag particles were the predominant species in both concentrated and dilute sols. The strong plasmon absorption at 414 nm (ε = 1.48 x 10^4 M^{-1} cm^{-1}) enabled highly sensitive detection of particle concentration. Identical results were obtained when eicosane was the solvent.

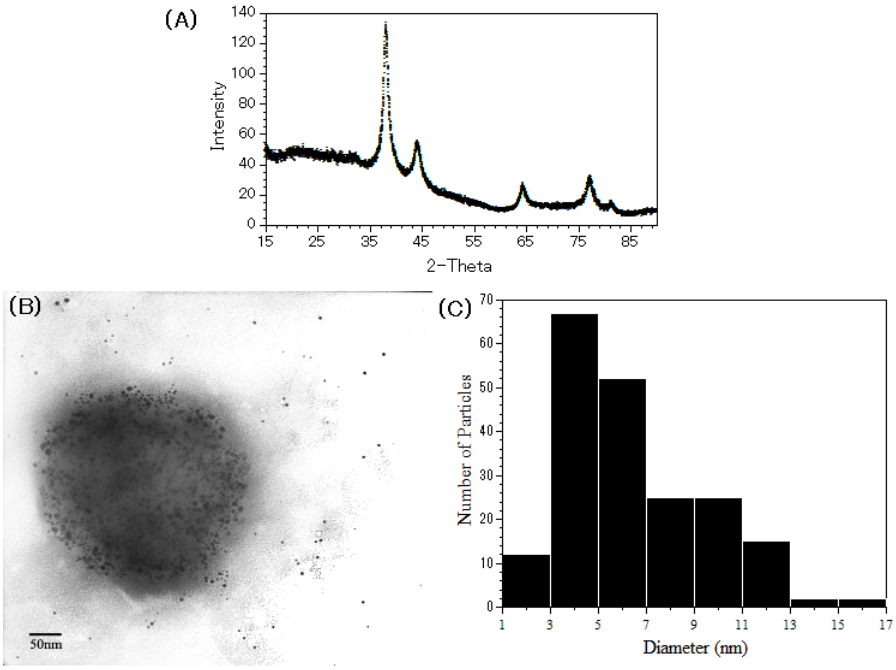

Figure 1.13. A) XRD data from a dry colloid showing diffractions from fcc Ag. B) TEM image of a sample prepared from a 0.1 M Ag colloid depicting nearly spherical metal crystallites together with an aggregate of silver particles. Length of marker = 50 nm. C) Corresponding size histogram, average particle diameter = 6.4 nm.

Figure 1.13A depicts powder XRD data consisting of reflections from the 111, 200, 220, 311, and 222 lattice planes of fcc metallic silver, which confirmed the presence of Ag crystallites in the colloids. As shown in the TEM image of Figure 1.13B, nearly spherical crystallites were produced. Figure 1.13C is a size histogram showing diameters between 1-17 nm with d_{av} = 6.4 nm. Long-term colloid stability was assessed via visual

observation, spectrophotometric evaluation and TEM. Colloids containing 0.1 M Ag have, thus far, remained stable against coagulation for more than 12 months after their synthesis. The optical spectra showed no decrease in peak intensity; a slight increase in the width at half maximum was noticed, which could be attributed to modest particle growth. TEM analysis of a concentrated colloid conducted after 6 months of aging provided support to such an interpretation. Images similar to those of a freshly prepared colloid were obtained and their analysis resulted in a minor increase in d_{av} to 6.9 nm. Stability experiments performed at 90 °C revealed that a slight metal precipitation took place several months after heating 0.1 M Ag colloids for 100 h. Additional tests showed that some metal precipitated after subjecting 0.1 M colloids to three cycles of freezing and thawing but sols with a ten times lower [Ag] remained stable for 30 cycles.

Thermal conductivities of silver colloids were determined in the range of 10 ≤ [Ag] ≤ 80 mM, or 0.125 to 1 wt%, at a constant [OS] = 0.1 M and from 0 to 50 °C. Representative data are included in Figure 1.14 showing the TC values for a 1 wt% colloid together with those of the solvent. The experimental TC values of pure dodecane decreased with increasing temperature and agree within experimental error with the reference data.[11] A similar but less pronounced trend was followed by the Ag colloid that, at all

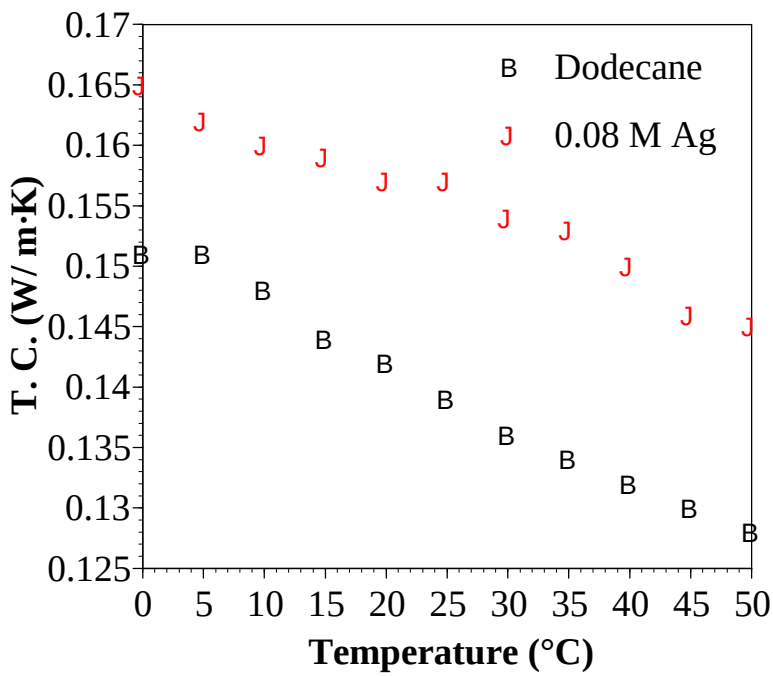

Figure 1.14. Comparison of the thermal conductivity of a 0.08 M, 1 wt%, Ag colloid with 0.1 M OS as a function of temperature (●) versus the TC values for the $C_{12}H_{26}$ solvent (■).

temperatures, exhibited TC values higher than those of $C_{12}H_{26}$. Analogous plots were obtained irrespective of metal concentration but TC increased by only 10% when [Ag] was varied between 10 and 80 mM at any temperature. The TC enhancement increased modestly with raising temperature; the largest change was found at 80 mM Ag where ΔTC varied between 9.5 to 13.8% in the range of 0 ≤ T ≤ 50 °C. Such values

agree, within a factor of 2, with predictions based on the classical formulations from Maxwell for dispersed metal particles.[18] The maximum TC enhancement for 80 mM sols in dodecane was only slightly higher than the value (10%) for 5 mM Ag colloids in octane at 50 °C,[16] indicating that in alkanes ΔTC is not a strong function of particle concentration. Despite the seemingly ideal properties of the Ag colloids in dodecane (high concentrations of stable, spherical crystallites with nm dimensions and reasonable size distribution), their low TC values rendered them unsuitable for PCM applications. A comprehensive study, submitted for publication, reports on the mechanistic aspects of the thermal reduction process, which indicated that the neodecanoate ligand is the source of electrons that drives the reduction of the silver ions.[19]

1.3b Colloidal synthesis in PEG 600

Poly(ethylene glycols), PEG, have been suggested as alternative materials for PCM systems as they exhibit a wide range of T_m values that are also a function of chain length.[20] While their melting enthalpies are lower than those of hydrocarbons, the polymers are less flammable. Our earlier study showed that PEG can serve as reducing agents and also as particle stabilizers during the formation of Ag crystallites.[21] Thus, efforts were made to attempt the synthesis of Ag colloids using PEG 600 as the solvent since this polymer is a liquid at room temperature. The goal of this study was to obtain stable Ag colloids with higher metal concentrations. Poly(vinyl pyrrolidone), PVP, was also added since this polymer is not only an effective reductant and particle stabilizer, but also decreases (dampens) significantly the strength of the Ag plasmon band.[22] Concentrated metal colloids exhibiting weak colors are desirable for lubrication applications that are studied by co-PI Jackson. Heating a PEG 600 solution containing 10 mM PVP and 0.2 M (2.6 wt%) $AgNO_3$ for 4 min at 90°C yielded complete reduction of the silver ions. The resulting colloids consist of spherical particles with d_{av} = 6.4 nm and exhibit a plasmon signal centered at 400 nm but with ε = 628 M^{-1} cm^{-1}, which is 24 times smaller than the extinction coefficient of Ag sols prepared in dodecane. These colloids have not precipitated after 8 months of preparation and data obtained by co-PI Jackson indicate that they exhibit very good lubrication properties. Preparation of Ag colloids with a concentration of 1 M (13 wt%) has also been accomplished and no sign of particle precipitation has been noticed after several weeks of aging.[23]

1.4 Synthesis of colloidal metals in aqueous cyclodextrin solutions

Cyclodextrins, (CD)s, have been long known to be excellent stabilizers of colloids consisting of small metal particles.[24] While CDs are mainly soluble in water, derivatives of CDs soluble in hydrocarbons could possibly serve as particle stabilizers in such solvents. Thus, the possibility of preparing highly concentrated metal colloids first in water using CDs as particle stabilizers and glucose as a reducing agent was explored. Figure 1.15 depicts optical spectra of these particles as well as an image of the resulting colloidal solutions of Ag, Au, Pd and Pt colloids. TEM analysis showed the presence of spherical particles with d_{av} values of 18, 11, 12, and 12 nm for Ag, Au, Pd and and Pt. Colloids with metal concentrations of 5 mM were obtained that showed no precipitation after aging for three years. However, maximum TC enhancements of only 3% were noticed at the highest particle concentrations. These results are the basis for a manuscript that has been submitted for publication.[25] The investigations carried out by

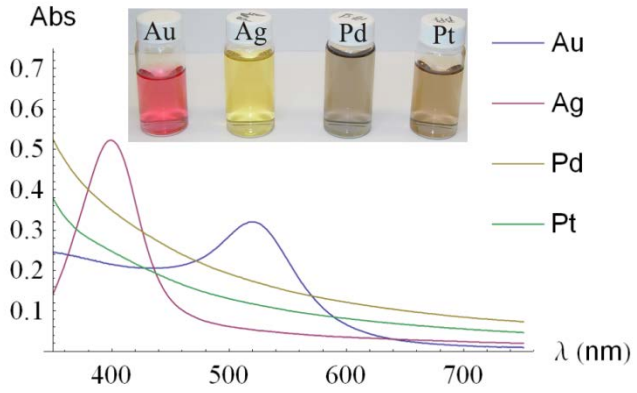

Figure 1.15. Absorption spectra of colloids containing 0.1 mM Au, 0.025 mM Ag, 0.1 mM Pd, and 0.5 mM Pt. Shown in the inset is an image of the corresponding colloids.

Dan Clary have been summarized in his Ph.D. dissertation.[26] M. Sharif Hossain is currently studying the preparation of colloidal rods for PCM applications.

1.5 Summary

The chemistry group addressed the lack of Cu-based colloidal dispersions that can function as nanofluids and expedite heat transport in phase change materials. Colloids containing high concentrations of nanometer-sized particles in various hydrocarbon solvents were considered ideal. Strong interactions between stabilizing agents and particles were deemed essential in order for the colloids to remain stable against precipitation over extended periods of time. A stepwise procedure was identified that produced surface-coated spherical CuO nanoparticles useful for the preparation of colloids with concentrations of up to 20 wt% in a variety of hydrocarbons. Long-term stability against particle precipitation was observed for CuO concentrations ≤ 5 wt%. The results presented in reference 8 demonstrate that our synthetic method was able to successfully meet all the stringent requirements of this project. Cu colloids stable in air-free octane were prepared via a simple photochemical method in which the solvent acted as the agent that reduced Cu(II) ions. Detailed mechanistic information about the generation of this novel colloid is presented in reference 16. Such information enabled utilization of the photosynthetic method to achieve stable colloids of Ag, Pd and Pt in alkanes. Data concerning the synthesis of the nanometer-sized metal particles and also of thermal conductivity determinations are included in reference 17. The photochemical studies provided important knowledge about the key role played by oleoyl saecosine as a particle stabilizer. Utilization of this knowledge enabled optimization of reaction parameters (choice of solvent and amount of stabilizer) that ultimately resulted in a very straightforward thermal procedure for the synthesis of concentrated Ag colloids in alkanes. Despite their seemingly ideal properties, presented in reference 19, only modest enhancements in thermal conductivity were exhibited by the Ag colloids. These results indicate that nanofluids based on spherical nanometer-sized particles are not suitable for enhancing the transport of heat in PCM systems.

1.6 References

1. J. J. Wang, R. T. Zheng, J. W. Gao and G. Chen, Heat conduction mechanisms in nanofluids and suspensions, Nano Today, Vol. 7, pp. 124-136, 2012.
2. N. I. Kovtyukhova, B. R. Martin, J. K. N. Mbindyo, P. A. Smith, B. Razavi, T. S. Mayer and T. E. Mallouk, Layer-by-Layer Assembly of Rectifying Junctions in and on Metal Nanowires, J. Phys. Chem. B, Vol. 105, pp. 8762-8769, 2001.
3. L. Spanhel and M. A. Anderson, Semiconductor Clusters in the Sol-Gel Process: Quantized Aggregation, Gelation, and Crystal Growth in Concentrated ZnO Colloids, J. Am. Chem. Soc., Vol. 113, pp. 2826-2833, 1991.
4. A, Sharma, V. V. Tyagi, C. R. Chen and D. Buddhi, Review on thermal storage with phase change materials and applications, Renewable Sustainable Energy Rev., Vol. 13, pp. 318-345, 2009.
5. J. M. Khodadadi, L. Fan and H. Babaei, Thermal conductivity enhancement of nanostructure-based colloidal suspensions utilized as phase change materials for thermal energy storage: A review, Renewable Sustainable Energy Rev., Vol. 24, pp. 418-444, 2013.
6. S. Reuter and S. Franke, Models for the Charging of Particles in Liquid Toners: A Summary, J. Imaging Sci. Technol., Vol. 48, pp. 319-323, 2004.
7. C.-C. Li, and M.-H. Chang, Colloidal Stability of CuO nanoparticles in alkanes via oleate modification, Mater. Lett., Vol. 58, pp. 3903-3907, 2004.
8. D. R. Clary, D. and G. Mills, Preparation and Thermal Properties of CuO Particles, J. Phys. Chem. C, Vol. 115, pp. 1767-1775, 2011.
9. L. M. Raff, Principles of Physical Chemistry; Prentice Hall: New Jersey, 2001; Chapters 3 and 8.
10. M. W. Chase, Jr., NIST-JANAF Thermochemical Tables, Fourth Edition, J. Phys. Chem. Data, Monograph 9, pp. 1-1951, 1998.
11. C. L. Yaws, Transport Properties of Chemicals and Hydrocarbons; William Andrew: New York, 2009; pp. 344, 371, 389, 405 and 406.
12. H. Bönnemann, S. S. Botha, B. Bladergroen and V. M. Linkov, Monodispersed copper- and silver-nanocolloids suitable for heat conductive fluids. Appl. Organometal. Chem., Vol. 19, pp. 768-773, 2005.
13. A. Gilbert and J. Baggott, Essentials of Molecular Photochemistry; CRC Press: Boca Raton, Fl, 1991; Chapter 7.
14. A. S. Korchev, T. S. Shulyak, B. L. Slaten, W. F. Gale and G. Mills, Sulfonated Poly(Ether Ether Ketone)/Poly(Vinyl Alcohol) Sensitizing System for Solution Photogeneration of Ag, Au and Cu Crystallites. J. Phys. Chem. B, Vol. 109, pp. 7733−7745, 2005.
15. R. J. Mehrotra and R. Bohra, Metal Carboxylates; Academic Press: London, 1983; Chapter 2.
16. D. R. Clary, D. and G. Mills, Photochemical Generation of Nanometer-Sized Cu Particles in Octane, J. Phys. Chem. C, Vol. 115, pp. 14656-14663, 2011.
17. D. R. Clary, M. Nabil, M. M. Sedeh, Y. El-Hasadi and G. Mills, Photochemical Generation of Ag, Pd and Pt Particles in Octane, J. Phys. Chem. C, Vol. 116, pp. 9243-9250, 2012.

18. J. Eapen, R. Rusconi, R. Piazza and S. Yip, On the Classical Nature of Thermal Conduction in Nanofluids, J. Heat Transfer, Vol. 132, pp. 102402-1 – 102402-14, 2010.
19. J. R. Darvin, M. Nabil, J. Uertz and G. Mills, Synthesis of Concentrated Ag Colloids in Dodecane Relevant to NEPCM; submitted to J. Phys. Chem. C.
20. D. P. Bentz and R. Turpin, Potential applications of phase change materials in concrete technology, Cement & Concrete Composites, Vol. 29, pp. 527-532, 2007.
21. L. Longenberger and G. Mills, Formation of Metal Particles in Aqueous Solutions by Reactions of Metal Complexes with Polymers, J. Phys. Chem., Vol. 99, pp. 475-478, 1995.
22. I. P. Santos and L. M. Marzan, Formation of PVP-Protected Metal Nanoparticles in DMF, Langmuir, Vol. 18, pp. 2888-2892, 2002.
23. M. S. Hossain, J. Uertz and G. Mills, Preparation of Concentrated Ag Colloids in PEG 600; to be submitted to J. Phys. Chem. C.
24. A. Denocourt-Rowiki and A. Roucoux, Noble Metal Nanoparticles Stabilized by Cyclodextrins: A Pertinent Partnership for Catalytic Applications, Curr. Org. Chem., Vol. 14, pp. 1266-1283, 2010.
25. D. R. Clary, L. Fan and G. Mills, Preparation of Aqueous, Cyclodextrin-Based Noble Metal Colloids; submitted to J. Cluster Sci.
26. D. R. Clary, Ph.D. Dissertation, Auburn University, Auburn, Alabama, November 2011.

2. NePCM Modeling and Testing
(Dr. Jay M. Khodadadi, Mechanical Engineering Department, Auburn University)

Concurrent to the preparation component of the NePCM project, determination of the thermal conductivity of eicosane-based nanostructure-enhanced phase change materials was conducted in both liquid and solid phases using the transient plane source (TPS) technique. The results of the early effort were summarized in Fan (2011) and Fan and Khodadadi (2012a,b), whereas a later phase of the study was conducted and reported by Nabil (2013). Moreover, modeling of the effectiveness of the widely-used transient hot wire (THW) apparatus near the liquid-solid phase transition temperature was investigated using experimental and numerical approaches. Specifically, a numerical analysis was performed in order to solve the 1-D transient heat conduction equation for melting/solidification of a PCM with a center-located wire heat source/sink via MATLAB. With the aid of ANSYS® FLUENT software, a 1-D transient axisymmetric model of a commonly-used THW apparatus is also formulated and solved using a phase change enthalpy model to verify the MATLAB code results.

Covering the period of 2001 to mid-2013, the number of published papers on phase change materials along with their publication year is summarized in Figure 2.1. Prior to 2005, on average 34 papers per year were published. However, a new surge of interest on research of PCM has been witnessed. A review of 20 recent research papers on NePCM, i.e. from 2009 to early 2013, that focused on enhancing the thermal conductivity due to introduction of nanostructures into phase change materials for thermal energy storage was discussed by Nabil (2013), whereas the limited pre-2009 papers were reviewed by Khodadadi et al. (2013). The main aim of the NePCM studies has been to study the dependence of the enhanced thermal conductivity on mass fraction of the nanostructures and temperature for both liquid and solid phases. It is concluded that carbon-based nanostructures and carbon nanotubes generally exhibit far greater enhancement of thermal conductivity in comparison to metallic/metal oxide nanoparticles. However, great care should be taken in order to properly functionalize the nano-additives within PCM matrix to obtain well-dispersed NePCM colloids.

2.1 Experimental Study on the Thermal Conductivity Measurements of NePCM Composites: Eicosane ($C_{20}H_{42}$) with a melting point of 37 °C was selected as the base PCM. Copper (II) oxide (CuO) nanoparticles stabilized by sodium oleate acid ($C_{18}H_{33}O_2Na$) were selected as nano-scale thermal conductivity enhancers, whereas preliminary studies with multi-walled carbon nano-tubes (MWCNT) were also conducted. Three distinct batches of solid eicosane-CuO samples with the same mass fraction of nanoparticles were obtained under an ice-water bath, ambient temperature and oven solidification schemes. Thermal conductivity of solid NePCM composites with eight different loadings of CuO nanoparticles (0, 1, 2, 3.5, 5, 6.5, 8 and 10 wt%) and a constant concentration of 0.1 vol% (0.27 wt%) of MWCNTs were measured experimentally at various temperatures using the transient plane source (TPS) technique. Using a controllable temperature bath, measurements were conducted at various temperatures between 10 and 35 °C for the solid samples using a support-setup

(Figure 2.2). The measured thermal conductivity values are presented in Figures 2.3-2.6. The pertinent conclusions drawn from these investigations were:

1. Measured thermal conductivity values of the composites were found to be independent of the measurement temperature for a given particle loading regardless of the solidification procedure.

2. Irrespective of the preparation/solidification scheme, as the melting temperature was approached, thermal conductivity of the composites rose sharply for all sets of solid disks.

3. The ice-water bath solidification route for the eicosane-CuO samples consistently exhibited the lowest values of thermal conductivity, whereas the samples of oven solidification scheme corresponded to the highest values. This behavior might be due to the greater void population of ice-water bath samples and/or crystal structure deviations due to processing routes.

4. Considering eicosane-CuO composites, for mass fractions greater than 2 wt%, a non-monotonic relation between the thermal conductivity and the mass fraction, independent of the temperature range studied, was exhibited.

5. Although no functionalization was performed on the MWCNTs, the amount of thermal conductivity enhancement for 0.27 wt% eicosane-MWCNTs solid samples (~25-35%) was much higher than that of 1 wt% eicosane-CuO solid disks (~1-4%).

One journal paper (Nabil and Khodadadi, 2013) and three (3) conference papers have resulted from the work of M. Nabil since 2011.

2.2 Analytical/Numerical Work on Explaining Anomalous Thermal Conductivity Measurements near the Melting Temperature: A 1-D transient heat conduction problem was formulated and solved over a finite cylindrical domain (Figure 2.7) with and without phase transition using the ANSYS® FLUENT and MATLAB software. The objective was to model the behavior of a THW apparatus near the melting temperature of the medium. The following results were obtained:

1. The defined FLUENT model was first successfully verified against an ideal mathematical transient hot wire theory for a perfect conductor with a 0.01% error for the monitored temperature values.

2. An exact mathematical analysis for a similar melting problem was also adopted to verify the predictions of the FLUENT model under phase transition condition. The plots of temperature rise on the wire surface were nearly following the same trend with an error of less than 0.5% for the monitored temperature values.

3. Using the FLUENT model, thermal conductivity predictions in both liquid and solid phases were performed in the absence of phase change phenomenon. The difference between the extracted thermal conductivity values and the initially-assigned values based on the literature was less than 1% and 0.81% for the solid and liquid phases, respectively (Figures 2.8-2.9).

4. The effect of the initial solid state temperature on the predicted thermal conductivity values under the presence of melting was also explored. Five different cases were considered for study if any sharp rise in thermal conductivity values occured near the melting point of the PCM. There were no abrupt behavior changes as temperature approached the melting point of eicosane, all the predicted thermal

conductivity values were between the assigned values of the liquid and solid states (Figure 2.10).

Molecular-level simulations were utilized to study thermal transport within nanoparticle suspensions (nanofluids) and nanostructure-enhanced phase change materials (NePCM).

2.3 Thermal Conductivity of Nanofluids: Firstly, the research was focused on the improvement of thermal conductivity of spherical nanoparticle suspensions (nanofluids), a highly debated topic over the last decade. During this first step, it was found that a precise definition for the heat current utilized in the Green-Kubo method for multicomponent systems was required. The key component in heat current expression was the kinetic term involved in the partial enthalpy, which has been overlooked in some previous works, resulting in erroneous reported high enhancements in thermal conductivity of nanofluids. In order to validate the heat current expression, extensive simulations were carried out on different multicomponent systems including a nanofluid system and mixture systems in gas, liquid and solid phases. The consistent results from the Green-Kubo and the non-equilibrium direct methods corroborate the correctness of the heat flux expression (Tables 2.1 and 2.2). The results of the work were published in the Journal of Applied Physics (Babaei et al., 2012). Using the validated expression, the thermal transport in nanofluids was investigated. The results showed that for nanofluids at different temperatures and volume fractions, the thermal conductivity improvements were in agreement with the Maxwell's model predictions for well-dispersed nanofluids and no additional enhancement was observed (Figure 2.11). By decomposing the resulting thermal conductivity values, the effect of the Brownian motion-induced micro-convection, which was proposed by many researchers, was studied (the results are shown in Tables 2.1 and 2.2). It was found that while the convection-based potential and enthalpy components in thermal conductivity were considerably high, these terms cancel each other leaving an insignificant contribution to the overall thermal conductivity. The results of this work were published in the Journal of Applied Physics (Babaei et al., 2013b).

2.4 Improvement in thermal conductivity of paraffin by adding high aspect-ratio carbon-based nano-fillers: Regarding carbon-based high aspect-ratio nano-fillers, e.g. graphene and carbon nanotubes (CNT), the effect of such nanoparticles on thermal conductivity of liquid and solid paraffin, which is the PCM mainly studied in our group, was investigated by using molecular dynamic simulations. The introduction of CNT and graphene nanofillers leads to considerable ordering of paraffin molecules (Figure 2.12) and associated thermal conductivity enhancement. More notably, carbon nano-fillers provide a template for directed crystallization and lead to even greater thermal conductivity increases in solid phase mixtures. The results indicate that introducing carbon nanotubes and graphene into long-chain paraffins leads to a considerable improvement in thermal conductivity, not only due to the presence of a conductive filler, but also due to the filler-induced alignment of paraffin molecules. The dependency of thermal conductivity of paraffin on the alignment factor for its molecules suggests that there is a strong relationship between thermal conductivity and the alignment factor

(Figures 2.13 and 2.14). Thermal conductivity of liquid paraffin, which has the lowest alignment factor (0.02) due to the random distribution of molecules, is the minimum, whereas the thermal conductivity of a perfect crystal, which has the highest alignment factor (0.99), is the maximum value. We compared the predicted thermal conductivity values based on two sets of simulations. In one set, considering the full dynamics of carbon atoms in graphene/CNT and in another one, freezing the atomic motions for graphene/CNT atoms, showed that the main mechanism for thermal conductivity improvement in such mixtures is the nanofiller-induced ordering in paraffin molecules. The results of this work were published as two articles in the International Journal of Heat and Mass Transfer (Babaei et al., 2013c) and the Physics Letters A (Babaei et al., 2013a).

2.5 Interfacial thermal conductance between graphene and paraffin: The interfacial thermal conductance between graphene nanofiller and paraffin matrix was also studied. The effect of the paraffin phase and the filler's thickness on the interfacial thermal conductance was investigated (Figure 2.15). The results indicated that the systems containing thin graphene layers exhibit higher interfacial thermal conductance which for liquid mixtures converges to 110 MW/m^2 K with increasing filler thickness. The other finding was that the interfacial conductance for solid paraffin-graphene is higher than the conductance of the corresponding liquid paraffin-graphene interface (Figure 2.15).

2.6 Development, utilization and thermal conductivity improvement of carbon foam-based thermal energy storage composites: Thermal energy storage (TES) composites consist of phase change materials (PCM and NEPCM) infiltrated into highly conductive porous structures. TES composites open new opportunities in utilization of renewable energies and recycling waste heat. Development, utilization and thermal conductivity improvement of TES composites were investigated in this study and reported here.

2.6.1 Development of TES composites: Development of TES composites mainly depends on the characteristics of the infiltration process that is linked to the formation of voids and was investigated numerically and experimentally. The numerical investigation was conducted with the purpose of extracting the details of liquid interface behavior and evolution during the infiltration at pore level. The penetration of wetting and non-wetting liquids (corresponding to hydrophilic and hydrophobic surfaces) into a highly conductive porous structure (graphite foam) and simultaneous escaping of air from the pores was investigated using the volume-of-fluid (VOF) method as a multiphase approach. The infiltration driving forces include forces due to gravity, pressure difference and interfacial effects (i.e. surface tension and contact angle). The effects of different driving forces and interface behavior (shape, position and velocity) were investigated. Different behavior was observed for wetting liquids in comparison with non-wetting liquids. Temporary and permanent pinning of the liquid interface and wicking flow were observed during the infiltration of wetting liquids into the pore, whereas pore-level fingering, entrapment of air and formation of voids were observed during infiltration of non-wetting liquids. The obtained results of void formation during infiltration of non-wetting liquids were found to be in agreement with experimental results reported in the

literature. The infiltration criteria and the infiltration behavior (i.e. the generic variation of pore infiltration time with driving forces in dimensionless form) were also extracted for wetting and non-wetting liquids, as shown in Figure 2.16 (Moeini Sedeh and Khodadadi, 2013a).

The numerical results of liquid interface shape and position were verified against those obtained from the coupled VOF-Level Set method, and known to have higher accuracy in tracking/capturing the interface. Furthermore, the numerical results of horizontal wicking flow through a network of pores in series were validated against the experimental results with a good agreement (Moeini Sedeh and Khodadadi, 2013 a,b). The wicking through the porous structure was also studied using a modified Washburn equation and the results were found to be in agreement with obtained numerical and experimental results, as presented in Figure 2.17.

2.6.2 Utilization of TES composites: Employment and utilization of TES composites consists of freezing/thaw cycles during which thermal energy can be stored/extracted from PCM. Regarding the utilization of TES composites, the numerical simulation of the phase change processes (solidification and melting) was conducted. Since void formation occurs during the development of such composites (i.e. infiltration process) and voids can have a significant effect on thermal behavior of the composite, the presence of voids within the pore was considered in the numerical investigation. A combination of the VOF and enthalpy-porosity method was proposed to consider two phases of liquid (PCM) and gas within the pore as well as solidification and melting processes for PCM. The proposed method took into account the variation of density with temperature, making it capable of predicting the shrinkage void (i.e. the volume change during the phase change).

Numerical simulations were conducted at the pore level over a two-dimensional model of the pore and the details of phase change processes (solidification and melting) were elucidated. For instance, the evolution of the freezing front is shown (Figure 2.18) at different time instants during the solidification of cyclohexane (as a typical hydrocarbon-based PCM) within the pore (Moeini Sedeh and Khodadadi, 2012, 2013c, d).

Since the simulation is time-dependent and accounts for volume change (contraction or expansion) during the phase change, the temporal evolution of shrinkage void was obtained during the solidification process which eventually led to prediction of the volume and distribution of the shrinkage void within the pore. The shrinkage void can be realized by comparing the PCM-void interface before and after solidification, as shown in Figure 2.19. The void content of the pore after solidification is larger than the initial void content meaning there is a volume contraction due to solidification of PCM (cyclohexane). With regard to verification of the results, it was found that the volume of the shrinkage void is in good agreement with the theoretical volume change due to density variation. Moreover, the distribution of the shrinkage void (i.e. shape of the void within the pore, given in Figure 2.19) was found to be in accordance with the observed convection patterns within the pore. Such convection patterns are shown at two different time instants during the solidification in Figure 2.20.

Furthermore, during the phase change processes, a temperature gradient was observed along the interface between phase change material (PCM) and void. Since

surface tension forces play the major role at the pore level, the temperature gradient along the interface triggered the thermocapillary convection. Therefore, thermocapillary effect was included by considering the variation of the surface tension with temperature. The final status of phase change processes, position and shape of infiltration and shrinkage voids, convection patterns within the pore and phase change duration were extracted and compared between cases with and without thermocapillary convection. It was found that thermocapillary forces influence the convection pattern within the pore significantly as shown in Figure 2.21. They also cause a reduction of about 8% in duration of phase change compared to the case when the void is present at the pore and thermocapillary effects are neglected.

2.6.3 Thermal conductivity improvement of TES composites: As a novel method for thermal characterization of graphite foam/PCM composites, the effective thermal conductivity of the composite was investigated numerically and experimentally. For numerical investigation, a three-dimensional, body-centered, cube arrangement of uniform spherical pores saturated with PCM was considered as the numerical model. The developed representative elementary volume (REV) retains the same porosity as the selected graphite foam structure (75%), since porosity of highly-conductive solid structure plays a major role in the resulting effective thermal conductivity of the composite. Unidirectional thermal analysis was conducted on the developed model using the isothermal (periodic) boundary conditions over the hot and cold walls in one direction, while all other walls in other directions are insulated. As a result of thermal analysis, the temperature distribution was obtained within PCM and graphite foam domains as shown separately in Figure 2.22 for a selected hot/cold temperature of 301/300 K. Having the temperature distribution, the total heat flux was integrated over hot/cold surfaces (that are equal upon converging the numerical solution). Knowing the applied heat flux and temperature difference, the effective thermal conductivity can be evaluated based on the Fourier's law (Moeini Sedeh and Khodadadi, 2013e).

Experimental investigations were conducted on samples of graphite foam and graphite foam/PCM composites using the direct (absolute) method of thermal conductivity measurements. A unidirectional heat flux was applied on the samples using a thermo-electric heater and by measuring/controlling the input electric voltage and current. The temperature distribution was measured within the composite sample (using four thermocouples installed in known positions within the sample in the direction of heat flux) until the sample reached the steady-state thermal conditions. Knowing the applied heat flux and the measured temperature distribution (i.e. temperature gradient) within the sample, the effective thermal conductivity was evaluated based on the Fourier's law (known as direct or absolute method of thermal conductivity measurement). The measurements were repeated to ensure the repeatability and to extract the uncertainties in the effective thermal conductivity. The obtained numerical and experimental results were found to be in good agreement for both graphite foam (bulk thermal conductivity of the foam) and graphite foam/PCM composite, as compared against each other in Figure 2.23.

Furthermore, our results of graphite foam's effective thermal conductivity (obtained from a steady-state method) are in good agreement with the experimental results,

reported in the literature, obtained using the laser flash technique as a transient method in measuring the thermal conductivity.

It is concluded that graphite foam with its highly-conductive and highly-porous structure, is an excellent candidate for improving the thermal conductivity of PCM. In this study, high values of the effective thermal conductivity varying from 30 W/m.K (at 20°C) to 25 (at 90°C) were obtained in comparison with the thermal conductivity of cyclohexane (0.13 W/m.K). Furthermore, the role of natural convection within the graphite foam pores (with average diameter of 400 µm) was found to be negligible.

2.7 Modeling of Solidification of Colloidal Suspensions: Building on the experience with modeling of phase change systems using continuum-based techniques dating back to mid-90s, extensions of the existing binary mixture models to account for nanoparticle transport and constitutional supercooling were studied (El Hasadi and Khodadadi, 2013a). The effect of the size of the nanoparticles on the morphology of the solid-liquid interface and the evolving concentration field during solidification was also studied. Combining a one-fluid-mixture approach with the single-domain enthalpy-porosity model for phase change and assuming a linear dependence of the liquidus and solidus temperatures of the mushy zone on the local concentration of the nanoparticles subject to a constant value of the segregation coefficient, thermal-solutal convection as well as the Brownian and thermophoretic effects were considered. A square cavity containing a suspension of copper nanoparticles (diameter of 5 and 2 nm) in water was the model NePCM used. Subject to a 5 degrees centigrade temperature difference between the hot (top) and cold (bottom) sides and with an initial loading of the nanoparticles equal to 10 wt% (1.22 vol%), the colloid was solidified from the bottom. The solid-liquid interface for the case of NePCM with 5 nm particle size was almost planar throughout the solidification process. However, for the case of the NePCM with particle size of 2 nm, the solid-liquid interface evolved from a stable planar shape to an unstable dendritic structure (Figure 12). This transition was attributed to the constitutional supercooling effect, whereby the rejected particles that are pushed away from the interface into the liquid zone, form regions of high concentration thus leading to a lower solidus temperature. Moreover, for the smaller particle size of 2 nm, the ensuing solutal convection at the liquid-solid interface (note the velocity vectors in Figure 2.24) due to the concentration gradient was affected by the increased Brownian diffusivity. Due to size-dependent rejection of nanoparticles, the frozen layer that resulted from a dendritic growth contains regions of depleted concentration. Despite the higher thermal conductivity of the colloids, the amount of frozen phase during a fixed time period diminished as the particle size decreased (El Hasadi, 2013). El Hasadi and Khodadadi (2013b) have also developed an analytical solution to the 1-D freezing problem that accounts for rejection of nanoparticles at the interface and constitutional supercooling.

2.8 References

Babaei, H., P. Keblinski, and J. M. Khodadadi, Equilibrium Molecular Dynamics Determination of Thermal Conductivity for Multi-Component Systems, **J. Appl. Phys.** 112, 054310, 2012.

Babaei, H., P. Keblinski, and J. M. Khodadadi, Improvement in thermal conductivity of paraffin by adding high aspect-ratio carbon-based nano-fillers, **Physics Letters A**, 377, 1358–1361, 2013a.

Babaei, H., P. Keblinski, and J. M. Khodadadi, A Proof for Insignificant Effect of Brownian Motion-Induced Micro-Convection on Thermal Conductivity of Nanofluids by Utilizing Molecular Dynamics Simulations, **J. Appl. Phys.**, 113, 084302, 2013b.

Babaei, H., P. Keblinski, and J. M. Khodadadi, Thermal conductivity enhancement of paraffin by increasing the alignment of molecules through adding CNT/Graphene, **International Journal of Heat and Mass Transfer**, 58, 209, 2013c.

El Hasadi, Y. M. F., "Continuum Modeling of Transport Phenomena during Melting and Solidification of Nanostructure-enhanced Phase Change Materials", PhD Dissertation, Department of Mechanical Engineering, Auburn University, 2013.

El Hasadi, Y. M. F. and J. M. Khodadadi, "Numerical Simulation of the Effect of the Size of Suspensions on the Solidification Process of Nanoparticle-Enhanced Phase Change Materials," **Transactions of the ASME, Journal of Heat Transfer**, 135, 052901-1, 11 pages, 2013a.

El Hasadi, Y. M. F. and J. M. Khodadadi, "One-Dimensional Stefan Problem Formulation for Solidification of Nanostructure-enhanced Phase Change Materials (NePCM)," **International Journal of Heat and Mass Transfer**, 67, pp. 202-213, 2013b.

Fan, L., "Enhanced Thermal Conductivity and Expedited Freezing of Nanoparticle Suspensions Utilized as Novel Phase Change Materials", PhD Dissertation, Department of Mechanical Engineering, Auburn University, 258 pages, 2011.

Fan, L., and J. M. Khodadadi, "A Theoretical and Experimental Investigation of Unidirectional Freezing of Nanoparticle-Enhanced Phase Change Materials," **Transactions of the ASME, Journal of Heat Transfer**, Vol. 134, No. 9, 092301, 9 pages, 2012a.

Fan, L., and J. M. Khodadadi, "An Experimental Investigation of Enhanced Thermal Conductivity and Expedited Unidirectional Freezing of Cyclohexane-Based Nanoparticle Suspensions Utilized as Nano-Enhanced Phase Change Materials (NePCM)," **International Journal of Thermal Sciences**, *Special Issue on Thermal and Materials Nanoscience and Nanotechnology*, Vol. 62, pp. 120-126, 2012b.

Khodadadi, J. M., Fan, Liwu, and Babaei, H., "Thermal Conductivity Enhancement of Nanostructure-Based Colloidal Suspensions Utilized as Phase Change Materials for Thermal Energy Storage: A Review," **Renewable and Sustainable Energy Reviews**, 24, pp. 418-444, 2013.

Moeini Sedeh, M. and Khodadadi, J. M., "Effect of voids on solidification of phase change materials infiltrated in graphite foams," Proceedings of the ASME 2012 Summer Heat Transfer Conference, Rio Grande, Puerto Rico, July 8-12, 2012.

Moeini Sedeh, M. and Khodadadi, J. M., "Interface behavior and void formation during infiltration of liquids into porous structures," **Int. J. Multiphase Flow**, 57, 49-65, 2013a.

Moeini Sedeh, M. and Khodadadi, J. M., "Experimental investigation of wicking flow through a porous medium as a verification approach for numerical simulations," Proceedings of the ASME 2013 Fluids Engineering Summer Meeting, FEDSM2013-16466, Incline Village, Nevada, USA, July 7-11, 2013b.

Moeini Sedeh, M. and Khodadadi, J. M., “Solidification of phase change materials (PCM) infiltrated in porous media in presence of voids,” Submitted to **Transactions of the ASEM, J. Heat Transfer**, 2013c.

Moeini Sedeh, M. and Khodadadi, J. M., “Effect of Marangoni convection on solidification of phase change materials infiltrated in porous media in presence of voids,” Proceedings of the ASME 2013 Summer Heat Transfer Conference, Minneapolis, MN, USA, July 14-19, 2013d.

Moeini Sedeh, M. and Khodadadi, J. M., “Thermal conductivity improvement of phase change materials/graphite foam composites,” **Carbon**, 60, 117–128, 2013d.

Nabil, M., “Improvement of Thermal Conductivity of Nanoparticle Suspensions Utilized as Novel Phase Change Materials”, MS Thesis, Department of Mechanical Engineering, Auburn University, 212 pages, 2013.

Nabil, M. and J. M. Khodadadi “Experimental Determination of Temperature-Dependent Thermal Conductivity of Solid Eicosane-Based Nanostructure-Enhanced Phase Change Materials”, **International Journal of Heat and Mass Transfer**, 61, pp. 301-310, 2013.

Table 2.1 Predicted values of the thermal conductivity (W/m K) for the pure liquid and nanofluid based on the Green-Kubo and Direct methods

	Direct method	*Green-Kubo method*				
	k_{total}	k_{total}	k_{CC}	k_{CV}	k_{VC}	k_{VV}
Pure liquid	0.153±0.001	0.154±0.003	0.0067	0.0147	0.0117	0.121
Nanofluid	0.150±0.003	0.159±0.002	0.0161	0.0108	0.0110	0.1225

Table 2.2 Predicted values of the thermal conductivity (W/m K) for the pure and 50-50 gas, liquid and solid mixtures based on the Green-Kubo and Direct methods

	Direct method	*Green-Kubo method*				
	k_{total}	k_{total}	k_{CC}	k_{CV}	k_{VC}	k_{VV}
Gas, pure	0.045±0.004	0.040±0.004	0.037	0.001	0.002	0.0001
Gas, mixture	0.055±0.009	0.071±0.002	0.066	0.002	0.002	0.0002
Liquid, pure	0.132±0.002	0.138±0.004	0.004	0.011	0.011	0.1120
Liquid, mixture	0.139±0.004	0.146±0.003	0.005	0.011	0.011	0.1213
Solid, pure	0.345±0.004	0.316±0.003	0.001	0.015	0.013	0.2854
Solid, mixture	0.132±0.001	0.149±0.001	0.001	0.005	0.007	0.1338

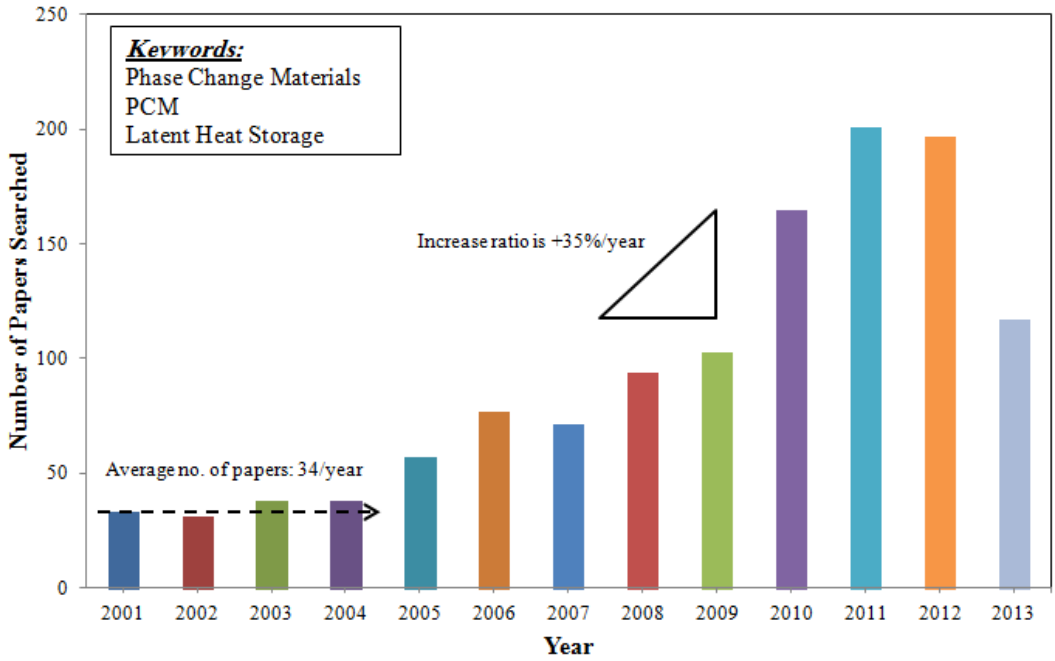

Figure 2.1 Year and number of PCM-related papers since 2001, using the search engine of the 'ScienceDirect' (search date: May 26, 2013)

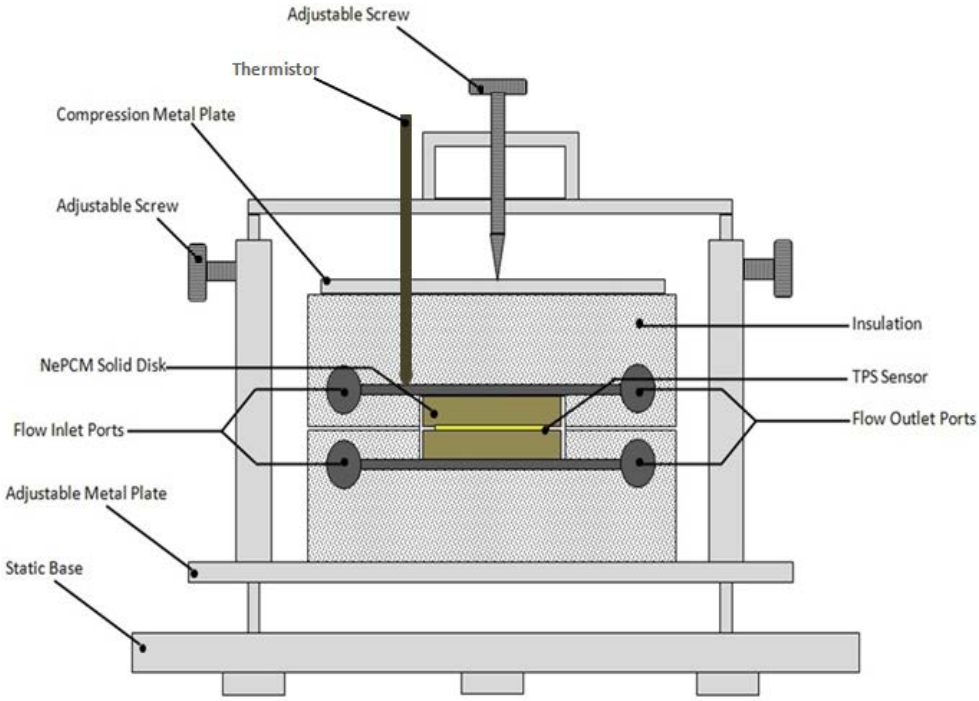

Figure 2.2 Schematic of the support set-up for the samples supplied with the TPS 500 instrument (Hot Disk AB, Gothenburg, SWEDEN)

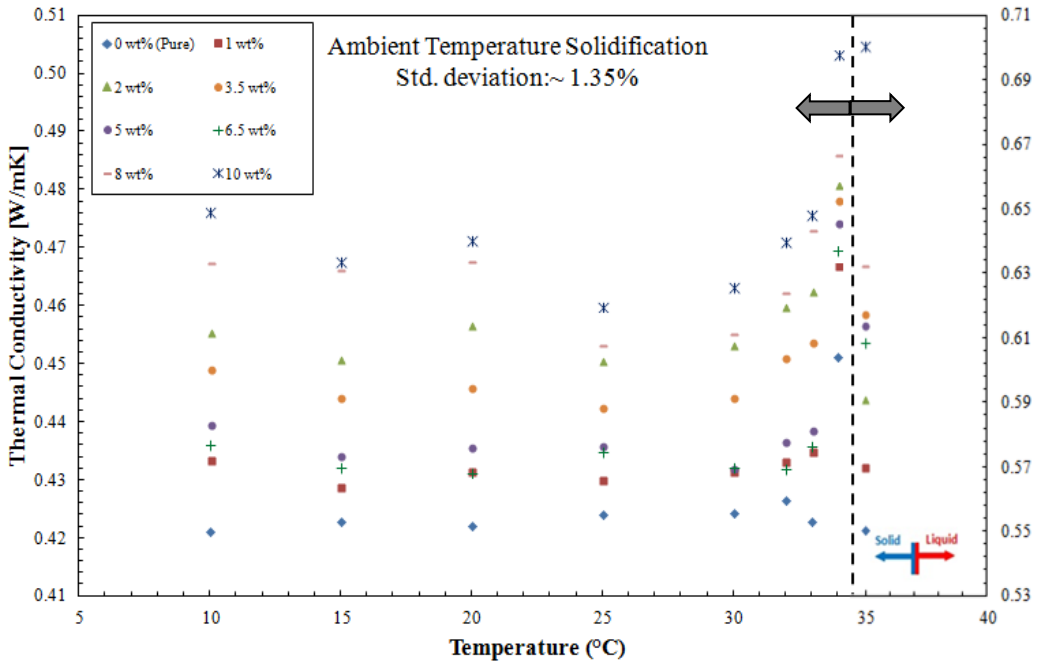

Figure 2.3 Thermal conductivity of solid pure eicosane and eicosane-CuO composites prepared following the ambient temperature solidification route

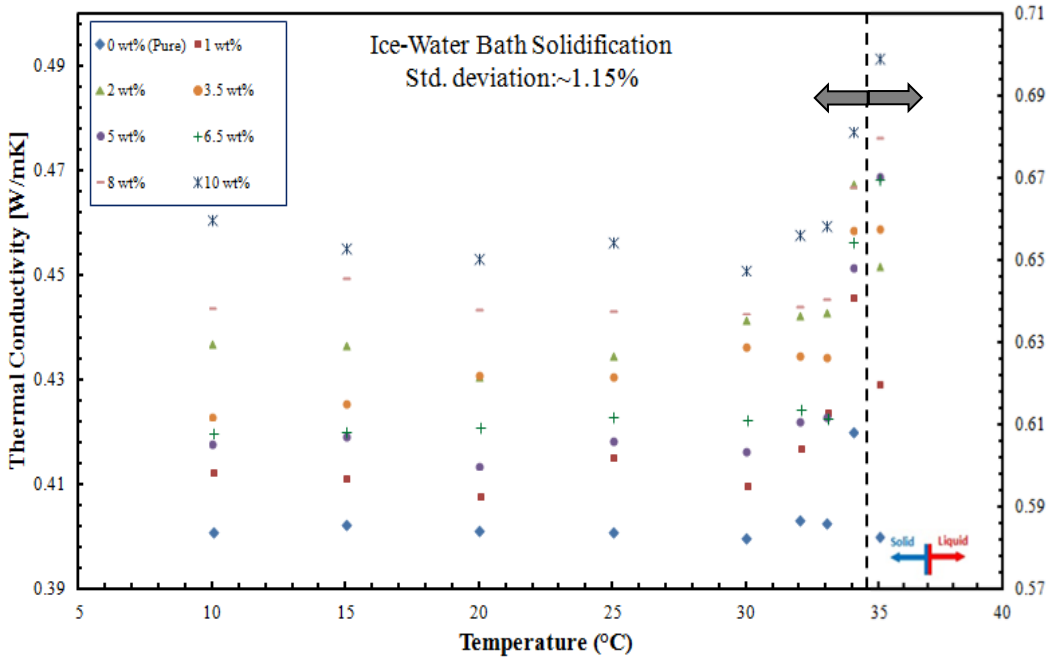

Figure 2.4 Thermal conductivity of solid pure eicosane and eicosane-CuO composites prepared following the ice-water bath solidification route

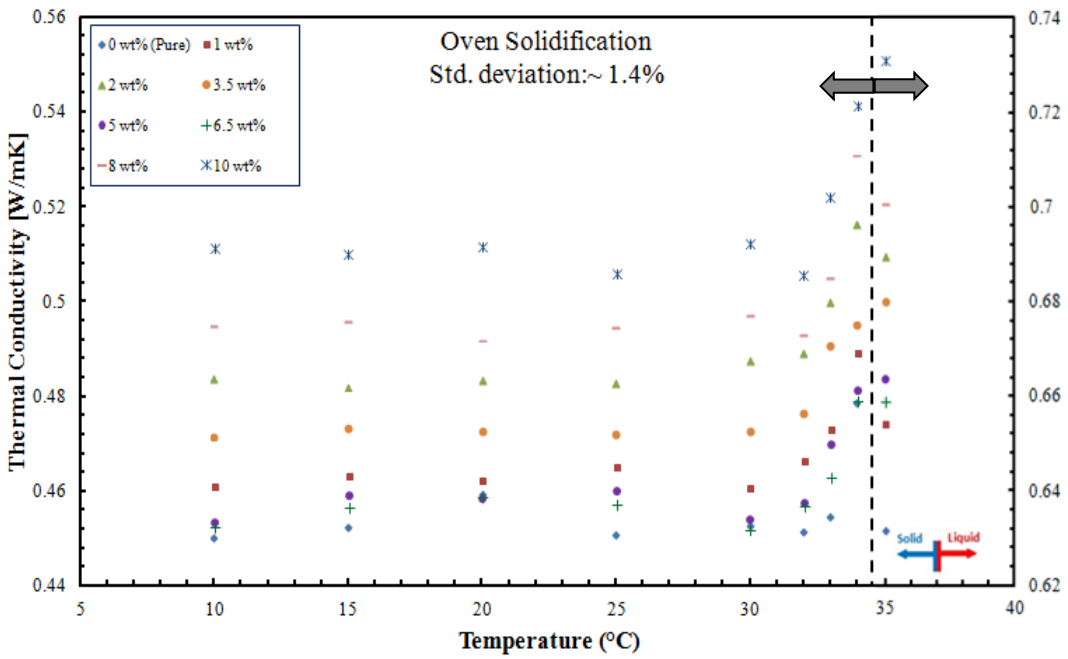

Figure 2.5 Thermal conductivity of solid pure eicosane and eicosane-CuO composites prepared following the oven solidification route

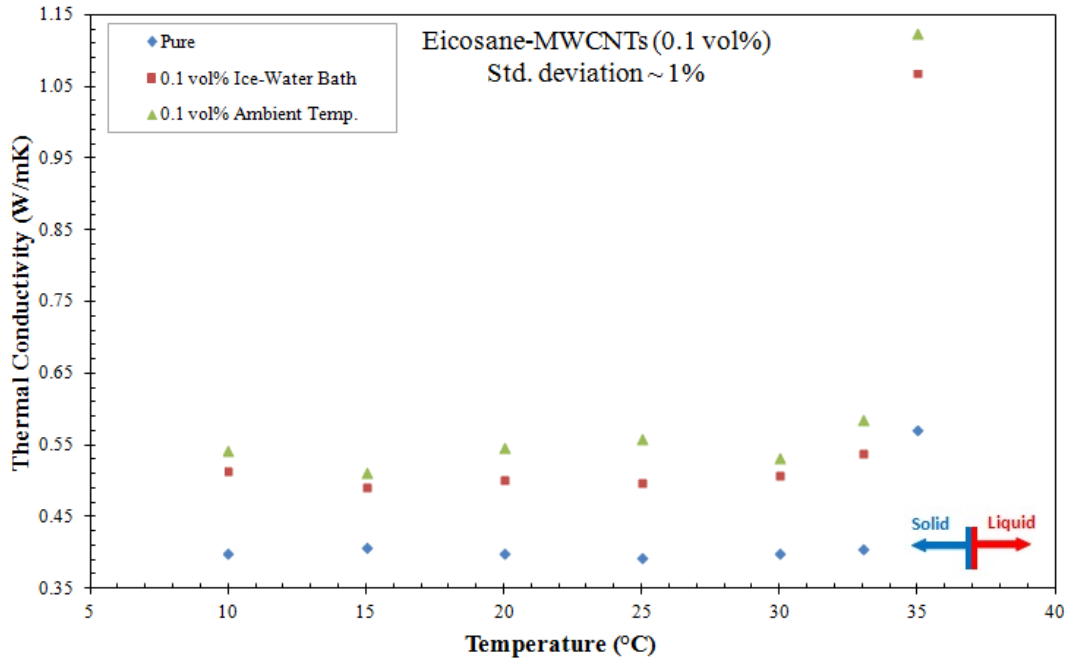

Figure 2.6 Thermal conductivity data of solid pure eicosane and 0.1 vol% eicosane-MWCNTs composites prepared following the ambient solidification/ice-water bath solidification routes

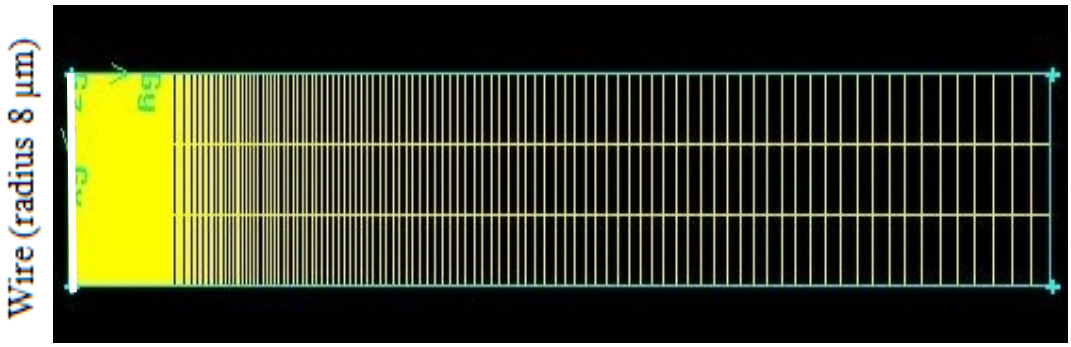

Figure 2.7 Generated 2-D mesh for the solution domain that consists of a thin wire of radius of 8 microns positioned along the vertical direction and the initially-solid material

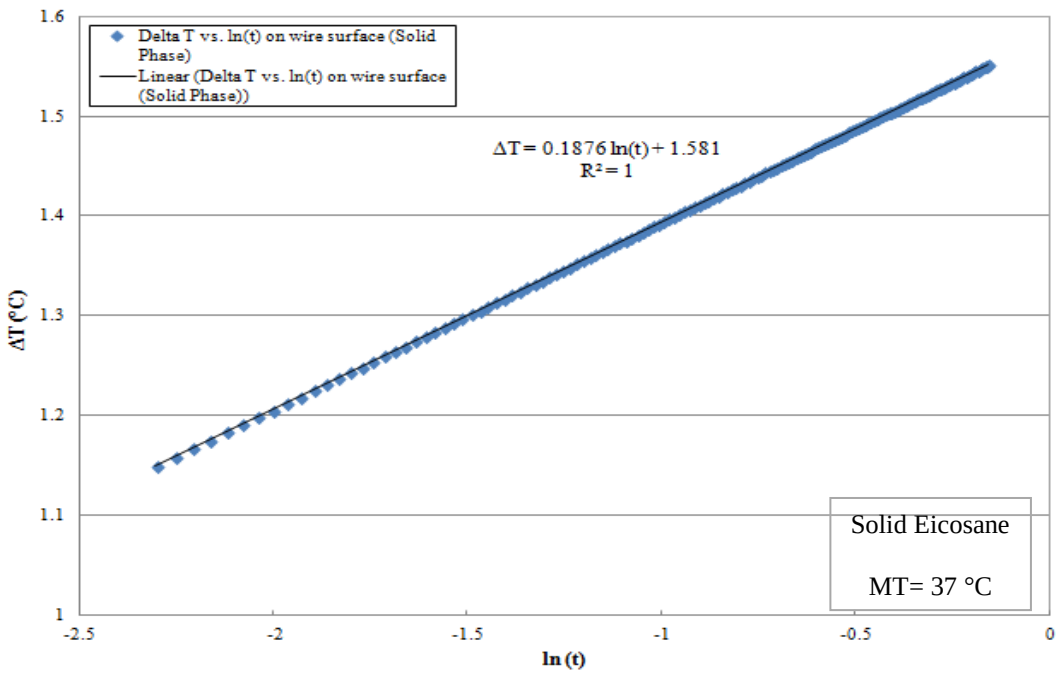

Figure 2.8 Plot of the solid phase eicosane temperature rise on the surface of the wire versus natural logarithm of time with an initial temperature of Ti=306 K using the FLUENT model

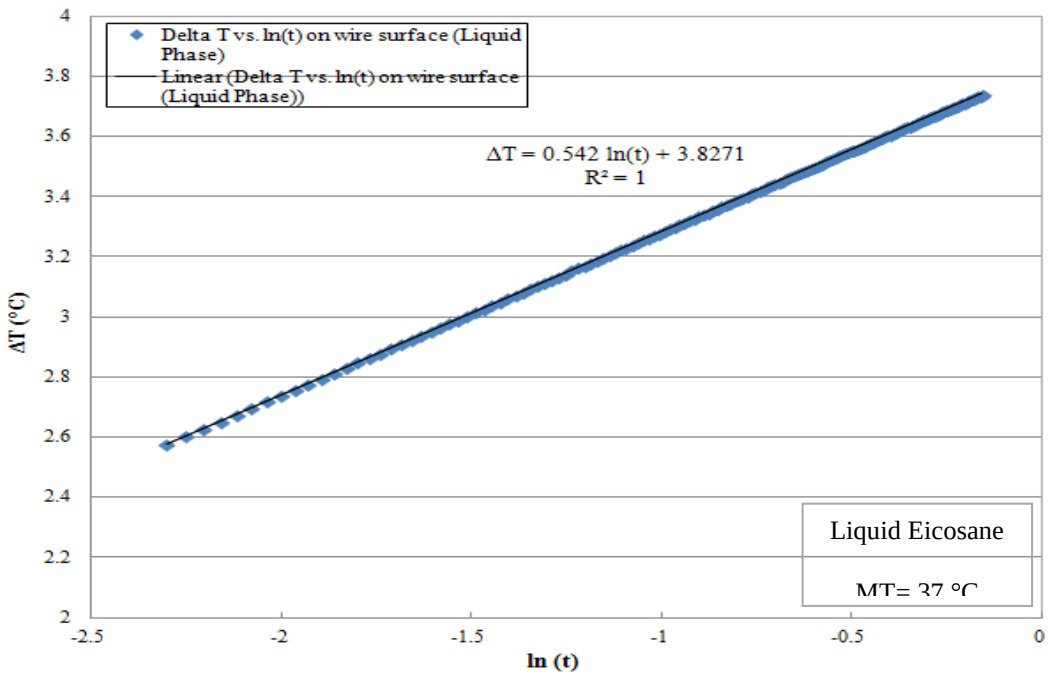

Figure 2.9 Plot of the liquid phase eicosane temperature rise on the surface of the wire versus natural logarithm of time with an initial temperature of T_i=313 K using the FLUENT model

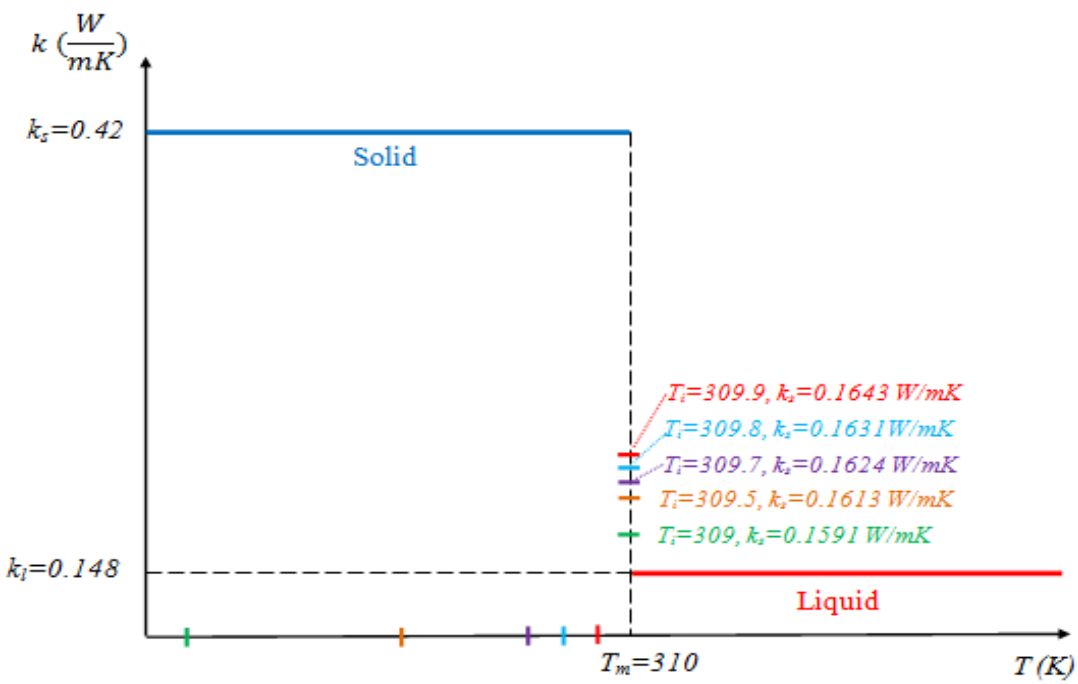

Figure 2.10 Predicted “effective” thermal conductivity values of eicosane as a function of the initial solid state temperature using the FLUENT model

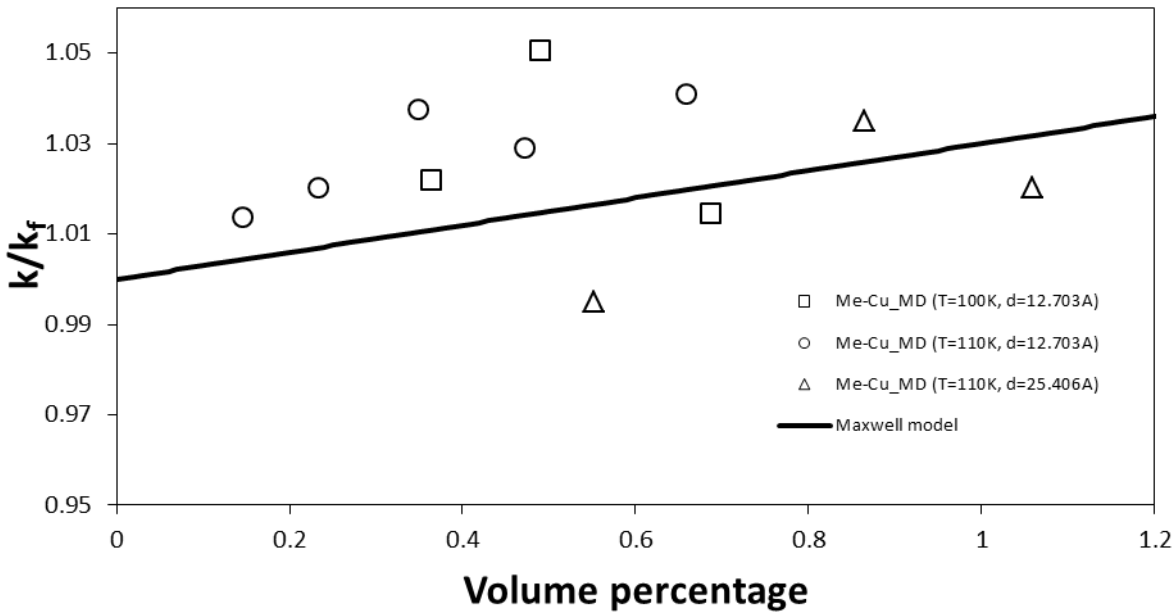

Figure 2.11 Thermal conductivity enhancement for different nanofluid cases along with the predicted results based on the Maxwell's model

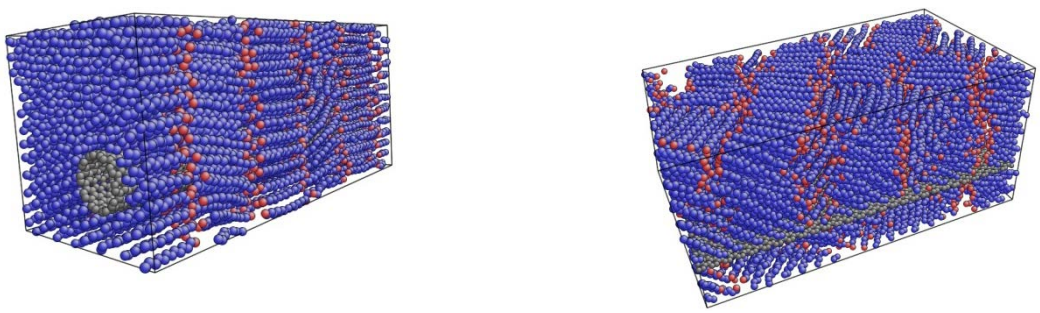

Figure 2.12 Ordering of paraffin molecules in CNT/paraffin (left) and graphene/paraffin (right) composites

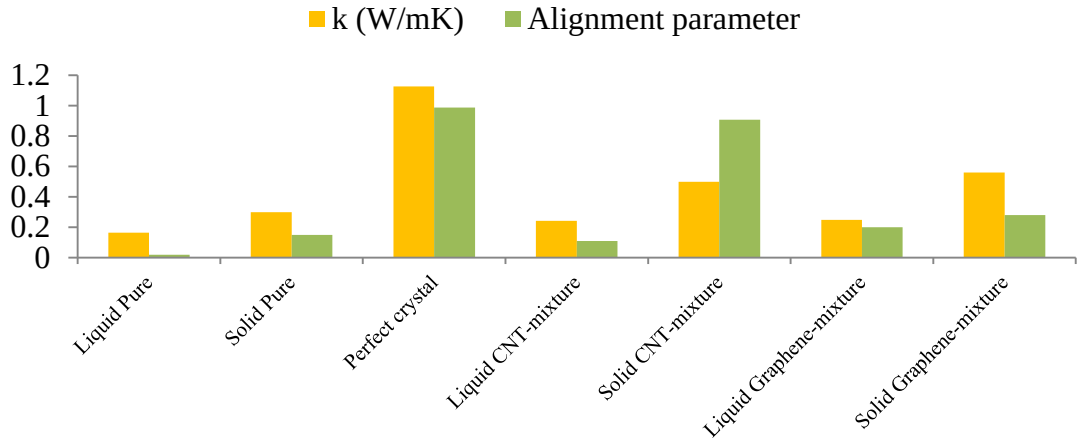

Figure 2.13 Thermal conductivity and alignment factor for different systems of paraffin

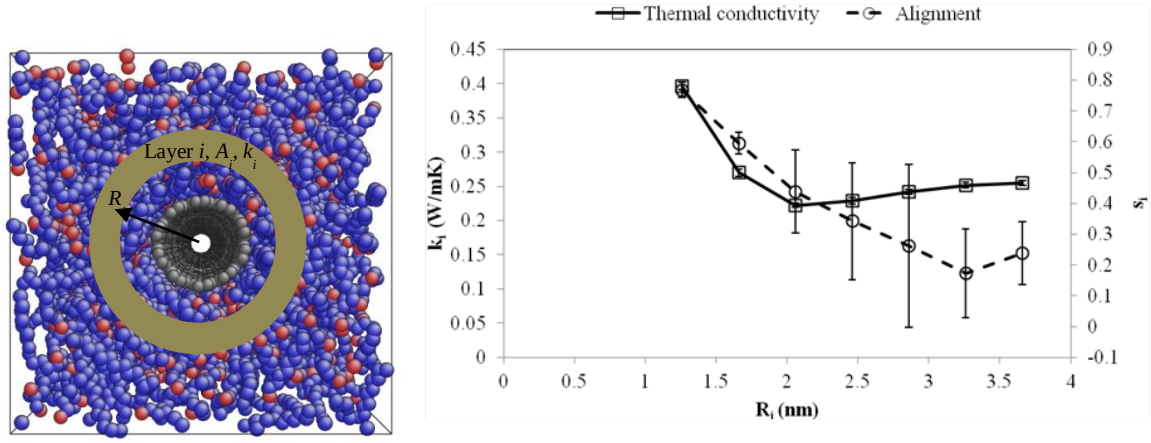

Figure 2.14 Local thermal conductivity and alignment parameter for the liquid CNT/paraffin mixture as functions of the distance from the CNT axis (CNT radius is equal to 0.7 nm)

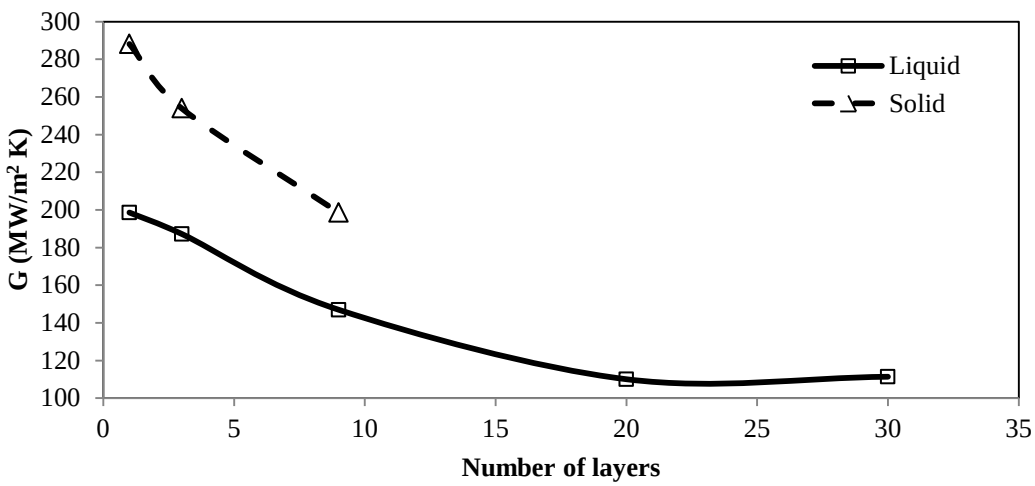

Figure 2.15 Dependence of thermal conductance on the number of layers of graphene

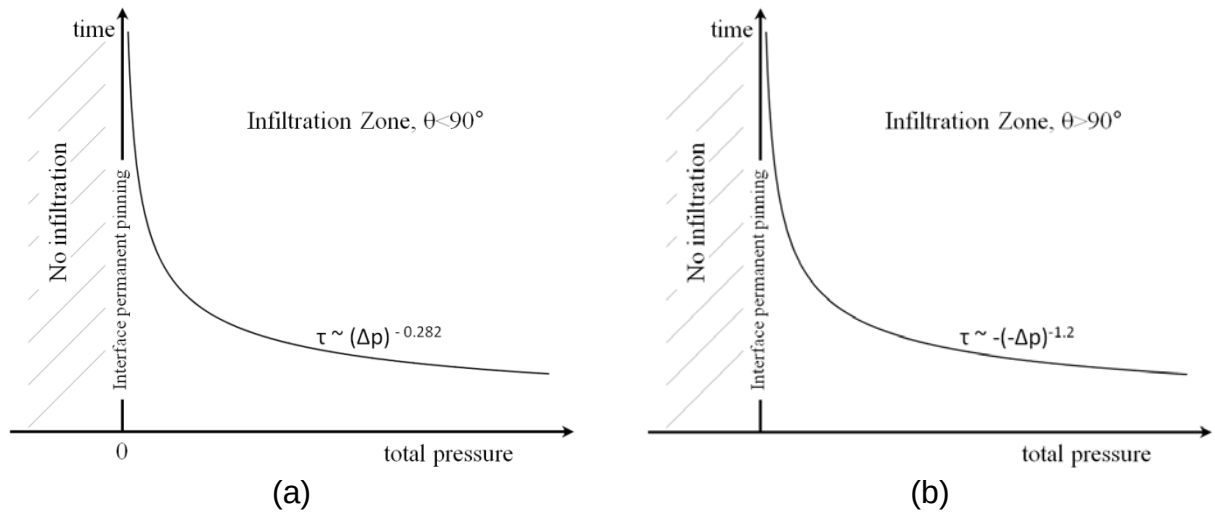

Figure 2.16 The infiltration criteria for (a) wetting liquids, and (b) non-wetting liquids with τ, Δp, and θ standing for dimensionless time and pressure and the wall contact angle

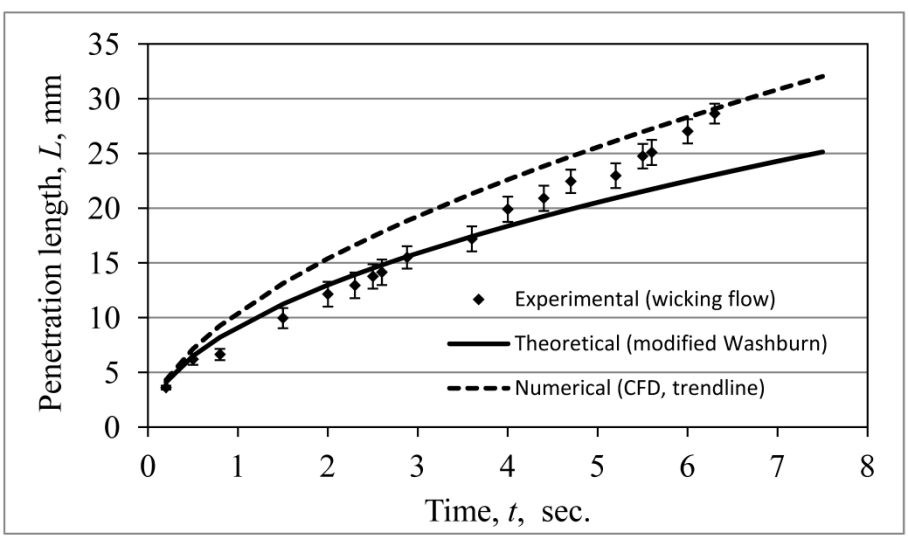

Figure 2.17 Experimental results of the average penetration length (filled symbols) versus time and corresponding uncertainties with a confidence level of 95% (vertical bars), in comparison with theoretical (modified Washburn equation) and numerical (VOF) results

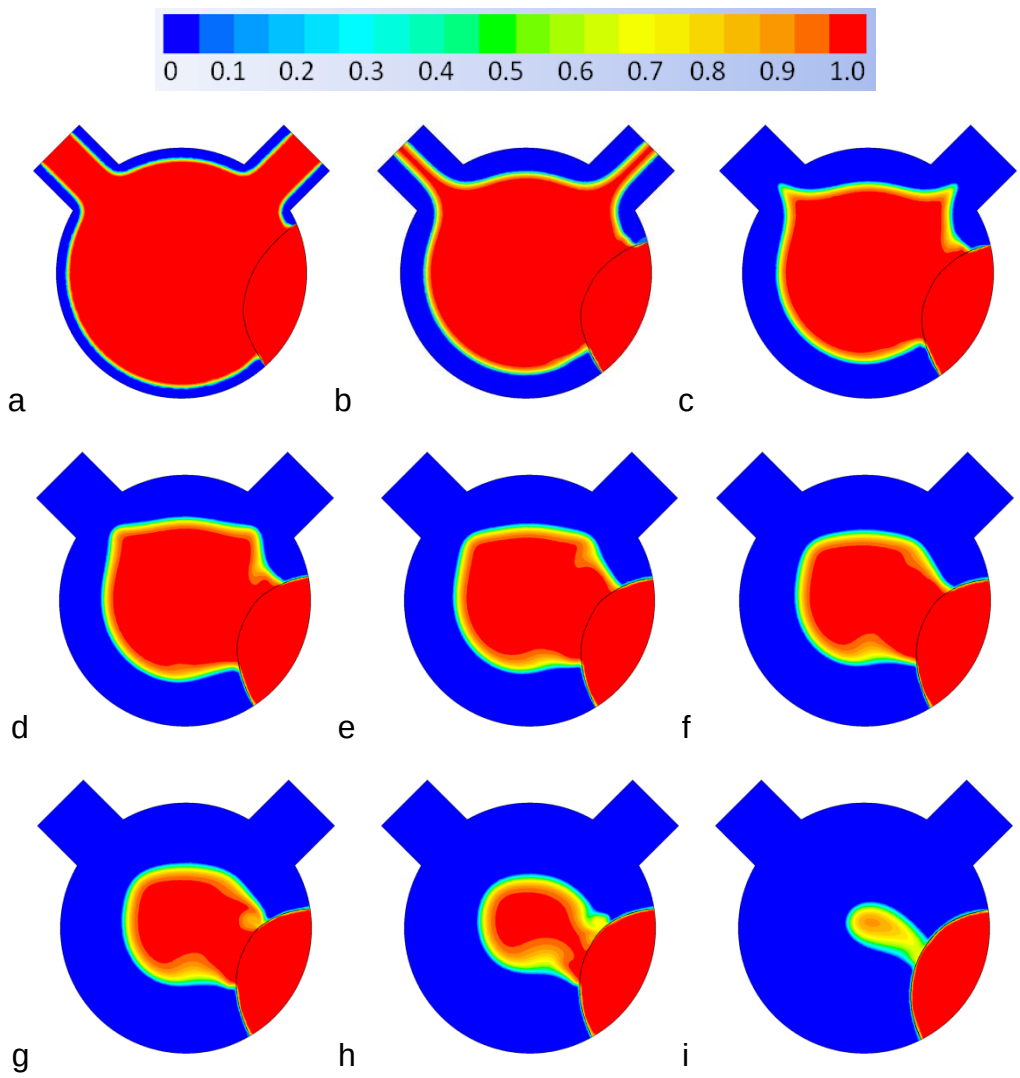

Figure 2.18 Contours of solidification liquid fraction (ε) at time instants of (a) 1, (b) 5, (c) 10, (d) 15, (e) 20, (f) 25, (g) 30, (h) 40, and (i) 65 ms (frozen PCM is in blue while liquid and air are in red and the black line shows the PCM-void interface)

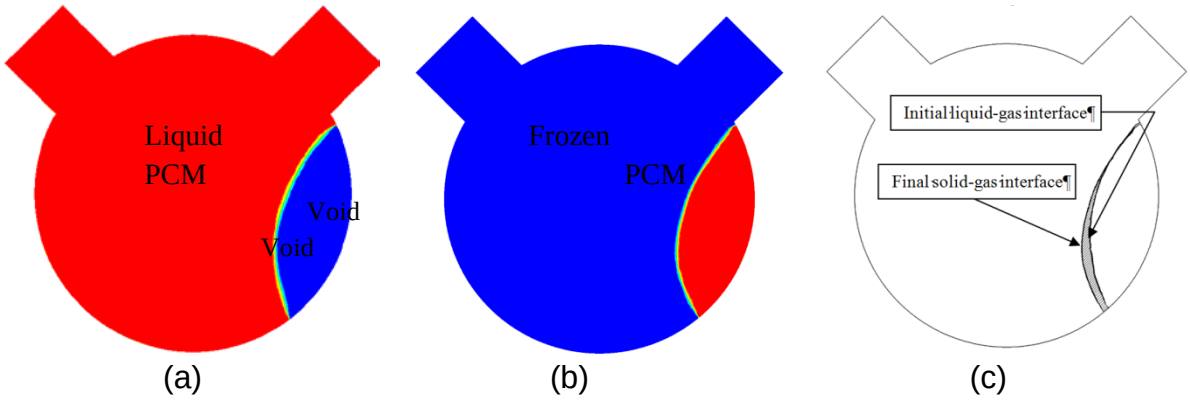

Figure 2.19 Formation of shrinkage void during the solidification process within the pore. (a) Contours of volume fraction before solidification, (b) Contours of liquid fraction after solidification, and (c) Comparison of void contents of the pore before and after solidification indicating the presence of 1.3% (based on area) shrinkage void within the pore upon freezing the whole PCM content of the pore

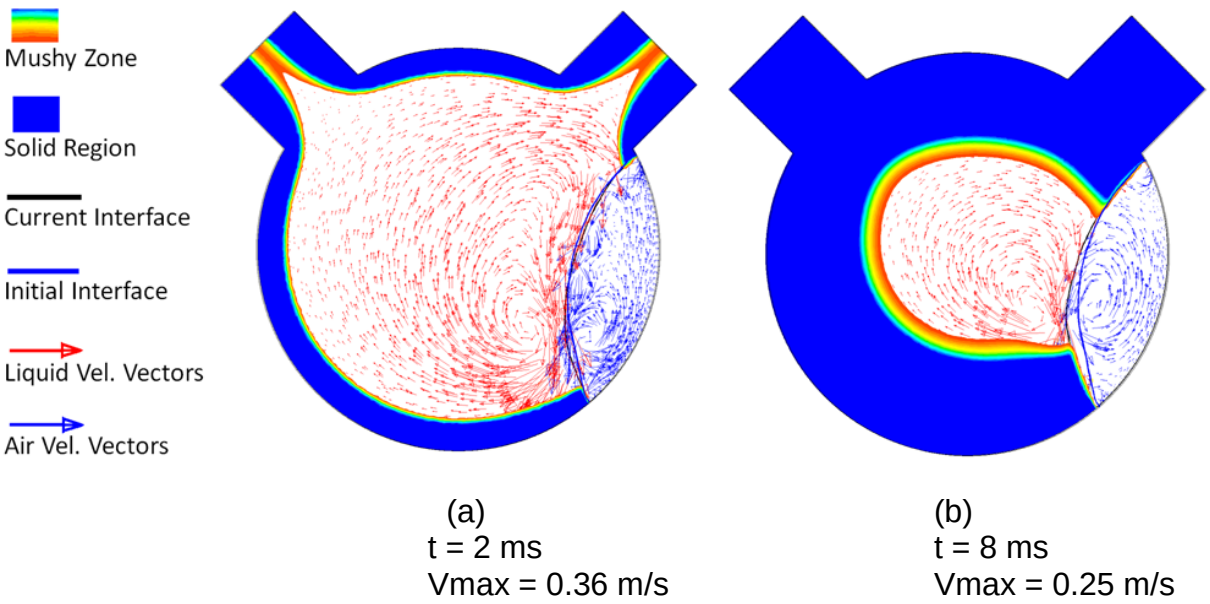

Figure 2.20 Natural convection patterns during the solidification of PCM within the pore in presence of void and its role in the distribution of the shrinkage void. The thermocapillary effects are not considered here. In presence of thermocapillary effects the distribution of the shrinkage void is altered due to a change in convection patterns within the pore; however, its volume remains unchanged

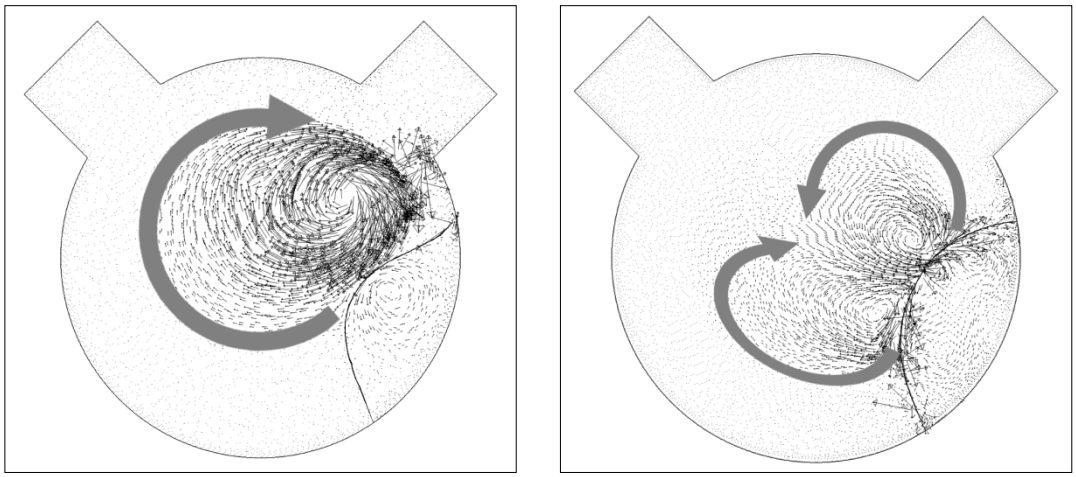

(a) (b)

Figure 2.21 Comparison of natural convection patterns within the pore during the solidification of PCM between (a) neglecting thermocapillary effect (Single buoyancy-driven clockwise vortex, V_{max}=0.092 m/s), and (b) including thermocapillary effect (Pair of surface tension-driven vortices, V_{max}=0.137 m/s)

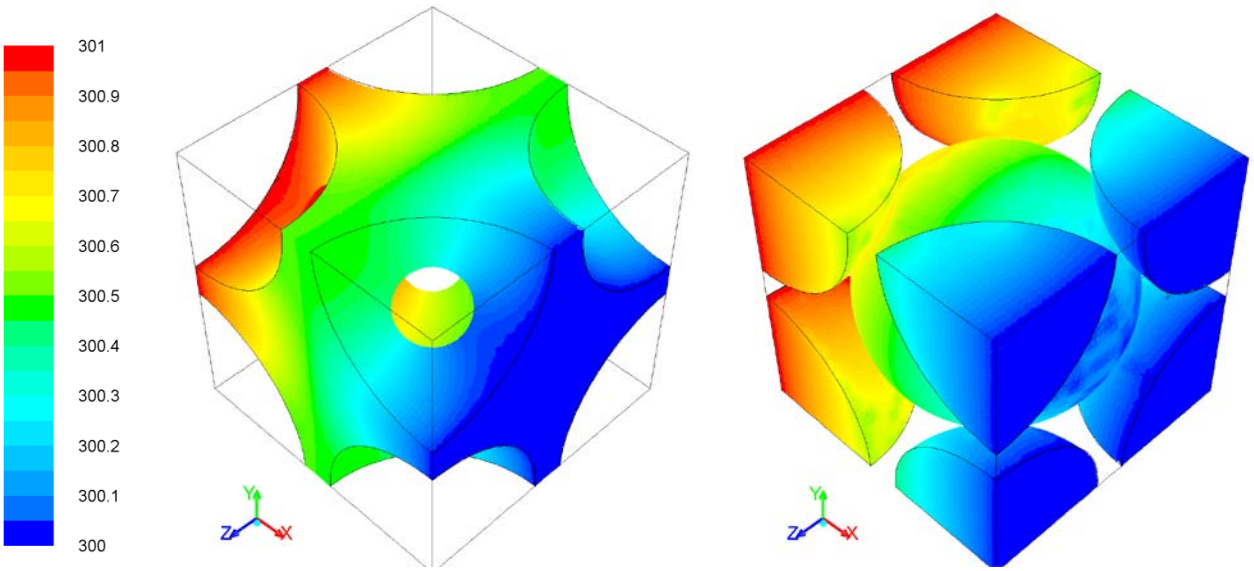

(a) (b)

Figure 2.22 Temperature distribution within (a) the graphite foam structure, and (b) the liquid PCM (cyclohexane) corresponding to selection of hot/cold temperature of 301 K/ 300 K as a periodic boundary condition

(a)

(b)

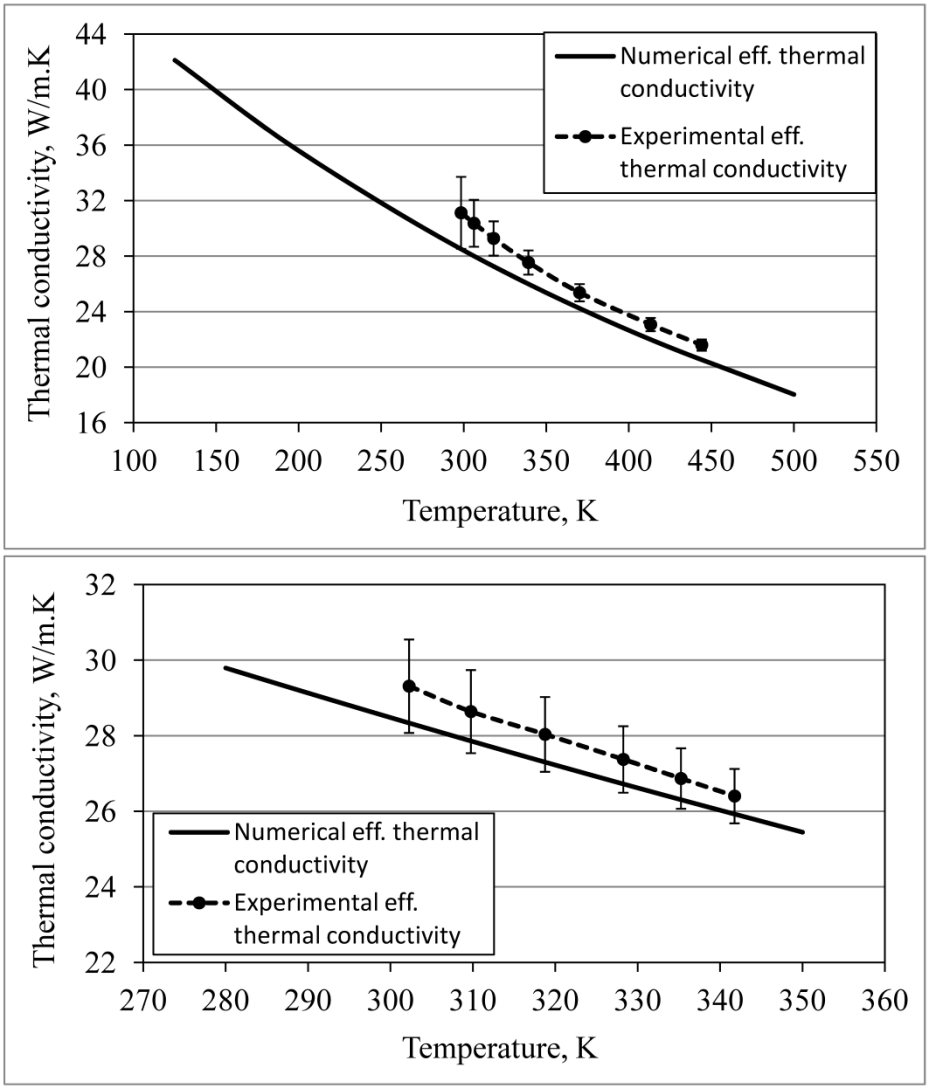

Figure 2.23 Experimental effective thermal conductivity compared to numerical predictions for (a) graphite foam and (b) graphite foam / cyclohexane composite (bars represent the corresponding uncertainties)

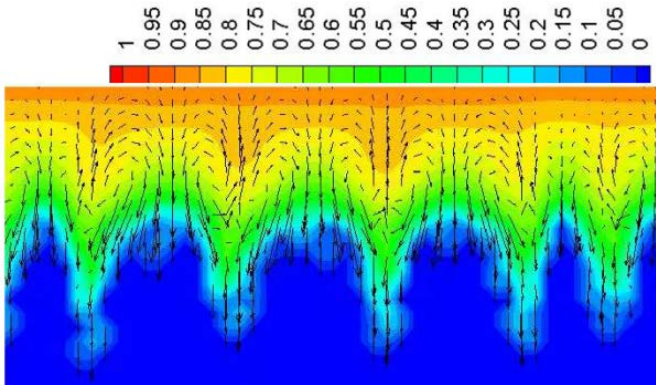

Figure 2.24 Velocity vectors in the vicinity of the liquid-solid interface after 1,000 s for an initial mass concentration field of 10% and d_p = 2 nm

3. Nanoparticle Separation/Reclamation
(Dr. Muhammad Ali Rob Sharif, Aerospace Engineering and Mechanics, The University of Alabama)

ABSTRACT: Phase change materials (PCM) are used in many energy storage applications. Energy is stored (latent heat of fusion) by melting the PCM and is released during re-solidification. Dispersing highly-conductive nanoparticles into the PCM enhances the effective thermal conductivity of the PCM, which in turn significantly improves the energy storage capability of the PCM. The resulting colloidal mixture with the nanoparticles in suspension is referred to as nanostructure enhanced phase change materials (NEPCM). A commonly used PCM for energy storage application is the family of paraffins (C_nH_{2n+2}). Mixing copper oxide (CuO) nanoparticles in the paraffin produces an effective and highly efficient NEPCM for energy storage. However, after long term application cycles, the efficiency of the NEPCM may deteriorate and it may need replacement with a fresh supply. Disposal of the used NECPM containing the nanoparticles is a matter of concern. Used NEPCM containing nanoparticles cannot be discarded directly into the environment because of various short term health hazards for humans and all living beings and un-identified long term environmental and health hazards due to nanoparticles. This problem will be considerable when widespread use of NEPCM will be practiced. It is thus important to develop technologies to separate the nanoparticles before the disposal of the NEPCM. This is the motivation behind this study. The primary objective of this research work is to develop methods for the separation and reclamation of the nanoparticles from the NEPCM before its disposal. It is aimed to find or design separation methods which are simple, safe, and economical. The specific NEPCM considered in this study is a colloidal mixture of dodecane ($C_{12}H_{26}$) and CuO nanoparticles (1% - 5% mass fraction and 5-15 nm size distribution). The nanoparticles are coated with a surfactant or stabilizing ligands for suspension stability in the mixture for a long period of time. Various methods for separating the nanoparticles from the NEPCM are explored. The identified methods include; (i) distillation under atmospheric and reduced pressure, (ii) high speed centrifugation, (iii) destabilization of the nanoparticles by adding chemical agents thereby inducing gravitational precipitation, (iv) silica-column chromatography, (v) silica adsorption and (vi) nanofiltration. These different nanoparticle separation methods have been pursued, and the results are analyzed and presented in this report.

3.1 INTRODUCTION

Phase change materials (PCM) are used in thermal energy storage applications where energy is stored (as latent heat of fusion) by melting the PCM and released during solidification [Nomura et al. (2009); Kuznik et al. (2011); Meng and Hu. (2008)]. Dispersing highly-conductive nanoparticles into the PCM enhances the effective thermal conductivity of the PCM, which in turn significantly improves the energy storage capability [Liu et al. (2012); Khodadadi et al. (2013); Fan and Khodadadi (2011)]. The resulting colloidal mixture with the nanoparticles in suspension is referred to as nanostructure enhanced phase change materials (NEPCM). A commonly used PCM for

energy storage application is the family of paraffins (C_nH_{2n+2}). Mixing copper oxide (CuO) nanoparticles (treated with surfactants for stability) in paraffin produces a stable and highly conductive NEPCM for energy storage. However, after long term application cycles, the functionality of the NEPCM deteriorates and it is required to replace it with fresh supply. Disposal of the used NECPM containing the nanoparticles is a matter of great concern as it cannot be discarded directly into the environment because of the short and long term environmental and health hazards [Gunawan et al. (2011); Heinlaan et al. (2011); Manusadžianas et al. (2012); Wang et al. (2012)]. Due to the widespread application potential of NEPCM, it is very important to develop proper technology to separate the nanoparticles before the disposal of the NEPCM. This is the motivation behind the present study.

Separation of particles/impurities from a solid-liquid mixture has been an age old problem. Various separation methods have been developed for various types of applications over the years. The separation method for a specific class of solid-liquid mixture depends on various factors such as the size of the particles, type/class of the liquid, mass/volume fraction of the particles in the mixture, physical properties of the base liquid and the particles, etc. The following methods are most widely used to separate particulate matter from liquid-solid mixture: Filtration, Distillation, Centrifugation, Electrophoresis, Magnetic Separation, Chromatography, and Chemical Methods. Every separation method has various operating requirements and the most critical ones being physical, chemical, and electrical properties of entities to be separated and the mixture to be processed [Liu et al. (2005); Lam et al. (2011); Xiong et al. (2011); Chen et al. (2007); Liu. (2009); Van der Bruggen et al. (2008)]. By studying and analyzing such properties of NEPCM, various methods have been attempted. In this work the following methods: distillation, centrifugation, chemical methods, chromatography, and nano filtration, which have produced successful results, have been reported along with brief description of the methods followed by analysis of the results and conclusion.

3.2 NEPCM CONFIGURATION

In this research, dodecane ($C_{12}H_{26}$) was used as the PCM base fluid and copper oxide (CuO) nanoparticles were employed to enhance thermal conductivity of dodecane. Ninety nine percent pure technical grade dodecane was used to obtain the NEPCM. Dodecane is a colorless liquid with a slight gasoline-like odor, has density of 0.753 g/cm^3, and boiling point of 216°C (Vertellus, 2005).The copper oxide nanoparticles are of spherical shape whose size varies from 5 – 15 nm with majority of them being about 9 nm. The density of CuO is 6.31 g/cm^3 and they appear black in color. The nanoparticles used in this research was manufactured and provided by the Chemistry Department of the Auburn University, a cluster partner of the NEPCM project (Clary and Mills, 2011).

Mixing the bare nanoparticles in the base fluid does not create a stable colloidal suspension. The particles coagulate together and quickly precipitate under the action of gravity because of the much higher density of the nanoparticles compared to that of the

base fluid. In order to disperse the nanoparticles evenly in the base fluid and to achieve a stable nano-colloid, it is required to prevent agglomeration of particles using suitable treatment of the particles. As the CuO particles do not carry any charge leading to electrically and magnetically neutral buoyant behavior, a viable method is to restrict the agglomeration by placing a barrier between two approaching particles. This is achieved by coating the nanoparticle surface with a stabilizing surfactant also known as ligands which act like a cushion among the particles. Sodium oleate ($C_{18}H_{33}NaO_2$) is used as the stabilizer (Clary and Mills, 2011). This forms numerous ligands on the particle surface which has a thread/string like structure as shown in Fig. 3.1. The resulting coated nanoparticles have an average mass composition of 69±1.4% copper oxide and 31±1.4% sodium oleate. The polar head of these ligands associate with particle surface whereas the non-polar tail interacts with the base fluid. The ligands on the particle surface provide a physical barrier (cushion) which prevents particle-to-particle contact and subsequent agglomeration. Furthermore, the string-like ligands exert additional opposing viscous drag on the particles against gravitational precipitation. Thus, a highly stable colloidal mixture of the nanoparticles and base fluid is obtained where the particles remain in the desirable homogeneous suspension for a long time with no or

egligible precipitation (Clary and Mills, 2011). This form of stabilization is known as steric stabilization.

3.3 EXPERIMENTAL SETUP AND PROCEDURES

3.3.1 Preparation of the NEPCM

Nearly homogeneous NEPCM samples were prepared by dispersing the desired amount of CuO nanoparticles into the base PCM, i.e., dodecane. The samples were prepared by following a mass fraction approach. In this approach, density of the nanoparticles and dodecane were used to find a required nanoparticle concentration (by mass) for a particular volume of NEPCM. The volume fraction, ϕ_{vol}, of CuO nanoparticles required for the preparation of NEPCM is calculated using law of mixtures, which is given by (photo below moved during editing)

$$\phi_{vol} = \frac{w_p}{\rho_p} \Big/ \left(\frac{w_p}{\rho_p} + \frac{w_{bf}}{\rho_{bf}} \right)$$

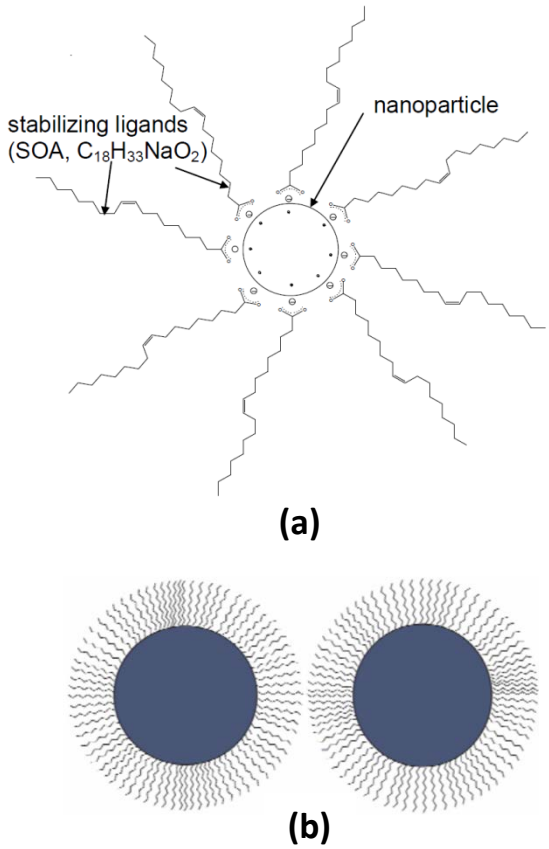

Fig. 3.1. (a) Schematic diagram of a nanoparticle with long ligands coated on its surface serving as the stabilizing cushion layer, (b) Ligands on particle surface to provide a physical barrier (cushion) which prevents particle contact and subsequent agglomeration.

where w and ρ are the weight and density and the subscripts p and bf are referred to nanoparticles and base fluid, respectively. In case the corresponding weight or mass fraction, ϕ_{wt}, are of interest, following relation is used for conversion for a two component system:

$$\phi_{wt} = \phi_{vol}\rho_p/[\phi_{vol}\rho_p + (1-\phi_{vol})\rho_{bf}]$$

The total mass of the particles, m_p, required to be mixed in a certain volume of the base fluid, V_{bf}, to get the mass fraction, ϕ_{wt}, is calculated as

$$m_p = V_{bf}\rho_{bf}\phi_{wt}/(1-\phi_{wt})$$

After determining mass of nanoparticles required, the next step involves dispersing this nanoparticle mass in the required volume of dodecane, then heating and stirring vigorously at 60°C on a hot-plate magnetic stirrer (SP131325Q, Thermo Fisher, Dubuque, IA), shown in Fig. 3.2, for 30 minutes to attain a stable colloidal suspension. This mixing in combination with heating produced a stabilized NEPCM, which appeared

Fig. 3.2. NEPCM Preparation.

like a black ink and was used for further experiments. Using the oleate stabilized CuO nanoparticles, long-term stability of colloidal suspensions in various hydrocarbons (hexane, octane, dodecane, and eicosane) was observed both qualitatively and quantitatively for mass fraction up to 20% corresponding to volume fraction of about 3% (Clary and Mills, 2011).

In this work, only dodecane was considered as the base fluid to prepare the NEPCM and to conduct different trials. Table 3.1 presents mass of nanoparticles required to mix in 100 ml of the base fluid for different mass concentrations.

Table 3.1: Amount of CuO NP required

Base Fluid Volume (ml)	Nanoparticle mass fraction	Nanoparticle mass required (g)
100	0.5%	0.3798
100	1%	0.7597
100	2%	1.5330
100	3%	2.3202
100	5%	3.9384

3.3.2 Atmospheric Pressure Distillation

Generally, distillation is used to separate one component liquid from a liquid mixture containing components of different volatilities or boiling points. In the simplest form of distillation, the liquid mixture is heated in a container until the liquid component with lower boiling point is vaporized and then subsequently condensed to yield the distillate [Coker (2010); Yang et al. (2010); Sánchez et al. (2009); Shi-chang (1987)]. The distillation process can also be used to separate suspended solid particles from a colloidal mixture. In the present context, the separation of the nanoparticles from the NEPCM was accomplished by evaporating the dodecane (base fluid) at 218°C using a distillation process. A standard distillation unit was used to carry out the distillation process at atmospheric pressure. An energy meter measured the amount of energy consumed during each experiment. Fig. 3.3a depicts the 100 ml NEPCM with a 1% by mass concentration of the CuO nanoparticles. The black color of the colloid is due to the presence of black CuO nanoparticles. Fig. 3.3b shows the nanoparticle residue left in the heating flask after completion of distillation. Nanoparticles were deposited in the form of a thin layer at the bottom of the flask.

3.3.3 Vacuum Distillation

The boiling point of the liquid varies depending upon the surrounding environmental pressure. A liquid at high pressure has a higher boiling point than a liquid at atmospheric pressure. Conversely, at lower pressure or under vacuum, boiling point of liquid is lower than at atmospheric pressure conditions. Distillation has long been criticized as slow and a high energy intensive process. Hence, in order to make it more energy efficient, distillations were performed at reduced pressure. To perform distillation under reduced pressure, a complete new setup was required, as the distillation unit for this purpose has to be airtight and of sufficient strength to withstand the applied vacuum. Hence a new vacuum distillation unit with vacuum pump of 1/6 HP power rating, 2.4 CFM free air displacement and 10 Pa ultimate vacuum was used. All standard procedures and safety measures were followed while conducting the trials.

Fig. 3.4 shows the vacuum distillation setup used to conduct trials.

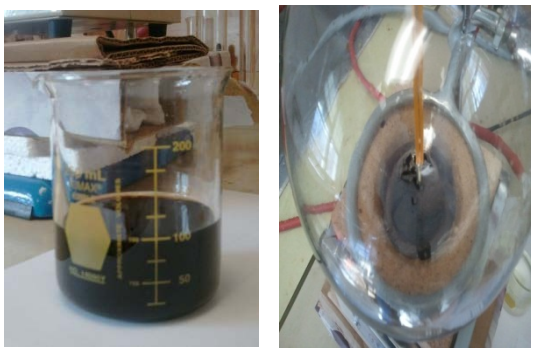

(a) Before Distillation
Sample: 100 ml
1 % (by mass) NEPCM

(b. After distillation:
Flask bottom showing
nanoparticle residue.

Fig. 3.3. NEPCM before and after distillation

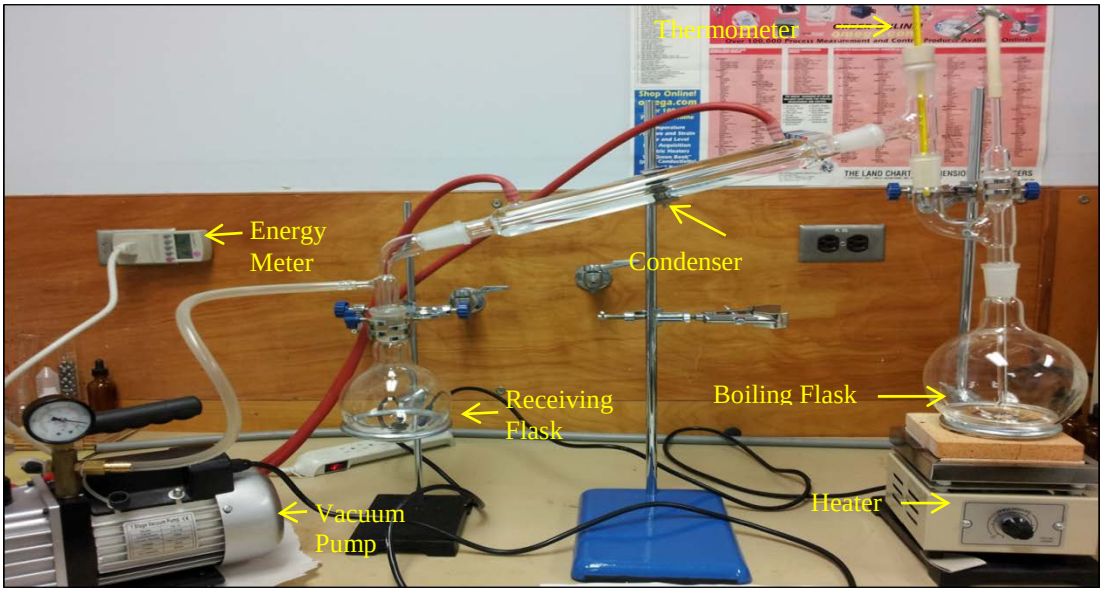

Fig. 3.4. Laboratory vacuum distillation unit.

3.3.4 Chemical Treatment of the NEPCM

It is hypothesized that, if the NEPCM is mixed with another heavier liquid in which the base fluid is soluble, then a portion of the dodecane in the NEPCM will be dissolved into the heavier liquid and settle at the bottom, leaving a more concentrated NEPCM layer on top. The concentrated top layer can then be separated and further processed. Based on a literature survey and consultation with the experts in chemistry, different heavier solvents were selected to verify the hypothesis. Initial attempts were made using methanol, ethanol, and a mixture of methanol and propanol as solvents. Equal volume of NEPCM and solvent were added in a test tube and were shaken for 30 min. at 450 rpm and 34°C using a Controlled Environment Incubator Shaker unit, available at the University of Alabama Biology Department. Three samples of alcohols containing pure methanol, pure ethanol, and a 50%-50% mixture (by volume) of propanol and methanol were tested. Of the three samples tested, the 50%-50% mixture of propanol and methanol showed satisfactory results.

3.3.5 Centrifugation of the NEPCM

Due to the density gradient between CuO nanoparticles (6.31 g/cm3) and base fluid dodecane (0.753 g/cm3), it is anticipated that centrifugation at higher speeds would precipitate the nanoparticles. Initial trials were performed on a micro-centrifuge at speeds up to 10,000 rpm and no precipitation was observed for a centrifugation duration of 30 min. Hence, in order to precipitate the nanoparticles out of the suspension, it was deemed necessary to apply greater centrifugal forces to overcome the stabilization effect. This force was applied using higher centrifugation speeds on a large size centrifugation machine. A SORVALL RC6 super-speed centrifuge floor model with a maximum speed rating of 21,000 rpm, which is equivalent to over 50,000× gravity or relative centrifugal force (RCF), was used to conduct high speed trials in conjunction with SM-24 rotor which is fixed angle rotor. Initial trials were done for up to six hours at 18,000 rpm which showed partial precipitation of nanoparticles indicating RCF for this duration is not enough to overcome stabilization completely. Further trials were done using 0.5%, 2%, and 5% concentration (by mass) of the NEPCM for the same operating conditions of 18,000 rpm for 19.5, 24, and 48 hrs.

3.3.6 Nanoparticle Ligands/Surfactants Destabilization

If the stabilizing ligand ends, which are attached to nanoparticle surfaces, can be detached by the same process, then steric stabilization will break down leading to nanoparticle destabilization and consequential precipitation due to gravity. After conducting several experiments and getting unsatisfactory results, interaction of potassium hydroxide (KOH) with the NEPCM, in the presence of ethanol, produced the desired result. It was observed that KOH interaction with NEPCM results in steric stabilization break down which makes nanoparticles fall down primarily due to gravity.

3.3.7 Silica Column Chromatography

Chromatography is a separation process in which the sample mixture to be processed is distributed between two phases in the chromatography bed (column or plane). One phase is stationary, and known as stationary phase, while the other phase passes through the chromatography column and is known as mobile phase or eluent. The substances in the mixture to be processed or separated must have different affinities for these two phases. The substance with a relatively higher affinity for the stationary phase moves with a lower velocity through the chromatography column than the substance with lower affinity. This difference in migration velocities of the components of the sample ultimately leads to physical separation of the components [Gaborieau et al. (2008); Bryant et al. (1994)]. A component of the sample mixture that leaves the stationary phase and moves with mobile phase is said to be eluted in a process known as elution.

A manual column chromatography using powder silicate was used to conduct NEPCM chromatography trials. A glass chromatography column of 10.5 mm internal diameter and 200 mm length was purchased from The Lab Dept., Inc., which came with a straight stopcock with a poly-tetrafluoroethylene (PTFE) plug. A cotton plug, sand (coarse) and silica grain size (230-400 mesh), were used to establish the column where a cotton plug and coarse sand served as the column base. In this formation silica gel was used as stationary phase and hexane was used as mobile phase. Fig. 3.5 shows the NEPCM

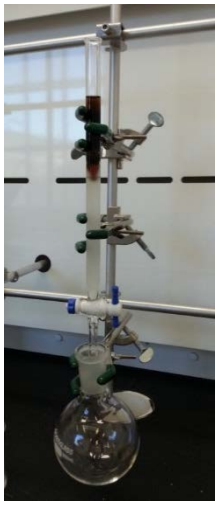

Fig. 3.5 Silica column chromatography

chromatography set-up. A silica column of 4 inch (approx.) was used for all trials. After the column was established, the NEPCM sample to be processed was added, followed by hexane, to aid in the elusion process. Hexane was added to fill to the top of the glass column (5 ml approx.) on the top of the NEPCM sample to increase elusion. Due to the pressure exerted by the hexane, movement of the NEPCM was observed through the silica column, which was easier to observe due to its black color. After reaching a certain length of the column, the nanoparticle elusion stopped. At this point nanoparticles are considered to be trapped by the silica matrix or column, allowing only transport of base fluid dodecane under action of hexane as an eluting agent.

3.3.8 Nanoparticle Separation by Adsorption on Silica Surface

At room temperature, silica can be seen coated by a mono-molecular layer of water molecules which tightly cling to its surface via extended hydrogen bonds to adjacent silanols which explains why silica is a highly hydrophilic material. Silica has a moderately strong acidity, negligible basicity, and moderately strong di-polarizability. Silanol groups (≡ Si – OH) are formed on the surface by the two processes. First, during silica synthesis, e.g., condensation polymerization of $Si(OH)_4$ where the supersaturated solution of the acid is converted into spherical colloidal particles containing Si – OH (silanol) groups on the surface. Upon drying, hydrogen yields xerogel as the final product which retains some or all of the silanol groups on the surface. Secondly, surface Si – OH groups can form as a result of re-hydroxylation of de-hydroxylated silica when it is treated with water or aqueous solutions. The surface silicon atoms tend to have a complete tetrahedral configuration and in an aqueous medium their free valence becomes saturated with hydroxyl groups. The various surface properties of amorphous silica, which is considered to be an oxide adsorbent, depend on the presence of silanol groups. The OH groups act as the centres of molecular adsorption during their specific interaction with adsorbates capable of forming a hydrogen bond with OH groups, or in general, undergo donor-acceptor interaction. It is no surprise that removal of hydroxyl groups from the silica surface leads to a decrease in the adsorption.

Silica with 40-63 µm grain size (230-400 mesh), pore size 60Å in dry form was purchased from SILICYCLE, UltraPure SILICA GELS, Canada and was used as is. The black color of the nanoparticles present in the NEPCM sample served as an indicator during these trials. For these trials, a known volume and concentration of NEPCM was taken as a sample in a test-tube and a measured amount of silica was added in steps of 0.1 gm followed by vigorous manual shaking for 1 min. A digital scale (Mettler Toledo MS204, USA) was employed to measure the weight of silica. The solution was allowed to settle for 15 seconds followed by the addition of more silica in the mentioned measured amount, if no settling of nanoparticles with silica was observed. Once enough silica was added to adsorb all of the nanoparticles and the process settled, two distinct layers were observed in the test-tube; a clear top layer of base fluid (dodecane) and a black layer at the bottom containing silica and adsorbed nanoparticles. A Whatman grade no. 1 filter paper of diameter 9 cm (Whatman 1001-090) was used in a funnel to separate the two phases. Hexane was used as a washing agent and as an aid in filtration. The filtrate, which is basically a mixture of dodecane and hexane, was air dried to get rid of excess hexane. The final solution containing dodecane and traces of hexane was analysed using UV-Vis photo-spectrometry to check and confirm nanoparticles are completely removed.

3.3.9 Nanofiltration

Filtration primarily works on the size-exclusion principle and has been widely used to separate impurities of different size ranges, e.g., nano, micro or higher. Separation of nanoparticles or nano-size entities from a solution dates back to late 1950s when reverse osmosis (RO) was used as a process mainly for the desalination of water. In the

1970s, relatively low pressure RO membranes were developed yielding higher water flux with added advantages of retaining essential minerals. Such membranes with lower rejections of dissolved components with higher water permeability proved to be a great improvement for separation technology. These low-pressure RO membranes are referred as “Nano-filtration” membranes. Nano-filtration (NF) is a process between reverse osmosis and ultrafiltration that rejects impurities or molecules which have sizes greater than the designated rating of membrane. This range of membrane is often specified in terms of the molecular weight cut-off ratio (MWCO) which is basically a number indicating the capacity of the membrane to hold 99% of the molecules or particles of a size greater than specified MWCO rating. Different membrane suppliers have different rules and guidelines to select membranes for an application.

For micro or bigger size impurities or particles, filtration is basically a sieving mechanism where large size entities get trapped at the filter/membrane surface allowing only small entities to pass through depending on the filtration membrane pore size rating. However, at nano-level, filtration becomes complex in terms of increased fouling and pressure requirements and is no longer size-exclusion dependent only. Though different theoretical models have been processed since its introduction in 1980s, this method of separation mechanism has long been debated as pure convection (sieving) or pure diffusion or a combination of both.

For lab scale applications to process small volumes of a sample, cross-flow filtration is more suitable due to its limited source requirements and lower cost compared to a tangential flow filtration system. The dead-end filtration system commonly consists of a membrane in combination with membrane holder or stirred cell. An in-house filter holder was designed and manufactured at the University of Alabama glass shop to analyze the separation efficiency of a ceramic membrane to process the NEPCM. Table 3.2 presents properties of the ceramic membrane.

Fig. 3.6 shows the in-house designed and manufactured nano-filtration set-up in dismantled form. This set-up has been designed for dead-end filtration trials by incorporating features of both: membrane holder and stirred cell. As shown, it consists of two glass parts: top and bottom, to hold the filtration membrane in between, and a pair of gaskets to provide necessary sealing and a pair of clamps to hold these parts together by means of 3 bolts. The top part of the set-up is designed with two inlets to apply pressure while the bottom part contains one inlet to apply a vacuum (if required) and/or to collect the filtrate. To manufacture top and glass parts of the set-up, Pyrex glass tubing of size 38.1 mm OD and 2.5 mm thickness was used which can withstand maximum internal pressure of 9 bar (131.2 psi). Glass was preferred to make the top and bottom parts of the nano-filtration set-up primarily due to its lower material and machining cost. Fig. 3.7 shows the assembled experimental set-up where assembly was done using 7/16 size spanner/wrench. As shown, the top part is subjected to pressure (1.4 bar – 2.75 bar) using pressurized nitrogen through one of the inlets while the other inlet served as a stopper or pressure relief port. Vacuum (0.02 mbar) was applied at the bottom part which was required during filtration trials to improve the filtration rate.

Table 3.2 Ceramic Membrane Specifications

Manufacturer	Sterlitech
Size	47 mm dia, 2.5 mm thickness
Pore Size Range	1 kDa to 1.4 µm
Maximum Operating Pressure	4 bar (58 psi)
Operating Temperature	< 350 °C (662 °F)
pH Range	0 – 14 , 2-14 (Nanofiltration)
Sterilization	Chemical or Autoclavable

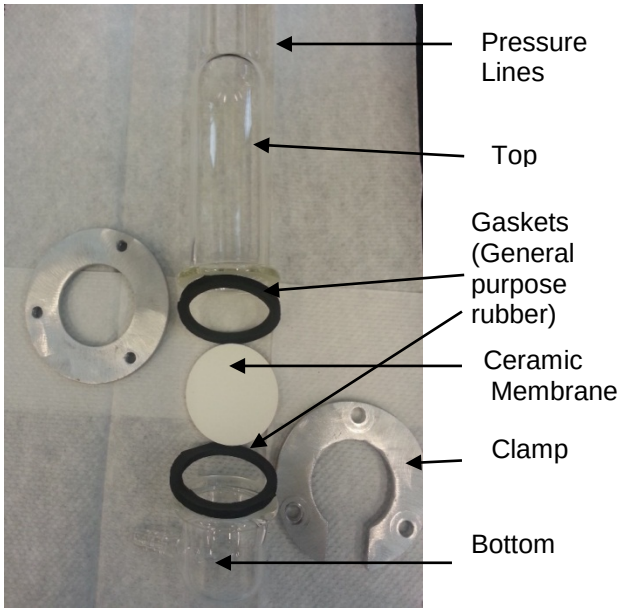

Fig. 3.6 Designed Filter Holder Parts

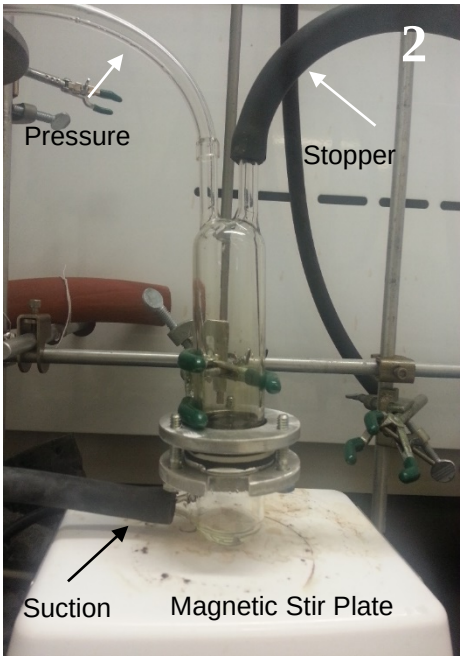

Fig. 3.7 Filtration Set-Up

3.4 Results and Discussion

3.4.1 Distillation

Fig. 3.8 and 3.9 shows the distillate collected after atmospheric pressure and vacuum pressure distillation respectively. The distillate collected resembles pure colourless dodecane used to prepare the nano-colloid. The absence of any colour clearly indicates that the collected distillate is free from any trace of copper oxide.

Fig. 3.8. Distillate: Atm. Pressure distillation.

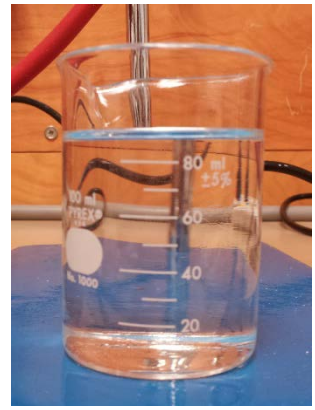

Fig. 3.9. Distillate: Vacuum distillation.

Table 3.3 summarizes the data collected using the atmospheric pressure distillation process. A total of six trials were performed for different combinations of the NEPCM volume and nanoparticles concentration. The mass concentration of nanoparticles chosen was 0%, 1% and 3%. A trend was observed for time required and energy consumed in relation to the amount of NEPCM used. Also it was observed that for the same volume, NEPCM with a higher concentration of nanoparticles distilled faster than NEPCM with a lower nanoparticle concentration. This is consistent with an increase in the thermal conductivity claim of the dodecane upon the addition of copper oxide nanoparticles.

Table 3.3. Atmospheric pressure distillation trials summary.

Trial Number	NEPCM Volume (ml)	Nanoparticles Mass Fraction (%)	Total Time (min)	Total Energy Consumed (kWh)	Distillate Volume (ml)	Energy/Volume (kWh/ml)
1	100	0	40	0.68	96	0.0068
2	50	1	35	0.60	48	0.0120
3	100	1	40	0.63	95	0.0063
4	150	1	40	0.65	146	0.0043
5	200	1	40	0.66	197	0.0033
6	100	3	32	0.51	97	0.0051

Table 3.4 shows the data collected for vacuum distillation trials conducted at 33.6 kPa vacuum. For a 100 ml volume of NEPCM, it was found that, as the amount of nanoparticles increased, the time required for vacuum distillation decreased which resulted in less power consumed. This is consistent with the fact that high heat conducting nanoparticles present in NEPCM increases the rate of distillation as was observed in the atmospheric distillation case as well. The final volume of distillate

measured was found to be lower than the initial volume of 100 ml due to the removal of nanoparticles and loss of dodecane vapours.

Table 3.4. Vacuum (33.6 kPa) distillation data summary.

Trial Number	NEPCM Volume (ml)	Nanoparticles Mass Fraction (%)	Total Time (min.)	Total Energy Consumed (kWh)	Distillate Volume (ml)	Energy/Volume (kWh/ml)
1	100	0	20	0.35	96	0.0035
2	100	1	15	0.24	97	0.0024
3	100	3	12	0.18	96	0.0018

Figs. 3.10 and 3.11 presents the distillation data for atmospheric pressure and vacuum distillation processes on energy required and time basis, respectively. It is evident that a vacuum distillation is much more efficient process to carry out distillation of NEPCM, as it consumes lower energy and takes less time than distillation at atmospheric pressure. Based on calculations it is found that for the same volume and nanoparticle concentration of NEPCM distilled, vacuum distillation consumes about 60% less energy as well as time. Though initial equipment cost for vacuum distillation setup is higher than for atmospheric distillation, the operating cost for vacuum distillation is much lower. Thus it can be concluded that for long term applications and higher volumes of the NEPCM to be processed, vacuum distillation is a better alternative.

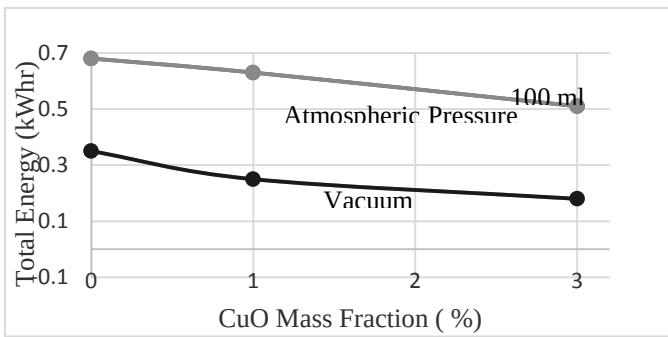

Fig. 3.10. Distillation data comparison on energy

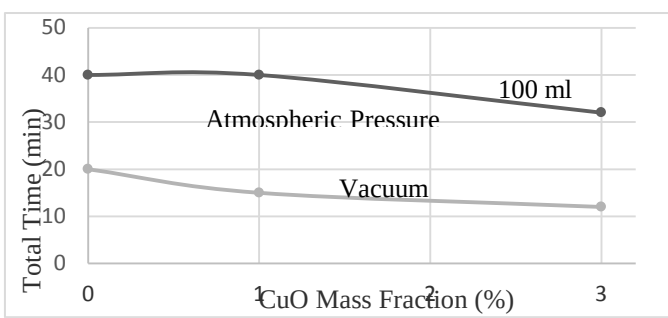

Fig. 3.11. Distillation data comparison on total time basis.

To verify the nanoparticle removal efficiency of the distillation processes, Scanning Electron Microscope (SEM) was utilized. All samples were prepared on a standard nickel grid having a carbon coating and were dried for 48 hours before imaging. Fig. 3.12 shows the comparison of SEM images taken for base fluid (pure dodecane), NEPCM before distillation, distillate at atmospheric pressure, and distillate collected by vacuum distillation. Fig. 3.12a shows the SEM image of the 99% pure dodecane, which has been used as a base fluid for the NEPCM preparation. The structure of carbon coating on the grid is clearly discernible

from this image which shows no sign of any nanoparticle present. Fig. 3.12b shows the structure of the NEPCM containing 0.5% (by mass) concentration of the CuO nanoparticles. The lump of nanoparticles sticking to the carbon web structure is clearly visible in the image. As 0.5% by mass is a higher concentration especially after preparing the SEM sample where it is dried, making nanoparticles agglomerate. These two images in Figs. 3.12a and 3.12b were compared with the SEM images of the distillate samples. Fig. 3.12c shows the image of the distillate collected from the atmospheric pressure distillation while Fig. 3.12d shows the image of the distillate collected from the vacuum distillation. No trace of the nanoparticle is detected in the distillate in these images asserting that the distillation results are in complete separation of nanoparticles from the NEPCM.

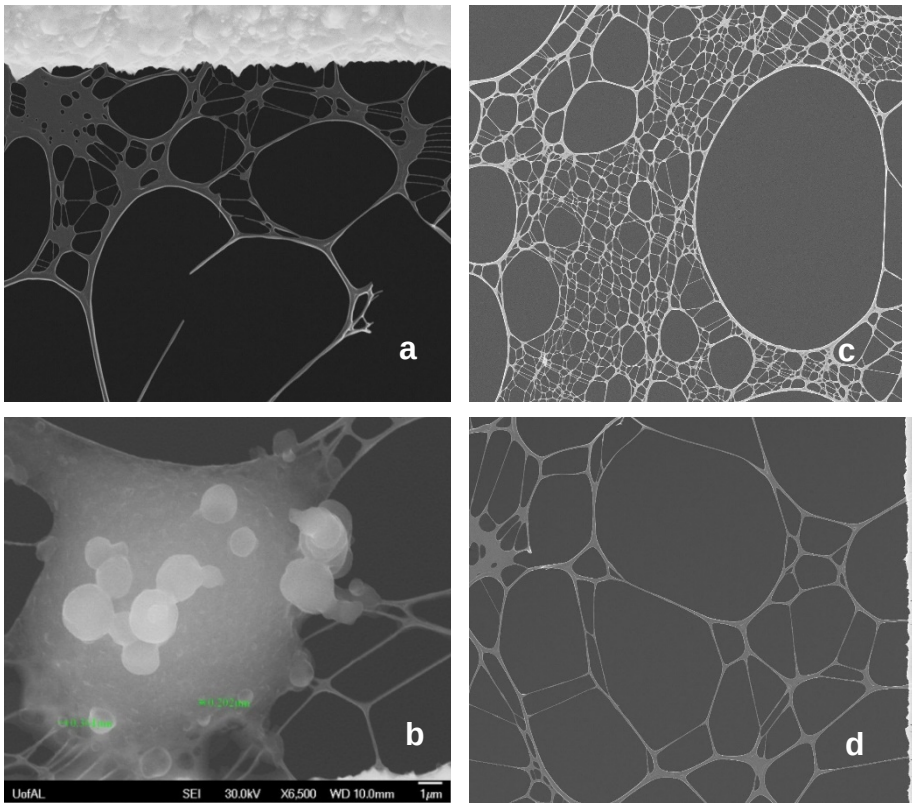

Fig. 3.12. Scanning Electron Microscope (SEM) images of: a) dodecane, b) NEPCM, c) distillate after atmospheric pressure distillation, d) distillate after vacuum distillation.

3.4.2 Chemical Treatment of the NEPCM

Fig. 3.13 shows the results obtained using the alcohol mixture. During sample preparation and before shaking, it was found that due to high density, the colorless alcohol mixture sits at the bottom of the test-tube occupying half of the filled tube length while the top half is filled by the black colored NEPCM. After shaking, it was observed that the volume of the black colored liquid part shrank while the volume of the colorless liquid part increased substantially. This is because a portion of the colorless dodecane (base fluid) in the NEPCM dissolved into the colorless alcohol mixture and settled at the bottom. Thus the process leads to a concentrated NEPCM on top.

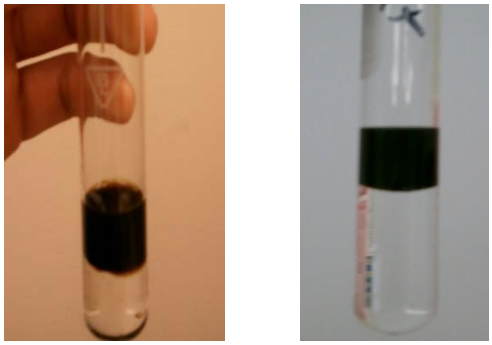

Before Shaking After Shaking

Fig. 3.13 NEPCM and alcohol mixture.

To obtain a quantitative data about the amount of dodecane dissolved using the procedure described above, 5 ml of NEPCM (containing 0.5% mass fraction of nanoparticles) was added to 5 ml of alcohol mixture and the experiment was repeated. Fig. 3.14 shows the results of first trial after shaking at 450 rpm for 30 min. The concentrated NEPCM on top after shaking was pipetted out and found to be 3.75 ml in volume. Using this concentrated volume the experiment was repeated again using another 5 ml of the alcohol mixture. It was found that the NEPCM concentrated to 2.5 ml as shown in Fig. 3.15.

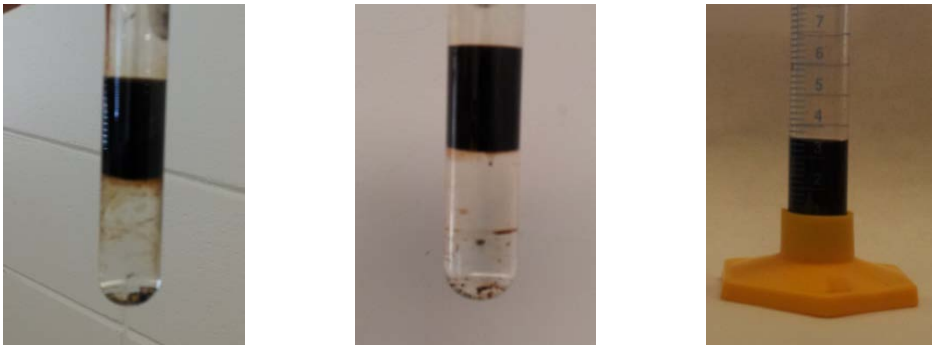

Before Shaking **After Shaking** **NEPCM volume ~ 3.75 ml**

Fig. 3.14 NEPCM (5 ml) and alcohol mixture (5 ml); NEPCM volume reduced to 3.75 ml after mixing.

Though visible observations indicate that some amount of dodecane has been mixed with alcohol and the clear layer shown in Fig. 3.15 does not contain any nanoparticles, experimental evidence is required to support this claim. Hence, in order to confirm the complete removal of nanoparticles after processing with the alcohol mixture, a pipetted sample of the clear alcohol and dodecane solution from the bottom was analyzed using UV-visible spectrophotometer.

Before Shaking **After Shaking** **NEPCM volume ~ 2.5 ml**

Fig. 3.15. NEPCM (3.75 ml) and alcohol mixture (5 ml); NEPCM volume reduced to 2.5 ml after mixing.

UV-visible spectrometry was selected to perform the analysis over other methods like electron microscopy due to its simplicity, versatility, speed, accuracy, and cost-effectiveness. A Varian Cary 100 UV-Vis spectrophotometer was employed to determine absorption wavelengths. It is a double beam, recording spectrophotometer controlled by a computer operating under Windows 2000 and WinUV software. It hosts tungsten halogen as a visible light source and a deuterium arc for ultra-violet light with a wavelength range from 190 to 900 nm. A 1 cm cell was used to feed the sample in the sample holder. A wavelength range of 300 nm to 800 nm was used to capture data. UV-Vis scan rate was set to 600 nm/min and data interval was 1 nm.

Fig. 3.16 shows UV-Vis spectrum of the collected sample, which is compared with the baseline (dodecane) spectrum and 0.01 wt% NEPCM spectrum. Due to the presence of nanoparticles, the NEPCM spectrum shows increasing absorbance values as the wavelength is varied from 800 nm to 300 nm, indicating the presence of light absorbing nanoparticles. Whereas, for the sample spectrum (Run1), no variation of the absorbance with respect to the wavelength is observed. Also, the sample absorbance spectrum resembles the pure dodecane spectrum which provides concrete evidence that the sample is free from any nanoparticles after treatment with the alcohol mixture.

It can be concluded from these trials that every mixing and shaking step yields about 25% more concentrated nano-fluid. The trial was done with a mixture of alcohol containing 50-50% of methanol and propanol. The concentrated NEPCM collected after a few cycles of mixing and shaking can be further processed by other separation methods such as distillation for complete separation of the nanoparticles with a significant reduction in energy and time.

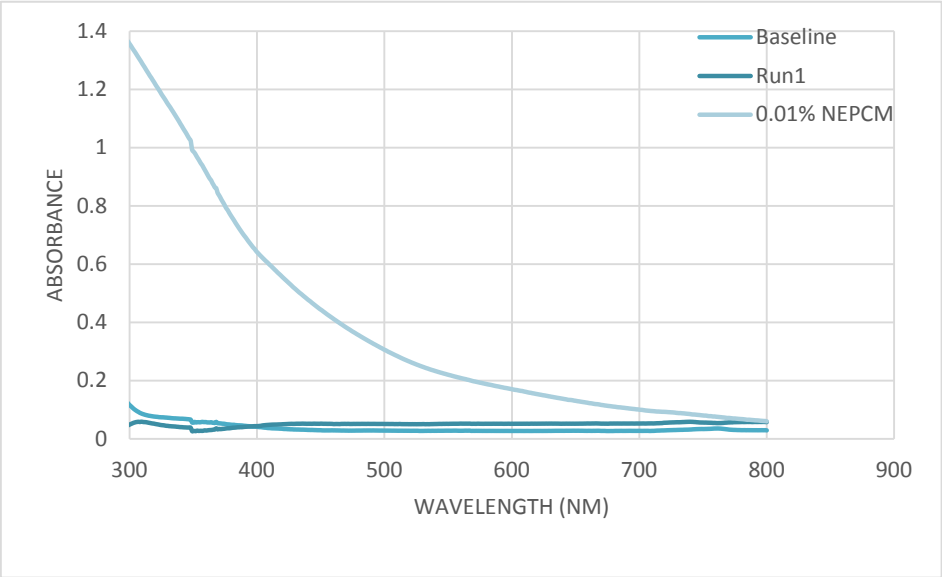

Fig. 3.16 UV-Vis Spectrum of Sample

3.4.3 Centrifugation

Fig. 3.17 shows the results for two centrifugation trials, showing partial precipitation of the nanoparticles. It is observed that centrifugation could not remove all of the nanoparticles from the given sample volume, as all the centrifuged samples have a reddish color indicating some of the nanoparticles are still in suspension. As the pure dodecane is colorless, a colored centrifuged sample indicates the presence of nanoparticles. Since the centrifugal force is proportional to the particle mass, the larger particles are precipitated and the smaller ones remained trapped in suspension. The nanoparticles still in suspension after the centrifugation giving the reddish color to the centrifuged samples, are of lower size in the nanoparticle size range of 5-15 nm. This is due to the fact that being light in weight small particles need greater force to sediment than that required by nanoparticles of large size range. Fig. 3.18 shows SEM image of non-precipitated particles after trial 1, which indicates these are particles of size less than 10 nm.

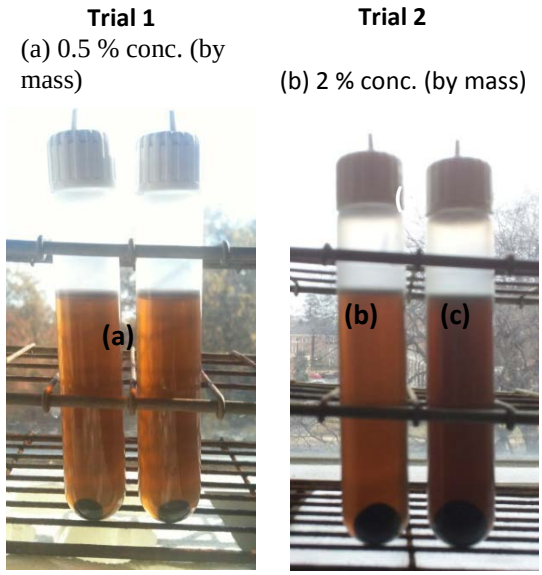

Sample: Volume: 13 ml, Speed: 18,000 rpm, Duration: 19.5 hr.

Fig. 3.17. Centrifugation: Nanoparticle precipitation.

Similar trials were conducted for 0.5, 1, and 2% wt concentrations of 12 ml of the NEPCM for 24 hrs. and 48 hrs. at 18,000 rpm in order to investigate the effect of the duration of centrifugation. Fig. 3.19 shows three samples (1, 2, and 3) of concentration 0.5 %, 1%, and 2%, respectively, before centrifugation. After 24 hours of centrifugation at 18,000 rpm, most of the nanoparticles were precipitated as shown in Fig. 3.19b. At this point, 1 ml of the centrifuged NEPCM sample was collected from each of the three samples for comparison.. Samples in Fig. 3.19b were centrifuged again for an additional 24 hours and after the end of 48 hour. Sample conditions are presented in Fig. 3.19c. General visual observation of Fig.3.19c indicates that the longer centrifugation duration of the additional 24 hours at 18,000 rpm results in no further precipitation of the nanoparticles because samples in Fig. 3.19 b and c bear similar color intensity. In order to quantify the particle removal efficiency of the centrifugation trials and to record the difference in concentration after 24 and 48 hours of centrifugation, a concentration based analysis was done where the concentrations of the NEPCM before and after centrifugation were used to calculate efficiency of particle removal by centrifugation. The concentration of a particular NEPCM sample was known before centrifugation. In order to determine concentration of NEPCM after trial, “Calibration Curve” or “Internal Standard” approach using UV-Vis photo-spectroscopy was employed.

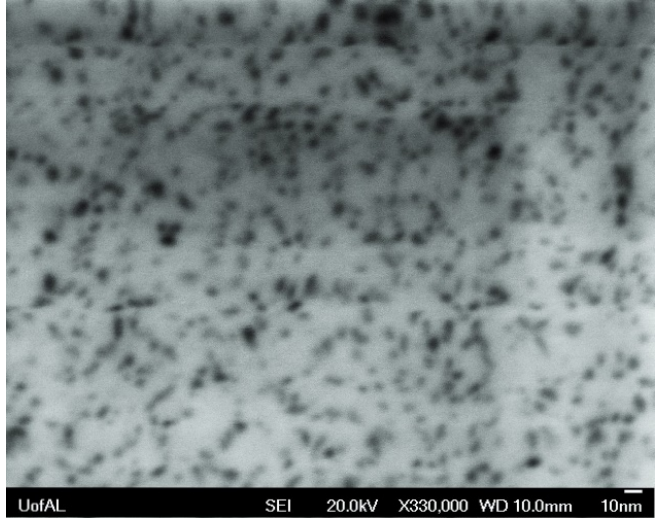

Fig. 3.18. SEM image of centrifuged sample (a).

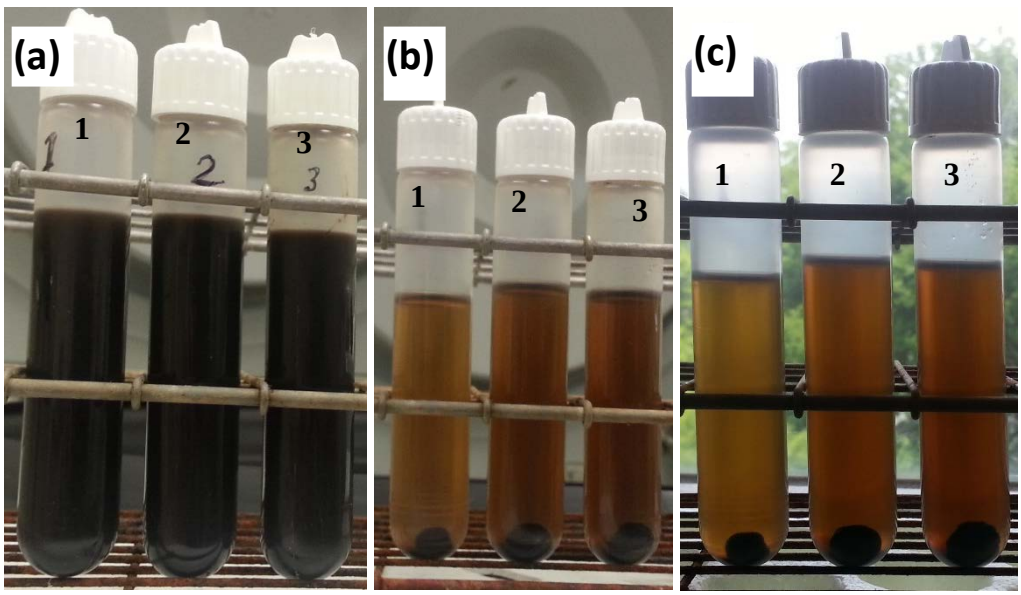

Fig. 3.19 (a) Before centrifugation, (b) after 24 hr. of centrifugation, (c) after 48 hr. of centrifugation.

To plot a calibration curve, which is a graph of concentration versus absorptivity for the solution, six samples of known concentrations were prepared in addition to the unknown centrifuged sample. Fig. 3.20 and 3.21 shows the samples of known varying nanoparticle wt% prepared to determine concentration of centrifuged sample after 24 hours of 2% concentrated NEPCM and 48 hours of 1% concentration NEPCM, respectively. These known concentrations were selected such that the unknown concentration sample falls in the middle of this sample concentration range. The color of the centrifuged NEPCM (or NEPCM) sample proved as an aid in preparing these samples with known varying concentrations to bracket unknown sample concentration.

For each sample, absorbance spectra were recorded using a UV-Vis spectrometer and the value of the absorbance of each of the spectrum curves at the highest absorbing wavelength (λ_{max}) is determined. Fig. 3.22(a) and (b) shows absorbance spectra of 2 wt% and 1 wt% respectively of NEPCM samples of different known concentrations and

unknown concentration. After determining absorbance values at λ_{max} calibration curves were plotted.

Fig. 3.20. UV-Vis spectrometry samples of 2 wt% NEPCM to find concentration after 24 hours of centrifugation

.

Fig. 3.23 (a) and (b) shows the calibration curve for sample 2 (1 wt %) and sample 3 (2 wt %), respectively. As shown, absorption spectra was recorded for samples with concentrations varying from 0.0066% wt to 0.016% wt for sample 2 and 0.0033 %wt to 0.021% wt for sample 3. Due to errors introduced during data recording and inconsistent concentration steps of the sample. The calibration curve deviates from being a perfect straight line. Using Calibration curve, a curve fit equation was determined to calculate x-value (concentration) of centrifuged samples for the known Y-

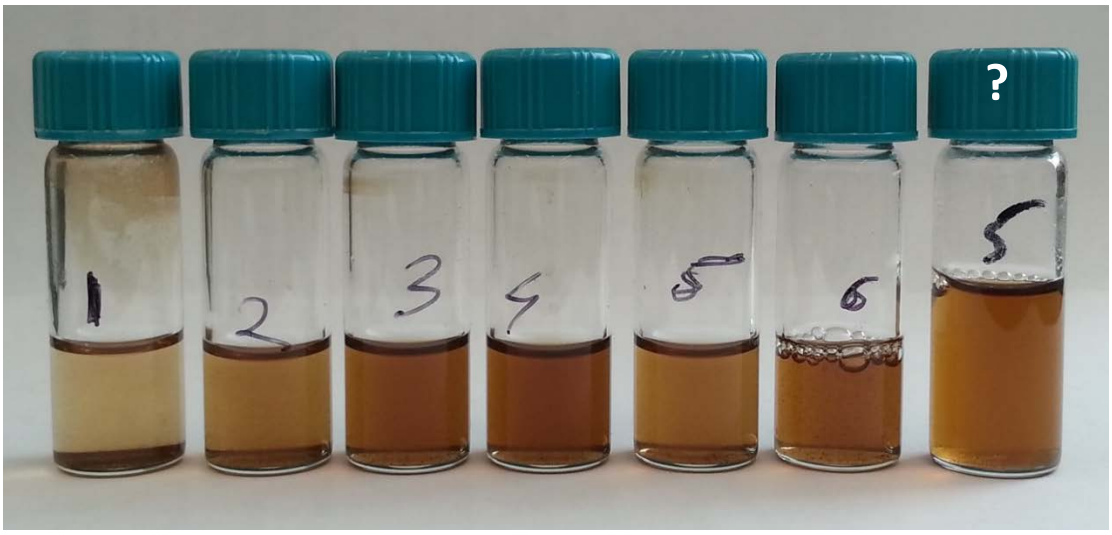

Fig. 3.21. UV-Vis spectrometry samples of 1 wt% NEPCM to find concentration after 48 hours of centrifugation.

value (absorbance) determined from absorbance spectrum.

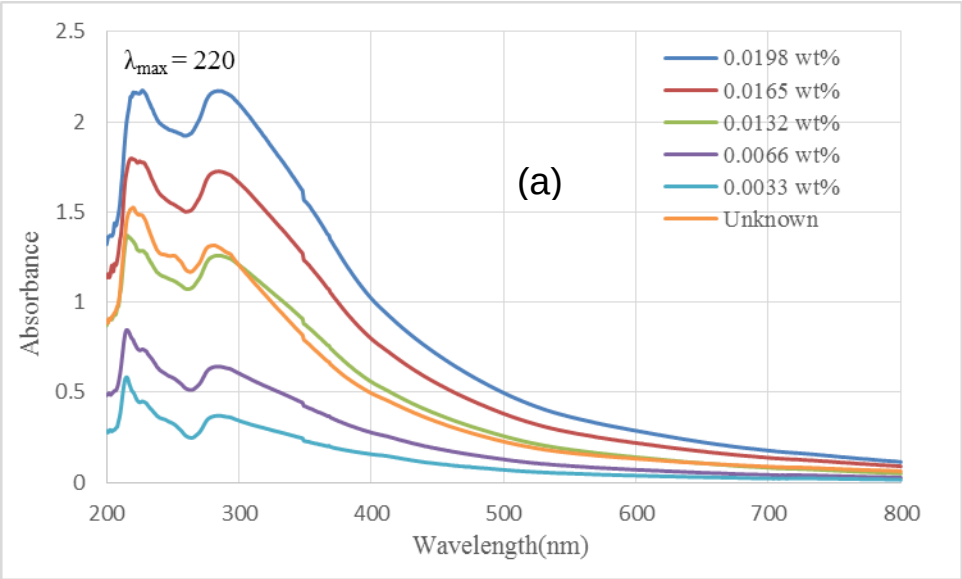

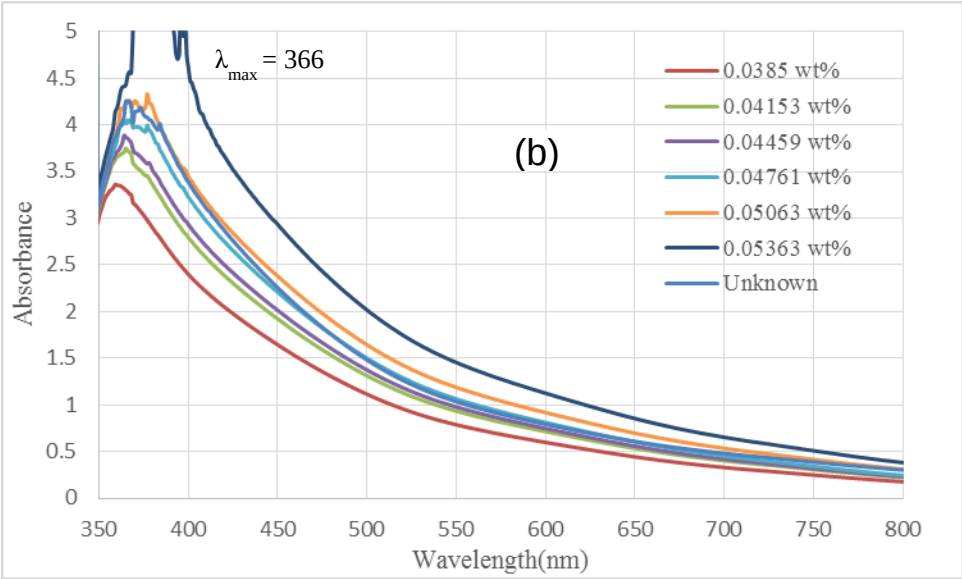

Fig. 3.22. (a). UV-Vis spectra of 2 wt% NEPCM and sample 3 (after 24 hrs.); (b). UV-Vis spectra of 1 wt % NEPCM and sample 5 (after 48 hrs.).

Using the calibration curve, concentrations (%wt) of the NEPCM after centrifugation were determined and compared with the initial concentration before centrifugation. Table 3.5.presents the summary of data collected for two centrifugation samples. For the same centrifugation speed, in this case 18,000 rpm equivalent to 40,173 x gravity (which is the maximum attainable speed with the available equipment), a 24 hour period resulted in about 95 % efficiency which remained almost the same without any significant further improvement for the additional 24 hour centrifugation period. This is evident from the overall efficiency values presented in Table 3.5. Referring to Fig. 3.17 b and c, remaining nanoparticles are of lower size range (dia < 10 nm), hence they need a stronger centrifugation force to bring them out of solution to make them precipitate and achieve separation. The primary hypothesis - applying the same centrifugation force for a longer duration should result in improved centrifugation efficiency, proved to be wrong.

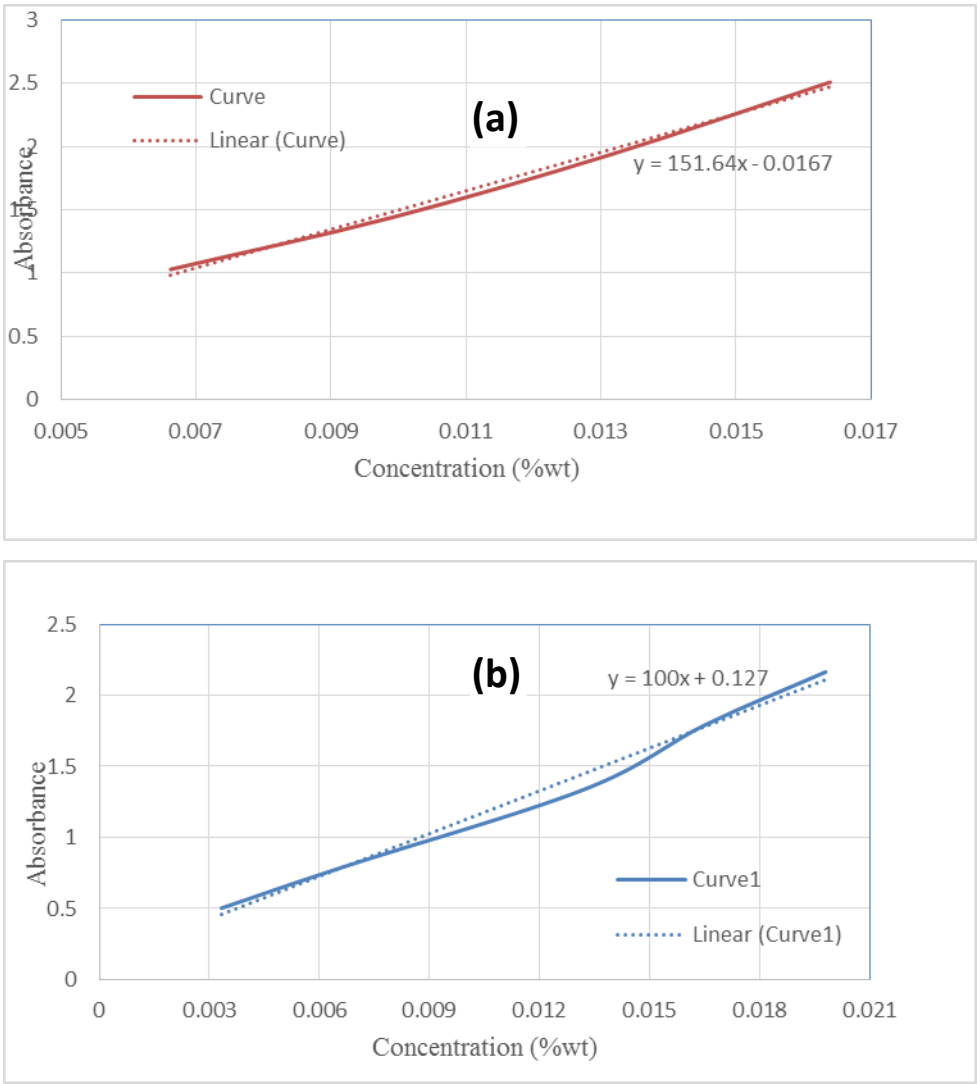

Fig. 3.23. Calibration curve for centrifugation, (a) sample 2, (b) sample 3.

Table 3.5 Centrifugation results.

Sample No.	Initial wt %	Centrifugation rpm (×Gravity)	wt % after 24 hrs	Overall Efficiency (%)	wt % after 48 hrs	Overall Efficiency (%)
2	1	18,000(40,173 × g)	0.044	95.6	0.043	95.70
3	2	18,000(40,173 × g)	0.084	95.8	0.081	95.95

3.4.4 Nanoparticle Ligands/Surfactants Destabilization

An initial trial was conducted using 5 ml of 0.5% CuO mass fraction NEPCM, 3 ml of saturated aqueous solution of KOH, and 0.5 ml of ethanol. The 5 ml of NEPCM was taken in a test-tube and 3 ml of KOH solution was added and followed by manual shaking for about 1 min. At this point little mixing was observed with no sedimentation of nanoparticles. A few drops of ethanol were added, followed by continuous shaking. Nanoparticles were observed to form a dense black layer at the bottom with a colourless top layer. Fig. 3.24 shows the end result of trial 1. The clear layer on top of the precipitated nanoparticles is thought of as a mixture of base fluid dodecane and ethanol. Hexane was added to wash the test-tube walls and to make layers look distinct. The removal of the oleate ligands from the CuO nanoparticles is believed to occur via the reaction mechanism illustrated in Fig. 3.25.

On left hand side, a CuO nanoparticle is shown with the oleate group attached to its surface. It is proposed that KOH saponifies the oleate ester linkage, resulting in the formation of potassium oleate. The detachment of oleate from the nanoparticle surface makes the particles unstable and results in precipitation as shown in Fig. 3.24. The top clear layer in the test tube in Fig. 3.24 was analysed by UV-Vis spectrometry to detect the presence of nanoparticles. To record data, a freshly prepared sample was irradiated at 20°C by a dual source of light. The solution was removed at fixed times and its UV spectrum recorded until no further spectral changes occurred. Pure dodecane (99 % technical grade) was used as reference sample (baseline). For the same sample UV – Vis spectrum was recorded and was compared with spectrum of 99 % pure dodecane and 0.0167 % conc. NEPCM as shown in Fig. 3.26.

Absorbance spectrum of sample, i.e., Run 1 resembles the spectrum of baseline whereas the NEPCM spectrum possesses very different behaviour with high absorbance values. Hence it can be concluded that the treated sample is free from the CuO nanoparticles. This demonstrates that aqueous KOH, in the presence of ethanol, is capable of removing oleate ligands from the particle surfaces resulting in the precipitation of all of the nanoparticles from the sample NEPCM yielding 100% separation efficiency.

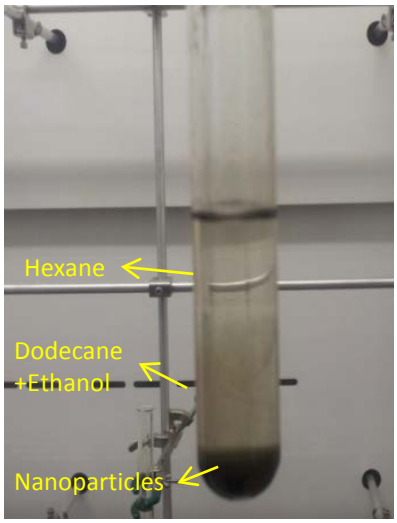

Fig. 3.24. Nanoparticle destabilization using saturated KOH solution.

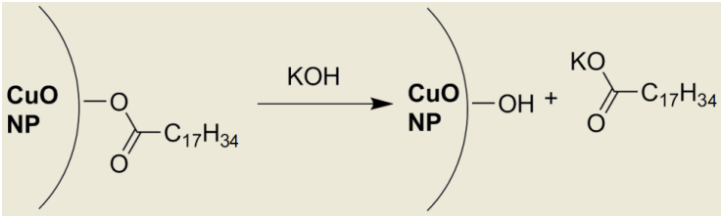

Fig. 3.25. Schematic of the chemical reaction between oleate and KOH.

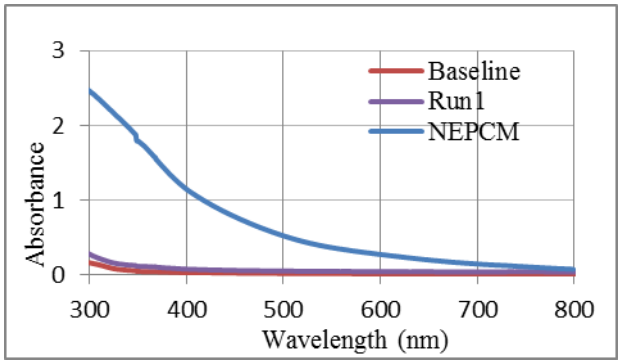

Fig. 3.26. UV-Vis Spectrum of trial 1.

3.4.5 Silica Column Chromatography

Table 3.6 shows the chromatography data for different volumes and concentrations of the NEPCM. It was observed that the elusion length of the column varies in relation with the NEPCM volume and concentration, whereas the time required for the complete elusion is a function of elutant volume used.

Table 3.6. Silica Column Chromatography results.

Trial No.	NEPCM Volume (ml)	Nanoparticle conc. (by mass)	Elusion Length (inch)	Elutant Volume (ml)	Time (min)
1	0.5	0.5%	0.25	15	70
2	1	1%	0.3	15	70
3	1	2%	0.3	15	75
4	2	2%	0.3	10	55

UV-Vis spectrometry was employed to confirm complete removal of nanoparticles. Fig. 3.27 shows the UV-Vis spectrum of the elutant obtained for trial 3. To record the data, a freshly prepared sample of elutant was irradiated at 20°C by a dual source of light. The solution was removed at fixed times and its UV spectrum recorded until no further spectral changes occurred. To capture the data, pure dodecane was used as a base or reference solution. UV-Vis spectral range captured (Fig. 3.27), incorporates the UV and visible portions of the electromagnetic spectrum from 300 to 800 nm. This spectrum was compared with pure dodecane (baseline) and 0.0167% conc. NEPCM spectra as shown in Fig. 3.27. Comparing the three spectra reveals that, after the chromatography, sample spectrum resembles closely the baseline spectrum where no light absorbance is detected for the entire wavelength spectrum indicating absence of any particulate matter. Difference in the NEPCM spectrum and sample spectrum provides additional evidence that the processed sample is free from nano-particles. Hence silica gel chromatography is proved to be an efficient, simple, and cost-effective alternative for nanoparticle separation from the NEPCM.

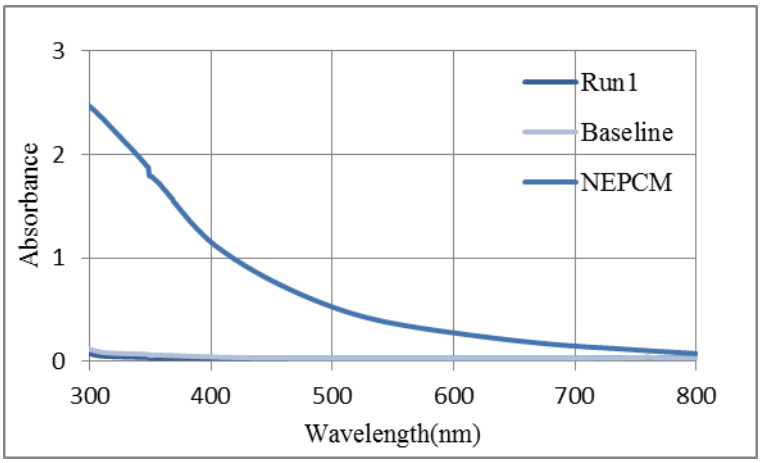

Fig. 3.27 Trial 3 (2% nanoparticle conc., 1 ml NEPCM) UV

3.4.6 Nanoparticle Separation by Adsorption on Silica Surface

Fig. 3.28 shows the steps followed during the experiment. Table 3.7 presents a summary of the trials performed for different concentrations and volumes of the NEPCM. Same UV-Vis procedure, as explained in previous section, was followed to analyze the processed sample. The amount of silica required to adsorb all nanoparticles increases almost linearly with nanoparticle mass concentration as evident from Fig. 3.29. This is in accordance with the adsorption mechanism explained. As the concentration of the nanoparticles increases, silica surface area required for adsorption increases proportionally, hence the amount of silica required increases. As adsorption is a surface phenomenon, grain size of silica is a critical factor to determine the amount (weight) of silica required. Silica with a bigger grain offers less surface area for adsorption compared to one with smaller grains. Reported results pertains to silica with grain size of 40-63 µm, hence using silica of smaller grains, amount of silica required to capture the nanoparticles in a given volume will be lesser in relation to grain size.

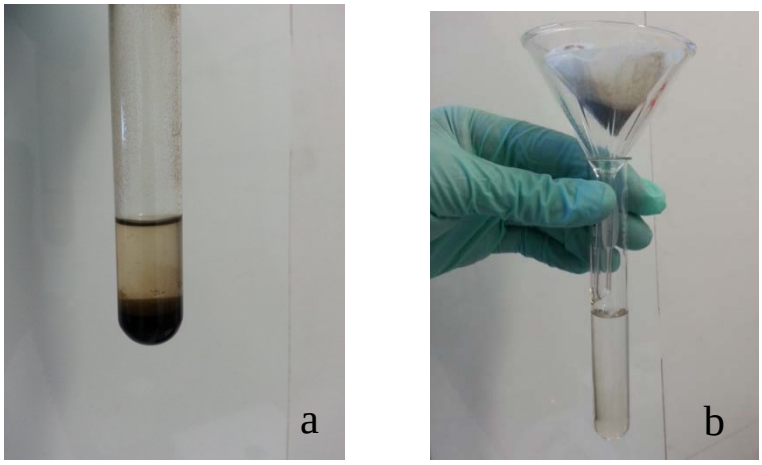

Fig. 3.28 Silica adsorbing nanoparticles.

Table 3.7: Silica adsorption trials summary.

Trial Number	NP conc. (%)	NEPCM Vol. (ml)	Silica required (mg)
1	0.5	5	750.1
2	1	5	2051.2
3	2	5	2854.4

The UV-Vis spectrum of the trial 1 sample along with reference dodecane and NEPCM sample is shown in Fig. 3.30. Pure dodecane was used as a reference to capture the

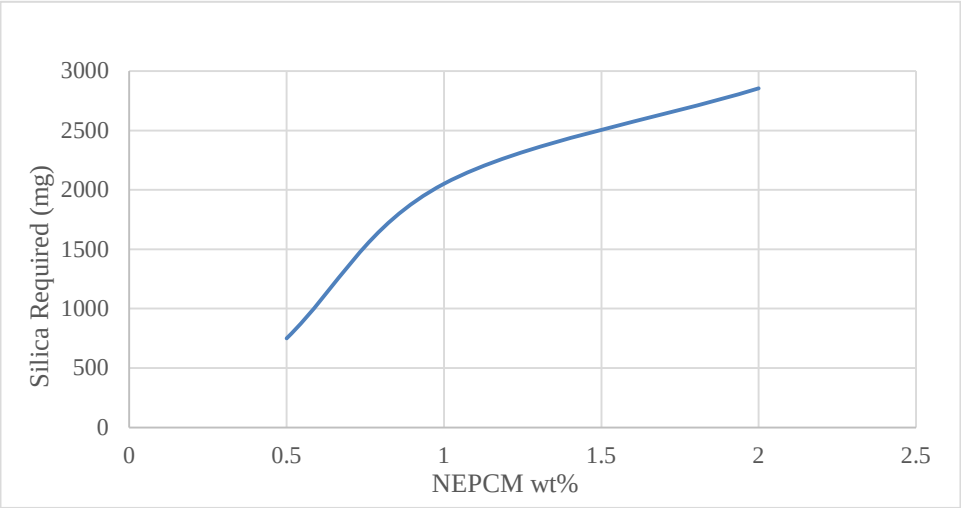

Fig. 3.29. Silica required Vs NEPCM wt%.

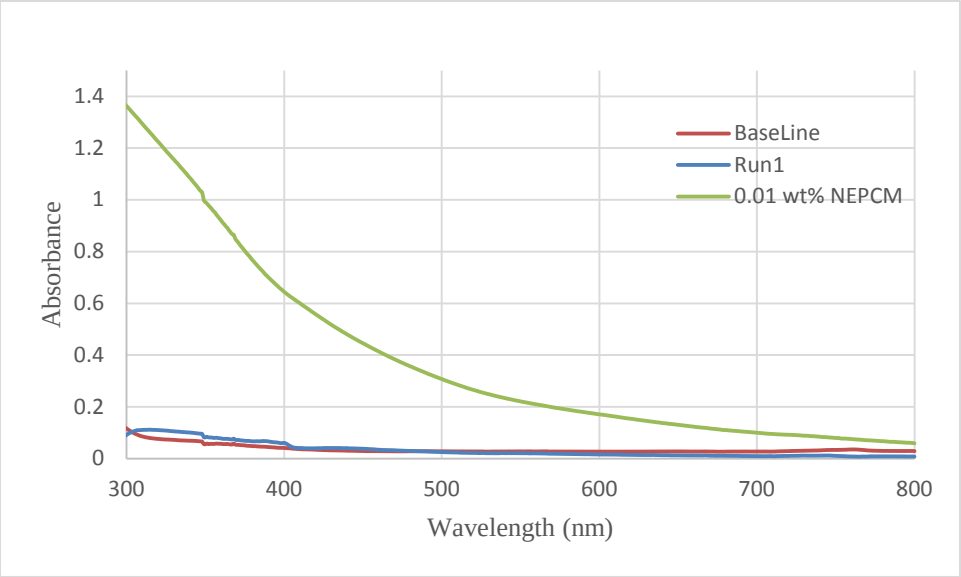

Fig. 3.30. UV Spectrum of trial 1 sample.

UV spectrum of sample 1. The resulting spectrum for sample 1 was recorded 3 times and the same behavior was observed. Comparing three spectra, it is clear that sample 1 shows very similar behavior and absorbance values as that of base fluid dodecane and unlike NEPCM which exhibits higher absorbance values. Hence it can be said that sample 1 does not contain any impurities or particles as such to absorb light. This result confirms that the sample obtained after running trial 1 is free from nanoparticles and all the particles were adsorbed by silica.

Fig. 3.31a shows the transmission electron microscopy (TEM) image of silica grains with no nanoparticles which clearly indicates size of silica grains which ranges from 40-

63 µm as per manufacturer specifications. Fig. 3.31b shows the surface structure of individual silica grain without nanoparticles. It can be observed that the selected silica grain has a clean surface with negligible irregularities. Fig. 3.31c, d, and e show silica grains after trial 1 indicating nanoparticles adsorbed on the silica grains surface. Fig. 3.31c shows adsorbed nanoparticles at lower magnification of 6,000 whereas Fig. 3.31d shows zoomed-in view at a magnification of 35,000 and Fig. 3.31e shows the highest possible magnification of 140,000 under applied settings. It can be observed that at the lower magnification of 6,000 (Fig. 3.31c) the presence of nanoparticles on silica grain surface is visible. Any further close-up view (Fig. 3.31d) gives a better picture, clearly depicting the presence of nanoparticles on the silica surface, though these particles look much bigger than the nanoparticles used (5 – 15 nm). Fig. 3.31e provides enough evidence to comment on the adsorption mechanism. On a scale of 100 nm, Fig. 3.31e clearly shows the cluster of nanoparticles forming bigger size structures which looks like a big nanoparticle as seen in Figs. 3.31c and d. This cluster formation result is mainly due to the presence of silanol (Si–OH) groups on the silica surface which act as an oxide adsorbent. The OH groups here acts as the centers of molecular adsorption during their interaction with adsorbates (i.e., CuO nanoparticles) forming a hydrogen bond. Hence being an oxide adsorbent, silanol groups attracts more and more nanoparticles by forming hydrogen bonds with available OH groups, till saturation is reached. Saturated surface of silica is clearly visible in Fig. 3.31e.

Nanoparticles separation or extraction from NEPCM using silica is proved to be an efficient and simple process. Silanol groups attached on the silica surface were responsible for adsorbing copper oxide nanoparticles, due to their inherent property. As adsorption is the sole mechanism for nanoparticles extraction, interaction of silica with nanoparticles in NEPCM is the most critical factor. The interaction was achieved using manual shaking in the trials and experiments so presented. If mechanical means like a shaking unit, mixing unit could be utilized for achieving nanoparticles and silica interaction, amount of silica required would be much less than that used in these trials. Due to mixing at a higher speed, more nanoparticles would come in contact with a silica grain, and get attached. The amount of silica required to extract all of the nanoparticles from a given sample of NEPCM will be less than that required using manual shaking.

3.4.7 Nanofiltration

The first trial was conducted for 10 ml of pure dodecane in order to study porosity and the diffusing ability of the membrane which is rated as 1 kDa according to manufacturer. Filtration started by producing filtrate in consistent drops and was observed to be very slow for the pressure gradient utilized. After 70 minutes, the trial time experiment was stopped which produced about 5 ml of filtrate. When compared, the collected filtrate carried some color and looked very different from the pure dodecane feed sample (Fig. 3.32a). Close observation showed the presence of black particles around the inner perimeter of the top glass part on the surface of the filter membrane. This provided an indication that these black particles are rubber gasket produced due to the reaction with the dodecane. As rubber gaskets are supporting the ceramic membrane and providing sealing from both the sides of membrane, filtrate comes in contact with rubber gaskets

before and after filtration. Due to the slower filtration rate, filtrate on the downstream or permeate side gets enough time to come in contact with rubber gasket which results in rubber reaction with dodecane leading to generation of particles and subsequent colored filtrate as shown in Fig. 3.32b. This was further confirmed by checking chemical compatibility of organic fluids like alkane with rubber material. General purpose rubber was selected as a gasket material due to its lower cost and easy availability.

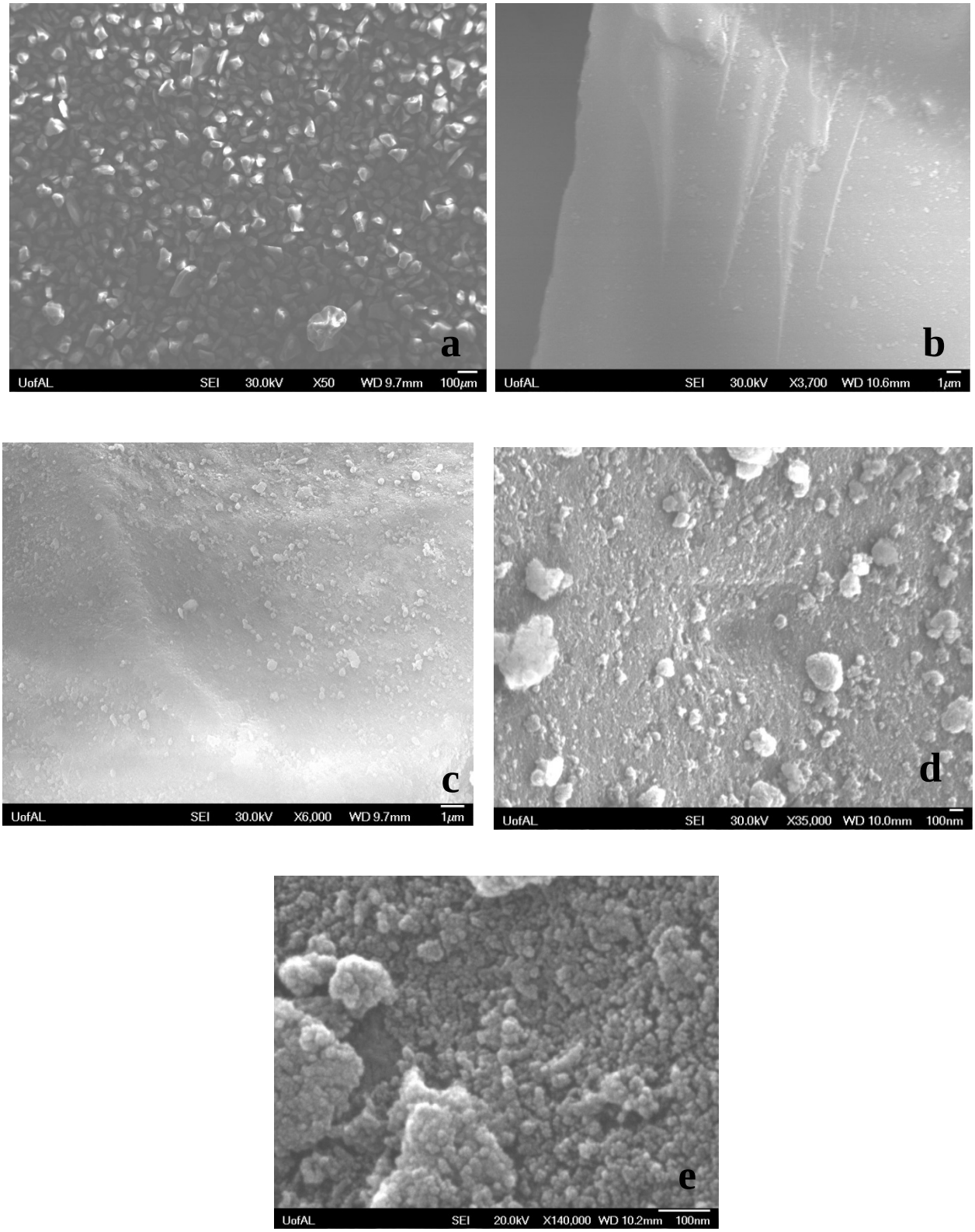

Fig. 3.31. Silica Grain surface with Adsorbed Nanoparticles.

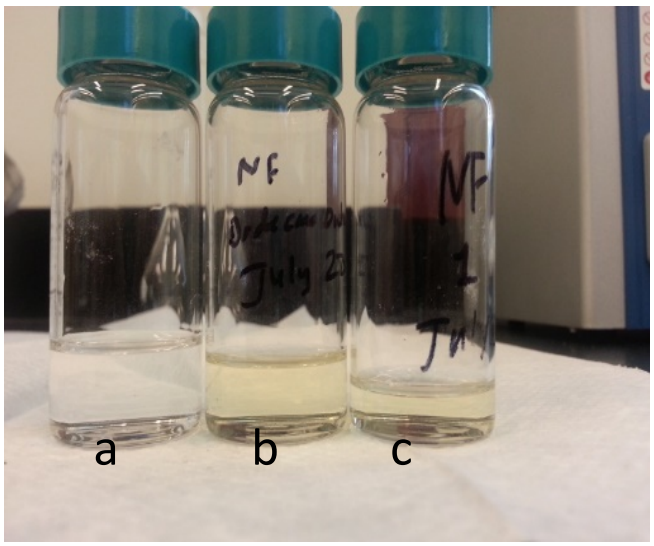

Fig. 3.32. Filtration Results.

The second trial was conducted using 10 ml of 0.5 wt% NEPCM by using the same set up and following the same procedure. Filtration is observed drop-by-drop and the rate of filtration was also slow for NEPCM. After a period of 70 minutes, the trial was stopped and the filtrate collected (Fig. 3.32c) bears the same color as that of the dodecane filtrate due to presence of rubber particles. By visual observation of samples shown in Fig. 3.32, it can be concluded that the ceramic membrane is capable of capturing all the nanoparticles from NEPCM sample. In order to confirm the presented hypothesis these samples were analyzed using UV-Vis spectroscopy.

Fig. 3.33a shows four UV-Vis spectra presented to compare the nanofiltration samples with the base fluid dodecane and concentrated NEPCM. As shown in Fig. 3.32, the nanofiltration samples of dodecane and 0.5 wt% NEPCM exhibit the same color due to the presence of rubber gasket particles; this is also confirmed by their respective spectra (Fig. 3.33a). This further confirms that both the filtrate sample contained the same size and type of particular matter which is generated by the reaction of dodecane with the gasket material (rubber). Also comparing these filtrate spectra with that of 0.0033 wt% NEPCM and dodecane reveals that filtrate spectra follows the same trend as dodecane. Fig. 3.25b presents zoomed view of the spectra for wavelength range of 400-800 nm which clearly indicates filtrate samples are free from nanoparticles.

Hence, based on the trial results and analysis, it can be concluded that nanofiltration using solvent resistant membrane, i.e., ceramic membrane of 1 kDa rating is capable of separating nanoparticles by yielding 100% separation efficiency. For the type of cost-optimized in-house designed set-up and under maximum applied pressure differential of 3.75 bar (approx.) across the membrane, nanofiltration was found to be a slow process. Higher filtration rates can be achieved by using the membrane manufacturer's recommended membrane holder in conjunction with highly pressurized feed.

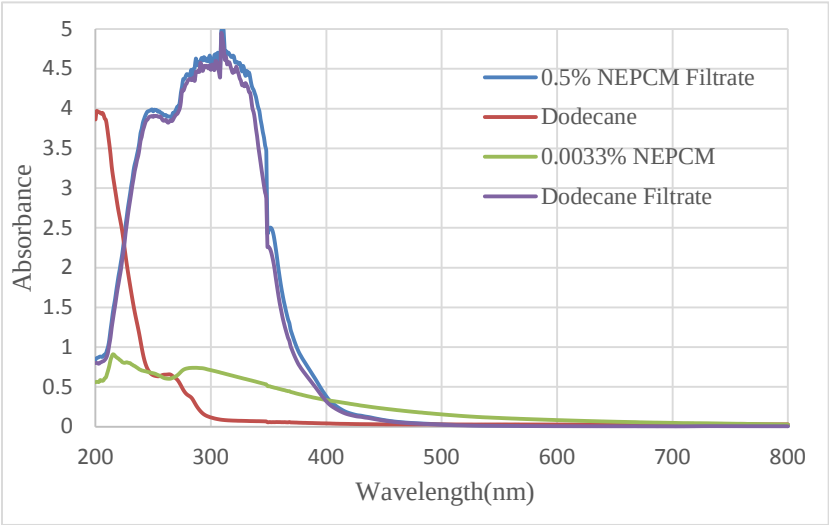

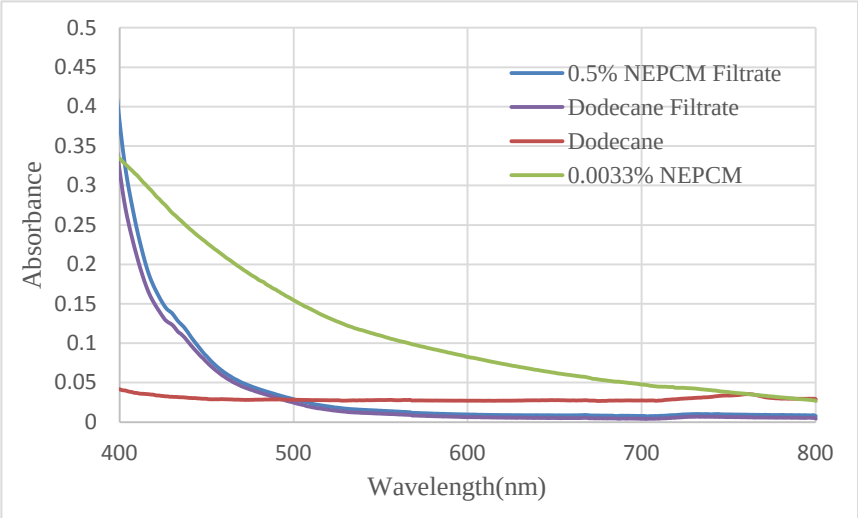

Fig. 3.33. (a) UV-Vis Spectra Comparison, (b) UV-Vis Spectra Comparison (zoomed In view).

3.4.8 Comparison of the Investigated Nanoparticle Separation Methods

Based on the experiments conducted, analysis performed and presented in section 4, separation methods have been compared on the basis of economical and functional parameters. Table 3.8 presents comparison summary. The comparison has been done strictly referring to the equipment used and practices followed to conduct trials.

Table 3.8 Separation Methods Comparison

Separation Method	Equipment Cost	Material Requirement	Processing Volume	Separation Efficiency	Nanoparticle Reclamation
Atm. Pressure Distillation	Low	None	Moderate	High	No
Vacuum Distillation	Moderate	None	Moderate	High	No
Chemical (alcohol) treatment	High	Low	Low	High	Yes
Centrifuga-tion	High	None	Low	Moderate	Yes
KOH-treatment	Low	Low	Low	High	No
Silica Chromato-graphy	Low	Moderate	Low	High	No
Silica Adsorption	Low	Moderate	Low	High	No
Nanofiltra-tion	High	None	Moderate	High	No

3.5 Conclusions

Referring to results presented in section 4 and the comparison of different methods presented in Table 3.8, the following conclusions can be drawn:

1. As evident from the results presented, distillation at atmospheric pressure is a highly efficient process to separate nanoparticles from NEPCM. The set-up used to conduct trials, the equipment costs was low and it did not require any material during operation other than a sample. Also it was able to handle moderate volumes of NEPCM, which resulted in high overall efficiency. For larger NEPCM volumes, distillation units on industrial scale are available and has been used successfully for different applications. Hence distillation at atmospheric pressure qualifies as one of the best methods to separate nanoparticles from NEPCM. However it has one inherent limitation of slow speed and comparatively high energy consumption.

2. Vacuum distillation demands a negative pressure set-up which adds to the equipment cost. However while conducting experiments, it was observed that operating costs, in terms of energy consumed, and time taken to process a given NEPCM sample was much lower when compared to distillation at atmospheric pressure. This mode of distillation also does not exhibit any additional material requirements. Moderate volumes (about 1000 ml) of NEPCM can be easily processed using the lab scale unit utilized in this work. For higher NEPCM, volume industrial scale units can be utilized. Similar to distillation at atmospheric pressure vacuum distillation yields 100 % efficiency.

3. Chemical (alcohol) treatment was proved to be another efficient process to separate nanoparticles from NEPCM. This method does not demand any special set-up as only test-tubes and beakers were used to conduct experiments. However, it requires a shaking unit capable of producing the required momentum to attain the desired results which adds to the equipment cost. As only a mixture of inexpensive alcohols is required, its material requirement cost is low. Presented trials were conducted to prove the functionality of the approach and record the data to provide grounds for further research. Hence low volumes of NEPCM were processed, however using the appropriate equipment, this approach can be used to process higher NEPCM volumes. This method does not destabilize the nanoparticles per se by dissolving surfactants rendering nanoparticles to be able to form stable NEPCM if re-dispersed back.

4. Centrifugation is another potential method to achieve nanoparticle separation from NEPCM. Referring to the data presented in chapter 5, it can be concluded that for the maximum relative centrifugation force used (40,173x gravity) this method yields 95% efficiency. This also clarifies that for NEPCM separation efficiency of centrifugation is a factor of centrifugal force and not of duration. This method bears high equipment cost and does not demand any additional materials for NEPCM processing. Trials were conducted using low volumes of

NEPCM, however, advanced centrifuges offer high volume processing capabilities. Hence for higher centrifugal force centrifugation may result in higher efficiency. One of the biggest advantages of centrifugation over distillation is nanoparticles separated in the form of precipitation can be re-dispersed back hence centrifugation facilitates nanoparticle reclamation.

5. Separation of nanoparticles from NEPCM via removal of surfactant using aqueous KOH is one of the most efficient and economical methods. This method does not require special equipment or expensive material to process NEPCM thus keeping equipment and material costs low. Based on the trials presented for low volumes of NEPCM, it can concluded that this method of separation can be easily adapted to suit large NEPCM volumes.

6. Silica chromatography is capable of removing all of the nanoparticles from a NEPCM sample using low cost equipment. It demands a fine grain silica to build a column which adds to material requirement costs. A lab scale unit was used to prove the concept, however, chromatography columns to handle large sample volumes are readily available which makes it suitable to process high NEPCM volumes with ease. As elusion of sample takes place solely due to gravity, this method is comparatively slower.

7. Separation of nanoparticles from the NEPCM via their adsorption on silica is one of the best methods discovered during this research work. It needs fine grain silica alone to process the NEPCM sample and achieve separation. Being economical, simple, and safe, this method also yields high separation efficiency. The silica amount required to process a sample is directly proportional to the volume and concentration of the NEPCM sample. Due to its operational simplicity and safety it can be easily adapted to process larger NEPCM volumes.

8. Nanofiltration is one of the separation methods which yield 100% separation efficiency. Due to process complexity, its equipment cost is high whereas material cost is low as it does not need additional materials. For the set-up used to conducted nanofiltration trails using the NEPCM, the processing volume was found to be moderate. However, using commercially available set-up nanofiltration can easily process large NEPCM volumes. All the nanoparticles so captured remains adhered to the filtration membrane rendering them unsuitable for reuse.

The presented methods fulfill most of the desired objectives of this research work, i.e., simplicity, safety, economic, and suitability of scaling up. Each method has its advantages and disadvantages in terms of characteristics and requirements and provide guidelines to make a selection as per application objectives. Based on the observation and analysis, vacuum distillation and silica adsorption proves to be the best approaches to separate nanoparticles from the NEPCM completely (with no reclamation plan). Whereas, to preserve the surfactant and re-disperse nanoparticles, treatment of NEPCM with alcohol mixture seems best.

3.6 Acknowledgements

This material is based upon work supported by the US Department of Energy under Award no. DE-SC0002470 (http://www.eng.auburn.edu/nepcm). This report was prepared as an account of work sponsored by an agency of the United States Government. Neither the United States Government nor any agency thereof, nor any of their employees, makes any warranty, express or implied, or assumes any legal liability or responsibility for the accuracy, completeness, or usefulness of any information, apparatus, product, or process disclosed, or represents that its use would not infringe privately owned rights. References herein to any specific commercial product, process, or service by trade name, trademark, manufacturer, or otherwise do not necessarily constitute or imply its endorsement, recommendation, or favoring by the United States Government or any agency thereof. The views and opinions of authors expressed herein do not necessarily state or reflect those of the United States Government or any agency thereof.

Dr. German Mills of the Chemistry Department, Auburn University, Dr. Paul Rupar of the Chemistry Department, the University of Alabama, and Dr. Hank Heath from the Biology Department, the University of Alabama were consulted and contributed on many occasions during the project operation.

3.7 References

Bryant CH, Adam A, Tayior DR, Rowe RC. A review of expert systems for chromatography. Analytica Chimica Acta, (1994) 297(3):317-47.

Chen H, Kaminski MD, Ebner AD, Ritter JA, Rosengart AJ. Theoretical analysis of a simple yet efficient portable magnetic separator design for separation of magnetic nano/micro-carriers from human blood flow. Journal of Magnetism and Magnetic Materials, (2007) 313(1):127-34.

D. Clary. The Extension of Colloid Chemistry from Aqueous to Non-Aqueous Media with Application to Nanofluid Research. PhD Dissertation, Chemistry Department, Auburn University (2011).

Clary D, Mills G. Preparation and Thermal Properties of CuO Particles. J. Phys. Chem. C, (2011) 115(5):1767-1775.

Coker AK. Chapter 10 - Distillation: Part 1: Distillation Process Performance. Ludwig's Applied Process Design for Chemical and Petrochemical Plants (Fourth Edition) Boston: Gulf Professional Publishing; (2010) p. 1-268.

Fan L, Khodadadi JM. Thermal conductivity enhancement of phase change materials for thermal energy storage: A review. Renewable and Sustainable Energy Reviews, (2011) 15(1):24-46.

Gaborieau M, Nicolas J, Save M, Charleux B, Vairon J, Gilbert RG, et al. Separation of complex branched polymers by size-exclusion chromatography probed with multiple detection. Journal of Chromatography A, (2008) 1190 (1–2):215-223.

Gunawan C, Teoh WY, Marquis CP, Amal R. Cytotoxic origin of copper(II) oxide nanoparticles: comparative studies with micron-sized particles, leachate, and metal salts. ACS Nano, (2011); 5(9):7214-7225.

Heinlaan M, Kahru A, Kasemets K, Arbeille B, Prensier G, Dubourguier H. Changes in the Daphnia magna midgut upon ingestion of copper oxide nanoparticles: A transmission electron microscopy study. Water Res. (2011) 45(1):179-90.

Khodadadi JM, Fan L, Babaei H. Thermal conductivity enhancement of nanostructure-based colloidal suspensions utilized as phase change materials for thermal energy storage: A review. Renewable and Sustainable Energy Reviews (2013), 24:418-444.

Kuznik F, David D, Johannes K, Roux J. A review on phase change materials integrated in building walls. Renewable and Sustainable Energy Reviews (2011), 15(1):379-391.

Lam KF, Sorensen E, Gavriilidis A. Towards an understanding of the effects of operating conditions on separation by microfluidic distillation. Chemical Engineering Science, (2011) 66(10):2098-2106.

Liu F. Using micellar electrokinetic chromatography for the highly efficient preconcentration and separation of gold nanoparticles. Journal of Chromatography A (2009);1216(12):2554-2559.

Liu F, Ko F, Huang P, Wu C, Chu T. Studying the size/shape separation and optical properties of silver nanoparticles by capillary electrophoresis. Journal of Chromatography A (2005) 1062(1):139-145.

Liu M, Saman W, Bruno F. Review on storage materials and thermal performance enhancement techniques for high temperature phase change thermal storage systems. Renewable and Sustainable Energy Reviews (2012); 16(4):2118-32.

Manusadžianas L, Caillet C, Fachetti L, Gylytė B, Grigutytė R, Jurkonienė S, et al. Toxicity of copper oxide nanoparticle suspensions to aquatic biota. Environ Toxicol Chem. (2012); 31(1):108-114.
Meng Q, Hu J. A polyethylene glycol-based smart phase change material. Solar Energy Mater.Solar Cells (2008); 92:1260-1268.
Nomura T, Okinaka Ni, Akiyama T. Impregnation of porous material with phase change material for thermal energy storage. Mater. Chem. Phys. (2009); 115(2–3):846-850.
Sánchez LMG, Meindersma GW, Haan AB. Potential of Silver-Based Room-Temperature Ionic Liquids for Ethylene/Ethane Separation. Ind. Eng. Chem. Res. (2009); 48(23):10650-10656.
Shi-chang W. Ten years' development on distillation in China. Desalination (1987); 64:211-215.
Van der Bruggen B, Mänttäri M, Nyström M. Drawbacks of applying nanofiltration and how to avoid them: A review. Separation and Purification Technology (2008); 63(2):251-263.
Wang Z, Li N, Zhao J, White JC, Qu P, Xing B. CuO nanoparticle interaction with human epithelial cells: cellular uptake, location, export, and genotoxicity. Chem Res Toxicol. (2012); 25(7):1512-1521.
Vertellus. Material safety data. http://www.vertellus.com/Documents/MSDS/N-Dodecane%20English.pdf. (2005).
Xiong B, Cheng J, Qiao Y, Zhou R, He Y, Yeung ES. Separation of nanorods by density gradient centrifugation. Journal of Chromatography A (2011); 1218(25):3823-3829.
Yang D, Martinez R, Fayyaz-Najafi B, Wright R. Light hydrocarbon distillation using hollow fibers as structured packings. J. Membr. Sci. (2010); 362(1–2):86-96.

4. NePCM in Thermal Management of Electronics
(Dr. Tamara Floyd-Smith, Chemical Engineering, Tuskegee University)

A platform for thermal management studies was fabricated and characterized. The platform consists of an aluminum base (Figure 4.1a) with a cartridge heater (1b) inserted to simulate the waste heat generated by microelectronics. A power transformer applies a voltage to the cartridge heater and thermocouples (1c) mounted on the surface of the aluminum base transduce the temperature. Data are recorded by an automated data acquisition system (1d). Analysis of the platform indicates that a lumped parameter model applies (Figure 4.2) and the performance of the system might be improved with the addition of more insulation and by reducing the size of the aluminum base for a faster thermal response. The results of this effort were disseminated in a journal article (Tigner et al., 2013).

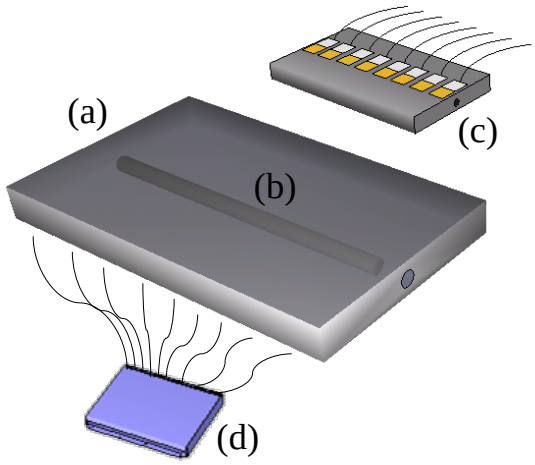

Figure 4.1: Platform for thermal management studies (a) aluminum base (b) cartridge heater (c) surface mounted thermocouples (d) data acquisition system

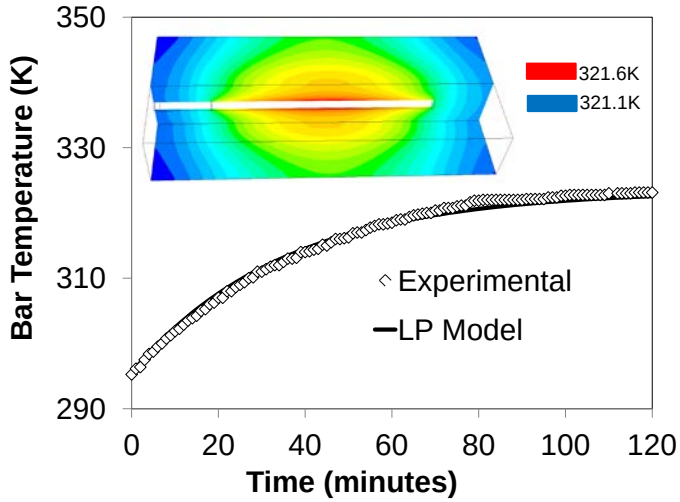

Figure 4.2: Comparison of experimental data for the aluminum base to a lumped parameter (LP) model (inset); 3D computational model results indicating that the base is isothermal

In addition to fabricating and characterizing a platform for thermal management studies, several microelectronics cooling methods were tested using the platform. These include traditional methods such as fans and thermal sinks as well as novel methods such as NePCM and microchannel cooling. The results indicate that all of the methods provide some cooling with the novel methods performing better than convection cooling but not as well as the thermal sink. The results of the study are shown in Table 4.1 with the power requirements of the cooling method also indicated.

Table 4.1: Comparison of Benchmark and Novel Cooling Methods

Method	**Delta T (°C)**	**Power (W)**
Fan	2 ± 1	0.9
Microchannels	4 ± 3	<0.1
NePCM	3 ± 1	0
Thermal sink	5 ± 1	0

The final thrust of the proposed effort is the combination of NePCM passive cooling and microchannel cooling. In this scheme (Figure 4.3), the NePCM removes heat from the system by melting and is subsequently circulated in microchannels as a secondary cooling mechanism. The cycle ends when the heat load is removed (the device is turned off) and the NePCM cools to its melting temperature and freezes. Our detailed investigation supported the theoretical feasibility of the method. However, practical demonstration was stymied because the melted NePCM re-solidified inside the circulation pump and caused the pump to malfunction. Both piezoelectric and peristaltic pumps were investigated, but both types of pumps malfunctioned. Consequently, we conclude that, although the proposed approach remains theoretically feasible, lagging pump technology makes the approach impractical at this time. In the future, when more robust pumps are developed by researchers and companies working in that area, demonstration of the novel cooling approach can be realized. The results of investigating the cooling methods and the theoretical investigation of the novel NePCM cooling method were published in a conference proceedings paper presented at the ASME 3rd International Conference on Micro/Nanoscale Heat and Mass Transfer.

After the proposed work ended during the award performance period, the co-PI transitioned to a fundamental investigation of how particle shape and size influence the thermal conductivity enhancement for PCM. The equation below was developed by Hamilton and Crosser in 1962 as a modification to Maxwell's equation to calculate the thermal conductivity of a material with particles infused at volume fractions below approximately 10%. The modified equation includes a parameter, n, that relates to the shape of the particle where $n = 3/\psi$ and ψ = the ratio of the surface area of a non-spherical particle to the surface area of a spherical particle when the particles have the same volume.

$$\frac{k_{eff}}{k_m} = \frac{k_p+(n-1)k_m-(n-1)\phi(k_m-k_p)}{k_p+(n-1)k_m+\phi(k_m-k_p)} \quad (4.1)$$

where k_{eff} = effective thermal conductivity
k_m = thermal conductivity of the matrix (PCM)
k_p = thermal conductivity of the particle
ϕ = particle volume fraction
n = shape parameter

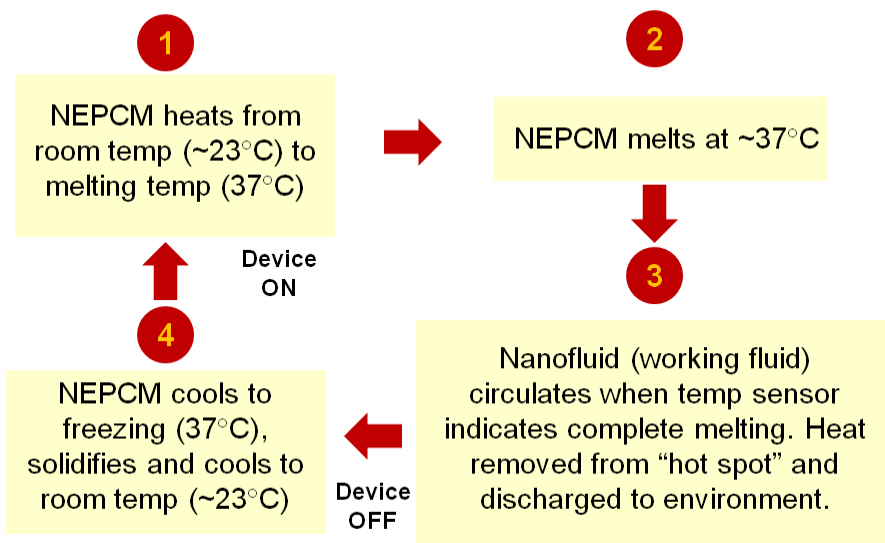

Figure 4.3: Schematic of microelectronics cooling with NePCM and microchannel transport integrated

Stop flow lithography (SFL) provides a method to synthesize micron-sized particles and, potentially, nanoparticles of any two-dimensionally extruded shape. Furthermore, related methods that pre-date SFL allow the synthesis of spherical and spheroidal particles. An overview of these methods is described in a review paper submitted by the co-PI to *Microfluidics and Nanofluidics* (Bah and Floyd-Smith, 2013).

Figure 4.4 shows representative results from the effort to investigate the role of particle shape and size on thermal conductivity enhancement. The graph predicts the thermal conductivity enhancement as a function of particle shape for metal oxide particles (k ~ 20 W/m·K) dispersed in PCM (k ~ 0.2 W/m·K). Inset 1 shows scanning electron micrographs of polymeric particles synthesized using SFL. The particles are monodisperse and lend themselves to the investigation of how particle size and shape influence thermal conductivity enhancement. Furthermore, in addition to polymeric particles, the co-PI has demonstrated a library of metal oxide particles in various sizes and shapes. Currently, the co-PI is performing experiments to compliment the predictions regarding thermal conductivity enhancement as a function of particle shape.

A journal article is currently in preparation to archive the results of this effort. Although the performance period for the award has ended, the work is ongoing. It is currently funded by the Alabama Louis Stokes Alliance for Minority Participation (ALSAMP) for Alayna Huckleby and a 3M endowment for Dr. Tamara Floyd-Smith.

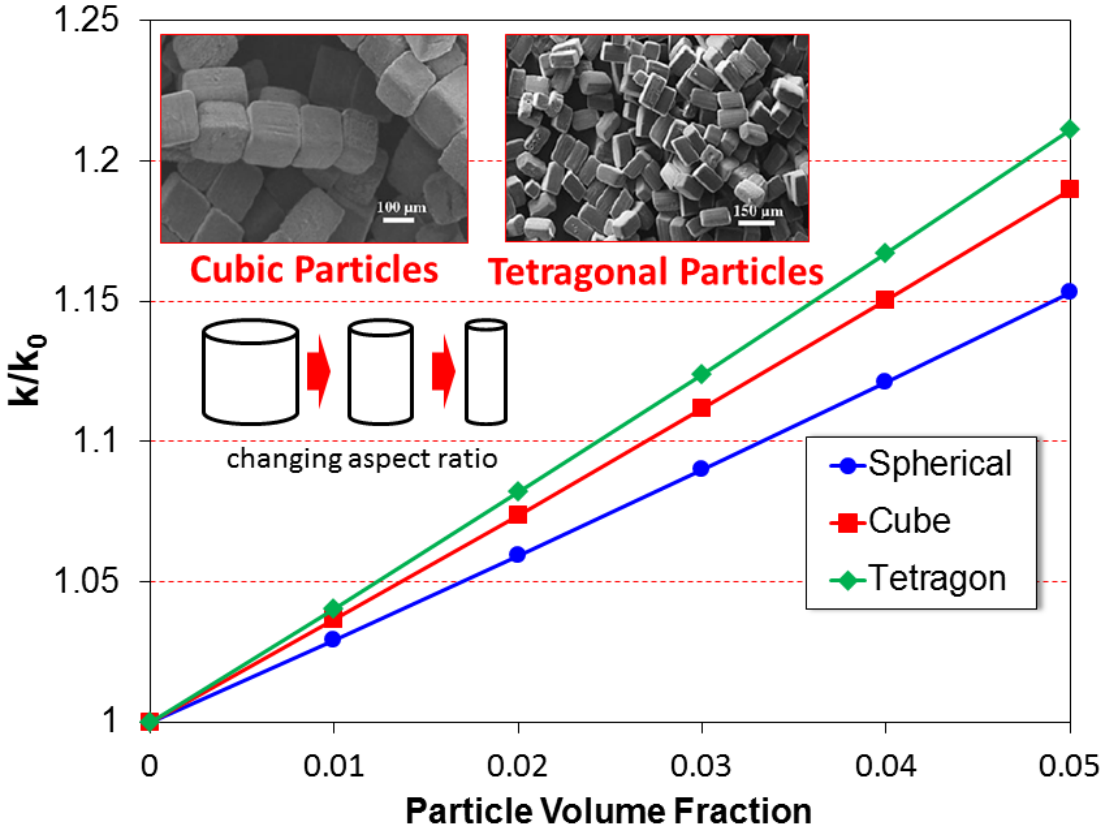

Figure 4.4: Plot of thermal conductivity enhancement with respect to particle volume fraction for different particle shapes. (Inset 1) Scanning electron micrographs (SEM) of particles synthesized by TU using SFL. (Inset 2) schematic demonstrating changing aspect ratio/sphericity for a rod-shaped particle.

Achievements

The major achievements by the Tuskegee University team include one published full length journal article, one submitted full length journal article, one full length journal article in preparation, and one published peer-reviewed conference proceedings paper. Additionally, the team members have presented at several conferences. Most notably, the co-PI was an invited speaker at the 2011 National EPSCoR Conference. Finally, this project produced one M.S. thesis in mechanical engineering (Julaunica Tigner) and contributed to one Ph.D. dissertation in materials science and engineering (David Baah).

References

Baah, D. and Floyd-Smith, T., “Microfluidics for Particle Synthesis from Photocrosslinkable Materials: A Review,” submitted to *Microfluidics and Nanofluidics*.

Floyd-Smith, T., Baah, D. and Huckleby, A. “PCM Thermal Conductivity Enhancement by Particles Synthesized Using Stop Flow Lithography,” in preparation.

Tigner, J. and T. Floyd-Smith, “Feasibility Assessment of the Integration of Microfluidics and NEPCM for Cooling Microelectronics Systems,” Proceedings of the ASME 2012 3rd Micro/Nanoscale Heat & Mass Transfer International Conference in Atlanta, GA, March 2012.

Tigner, J., M. Moeini Sedeh, T. Sharpe, A. Bufford and T. Floyd-Smith, “Analysis of a Platform for Thermal Management Studies of Microelectronics Cooling Methods,” *Applied Thermal Engineering*, (60) 2013, 88-95.

5. Multi-Scale, Multi-Physics Non-Continuum Modeling
(Dr. Luis A. Cueva-Parra, Mathematics, Auburn Univ. Montgomery)

The accomplishments of the research group at Auburn University at Montgomery (AUM) as part of the NEPCM Research Cluster are presented here. It includes major activities, significant results, major findings and conclusions. The main objective for this research group is the Objective 5 in the general proposal and it is described below.

Objective: *Development of multi-scale, multi-physics non-continuum modeling tools for NEPCM that will be led by AUM is a fresh, science-based initiative that relies on advanced mathematical and computational techniques. Non-continuum numerical tools will be used to predict the thermophysical property enhancement/modifications of NEPCM, thus complementing the materials characterization studies at AU and X-ray scattering analyses at ANL.*

To accomplish this objective initially we established the following major goals:

a. Development of Parallel Lattice Gas Automata (LGA) and Molecular Dynamics (MD) Techniques,
b. Development of Parallel Lattice Boltzmann (LB) Techniques,
c. Visualization and Computer Graphics
d. Distributed/Grid Lattice Boltzmann,
e. Parallel/Grid Hybrid LB-MD.

However, based on the preliminary results and the capability of our students working in this project (undergraduate students) we noticed that we overestimated our goals. At the end we have concentrated our efforts in fewer goals and these were the development of Molecular Dynamics, Monte Carlo, and Lattice Boltzmann modeling and simulation techniques, and the Visualization and Computer Graphics tools. Next we will discuss the achievements in these areas.

5.1) Molecular Dynamics Modeling and Simulation Techniques

A variety of molecular dynamics models have been developed using GROMACS (GROningen MAchine for Chemical Simulations) [5.1, 5.2], a MD simulation package. These models considered a variety of materials including Dodecane, Eicosane, Ethane, and Octanol and force fields including GROMOS [5.3-5.5] (G45a1, G45a2, and G45a3), TraPPE [5.6-5.8], OPLS-AA (all atom) [5.9], and COMPASS [5.10]. Initial models were developed to predict heat capacity: Cv and Cp for Dodecane using the force field G45a3. Later, these models were refined in order to predict heat capacity, viscosity [5.11] and heat conductivity for a wide range of temperatures. Specifically, force field parameters were adjusted and additional techniques for determining more adequate parameter values were explored and tested. This refinement included the design and execution of more validation cases as well as the consideration of alternate and complementary techniques, software development, and software adoption.

The calculation of thermal conductivity is not provided directly by GROMACS. Therefore, we have successfully developed a code for calculating the thermal conductivity, using the Green-Kubo [5.12] relation and the equilibrium MD simulation from GROMACS output files. Hundreds of simulations were performed of argon, ethane, copper, argon-copper nanofluids, and ethane-copper-nanofluids to test our calculations of thermal conductivity. Our results were compared to those produced by using different MD software: Large-scale Atomic/Molecular Massively Parallel Simulator (LAMMPS) [5.13, 5.14]. Both GROMACS and LAMMPS based simulations results were in agreement.

Specifically, MD simulations were performed to determine the thermal properties of an ethane-copper nanofluid. The nanofluid was 14.31% copper by weight and approximately 1% copper by volume. Simulations were performed in the NPT ensemble to predict density and isobaric heat capacity. Thermal conductivity was calculated by applying the Green-Kubo relation to trajectories in the NVE ensemble. Properties of the base fluid and copper were determined. The model considers the Lennard-Jones potential [5.15, 5.16] for all interactions (Table 5.1). Ethane methyl groups were treated as single interaction sites with Lennard-Jones parameters taken from the OPLS-UA (united atom) force field [5.17]. The methyl groups were constrained to a separation distance of 0.1526 nm by either the LINCS [5.18] or SHAKE [5.19] algorithm.

I	j	sigma_ij (nm)	Gamma_ij (kJ/mol)
CH3	CH3	0.3775	0.866088
Cu	Cu	0.23377	39.5202
CH3	Cu	0.29707	5.8505

Table 5.1. Lennard-Jones parameters

Simulations were performed with the GROMACS software package. Additional simulations for ethane were performed with the LAMMPS software package to compare the implementations of the Green-Kubo method. All systems were energy minimized and equilibrated until relevant properties converged. Density and isobaric heat capacity were determined from NPT simulations using the Nosé-Hoover thermostat and the Parrinello-Rahman barostat. Thermal conductivity was determined from NVE simulations where the Lennard-Jones potential was shifted to ensure energy conservation.

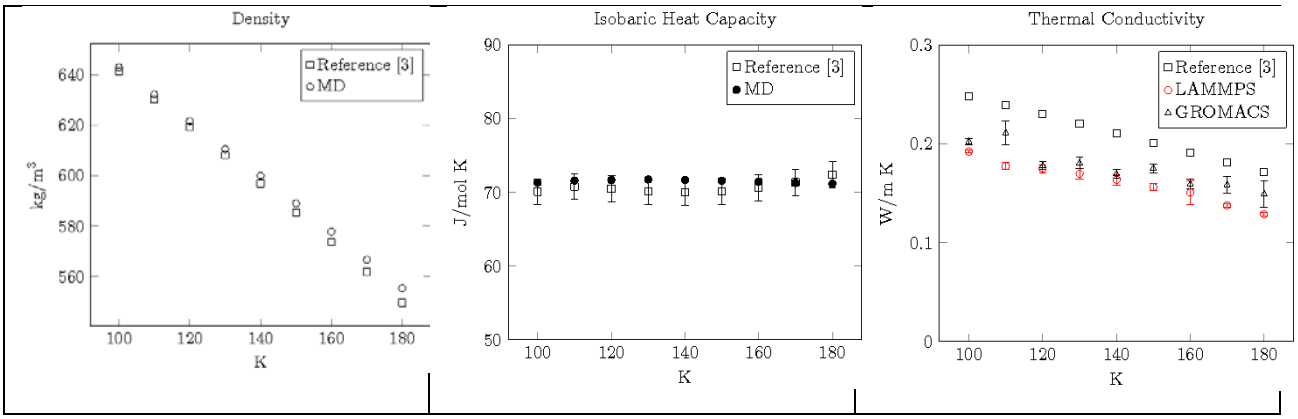

Figure 5.1 Ethane density, heat capacity and thermal conductivity vs. temperature.

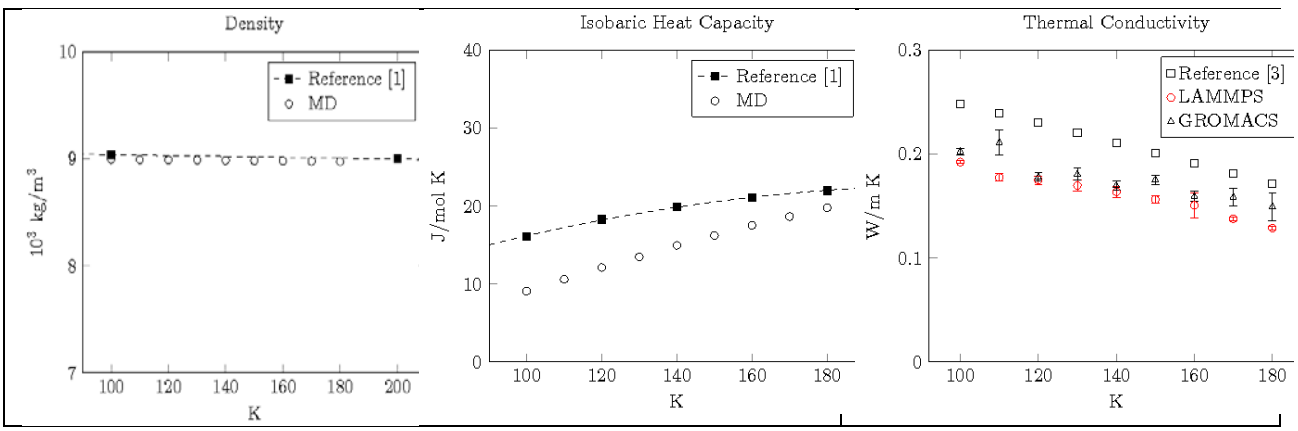

Figure 5.2 Cooper density, heat capacity and thermal conductivity vs. temperature.

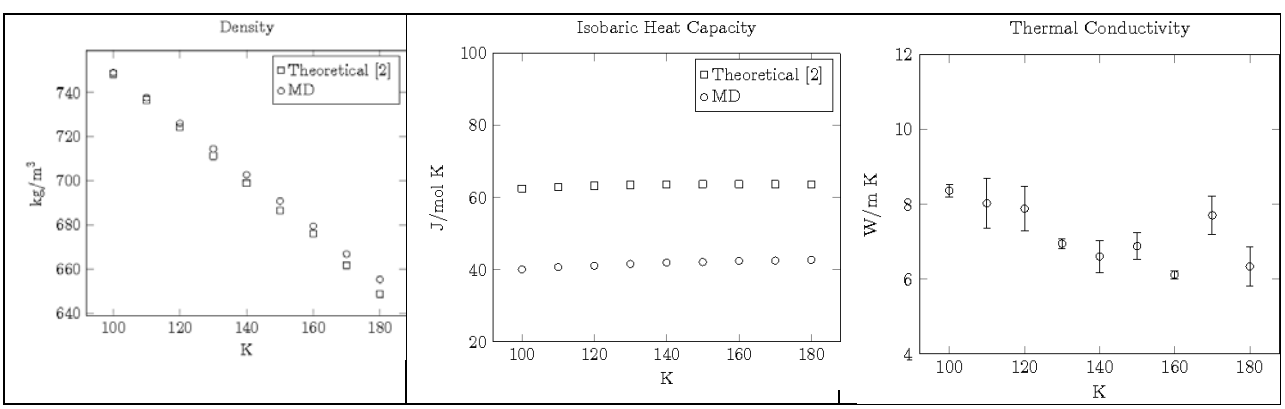

Figure 5.3 Ethane-cooper nanofluid density, heat capacity and thermal conductivity vs. temperature.

The model successfully recreates the density and isobaric heat capacity of ethane at the considered temperatures (Figure 5.1). LAMMPS results for thermal conductivity under-predict the thermal conductivity of ethane by 21% to 26% while GROMACS values have a percent error of 12% to 20%. This may be due to the use of constraints and the fact that rotational contributions to energy were not considered in the Green-Kubo relations. From Figure 5.2 we see that copper density values are predicted to within 1% error. The magnitude of the heat capacity is successfully recreated but the rate of increase with respect to temperature is exaggerated. MD values for the thermal conductivity of copper are drastically lower than the reference values (33% to 68% error). In Figure 5.3, the density of the nanofluid, predicted by the simulations, matches very well to that of the theoretical model. The MD values for the isobaric heat capacity of the nanofluid are approximately 33% lower than those predicted by the theoretical model. The MD values for thermal conductivity are approximately 32 times larger than those given by theoretical models (not shown). The reference data [1], [2] and [3] in the figures corresponds to [5.20], [5.21], and [5.22] respectively. Based on these results, a new model was needed for copper in order to give more accurate values for thermal conductivity. This was an expected result provided that for solid materials the force fields for MD simulations are drastically different than of a simple Lennard-Jones type.

Despite our early success using GROMACS, the increasing complexity of our MD systems has required us to switch to the LAMMPS software package. LAMMPS will allow us to simulate a fully realized nanofluid including stabilizer molecules and nanoparticles that require more than Lennard-Jones interactions. However, it is much more difficult/time-consuming to create initial systems in LAMMPS than it is with GROMACS. To that end, we have produced a code that simplifies the process greatly and works well with Packmol [5.23, 5.24]. Furthermore, LAMMPS includes an implementation of the Green-Kubo relation for thermal conductivity that does not consider the average enthalpy per molecule type. We have added an appropriate code (fix class) that includes this necessary calculation. Also, the inclusion of 3- and 4-body potentials to accommodate more complex molecules is considered.

Our initial efforts to model complex molecules (long chain Alkanes) started with the modeling of dodecane at the very beginning of this project with some mixing results. At the end with more experience and some techniques already validated we performed simulations of eicosane. Models of bulk eicosane comprised of periodic boxes containing 100, 500 and 1000 molecules have been prepared and simulated. The

results for these models are very similar, which yields us to believe that the size of the domain in this range does not affect density. The force field considered was OPLS-UA (united-atom). Figure 5.4 shows the density of eicosane for different values of temperature. The standard deviation of the density in the MD simulations is less than 3.1×10^{-4} while the comparison with reference values provided by [5.25] results in an overestimation of approximately 13.5%. Despite this relatively good approximation, we still need to check some force field parameters as well as cutoff distances, which possibly will affect these results. Also, we noticed that during the MD simulations the pressure was not well controlled but inside of a tolerable range.

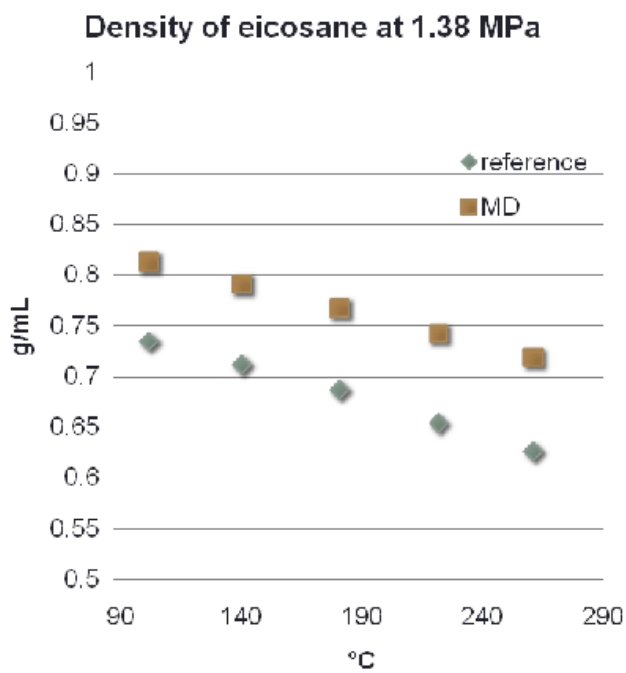

Figure 5.4 Density of eicosane vs temperature

Another attempt to improve the MD modeling of eicosane was the introduction of the OPLS-AA (all atom) force field, which was used in conjunction with techniques and parameters given in the literature especially in a recent paper by Caleman et al. [5.26]. Caleman et al. have simulated 146 organic liquids using OPLS-AA. In general there is good agreement between their MD results and experimental measurements. We converted the parameters given by Caleman et al. in order to be used in LAMMPS as well as Ryckaert-Balleman parameters used by Rizzo and Jorgensen [5.27] converted to OPLS format. Also, we included Lennard-Jones tail correction and are considering particle-particle particle-mesh (PPPM)[5.28] solver for long range Coulombic interactions and 1-4 Lennard-Jones factors.

We simulated eicosane using the OPLS-UA and OPLS-AA force fields to determine which model will be better to use when we simulate nanofluids. Hundreds of simulations (more than 130,000 CPU hours) have been performed in total. We also learned how LAMMPS handles electrostatic interactions, which proved to be very important for the fully realized nanofluids. Early results of eicosane thermal conductivity using OPLS-UA have approximations of same order of magnitude as for shorter n-alkanes with the same force field. As we mentioned before, LAMMPS does not account for the average enthalpy per particle type when calculating heat flux vector. So when using OPLS-UA force field the masses and parameters for both CH2 and CH3 are similar, thus ignoring average enthalpies in a pure eicosane system is reasonable. This does not apply when we use OPLS-AA for pure systems and certainly not for heterogeneous systems (nanofluids). For taking into account the effect of considering average enthalpy we modified the LAMMPS' code for the "compute heat/flux" command.

While Dr. Khodadadi's group was using non-equilibrium MD modeling, we continued modeling additional properties like shear viscosity by an equilibrium MD method. Initial tests have been on simple ethane systems using NPT ensemble. These tests were very promising and initial results are shown in Figure 5.5.

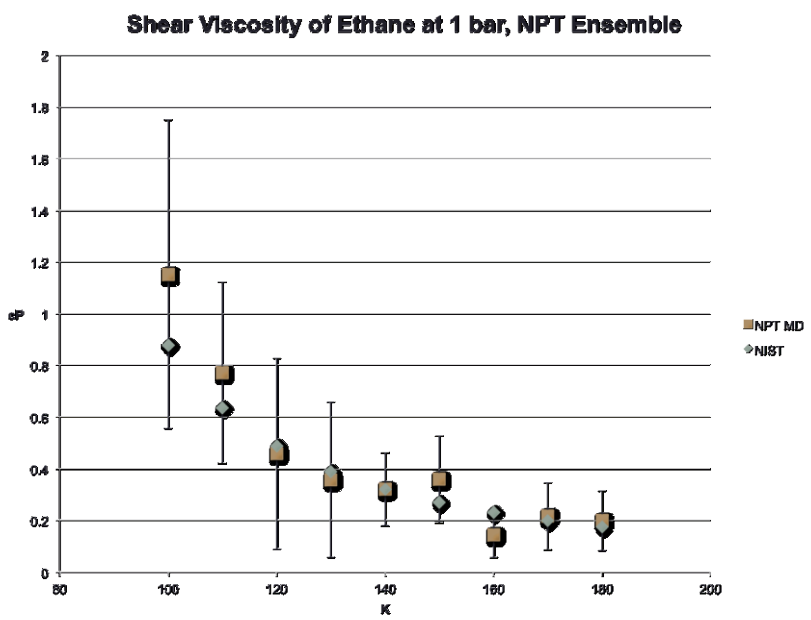

Figure 5.5 Shear viscosity of Ethane at 1 bar vs temperature.

In summary, we are able to design and simulate MD models for predicting thermophysical properties of Alkane-based NEPCM. The process includes the generation of initial domains (fluid base and nanoparticles) in the proper format (topology files) recognizable by GROMACS and LAMMPS. Also, we are able to correctly define all necessary molecule topologies by hand for multiple force fields. We have experience using several GROMOS force fields, the TRAPPE force field and both the united-atom and all-atom OPLS force fields. However, force field parameterization techniques were not implemented because it requires substantial resources, which we could not afford. A manuscript with detailed information in this area has being prepared and planned to be submitted for publication (see publications section).

Future plans (with no grant support) include the refinement of our models, which comprise the inclusion of realistic models for the CuO nanoparticles and sodium oleate (stabilizer). Also, we will study the phase change process in NEPCM. Additionally, we are interested in investigating the effect of non-regular nanoparticles in predicting thermophysical properties. For this effect we will develop a code for generating non-regular nanoparticles, and explore if the use the convex hull problem will help to orient stabilizer molecules on the nanoparticle surface. Finally, pure cooper- and silver-eicosane nanofluids will be studied.

5.2) Monte Carlo Modeling and Simulation Techniques

Atomic (mass) and thermal diffusion are inherently random processes, which can be modeled considering random walks [5.29] and the Brownian motion [5.30]. These processes have been studied extensively using statistical mechanics [5.31-5.34]. Specially, they can be studied using Interacting Lattice Gas (ILG) approaches which are based on the Monte Carlo (MC) method with Metropolis Algorithm (MA) [5.35, 5.36]. The main parameters for these processes are the atomic diffusivity: D and the thermal diffusivity: K. The thermal diffusivity is related to the specific heat capacity (C_P) and thermal conductivity (λ) according equation (1), where ρ is the density.

$$K = \lambda / (\rho C_P) \tag{5.1}$$

The Einstein equation (2) provides a relation between the mean squared mass displacement ($<R^2>$) and the atomic diffusivity, which can be used to relate the mean squared ``heat tracer'' displacement with the thermal diffusivity.

$$D = <R^2>/ 6t \tag{5.2}$$

The main objective was to develop a model for predicting thermal diffusivity, heat conductivity and heat capacity. Also, this model was used for performing qualitative analysis of how those properties change as a function of temperature and nanoparticle

concentration. Initially, we modeled and simulated mass and heat diffusion for a single component system. The computational domain of the model was a three dimensional, transversally periodic box (See Fig. 5.6) where high concentration of mass or “heat tracers” (normalized to 1 unit) is applied to the bottom plane of the box. Using this computer simulation model, we studied how the diffusion processes (caused by both mass and temperature gradients) interplay with each other. Center of mass displacement, flux of mass and “heat” particles, and particle distribution over time were analyzed. The computer implementation was performed using the C++ programming language [5.37] parallelized with the Message Passing Interface (MPI) [5.38-5.40]. It included the post-processing code for direct visualization using VMD (visualization package discussed in the last section).

The cubic domain of the model is represented in the Figure 5.6. Part (a) is a sketch of the lattice representation of the domain. It shows its sides of dimensions Lx, Ly and Lz with an equal number of lattice sites along the x- y- and z-axis respectively. Part (b) is a snapshot of the visualization of a simulation where mass particles and “heat tracers” are represented by small spheres.

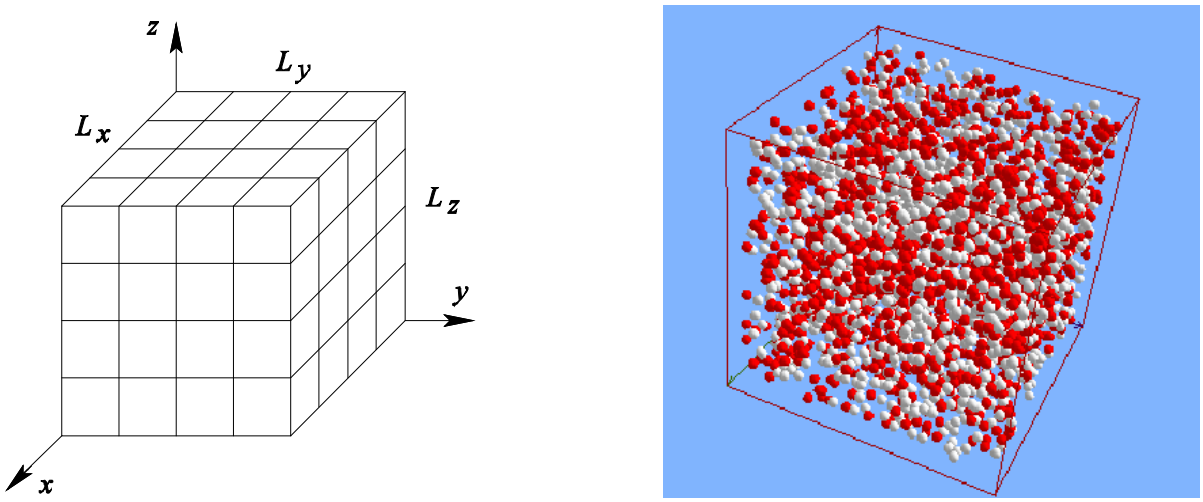

(a) (b)

Figure 5.6 Cubic domain
(a) Lattice representation, (b) Visualization with mass/heat particles.

The mass particle is denoted by m_M and the heat particle is denoted by m_H. Empty sites will represent the bulk material (pure substance or base fluid), the mass particles represent the nanoparticles and the flow of heat particle (aka heat tracers) will represent the heat flux. The heat particle concentration at the bottom plane is normalized to 1 (hot surface) and 0 (cold surface) at the top plane (free boundary). The quantities of interest are root mean squared displacement of the heat tracers as function of time (RMS(t)), the displacement of center of mass of the particles as a whole (CM), flux of particles (net heat transfer), density profile, and velocity profile of particles. The details of the implementation are given in a manuscript which will be submitted for publication. Next we will present the major results and conclusions.

We validated the model simulating heat conduction in a pure substance (base fluid). Figure 5.7 shows the number of heat (energy) particles per horizontal layer in a small domain (10 x 10 x10 cubic domain). It represents how heat will diffuse in this homogeneous domain, and the number of particles in a given layer will be proportional to the current temperature at that level. It shows the counts at different time steps. Figure 5.8 shows same result as above but we considered a bigger domain (25 x 25 x 25) and also when we let the system to reach the equilibrium or steady state. We can see the linear temperature distribution as expected. In order to have the steady state we monitored the heat flux (input and output), that is the number of heat particles entering the domain and exiting it. Figure 5.9 shows the input and output heat flux in function of time. When they reach the same value the system is considered in equilibrium.

Once the model was validated we proceeded with adding nanoparticles to the base fluid. We used as a parameter the nanoparticle concentration per volume. The nanoparticles were inserted into the domain at random positions. These nanoparticles can be fixed in a site or have certain mobility controlled by the value of the parameter T_{np} that is greater than that of the heat particles T_h.

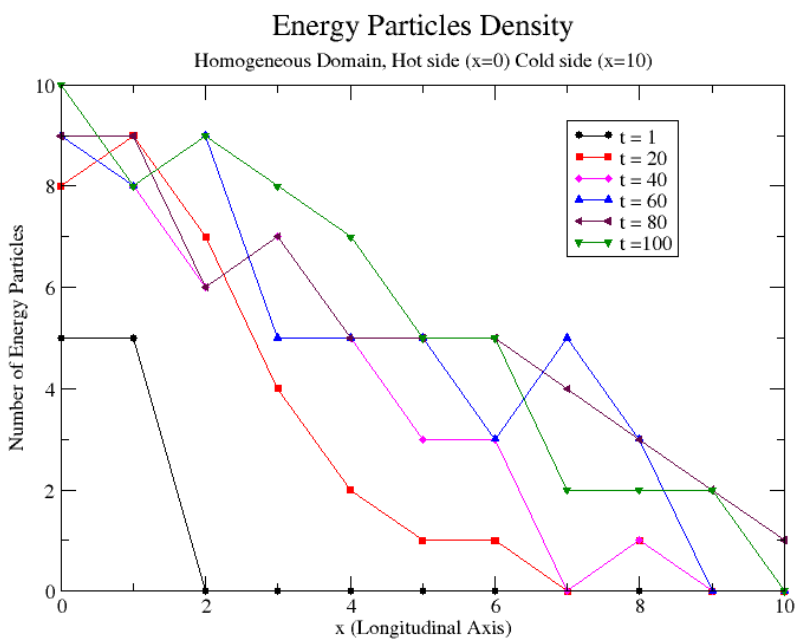

Figure 5.7 Energy (heat) particles density at different layers for various time-steps.

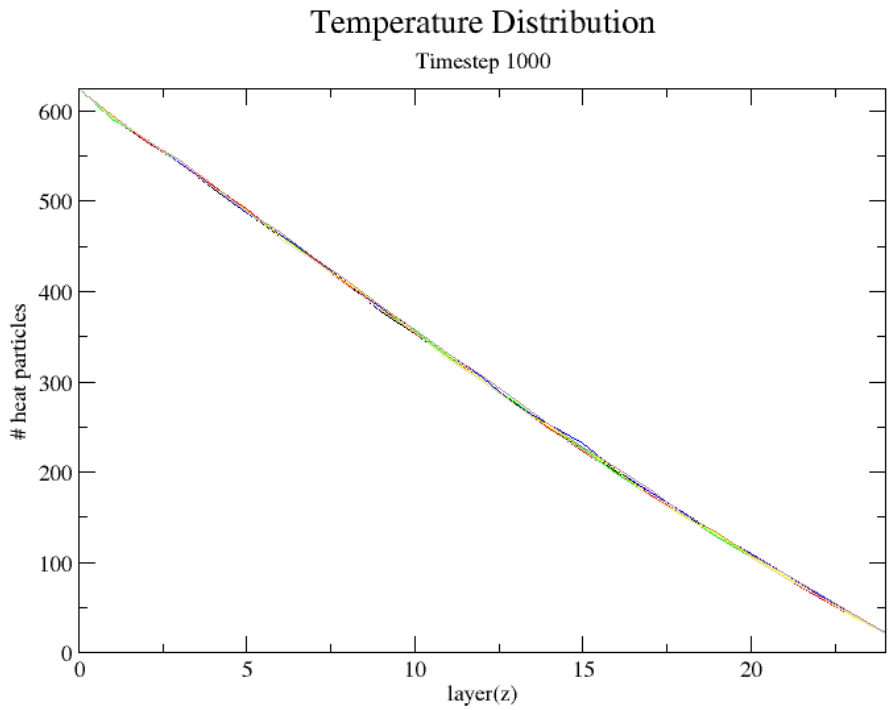

Figure 5.8 Temperature Distribution (Number of heat particles per layer) at steady state.

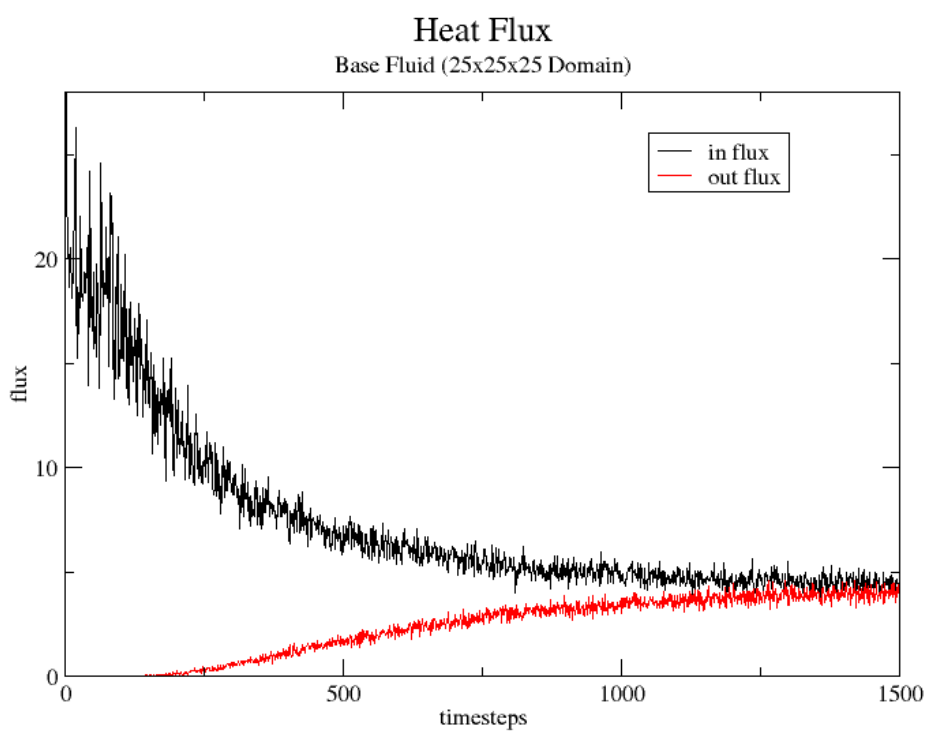

Figure 5.9 Heat in- and out-flux with respect to time

If the nanoparticles are mobile, they move with periodic boundary conditions on all axes. The heat particles and nanoparticles can occupy the same lattice point. If a heat particle is attempting to move to or from a site that contains a nanoparticle, it will move with a higher mobility (probability) using the parameter T_{np} for the nanoparticle. The nanoparticles move randomly as long as the destination does not already contain another nanoparticle, in which case a weak collision (the nanoparticle cannot move) is considered. If the site that a nanoparticle is moving from contains a heat particle, then the heat particle travels with the nanoparticle.

Since the MC simulation is a stochastic method, multiple simulations should be performed and the average value of the results considered. Statistically, the greater number of simulations, the better the accuracy (smaller standard deviation) of the results. However, a minimum of 30-40 simulations should be performed for obtaining a meaningful result. In the implementation of the computer code, we assured that each simulation had a different seed for the pseudo random number generator. The results obtained averaging 64 simulations using a parallel computer code is shown in the Figure 5.10. In this figure the displacement of the heat particles' center of mass with respect to time is shown. The evolution of the center of mass with respect to time represents the transient solution of the conduction heat equation. This curve is proportional to the square root function and later it is used to determine the heat diffusivity of the material at hand (pure/base fluid or nanofluid).

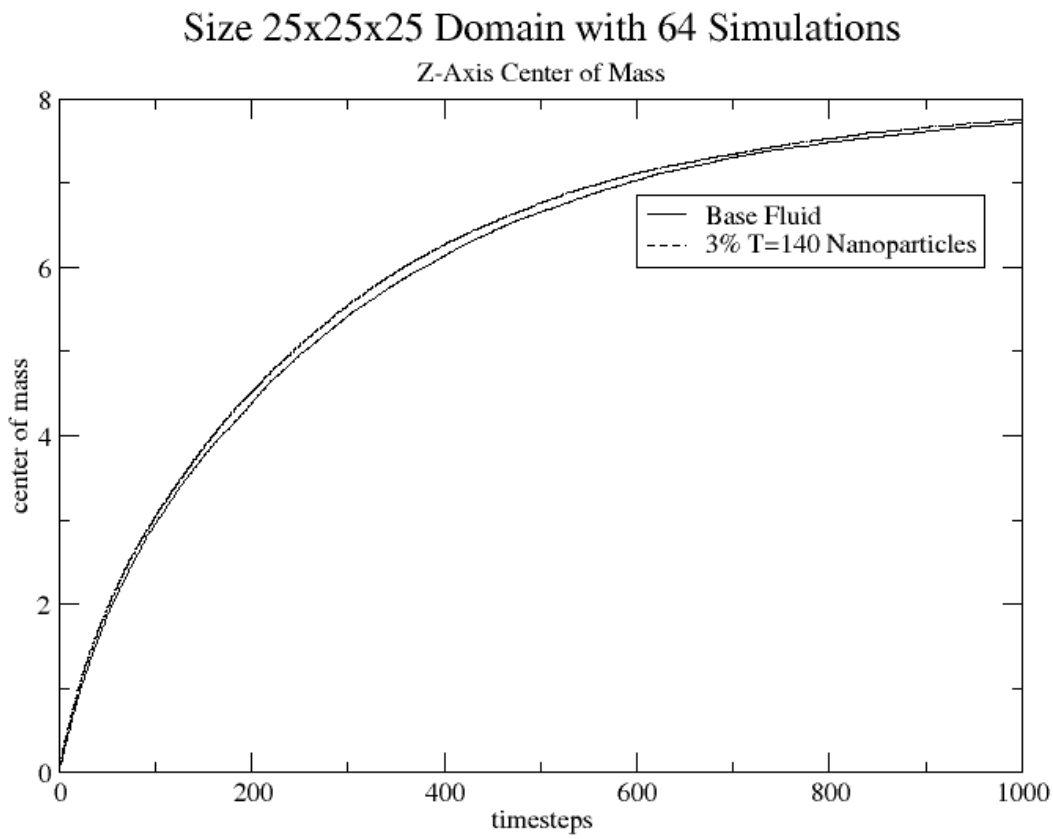

Figure 5.10 Heat particles' center of mass displacement with respect to time.

Fluid	A	Diffusivity (D)	Heat Flux (q)	Heat Conductivity (κ)
Base Fluid (BF)	0.306	0.0156	4.22	0.172
BF+1% fixed NP	0.307	0.0157	4.21	0.176
BF+1% mobile NP	0.308	0.0158	4.25	0.182
BF+3% fixed NP	0.309	0.0159	4.18	0.174
BF+3% mobile NP	0.314	0.0164	4.33	0.180
BF+5% fixed NP	0.311	0.0161	4.23	0.173
BF+5% mobile NP	0.317	0.0167	4.42	0.180

Table 5.2 Qualitative comparison of the heat flux, diffusivity and heat conductivity for different types of nanofluids

The Table 5.2 shows the results for a set of computer experiments (simulations). It presents a qualitative comparison of heat flux, diffusivity and heat conductivity for different cases of nanofluids in contrast with the base fluid. For these simulations we considered a cubic domain of size 25 x 25 x 25, the parameter for the mobility of heat particles is T_h = 1 and for the nanoparticles is T_{np} = 140, the number of simulations per

case is 64. The eight cases include base (pure) fluid and with 1%, 3%, and 5% nanoparticles (NP) added at fixed locations and with random mobility. The parameter A is a proportionality factor for the square root function in order to fit the curve of the heat particles center of mass. This factor is related to the diffusivity.

In summary we accomplished a MC modeling tool for estimating qualitatively, the heat flux, diffusivity, and heat conductivity of nanofluids. This tool is a complex parallel computer code which has post-processing capabilities for visualization. A manuscript related to these results is planned to be submitted for publication.

5.3) Lattice Boltzmann Modeling and Simulation Techniques

We evaluated a set of codes which use the Lattice Boltzmann (LB) technique for simulation of fluid flow and heat transfer. We selected the code named PALABOS (PArallel LAttice BOltzmann Solver) [5.41], which implements the Lattice Boltzmann Method [5.42-5.44]. PALABOS is an open source code written in C++ and easily extensible. We added and tested new routines in the code for a variety of multi-component and multi-physics problems. Those include curved flow in a 2D semicircle channel; spherical domains of heavier fluid which dissolve in a lighter fluid, convection rolls in a 2D domain with hot top and cold bottom. The main purpose for using the LB technique is to be able to simulate phase change at higher scales than molecular and micro-scales.

After having some experience using manipulating PALABOS, we were able to handle the thermal application function of the code. One of the simulations we conducted was the Boussinesq Thermal 2D. This simulation demonstrated our ability to incorporate thermal flow into the simulation. This was accomplished by defining a second domain of lattice points to become the temperature field and incorporating a function that would merge the two together so that they could affect one another. The simulation describes a fluid constrained between a hot bottom wall (no-slip for the velocity) and a cold top wall (no-slip for the velocity). The lateral walls are periodic. Under the influence of gravity, convection rolls are formed.

Thermal effects are modeled by means of a Boussinesq approximation: the fluid is incompressible, and the influence of the temperature is visible only through a body-force term, representing buoyancy effects. The temperature field obeys an advection-diffusion equation. The simulation is first created in a fully symmetric manner. The symmetry is therefore not spontaneously broken; while the temperature drops linearly between the hot and cold wall, the convection rolls fail to appear at this point. In a second stage, a random noise is added to trigger the instability. The simulations took a long time to form the convection rolls. We modified the code by elilminating the second stage and setting the entire domain, with the exception of the bottom wall, to the same temperature as the

top wall (cold). The bottom wall is kept at a higher temperature (hot). The Figure 5.11 shows the formation of convection rolls at various time steps within the simulation.

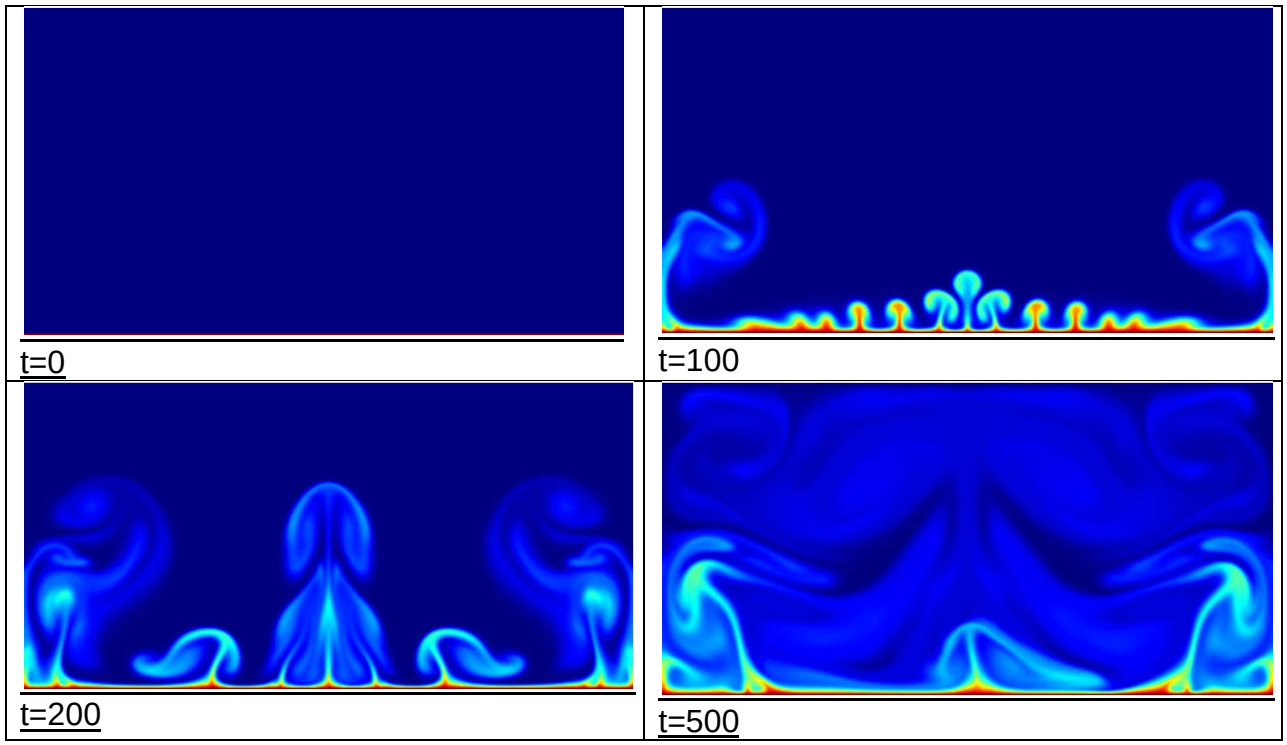

Figure 5.11 Convection rolls simulation. Closed cold domain and bottom wall hot.

In other model we incorporated modified the major aspects of the fluid flow simulation into another with thermal effects. Specifically, we added a thermal component to the Cylinder 2D simulation. We changed the dimensions of the domain, and eliminated the fluid flow part by creating bounce back conditions on the lateral walls and setting the initial velocity to zero. We changed the obstruction to a square block and defined a thermal field on the block whereby the block would get a boundary temperature of 1 and the surrounding fluid would get an initial temperature of 0. A gravity field was implemented so that the change of temperature would induce fluid flow around the box. In order to test that these modifications were consistent, we chose to also start with the Boussinesq Thermal 2D simulation and modify it until it would give the same results as the modified Cylinder 2D. Both modified codes' results were exact when compared to the other. The Figure 5.12 shows the temperature distribution of the domain at various time steps within the simulation.

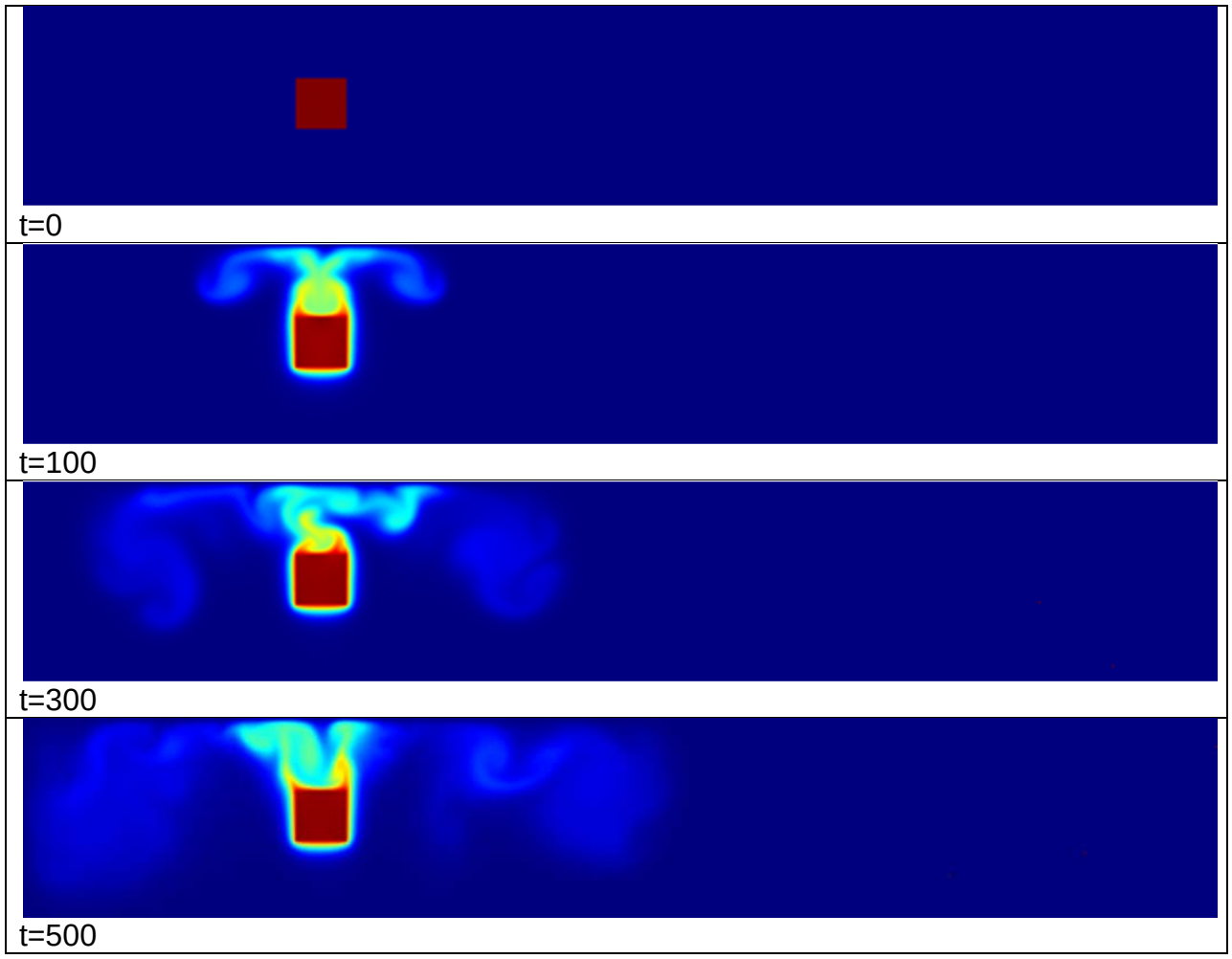

Figure 5.12 Convection rolls simulation. Temperature distribution of a closed cold domain with a hot square.

The next step was to implement Lattice Boltzmann Models for phase change simulations. For this end we needed a validation problem, which can be solved analytically and numerically and eventually serve us as a reference. We analyzed the basic Stefan Problem [5.45, 5.46], its derivation and general formulation. Tracking the interface between solid and liquid phases with respect of time requires solving the heat equation at both phases, and imposing some initial conditions on the temperature distribution and a particular boundary condition, the Stefan condition, on the evolving boundary between those two phases. Since the position of the interface between the two phases is unknown with respect to time the Stefan Problem is an example of a free boundary problem. We solved some particular problems using Gupta's book [5.45] and implemented codes (written in C++) for their numerical solutions. Also, we implemented the numerical solution of a type of Stefan Problem solved by Meyer [5.47]. This problem has a well-defined analytical solution and the developed numerical implementations (two implementations: Euler/Bisection and Runge-Kutta-Fehlberg/Secant) give a very close approximation for two distinct initial and boundary conditions. These included

periodic boundary conditions to simulate alternating heating and cooling processes. Figures 5.13a and 5.13b show the position of the interface vs. time.

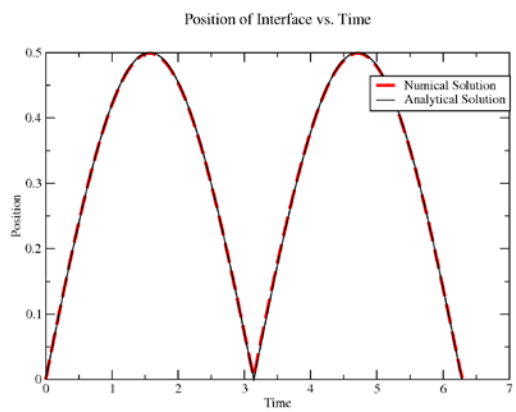

Figure 5.13.a Position of Interface vs. Time (Case I)

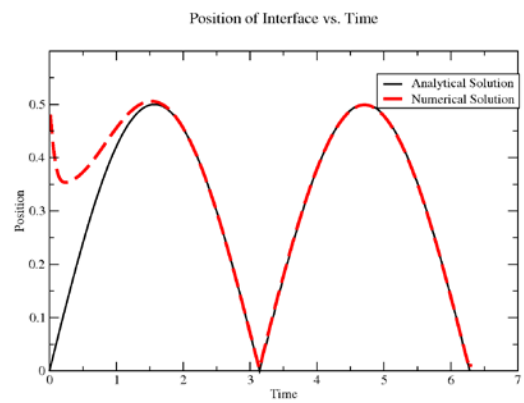

Figure 5.13.b Position of Interface vs. Time (Case II)

This established our test case for validation of the Lattice Boltzmann modeling of phase change. Also, at this stage we were performing an extensive literature review. The aim was to explore existing LB implementations for heat transfer and phase change. Some of most the relevant literature in this topic is listed as references [5.48-5.67]. The task was performed during the duration of the grant period. It culminated with a review manuscript to be submitted for publication.

In the next phase we developed our own code for natural convection and phase change for nanofluids using the LB method. This code has being implemented using C++. Figure 5.14 shows the temperature distribution of a natural convection simulation in a rectangular closed domain with initial cold temperature (dark color) and a hot left wall.

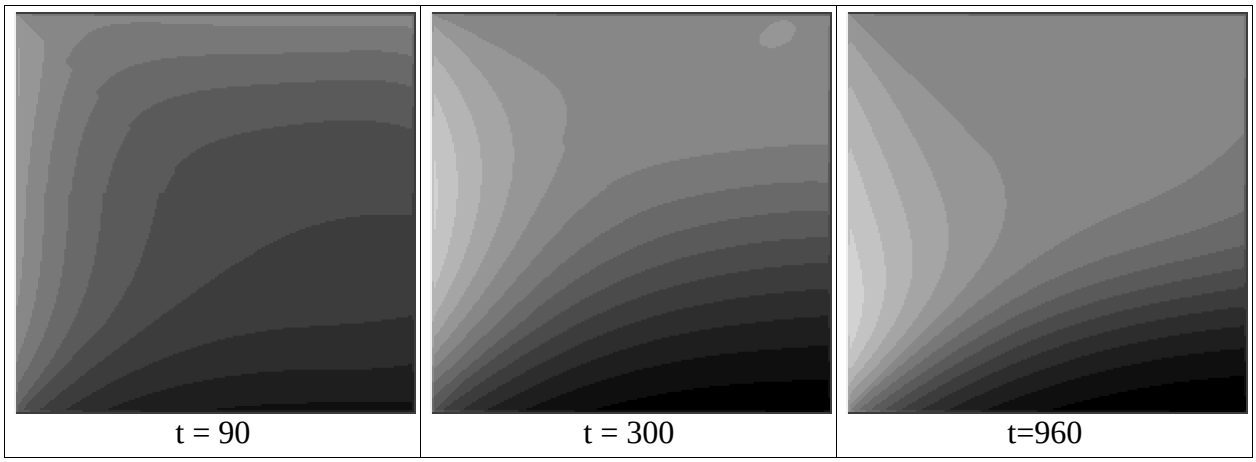

Figure 5.14 LB simulation of natural convection in a rectangular closed domain with initial cold temperature and a hot left wall. Darker is colder.

Figure 5.15 depicts a phase change simulation using our LB-based code of a pure substance. It is a rectangular domain, initially in solid phase (black color) with left and bottom walls heated. It shows the melting process for three different times.

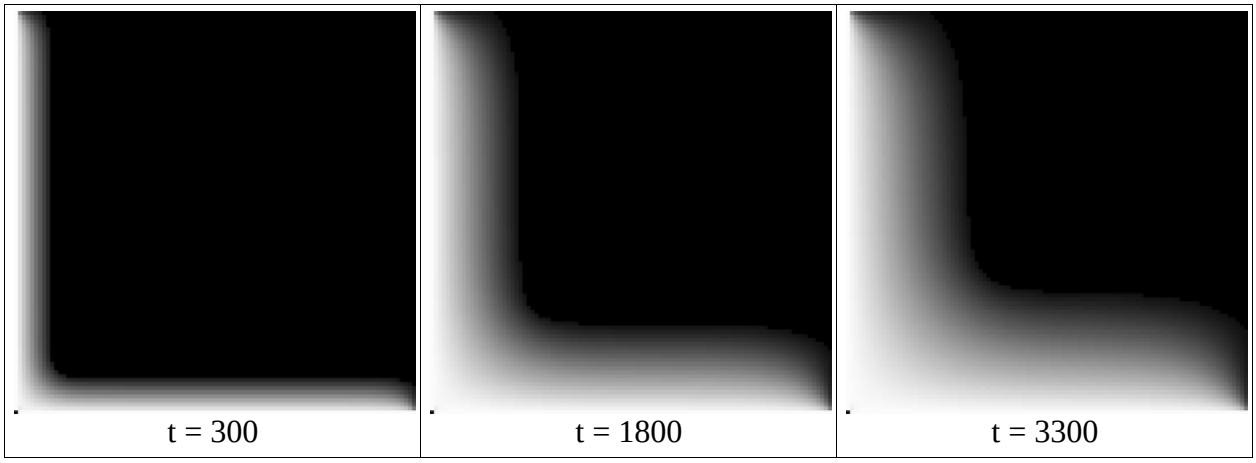

Figure 5.15 LB simulation of a melting process in a rectangular domain initially solid (black) when bottom and left walls are heated.

Next, we implemented a multiphysics model which included phase change and natural convection in NEPCM (nanofluids). The physical description of this model is represented in the Figure 5.16.

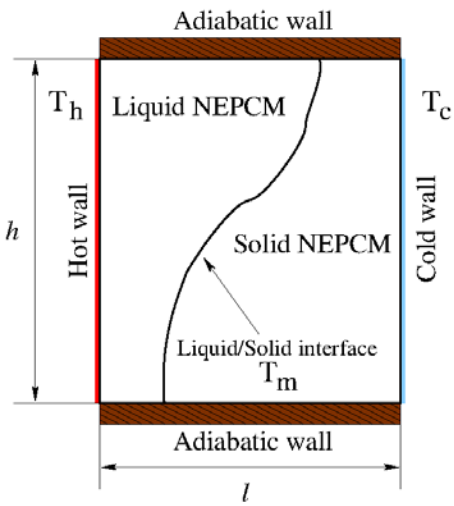

Figure 5.16 Physical model for phase change and natural convection in NEPCM

We considered a 2D rectangular domain with length *l* and height *h.* The temperature of the hot wall (left side) is Th and of the cold wall (right side) is Tc. Tm is the NEPCM melting temperature with Tc < Tm < Th. Top and bottom sides are adiabatic (thermally insulated). Initially the temperature in the domain is Tc (NEPCM is solid). For this model we used the enthalpy formulation for heat conduction [5.68] given by

$$\partial_t (\rho H) = \partial (\kappa \partial T), \tag{5.3}$$

where H is the total enthalpy and H = Cp T + fl L, Cp is the heat capacity, T is temperature, κ is the heat conductivity, ρ is density, fl is the liquid fraction in volume (0 for pure solid and 1 for pure liquid), and L is the latent heat. The enthalpy method provides a relation between H and T as follows

$$\begin{aligned} T &= H / Cp, \text{ if } H < Hs \\ T &= Ts + (H - Hs)/L, \text{ if } Hs <= H <= Hl \\ T &= (H - L)/Cp, \text{ if } H > Hl, \end{aligned} \tag{5.4}$$

where Hs and Hl are the enthalpy values corresponding to the temperatures at the beginning (Ts) and at the end (Tl) of a phase change. Also

$$fl = (H - Hs)/(Hl - Hs) \tag{5.5}$$

Then we considered the multi-distribution function of the LB method for combining in one single model both phase change and natural convection for nanofluids.

- Multi-distribution function LBM for melting with natural convection of nanofluids.

$$f_i^\sigma(\mathbf{x}+\mathbf{e}_i\Delta t, t+\Delta t) - f_i^\sigma(\mathbf{x},t) = -\frac{1}{\tau^\sigma}\left[f_i^\sigma(\mathbf{x},t) - f_i^{\sigma,eq}(\mathbf{x},t)\right] + \frac{2\tau^\sigma - 1}{2\tau^\sigma}\frac{D\Delta t}{B_i c^2}\mathbf{F}^\sigma \cdot \mathbf{e}_i$$

$\sigma = f$, for the base fluid.
$\sigma = p$, for the nanoparticles.
$c = \Delta x/\Delta t$: lattice velocity.
$\tau^\sigma = \lambda^\sigma/\Delta t$: collision-relaxation time constant.

$\mathbf{F}^\sigma$: total force on σth comp.
D : dimension.
$B_i = \begin{cases} 6, & i = 1,\cdots,4 \\ 24, & i = 5,\cdots,8 \end{cases}$

(5.6)

The upper script in the function *f*, distinguishes the two components in this system (base or pure fluid and the nanoparticle). The subscript in the function refers to the spatial directions, which in our case are 9 directions $\boldsymbol{e_i}$ (lattice D2Q9). The spatial coordinate is the vector $\boldsymbol{x}$, and the temporal variable is *t.* The equilibrium functions, are functions which depend on the lattice and equilibrium velocities, *c* and $\boldsymbol{v^{eq}}$ respectively. These equilibrium functions are given below.

$$f_i^{\sigma,eq}(\mathbf{x},t) = w_i\rho^\sigma(\mathbf{x},t)\left[1 + 3\frac{(\mathbf{e}_i\cdot\mathbf{v}^{\sigma,eq})}{c^2} + \frac{9}{2}\frac{(\mathbf{e}_i\cdot\mathbf{v}^{\sigma,eq})^2}{c^4} - \frac{3}{2}\frac{(\mathbf{v}^{\sigma,eq})^2}{c^2}\right]$$

$w_i = \begin{cases} 4/9, & i = 0 \\ 1/9, & i = 1,\cdots,4 \\ 1/36, & i = 5,\cdots,8 \end{cases}$

$\rho^\sigma(\mathbf{x},t) = \sum_i m^\sigma f_i^\sigma(\mathbf{x},t)$

m^σ : molecular mass of σth comp.

$\mathbf{v}^{\sigma,eq} = \mathbf{u}^{\sigma,eq} + \mathbf{F}^\sigma\frac{\Delta t}{2\rho^\sigma}$

$\mathbf{u}^{\sigma,eq} = \mathbf{u}^{eq} = \frac{\sum_\sigma \frac{\rho^\sigma\mathbf{u}^\sigma}{\tau^\sigma}}{\sum_\sigma \frac{\rho^\sigma}{\tau^\sigma}}$

$\rho^\sigma(\mathbf{x},t)\mathbf{u}^\sigma(\mathbf{x},t) = m^\sigma\sum_i f_i^\sigma(\mathbf{x},t)\mathbf{e}_i$

(5.7)

And the forces acting on the nanoparticles $\boldsymbol{F^P}$ and on the fluid particles $\boldsymbol{F^f}$ are given by

$$\mathbf{F}^p = n\left(\mathbf{F}_B + \mathbf{F}_H + \mathbf{F}_D + \mathbf{F}_A\right)/V$$

$\mathbf{F}_B = C_B \frac{K_B T}{r}$: Brownian force.
$\mathbf{F}_H = -\frac{4}{3}\pi r^3 g \Delta\rho'$: Buoyancy force.
$\mathbf{F}_D = -6\pi\mu r \Delta\mathbf{u}$: Drag force.
$\mathbf{F}_A = \sum_{i=1}^{8} n_i \frac{\partial V_A}{\partial \mathbf{r}_i}$: Potential force.
$V_A =$
$-\frac{1}{6}A\left(\frac{2r^2}{d^2-4r^2} + \frac{2r^2}{d^2} + \ln\frac{d^2-4r^2}{d^2}\right)$

$$\mathbf{F}^f = -n(\mathbf{F}_B + \mathbf{F}_D)$$

n : total # particles.
V : lattice volume.
r : nanoparticle radius.
$\Delta\rho'$: density difference (f/p).
μ : fluid viscosity.
$\Delta\mathbf{u}$: velocity difference (f/p).
n_i : adjacent # particles.
V_A : interaction potential.
A : Hamaker constant.
d : distance between particles.

Additionally, to complete the model we need to have the energy equation for coupling the fluid flow (mass transport) with the phase change and temperature distribution. This equation in its discrete form using the LB method is given by *g*. Upper and lower scripts for this function are similar to those for the f function. However, the extra upper script k in the function *g* is a parameter for the identification of liquid or solid phase at a given time step. The function *g* is similar in its structure to the function *f*, so for the actual implementation of this model we require 2 similar lattices, one for the function *f* and other one for the function *g*. Also, the function *g* includes the enthalpy formulation discussed above. Therefore, physical properties like latent heat *L*, heat capacity *Cp* and enthalpies *H* are introduced with the *g* function. Below you find the explicit formulation of the energy equation for the LB method (the *g* function).

- Energy equation for LBM

$$g_i^{\sigma,k}(\mathbf{x}+\mathbf{e}_i\Delta t, t+\Delta t) - g_i^{\sigma}(\mathbf{x},t) = -\frac{\Delta t}{\tau_\theta^\sigma}\left[g_i^\sigma(\mathbf{x},t) - g_i^{\sigma,eq}(\mathbf{x},t)\right] - w_i\frac{L}{C_p}\left[f_{l,i}^{k-1}(t+\Delta t) - f_{l,i}(t)\right]$$

$$H^k = C_p T^k + f_l^{k-1} L$$

$$f_l^k = \begin{cases} 0, & H^k < H_s \\ \frac{H^k - H_s}{H_l - H_s}, & H_s \le H^k \le H_l \\ 1, & H^k > H_l \end{cases}$$

$$\theta^\sigma(\mathbf{x},t) = \sum_i g_i^\sigma(\mathbf{x},t)$$

$$T(\mathbf{x},t) = \frac{\sum_\sigma \theta^\sigma(\mathbf{x},t)}{\sum_\sigma \rho^\sigma C_p^\sigma}$$

(5.8)

$$g_i^{\sigma,eq}(\mathbf{x},t) = w_i\theta^{\sigma}(\mathbf{x},t)\left[1 + 3\frac{(\mathbf{e}_i\cdot\mathbf{u}^{\sigma,eq})}{c^2} + \frac{9}{2}\frac{(\mathbf{e}_i\cdot\mathbf{u}^{\sigma,eq})^2}{c^4} - \frac{3}{2}\frac{(\mathbf{u}^{\sigma,eq})^2}{c^2}\right]$$

The D2Q9 Lattice:

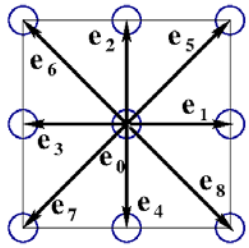

Using the previous formulae we implemented a computer code in C++. It is a general code for three dimensional domains and optimized for running in multicore and parallel computer systems. The validation of this implementation was performed for simple cases and the results were consistent with theoretical solutions. See Figure 5.17 for the validation results. Also, we performed some experiments using our model and the visualization of the results is given in Figure 5.18. The results of this project are summarized in a manuscript to be submitted for publication.

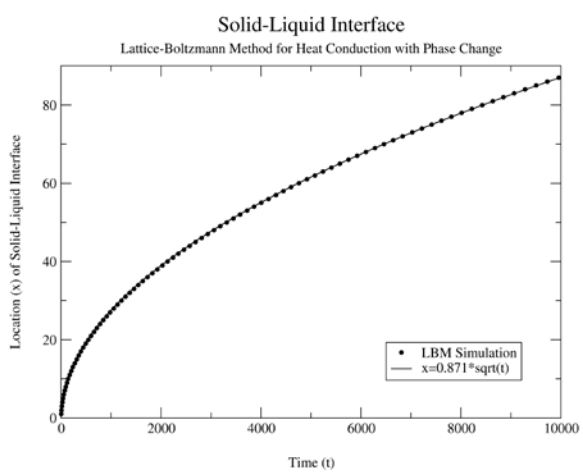

Figure 5.17a

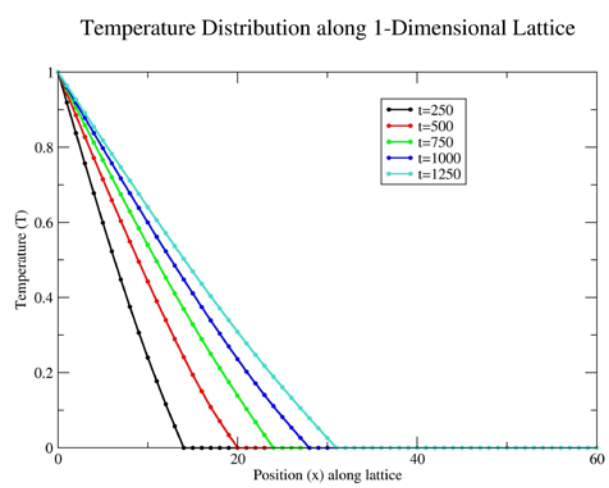

Figure 5.17b

Figure 5.17 Validation results for the LB model with phase change and natural convection

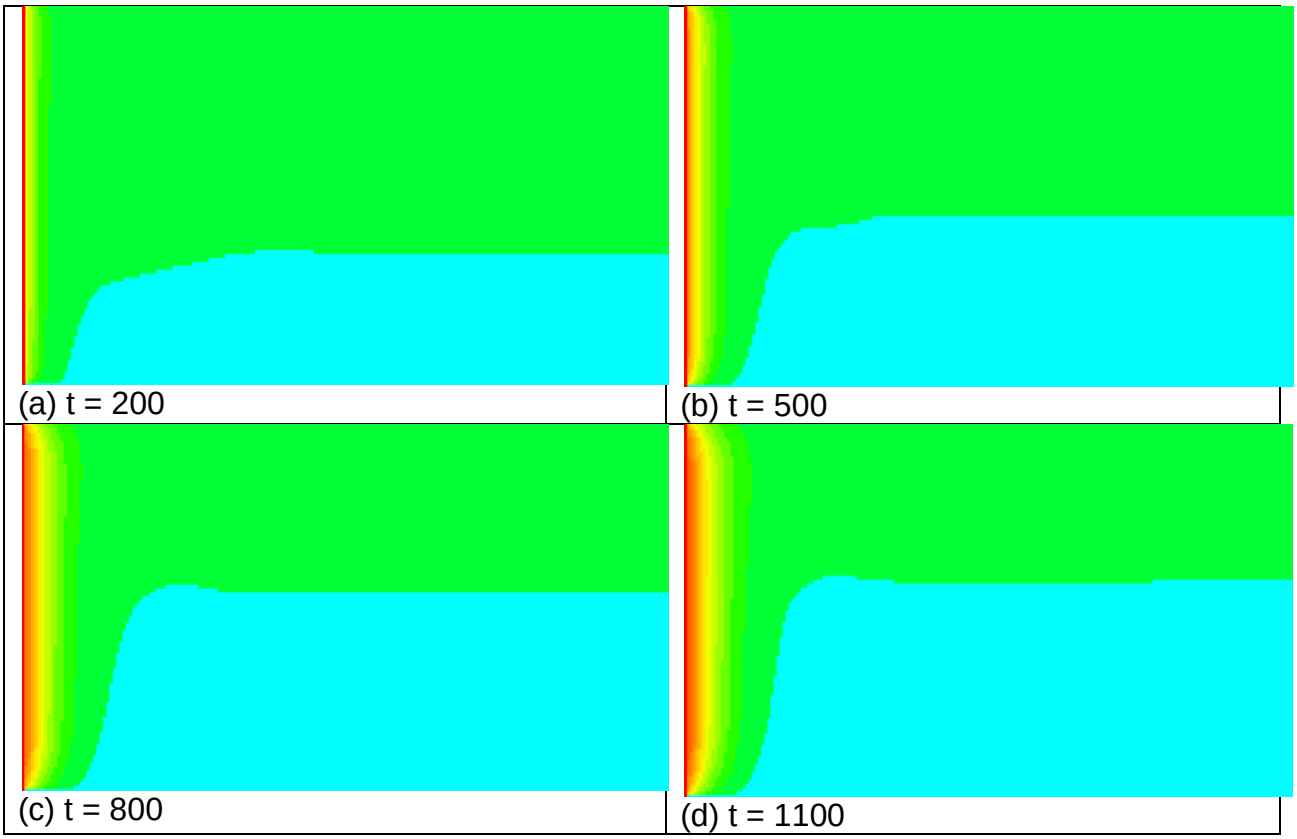

Figure 5.18 Phase change with natural convection for Dodecane with 2.5% mass fraction of silver nanoparticles.

5.4) Visualization and Computer Graphics Tools

After an extended evaluation of various visualization and computer graphics software, we selected the Visual Molecular Dynamics (VMD) [5.53, 5.54] package as a post-processing tool for visualizing and animating our resulting modeling and simulation systems. Figure 15.9 shows the graphical interface of VMD displaying two dodecane molecules. We learned how to work with it and generated most of our MD images and movies using this tool. VDM manipulates a variety of graphics formats which makes it easy to interact with GROMACS and LAMMPS.

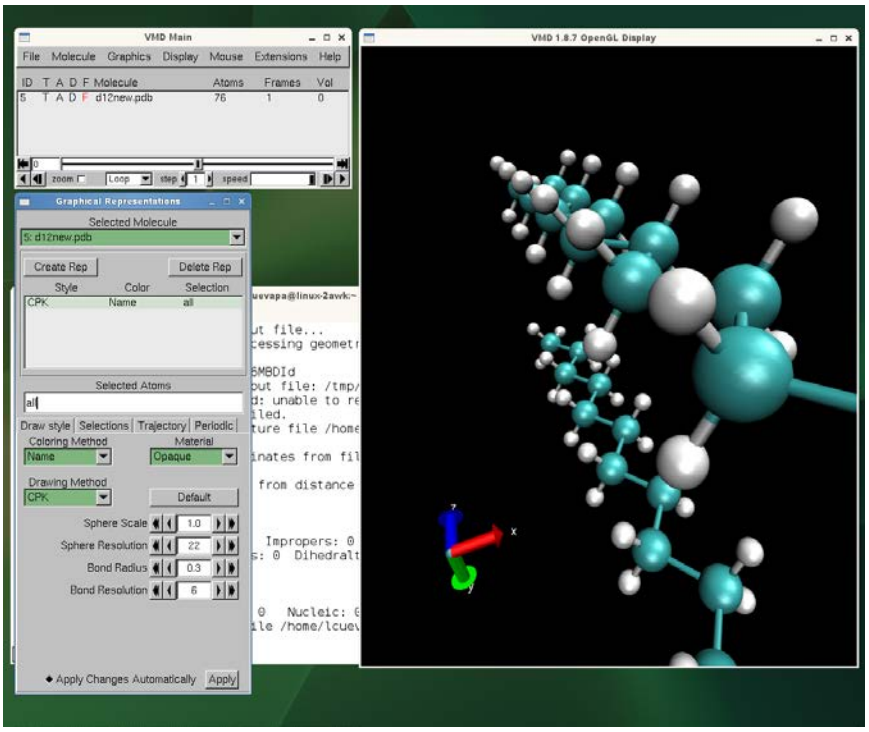

Figure 5.19 Snapshot of VMD interface displaying two Dodecane molecules.

VMD can handle very large and complex systems (large quantities of atoms and molecules), especially large biomolecular systems. Using additional tools (PackMol [5.71-5.73]), which provide information about the geometrical conformation of molecules and their initial packing we will be able to export that information to VMD for the corresponding visualization. An example of the visualization of a large number of components is shown in Figure 5.20. This image shows a visualization of a sample domain containing a CuO nanoparticle (light blue and red sphere) surrounded by stabilizer (white molecules) and immersed in Dodecane (blue molecules). Additional examples of using VMD for visualization of molecular are show in Figure 5.21 and 5.22.

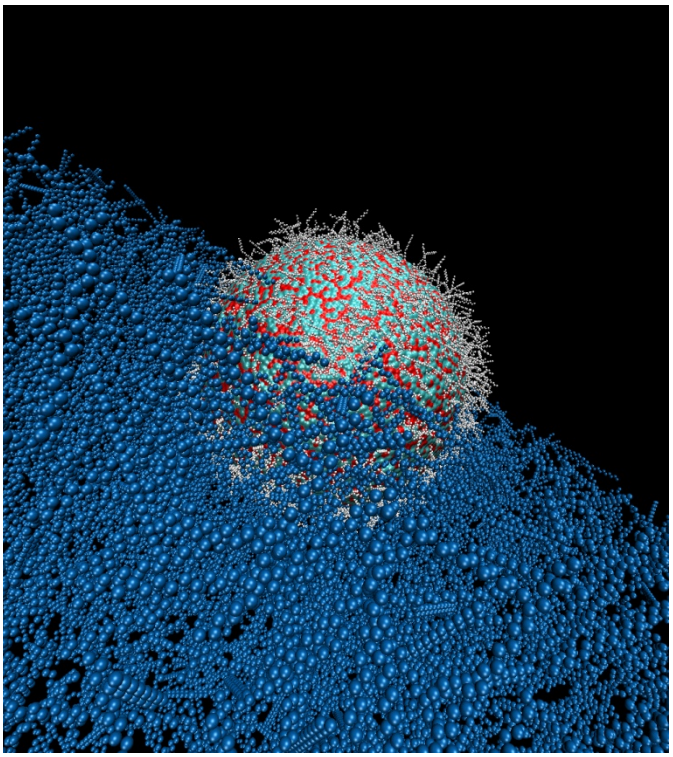

Figure 5.20 A CuO nanoparticle with stabilizer immersed in Dodecane

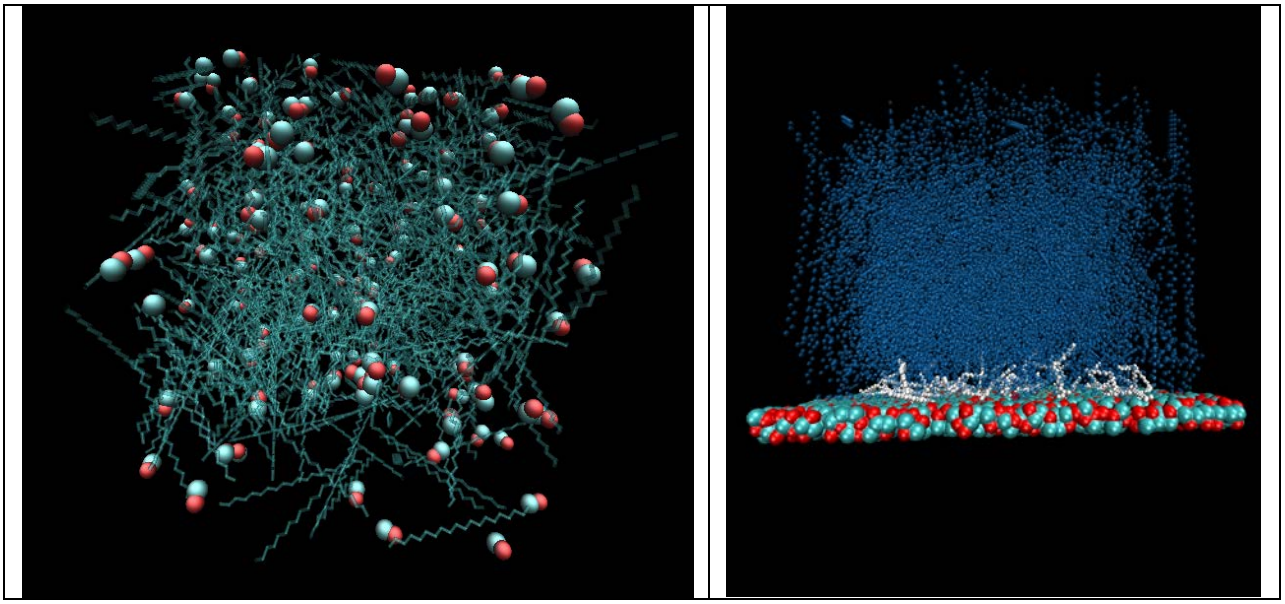

Figure 5.21 (Left) CuO molecules immersed in Dodecane, (Right) Layer of a CuO crystal with some stabilizer (white molecules) and Dodecane molecules on top.

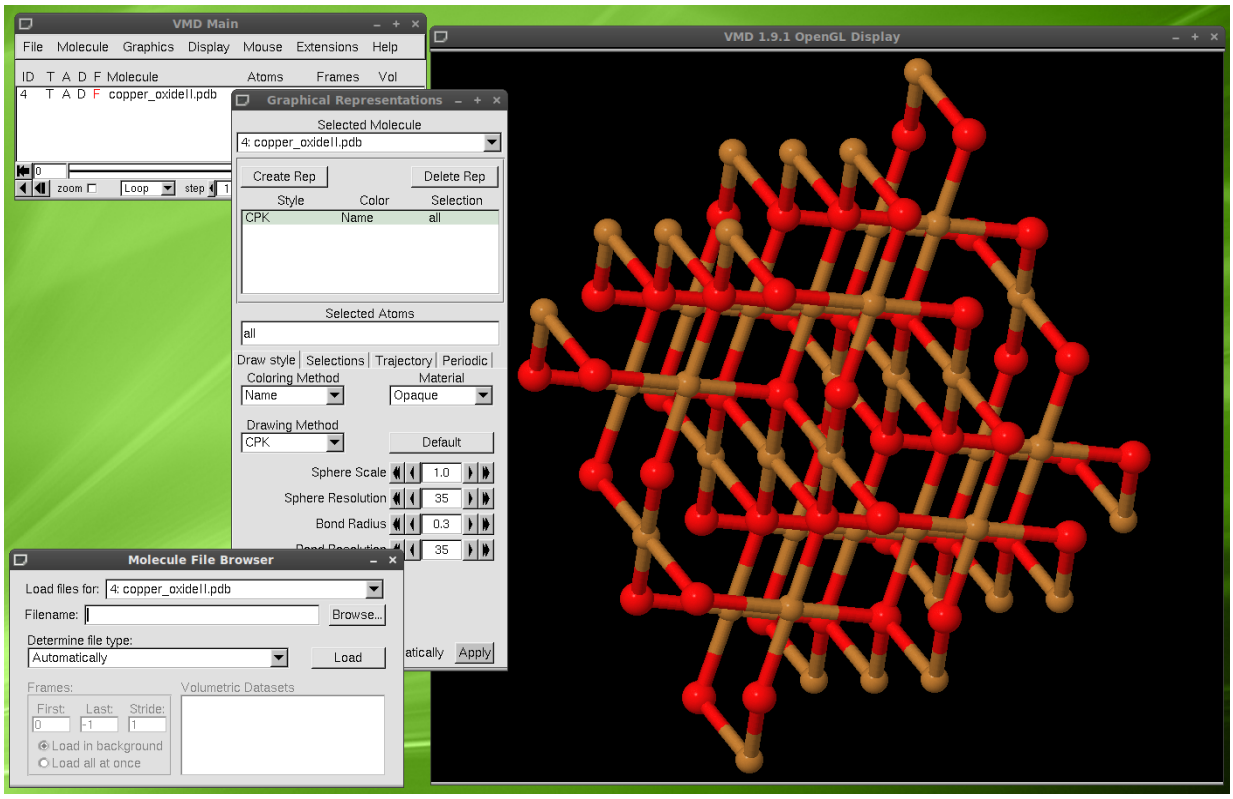

Figure 5.22 Copper Oxide II crystal representation using VMD. Oxygen atoms are red and Copper atoms are brown.

Our Monte Carlo code is fully integrated with VMD to handle the visualization of the simulations. For the Lattice Boltzmann modeling and its corresponding visualization we had a different approach depending on the code employed. If we use PALABOS, the output files are stored in the format vtk with file name extension .vti. Then these files can be easily read using the program called Paraview [5.74]. The output files of a LB simulation give dimensionless values of velocity in three directions and temperature. Paraview produces various slides in .gif or .ppm format. These slides use different colors to show the difference in magnitude of the velocities or temperature between the different lattice points. We have been successful turning these images into movies through the use of the Unix command ppmtompeg. To accomplish this we would manually request that the images be printed as .ppm files instead of .gif. Next, we had

to create a separate file which lists all the parameters needed to make a movie according to the requirements of the Unix command. In this file you would define the location of the ppm's you wish to turn into a movie as well as all the formatting and encoding parameters. After that, we run the command with the location of the file with all the parameters. If we use our own code for LB simulations, then the output files can directly be processed for visualization using an in-house code written in C++.

5.5) Publications

Journal Publications

Mark Guest and Luis Cueva-Parra, “Predicting Thermal Properties of Ethane-Copper Nanofluid by Molecular Dynamics Simulation", manuscript in preparation to be submitted to ***Journal of Heat Transfer***.

Vincent Heningburg and Luis Cueva-Parra, "Review of Lattice Boltzmann Method applied to Phase Change Modeling/Simulation", manuscript in preparation to be submitted to ***International Journal of Modern Physics C***.

L. A. Cueva-Parra and Derek Lathan. “Monte Carlo Simulation of Heat Conduction in Nanofluids”, manuscript in preparation to be submitted to **Applied Physics Letters**.

L. A. Cueva-Parra and Augustine Bertagnolli, “Nanofluid Phase Change and Natural Convection Modeling using the Lattice Boltzmann Method”, manuscript in preparation to be submitted to ***International Journal of Modern Physics C***.

Conference Papers/Presentations

L. A. Cueva-Parra and Augustine Bertagnolli, “Nanofluid Phase Change and Convection Modeling using the Lattice Boltzmann Method”, Auburn University’s Research Week 2013, Auburn University, April 01-04, 2013.

L. A. Cueva-Parra and Augustine Bertagnolli, “Lattice Boltzmann simulation of nanofluid melting with natural convection”, 9th Differential Equations and Computational Simulations MS-UAB Conference, October 4-6, 2012.

T. Hornsby and L. A. Cueva-Parra. ”Monte Carlo Simulation of Mass and Heat Diffusion”, Alabama Alliance for Students with Disabilities in STEM (AASD-STEM) Second Annual Conference, Auburn University, March 31, 2012. [Poster presentation].

Mark Guest and Luis Cueva-Parra, “Predicting Thermal Properties of Ethane-Copper Nanofluid by Molecular Dynamics Simulation", International Conference for High

Performance Computing, Networking, Storage and Analysis. Seattle, WA, November 12-18, 2011. [Poster presentation]

V. Heningburg and L. A. Cueva-Parra. “Numerical Approximations of Fluid Flow and Phase Change using Lattice Boltzmann Method and the Stefan Model”, Alabama DOE EPSCoR Site Visit, Auburn University, September 11-13, 2011. [Poster presentation]

J. Morris, T. Hornsby and L. A. Cueva-Parra. ”Monte Carlo Simulation of Mass and Heat Diffusion”, Alabama DOE EPSCoR Site Visit, Auburn University, September 11-13, 2011. [Poster presentation]

M. Guest and L. A. Cueva-Parra. “Predicting Thermal Properties of an Ethane-Copper Nanofluid by Molecular Dynamics Simulation”, Alabama DOE EPSCoR Site Visit, Auburn University, September 11-13, 2011. [Poster presentation]

5.6) Software developed

Our research group developed the following software:

- Multiple input files developed for MD simulations. Those include information about specific parameters and force fields.
- Code “***pdb2lammps***”: Assists with creating initial simulation domains by converting *pdb* files to LAMMPS data files. Atom coordinates are pulled from a *pdb* file produced by a program like *Packmol*. A custom file format is used to define molecule topologies. Molecule names in the topology files are matched with residue names in the *pdb* file to provide bond, angle and dihedral information.
- Code “***kappacc***”: Calculates thermal conductivity by applying the Green-Kubo relation to GROMACS output files. Atom coordinates and velocities are read from binary *trr* files. Interatomic forces are determined only by Lennard-Jones interactions. This code is not being maintained anymore since the switch to LAMMPS.
- Code “***stripxyz***”: Parses pdb files to extract atom coordinates for post-processing by computational geometry programs like *qhull*. Allows filtering based on atom or residue type.
- Code “***lattice***”: Creates crystalline structures in *gro* file format (easily convertible to *pdb*). Allows making an ideal spherical nanoparticle with a distinct residue name to be replicated in *Packmol*.
- Code “***dat2xvg***”: Converts *dat* files generated by LAMMPS autocorrelation methods into *xvg* format. Allows per-frame and overall averaging of data fields.
- Code “***genSurface***”: In development phase, not production ready. Will allow creation of nanoparticles with irregular shapes and surfaces.
- Code “***autocorrelate, integrate, filter, hfdft***”: Small utility programs for performing numerical methods such as autocorrelations, numerical integration, low pass filtering and discrete Fourier transforms on data in file formats

commonly produced by MD software. Now recommended to process such data with Octave or MATLAB, converting formats if necessary.

- Code "***compute heat/flux/enthalpy***": This code extends the original LAMMPS "*compute heat/flux*" to include calculation of the average partial enthalpies per atom type. This is very important as the original version will produce incorrect results for heterogeneous systems.
- Modifications and additions to PALABOS code have been developed. These are for some applications including multi-component fluid flow and multi-physics (fluid flow and heat transfer) for simple fluids.
- A parallel Monte Carlo code in C++ and MPI, for modeling and simulation nanofluid mass and heat transfer.
- A Lattice Boltzmann code in C++ for phase change and natural convection has been developed.

5.7) People

Besides Dr. Cueva-Parra, who was the lead of this research group, the following **undergraduate** students were involved with this project:

Mr. Mark Guest was involved with the development of MD models. He worked from September 2009 to May 2012. He graduated majoring in Mathematics with Computer Science option on May 2011 and started his Ph.D. in Mathematics on August 2012 at Auburn University.

Mr. Vincent Heningburg was involved with the development of LB models. He focused on using and modifying the PALABOS code and developing C++ code for the solution of the Stefan Problem. He worked from November 2009 to May 2012. He graduated majoring in Mathematics with Computer Science option on December 2010 and started his Ph.D. in Mathematics on August 2012 at University of Tennessee at Knoxville. He received a very prestigious fellowship.

Ms. Jessica Morris was involved with the implementation of the MC modeling for mass and heat diffusion. She worked from August 2010 to May 2012. She graduated majoring in Mathematics with Computer Science option on May 2011. Currently she is working as tutor for Mathematics and preparing herself for graduate studies.

Mr. Tim Hornsby was involved with the implementation of the MC modeling for mass and heat diffusion during summer 2011. He was in the pre-engineering program at AUM and currently is majoring in Electrical Engineering at Auburn University. He plans to graduate on December 2013.

Mr. Augustine Bertagnolli was involved with the development of the LB model for phase change and natural convection. He will graduate on December 2013 majoring in Mathematics with Computer Science option.

Mr. Derek Lathan was involved with the development of the MC model for predicting thermophysical properties of nanofliuds. He developed a parallel code in C++ and MPI. He will graduate on December 2013 majoring in Mathematics with Computer Science option.

5.8) Conclusions

We accomplished to create basic models for predicting thermophysical properties of NEPCM using three non-continuum methods: MD, MC and LB. Also we have included in the LB model phase change and natural convection. We have exposed six undergraduate students to research at the graduate level, and helped them to make advancements in their educational endeavors. Two of them are pursing Ph.D. studies, while the other four are very motivated to continue their education at the graduate level. Besides learning new areas of research, they interacted and communicated with graduate students from the other research groups in the NEPCM research cluster. Also, they prepared research papers, which are on their way for review and eventual publication. This project also helped in leveraging future research collaborations and eventual financial research support from other sources than the DOE. For example, Dr. Cueva-Parra was named XSEDE Campus Champion Fellow and will receive financial support to collaborate with XSEDE staff at Pittsburgh Supercomputing Center in helping researchers from the University of Arkansas to develop MD codes for X-ray diffraction and include it as compute module in the LAMMPS code.

On the other hand, based on the results of the research activities supported by the DOE-EPSCoR grant, we have envisioned a long term research plan in this area. It includes the development of force fields for relevant NEPCM and the inclusion of quantum effects for more realistic models. Other materials such as polymers will be included as base fluids for NEPCM. The development of hybrid LB-MD/LB-MC as well as multi-scale models coupling are considered for future research endeavor.

5.9) References

[5.1] David van derSpoel, Erik Lindahl and Berk Hess, *GROMACS User Manual*. 2006.
[5.2] *GROMACS* webpage, http://www.gromacs.org
[5.3] Wilfred F. Van Gunsteren and H. J. C. Berendsen, *Groningen Molecular Simulation (GROMOS) Library Manual*, BIOMOS b.v., Groningen, 1987.
[5.4] W. F. Van Gunsteren, S. R. Billeter, A. A.Eising, P. H. Hünenberger, P. Krüger, A. E. Mark, W. R. Scott, and I. G. Tironi, *Biomolecular Simulation: The GROMOS96 Manual and User Guide*; vdf Hochschulverlag AG an der ETH Zürich and BIOMOS b.v.: Zürich, Groningen, 1996.

[5.5] Lukas D. Schuler, Xavier Daura, Wilfred F. Van Gunsteren, *An Improved GROMOS96 Force Field for Aliphatic Hydrocarbons in the Condensed Phase*. Journal of Computational Chemistry. Vol. 22. No. 11. 1206-1218. 2001.
[5.6] M.G. Martin and J.I. Siepmann, *Transferable potentials for phase equilibria. 1. United-atom description of n-alkanes*, J. Phys. Chem. B*,* 102**,** 2569-2577 (1998).
[5.7] M.G. Martin and J.I. Siepmann, *Novel configurational-bias Monte Carlo method for branched molecules. Transferable potentials for phase equilibria. 2. United-atom description of branched alkanes*, J. Phys. Chem. B, 103, 4508-4517 (1999).
[5.8] B. Chen, and J.I. Siepmann, *Transferable potentials for phase equilibria. 3. Explicit-hydrogen description of n-alkanes*, J. Phys. Chem. B, 103, 5370-5379 (1999).
[5.9] W. L. Jorgensen, D. S. Maxwell and J. Tirado-Rives, *Development and testing of the OPLS all-atom force field on conformational energetics and properties of organic liquids*, J. Am. Chem. Soc. 118, 11225-11236, 1996.
[5.10] H. Sun*, COMPASS: An ab Initio Force-Field Optimized for Condensed-Phase Applications – Overview with Details on Alkane and Benzene Compound,* J. Phys. Chem. B*, 102 (38), pp 7338–7364, 1998.*
[5.11] A. J. Queimada, I. M. Marrucho, J. A. P. Coutinho and E. H. Stenby, Viscosity and Liquid Density of Asymmetric n-Alkane Mixtures: Measurement and Modeling, *International Journal of Thermophysics,* Vol. 26, No. 1, January 2005.
[5.12] Denis J. Evans and Gary P. Morriss, *Statistical Mechanics of Non Equilibrium Liquids*, Academic Press, Theoretical Chemistry Monograph Series, London 1990.
[5.13] S. Plimpton, *Fast Parallel Algorithms for Short-Range Molecular Dynamics*, J Comp Phys, 117, 1-19 (1995).
[5.14] *LAMMPS* webpage, http://lammps.sandia.gov.
[5.15] Lennard-Jones, J. E., *On the Determination of Molecular Fields* ,Proc. R. Soc. Lond. A 106 (738): 463–477, 1924.
[5.16] Frenkel, D. and Smit, B., *Understanding Molecular Simulation* (Second ed.), San Diego: Academic Press, 2002.
[5.17] W. L. Jorgensen, J. D. Madura, and C. J. Swenson. *Optimized Intermolecular Potential Functions for Liquid Hydrocarbons*, J. Am. Chem. Soc. 106, 6638-6646, 1984
[5.18] Hess, B; Bekker H, Berendsen HJC, Fraaije JGEM. *LINCS: A Linear Constraint Solver for Molecular Simulations*, Journal of Computational Chemistry 18 (12): 1463–1472, 1997.
[5.19] Ryckaert, J-P; Ciccotti G, Berendsen HJC. *Numerical Integration of the Cartesian Equations of Motion of a System with Constraints: Molecular Dynamics of n-Alkanes*. Journal of Computational Physics 23 (3): 327–341, 1977.
[5.20] J. E. Jensen, W. A. Tuttle, R. B. Stewart, H. Brechna, and A. G. Prodell, editors. *Selected Cryogenic Data Notebook*, volume 1. Brookhaven National Laboratory, 1980.
[5.21] K. Khanafer and K. Vafai. A critical synthesis of thermophysical characteristics of nanofluids. *International Journal of Heat and Mass Transfer*, 54:4410–4428, 2011.
[5.22] E. W. Lemmon, M. O. McLinden, and D. G. Friend. Thermophysical properties of fluid systems. In P. J. Linstrom and W. G. Mallard, editors, *NIST Chemistry WebBook, NIST Standard Reference Database, Number 69*. National Institute of Standards and Technology, Gaithersburg MD, 20899, http://webbook.nist.gov, (retrieved August 26, 2011).

[5.23] J. M. Martínez and L. Martínez. *Packing optimization for automated generation of complex system's initial configurations for molecular dynamics and docking*. Journal of Computational Chemistry, 24(7):819-825, 2003.
[5.24] L. Martínez, R. Andrade, E. G. Birgin, and J. M. Martínez. *Packmol: A package for building initial configurations for molecular dynamics simulations*. Journal of Computational Chemistry, 30(13):2157-2164, 2009.
[5.25] Rodden, J.B., C. Erkey and A. Akgerman, *High-temperature diffusion, viscosity, and density measurements in n-eicosane*, J.Chem.Eng.Data, 33, 344,1988.
[5.26] C. Caleman, P.J. van Maaren, M. Hong, J.S. Hub, L.T. Costa, and D. van der Spoel. *Force Field Benchmark of Organic Liquids: Density, Enthalpy of Vaporization, Heat Capacities, Surface Tension, Isothermal Compressibility, Volumetric Expansion Coefficient, and Dielectric Constant,* J Chem Theory Comput 8, 61-74, 2012.
[5.27] R. C. Rizzo and W. L. Jorgensen. *OPLS All-Atom Model for Amines: Resolution of the Amine Hydration Problem*. J. Am. Chem. Soc., 121, 4827-4836, 1999.
[5.28] Hockney and Eastwood, Computer Simulation Using Particles, Adam Hilger, NY, 1989.
[5.29] K Pearson. *The problem of the random walk*. Nature, 72:294, 1905.
[5.30] A. Einstein. *Ueber die von der molekularkinetischen Theorie der Waerme geforderte Bewegung von in ruhenden Fluessigkeiten supendierten Teilchen*, Annalen der Physik, 17, 549-560, 1905.
[5.31] D. Chandler. *Introduction to Modern Statistical Mechanics*, Oxford University Press, 1987.
[5.32] D. A. McQuarrie. *Statistical Mechanics*, University Science Books, 2000.
[5.33] G. A. Bird. *Recent advances and current challenges for DSMC*, Comput. Math. Appl. 35, 1, 1998.
[5.34] M. Grigoriu. *A Monte Carlo Solution of Heat Conduction and Poisson Equations*, J. Heat Transfer, vol. 122, Issue 1, 40(6 pages), 2000.
[5.35] N. Metropolis and S. Ulam. *The Monte Carlo Method*, Journal of the American Statistical Association (American Statistical Association) 44 (247), 335–341, 1949.
[5.36] H.L. Anderson. *Metropolis, Monte Carlo and the MANIAC*. Los Alamos Science, 14:96{108}, 1986.
[5.37] Bjarne Stroustrup, *The C++ Programming Language* (Third ed.), Addison-Wesley Professional, 1997.
[5.38] W. Gropp, E. Lusk, and A. Skjellum, *Using MPI: portable parallel programming with the message-passing interface*. Cambridge, MA, USA: MIT Press, Scientific and Engineering Computation Series, 1994.
[5.39] W. Gropp, E. Lusk, and A. Skjellum, *Using MPI, 2nd Edition: Portable Parallel Programming with the Message Passing Interface*. Cambridge, MA, USA: MIT Press, Scientific and Engineering Computation Series, 1999.
[5.40] W. Gropp, E. Lusk, A. Skjellum, *Using MPI-2: Advanced Features of the Message Passing Interface*. MIT Press, 1999.
[5.41] PALABOS (PArallel LAttice BOltzmann Solver) webpage http://www.palabos.org.
[5.42] Sauro Succi. *The Lattice Boltzmann Equation for Fluid Dynamics and Beyond* (Numerical Mathematics and Scientific Computation), Oxford University Press, 2001.
[5.43] Dieter A. Wolf-Gladrow. *Lattice-Gas Cellular Automata and Lattice Boltzmann Models: An Introduction* (Lecture Notes in Mathematics), Springer; 1 edition, 2000.

[5.44] Michael C. Sukop and Daniel T. Thorne. *Lattice Boltzmann Modeling: An Introduction for Geoscientists and Engineers*, Springer, 1st ed. 2006.
[5.45] S. Gupta. *The Classical Stefan Problem: Basic concepts, modelling and analysis*. Elsevier Science B.V., 2003.
[5.46] L. I. Rubinshteĭn. *The Stefan Problem*, American Mathematical Soc., 1971.
[5.47] G. Meyer. *A numerical method for two-phase stefan problems*, SIAM Journal on Numerical Analysis 8, 555-568, 1971.
[5.48] E. A. Semma, M. El Ganaoui, and R. Bennacer. *Lattice boltzmann method for melting/solidification problems*. C. R. Mecanique, 335:295–303, 2007.
[5.49] C. Sun, Z. Xu, B. Wang, and M. Shen. *Lattice boltzmann models for heat transfer*. Communications in Nonlinear Science & Numerical Simulation, 2, No.4:212–216, 1997.
[5.50] McNamara, G., Garcia, A., and Alder, B., *A hydrodynamically correct thermal lattice Boltzmann model*, Journal of Statistical Physics, vol. 87, no. 5, pp. 1111-1121, 1997.
[5.51] X. Shan, *Simulation of Rayleigh-B'enard convection using a lattice Boltzmann method*, Physical Review E, vol. 55, pp. 2780-2788, The American Physical Society, 1997.
[5.52] X. He, S. Chen, and G. D. Doolen. *A novel thermal model for the lattice Boltzmann method in incompressible limit*, Journal of Computational Physics, vol. 146, pp. 282-300, 1998.
[5.53] D. Chatterjee and S. Chakraborty, *A hybrid lattice Boltzmann model for solid-liquid phase transition in presence of fluid flow*, Physics Letters A 351, 359-367, 2006.
[5.54] D. Chatterjee and S. Chakraborty, *An enthalpy-source based lattice Boltzmann model for conduction dominated phase change of pure substances*, International Journal of Thermal Sciences 47, 552-559, 2008.
[5.55] K. Kono, T. Ishizuka, H. Tsuda, and A. Kurosawa, *Application of lattice Boltzmann model to multiphase flows with phase transition*, Computer Physics Communications 129, 110-120, 2000.
[5.56] W. Miller and S. Succi, *A lattice Boltzmann model for anisotropic crystal growth from melt*, Journal of Statistical Physics 107, 173-186, 2002.
[5.57] W. Miller, S. Succi, and D. Mansutti, Lattice Boltzmann model for anisotropic liquid-solid phase transition, Physical Review Letters 86, 3578-3581, 2001.
[5.58] A. Orazio and S. Succi, *Boundary conditions for thermal lattice Boltzmann simulations*, Lecture Notes in Computer Science 2657, 977-986, 2003.
[5.59] Y. Peng, *Thermal lattice Boltzmann two-phase flow model for fluid dynamics*, Dissertation, 2005.
[5.60] Y. Peng and Laura Schaefer. *A thermal lattice Boltzmann two-phase flow model and its application to heat transfer problems-part 1. theoretical foundation*, Journal of Fluids Engineering 128, 142-150, 2006.
[5.61] Y. Peng and Laura Schaefer. *A thermal lattice Boltzmann two-phase flow model and its application to heat transfer problems-part 2. integration and validation*, Journal of Fluids Engineering 128, 151-156, 2006.
[5.62] Y. Peng, C. Shu, and Y.T. Chew, *A 3d incompressible thermal lattice Boltzmann model and its application to simulate natural convection in a cubic cavity*, Journal of Computational Physics 193, 260-274, 2003.

[5.63] E. A. Semma, M. El Ganaoui, and R. Bennacer, *Lattice Boltzmann method for melting/solidification problems*, C. R. Mecanique 335, 295-303, 2007.
[5.64] C. Sun, Z. Xu, B. Wang, and M. Shen, *Lattice Boltzmann models for heat transfer*, Communications in Nonlinear Science & Numerical Simulation 2, No.4, 212-216, 1997.
[5.65] J. Wang, M. Wang, and Li Z., *A lattice Boltzmann algorithm for fluid-solid conjugate heat transfer*, International Journal of Thermal Sciences 46, 228-234, 2007.
[5.66] Y. Xuan, K. Yu, and Q. Li, *Investigation on flow and heat transfer of nanofluids by the thermal lattice Boltzmann model*, Progress in Computational Fluid Dynamics 5, 13-19, 2005.
[5.67] L. Zhou, Y. Xuan, and Q. Li, *Multiscale simulation of flow and heat transfer of nanofluid with lattice Boltzmann method*, International Journal of Multiphase Flow 36, 364-374, 2010.
[5.68] D. Gobin, Tomasz A. Kowalewski and Dominique Gobin, *Phase Change with Convection: Modelling and Validation*, CISM International Centre for Mechanical Sciences (Book 449), Springer, 2004.
[5.69] W. Humphrey, A. Dalke, and K. Schulten. *VMD – Visual Molecular Dynamics*, J. Molec. Graphics, vol. a4, pp. 33-38, 1996.
[5.70] VMD web page: http://www.ks.uiuc.edu/Research/vmd/
[5.71] L. Martínez, R. Andrade, E. G. Birgin, J. M. Martínez. *Packmol: A package for building initial configurations for molecular dynamics simulations*. Journal of Computational Chemistry, 30(13):2157-2164, 2009.
[5.72] J. M. Martínez and L. Martínez. *Packing optimization for automated generation of complex system's initial configurations for molecular dynamics and docking.* Journal of Computational Chemistry, 24(7):819-825, 2003.
[5.73] Packmol web page: http://www.ime.unicamp.br/~martinez/packmol/
[5.74] Paraview web page: http://www.paraview.org/

6. Nanoparticle-Enhanced Lubricating Tribology
(Dr. Robert L. Jackson, Mechanical Engineering, Auburn University)

6.1 Abstract

This work investigates the tribological effect of nanoparticle additives on lubrication through experimental and analytical investigations on colloidal lubricants. The focus of this work is to investigate and elucidate the enhancement mechanisms of nanoparticles. Different types of nanoparticles in various lubrication regimes have been used to conduct the studies.

Firstly, the tribological properties of a custom-prepared and stable nano-lubricant that consists of CuO nanoparticles (9nm average diameter) suspended in mineral base oil using sodium oleate (SOA) as a surfactant are investigated. Nano-lubricants with concentrations of 0.5, 1.0 and 2.0%wt were investigated using a disk-on-disk friction and wear test in the boundary lubrication regime. It was observed that CuO/SOA nanoparticle additives reduce the friction between the lubricated surfaces in the absence of any other conventional additives. Also, the steady state temperature of the lubricant is lower in the presence of nanoparticles. Measurements show that the viscosity of the nano-lubricants increases as more nanoparticles are introduced in the lubricant. Wear analysis based on profilometry results suggest that the wear increases with the nanoparticle concentration up to a 1.0%wt and then decreases for a 2.0 %wt nano-lubricant. SEM/EDS results suggest that nanoparticles are present on the surfaces after the tests. Based on the results, different possible mechanisms for nanoparticles at the boundary lubrication were evaluated and the reduction in the real area of contact was suggested as the possible mechanism for reducing friction.

The next component of this work deals with modeling nanoparticles in contact between surfaces. Although nanoparticle additives have been the topic of multiple studies recently, very little work has attempted to explicitly model the third body contact of nanoparticles. The second part of this work presents and uses a novel methodology to model nanoparticles in contact between rough surfaces. The model uses two sub-models to handle different scales of contact, namely the nano-sized particles and micron-sized roughness features. Silicon nanoparticles suspended in conventional lubricant are modeled in contact between steel rough surfaces. The effect of the particles on contact force and real area of contact has been modeled. The model makes predictions of the coefficient of friction and wear using fundamental models. The results suggest that particles would reduce the real area of contact and therefore decrease the friction force. Also, particles could induce abrasive wear by scratching the surfaces. The implications of the model are also discussed and the arguments and results have been linked to available experimental data. This work finds that particle size and distribution are playing a key role in tribology characteristics of the nano-lubricants.

The last component of the present work deals with the effect of nanoparticle in the thin film elasto-hydrodynamic lubrication regime. Careful friction tests for a nano-lubricant in the elasto-hydrodynamic lubrication regime show that the presence of nanoparticles reduces friction. By using surface analyses and molecular dynamics simulation, we

explored the effectiveness of different interactions in the system including the interactions between any pairs of nanoparticles/lubricant/surfaces. Based on the results, a novel friction reduction mechanism has been deduced, that is the nanoparticles can induce an obstructed flow in the thin film between lubricated surfaces.

6.1.1 List of Publications:

Peer Reviewed Journals:

1. Ghaednia, H., Jackson, R. L., On the Effect of Nanoparticles on the Real Area of Contact, Friction and Wear, *J. of Tribol., Trans. ASME,* , 135, 4, pp. 041603 (10 pages). DOI: 10.1115/1.4024297.
2. Ghaednia, H., Jackson, R. L., Khodadadi, J. M., Experimental Analysis of Stable CuO Nanoparticle-Enhanced Lubricants, 2013, *Journal of Experimental Nanoscience.* p. 1-18, DOI: 10.1080/17458080.2013.778424.
3. Jackson, R. L., Ghaednia, H., Yasser, A. E., Bhavnani, S. Knight, R., A Closed-Form Multiscale Thermal Contact Resistance Model, 2012, *Components, Packaging and Manufacturing Technology, IEEE Trans.,* 2, 7, 1158-1171.
4. Ghaednia, H., Hasan Babaei, H., Jackson, R. L., Bozack, M. J., Khodadadi, J. M., The effect of nanoparticles on thin film elasto-hydrodynamic lubrication, Submitted to the *Applied Physics Letters*.

Book Chapters:

Jackson, R. L., “Chapter 14: Lubrication,” in Handbook of Lubrication and Tribology, Volume II: Theory and Design, edited by Bruce, R.W., pp. 14.1-14.14 Boca Raton, FL, USA, CRC Press, 2012.

Jackson, R. L., "Contact Mechanics.” In *Tribology for Scientists and Engineers*, edited by Menezes, P.L.; Ingole, S.; Nosonovsky, M.; Kailas, S.V.; Lovell, M.R., p. 946: Springer US, 2013.

Conferences:

1. Ghaednia, H., Jackson, R. L., Khodadadi, J., Experimental Analysis of Stable CuO Nanoparticle-Enhanced Lubricants *2011 STLE Annual Meeting*, Atlanta, GA, May 15-19, 2011.
2. Ghaednia, H., Jackson, R. L., A Contact Model for Rough Surfaces Separated by Nano Particle Laden Lubricants, 2011 *ASME/STLE International Joint Tribology Conference*, Los Angeles, CA, October 24-26, 2011.
3. Ghaednia, H., Jackson, R. L., An Analysis of the Adhesion of Contacting Three-dimensional Wavy or Sinusoidal Surfaces, 2011 *ASME/STLE International Joint Tribology Conference*, Los Angeles, CA, October 24-26, 2011.
4. Jackson, R. L., Ghaednia, H., Bhavnani, S., Knight, R., An Experimental Evaluation of a Closed-Form Multiscale Thermal Contact Resistance Model, 2011 *ASME/STLE International Joint Tribology Conference*, Los Angeles, CA, October 24-26, 2011.

5. Ghaednia, H., Jackson, R. L., On the Effect of Nano-particles on Real Area of Contact, *2012 STLE Annual Meeting*, St. Louis, MO, May 6-10, 2012.
6. Ghaednia, H., Rostami, A., Jackson, R. L., The Influence of Thermal Expansion and Plastic Deformation on a Thermo-Electro Mechanical Spherical Asperity Contact, *The 58th IEEE Holm Conference on Electrical Contacts*, Portland, Oregon, USA, Sept. 23-26, 2012.
7. Ghaednia, H., Jackson, R. L., Experimental Analysis of Silver Nanoparticle-Enhanced Polyethylene Glycol Lubricants, *STLE 68th Annual Meeting*, Detroit, MI, May 5-9, 2013.
8. Ghaednia, H., Jackson, R. L., On Nanoparticles' Tribology: Reducing the Real Area of Contact to Reduce Friction and Control Wear, Southern Aerosol Technical Association (SATA) Fall Meeting, Destin, FL, Sept. 26-29, 2013 (invited seminar).

6.2 Introduction and literature review

The unique behavior of materials at the nano scale has drawn great attention as a possible solution to conventional engineering challenges. The first step toward this goal is through the fabrication and close observation of nano structures. Nano structures such as nano-whiskers, nanowires, pillars and nanoparticles have been the topic of intense research in recent years [1-11]. Historically, nano- and micron-sized additives for lubricants have been used without being explicitly explored as "nano-additives", sometimes referred to as "solid lubricant additives". Chemists have long been very active in investigating nanoparticle suspensions known as "colloidal fluids" but recently these colloidal fluids using a lubricant as the main solvent have been labeled nano-lubricants. A nano-lubricant usually consists of three components; the main solvent which is a conventional lubricant, the nanoparticles that are often made of metallic or anti-friction materials and the surfactant that occupies the interface area between the fluid and the particles [12]. Previous literature suggests that the nanoparticles as additives can induce marked effects on the lubricant properties [13-26]. Different combinations of nanoparticles and lubricants can result in numerous nano-lubricants. The focus of first part of this work is on the tribological properties of colloidal nano-lubricants of copper oxide (CuO) in organic solvents such as mineral oils.

A few researchers have investigated the effect of CuO on common lubricating oils and have shown promising results. Sajith et al. [16] found that although the CuO and Al_2O_3 particles had only a slight effect on the fluid viscosity, the flash temperature of the fluid decreased significantly, thus improving the fluid stability without affecting its lubricating capabilities. Wu et al. [25] found that the addition of CuO nanoparticles reduced friction and improved the wear resistance. Hernandez Battez et al. [22, 24] tested different concentrations of CuO nanoparticles suspended inside PAO6 using a block on a ring tribometer. They found that 2 %wt CuO nano-lubricant lowers the wear rate significantly but the modification of the friction coefficient is minor. They suggest that tribo-sintering of nanoparticles results in the formation of a tribofilm and consequently enhanced tribological properties. Lee et al. [23] evaluated fullerene and CuO nano-lubricants to enhance the overall performance of refrigerator compressors.

However, in some works, the nanoparticles were mixed into the oil along with a dispersing fluid such as glycol. The dispersing fluid was not added to the base oil used as the control and so could also be causing the change in the lubricant performance. In addition, usually commercial oils are used as base solvents for particles. High concentrations of different additives in commercial oils may result in secondary and uncontrolled chemical reactions of particles. Reaction between boundary lubricant additive and metallic nanoparticles could be a possible secondary reaction. Therefore, there is an uncertainty about the original cause of the changes in the oil properties. In addition some of the papers lack proper wear or viscosity measurements and therefore it is hard to draw a meaningful conclusion out of the data. For instance, a nano-lubricant is useless if the particles reduce friction and increase wear that in turn reduces the life of the surface. Lack of information on the stability of the nano-lubricants is another issue with some of the previous works in the literature. It is common practice to disperse dry particles in the lubricants using a sonicator and perform experiments quickly. Some of these friction experiments take hours to finish but there is uncertainty if the suspension is stable through the experiments. Also, unstable nano-lubricants would result in aggregations and clustering. Large clusters of nanoparticles could not enter through the gaps to the contact zone and be effective. In addition, instability would cause the properties and concentration of the nano-lubricant to change and decay with time. Therefore one the goals of this work is to study the effect of the nanoparticles on lubrication explicitly through investigation of the stable suspension of nanoparticles in base oils in the absence of other additives.

Although it has been well known for many years that the mechanics at the atomic scale or just above is very important for a complete understanding of friction and wear, in the past several decades advances in technology have allowed the actual control and fabrication of nano-scale tribological features. The incorporation of small size manipulation and measurement equipment such as atomic force microscope (AFM) and electron microscopy have resulted in the production of a great deal of data on various fundamental tribological phenomena [27]. Also, numerical chemistry methods such as molecular dynamics has shed light on many unobservable tribological aspects by providing in depth mechanical and chemical analysis tools for researchers as shown by the pioneering work of the late eighties and nineties [28-32]. The system of interest in this work, nanoparticles, have been the topic of many careful studies [2-4, 7, 8, 10, 11, 33-35] using methods such as single nanoparticle indentation and molecular dynamics modeling. Other researched topics include single nanoparticle fracture, scale dependent strength of free standing nano structures, surfactant coated nanoparticles and interfacial chemistry of nanoparticle. As a result, the literature on the nanoparticle tribology is rich and ever growing. Nonetheless, a review of nanoparticle lubrication literature [13-17, 19, 20, 22, 24, 36-42] shows many contradicting results and conclusions. It is claimed that the nanoparticles may exhibit mechanisms in the mixed and boundary lubrication regimes to affect performance, such as: (1) the particles affect oil viscosity [25], (2) the particles affect the thermal properties and thermal stability [26, 43], (3) the particles could roll between the surfaces and act as “nano ball bearings” [11], (4) the particles could mend worn surfaces by adhering to them and also forming a protective tribo-film [25, 44], (5) the particles can also induce abrasive wear which will result in a higher wear rate [22]. However, defining the active and dominant

mechanisms causing friction reduction and wear of nano-lubricated surfaces are also the subject of some debates.

There are two aspects of nano-lubricant systems which makes it difficult to produce conclusive investigations. First is the multiscale nature of the system, meaning that nanoparticles, micron size roughness features and macro size effects coexist and play roles simultaneously. Secondly, due to their nature, nanoparticles in lubricants are governed by a wide variety of physical mechanisms, such as adhesion, Brownian motion, scale dependent strength, interfacial and chemical interactions, cluster formation, hydrodynamics, abrasive wear and erosion. Therefore, the second goal of this work is to study the enhancement mechanism of the nanoparticle through analytical and experimental analyses. Analytical investigation of nanoparticles includes developing a third body contact problem for nano-lubricants between rough surfaces. Although a great deal of work exists on modeling rough surface contact, including very small scales [45-52] and individual nanoscale asperity contact, very little work has attempted to explicitly include nanoparticles in a rough surface contact model. Actually, the most relevant advances have been made in the area of modeling third bodies in contact such as powder and particulate lubrication [53-55] and third body abrasive wear analysis [56, 57]. The contact model proposed in this work includes different scales of contact in the system and helps to solve the multi-scale complexity of the nano-lubricants. The experimental methods consist of the preparation and characterization of nano-lubricants, performing various friction and wear tests in different lubrication regimes, viscometry and rheometry on the lubricants, and post-test evaluation using profilometry, SEM, EDX, AES and XPS.

The next section elaborates the results and progress of the project to date in three sub-sections. This section discusses the approaches, methodologies and techniques employed to effectively investigate the problem as well as the results and discussions on the topics.

Studies and Results

6.2.1 Experimental investigations of Stable CuO/SOA nanoparticle lubricants

In this work, base lubricants with no additives have been used as the base solvents to isolate the results and investigate the effect of particles explicitly. Also the effect of different concentrations of nano-lubricants on the friction and wear properties of lubricants is investigated. The nanoparticles used are unique CuO nano-particles developed recently by Clary and Mills [58]. The nano-lubricant used in this work is exceptionally stable which makes it a viable candidate for analysis and possibly for industrial applications. To perform the experiments, a disk-on-disk test setup is used that measures the friction coefficient using torque and load sensors, in addition to the temperature of the lubricant. The surface samples are submerged in a small reservoir of the nano-lubricant. The experiments will be discussed in more detail later. The wear and surface analysis is evaluated by surface profilometery, electron microscopy and electron dispersive X-ray spectroscopy.

6.2.2 Nano-lubricant description

CuO nanoparticles used in this paper are developed by Clary and Mills [58] which are especially designed for dispersion in hydrocarbons. In their method, sodium oleate (SOA) is used as a surfactant to help the dispersion of particles in non-polar solutions. They monitored the CuO concentration in non-polar solvents spectroscopically at room temperature and proved stability over a period of eight months. They also conducted stability studies for repeated phased change cycles and reported no significant precipitation. Particles were observed to be quasi-spherical in shape with an average diameter of 9 nm and 90% of the population existing within the range of 5-15 nm (Figure 6.1). It is also proven that the addition of these particles to alkanes modifies the thermal properties of the solution in terms of the specific heat and thermal conductivity [43]. The base oil used in this paper is a 50% volumetric blend of “mineral 600HC heavy base oil” and “mineral 100HC light base oil” (10%wt dodecane is also added to the final solution). The base oils used are group II base oils with more than 99% of saturates.

In order to make the nano-lubricant, first CuO particles are solved in dodecane ($C_{12}H_{26}$) at a 10% weight fraction (dodecane acts as a dispersing agent that helps create a more stable and higher concentration of nano-lubricants). The solution is first stirred and heated for 4 hours and then diluted to the desired weight fraction by blending with the base oil. A solution of the same concentration of dodecane in the blended base oil without nanoparticles is prepared as a control sample.

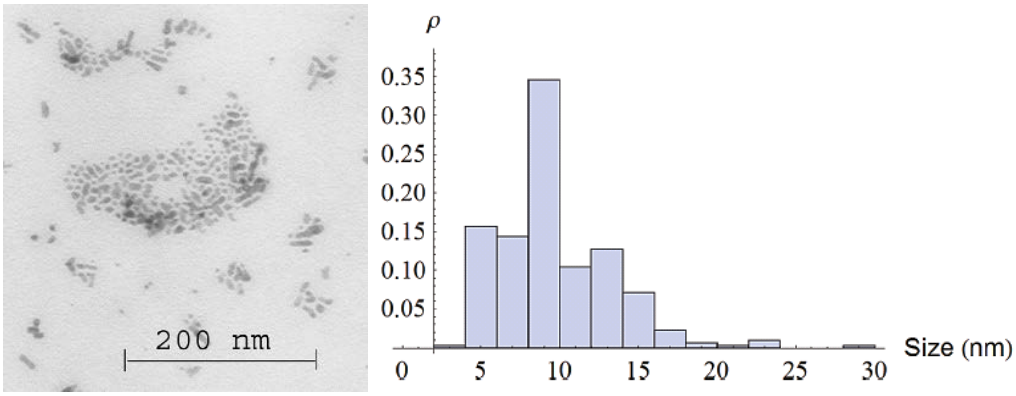

(a) (b)

Figure 6.5: (a) TEM image of CuO nanoparticles, (b) particle size distribution [58].

6.2.3 Experimental setup and results

Figure 6.2 shows the schematic of disk-on-disk test setup used in this work (also known as a thrust washer test). The drive shaft rotates the disks on one another and induces the desired sliding motion. Surface samples are submerged in the nano-lubricant inside a reservoir, see Figure 6.2. The frictional torque between the surfaces is measured using a torque sensor. The normal load is monitored using a load cell supporting the reservoir. The friction coefficient is calculated from the torque using the method introduced by Jackson and Green [59]. A thermocouple is also deployed to record the temperature of the lubricant. A data acquisition system and user interface software records and controls the experiments. This test setup is designed for conducting

boundary lubrication experiments with a small volume of lubricant. Surface samples are zinc plated steel disks with an inner and outer diameter of 9.5 mm and 22.2 mm, respectively. The average RMS roughness of the samples are 4 micrometers.

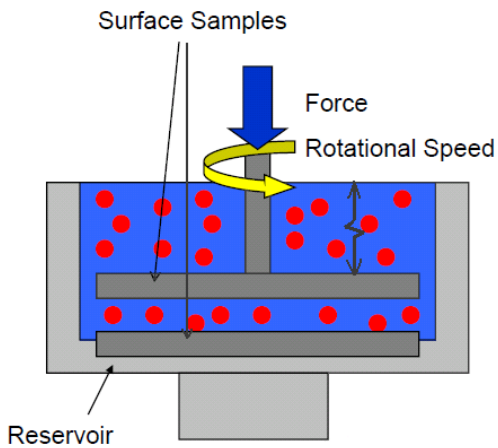

Figure 6.6: Schematic view of disk on disk test setup.

Friction enhancement of the nano-lubricants is investigated through direct friction coefficient analysis and viscosity measurements. Figure 6.3(a) presents the results of the tests for the control sample which is a 10%wt solution of dodecane in the blended base oil and also for several other concentrations of nano-lubricants. Each test is repeated three times. Surfaces went through a running in process and then data for 3 minutes at the rotational speed of 570 revolutions per minute (rpm) is recorded. Results indicate that the nanoparticles decrease the coefficient of friction. The effect of nanoparticles is more influential at higher loads and nanoparticle concentrations. The system works in the boundary lubrication regime which is the case where the lubricant film thickness between surfaces is smaller than the surface RMS roughness. In this lubrication regime, there is substantial contact between surfaces but also some parts of the surfaces are separated by the lubricant film. Therefore, an increase in the normal load would squeeze more lubricant out of the contact region which reduces the lubricant film thickness between surfaces. This would escalate the probability of contact between surfaces and hence, increases the probability of particle engagement in the contact (i.e. the particles are more influential further in the boundary lubrication regime).

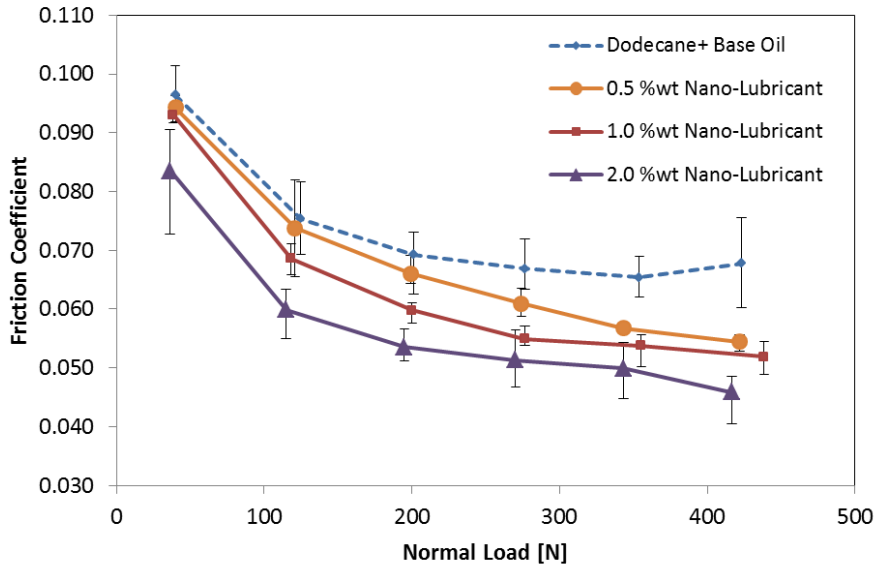

(a)

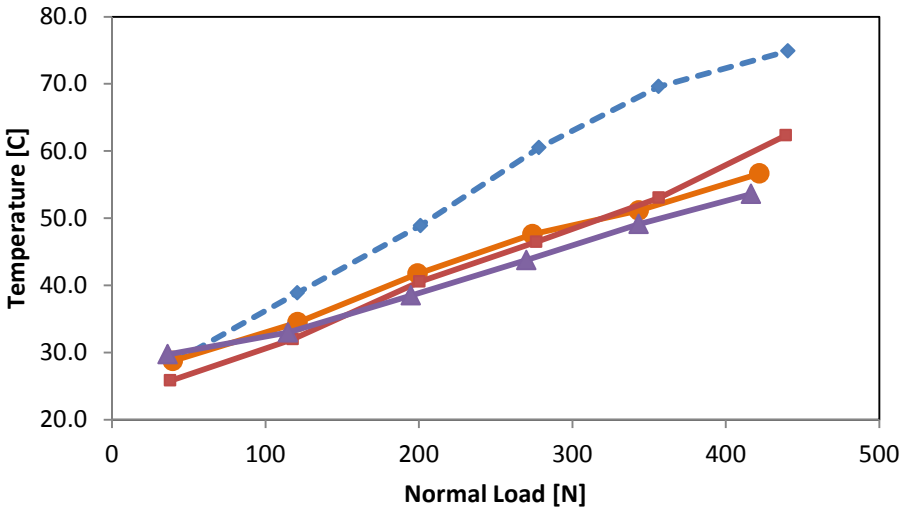

(b)

Figure 6.7: Results showing the effect of nanoparticle concentration on friction and temperature.

Figure 6.3(b) shows the steady state temperature of the lubricant at the end of the experiment. In the case of nano-lubricants, a lower friction coefficient results in less heat production and consequently the final temperature is less. As mentioned, the CuO nanoparticles also have proven to affect the thermal properties of the solution (such as conduction) which could result in better heat dissipation. Therefore the combination of these effects appears to result in a significant reduction in the temperature in comparison to the lubricant without nano particles. One of the known effects nanoparticles have on fluids is to change the viscosity. The fluid flow pattern is affected in the presence of the solid nanoparticles suspended in the liquid that results in an increase in dissipated energy and an increase in the viscosity of the nano fluids Figure 4

shows the results of viscometry for different concentrations of CuO nano-lubricants versus temperature using a Brookfield® DV-II +Pro rotational viscometer capable of measuring small volumes at controlled temperatures. The temperature range was selected to match the steady state temperatures reported in Fig. 6.3(b). Averages of five readings were taken for each temperature. The average error for the results shown in Fig. 6.4 is 2.30%. At a given temperature, an increase in the viscosity in response to raising the particle concentration is observed. The relative change in viscosity is fairly constant at different temperatures. For example, for all temperatures between 20°C and 70°C, the average viscosity increase for a 2.0%wt increase of nanoparticles is 20.4% with a standard deviation of 0.02%. The present viscosity results (see Fig 4(b)) confirm some of the experimental data from the literature [60] which report viscosities for nano-fluids that are greater than that predicted by the Einstein model [61].

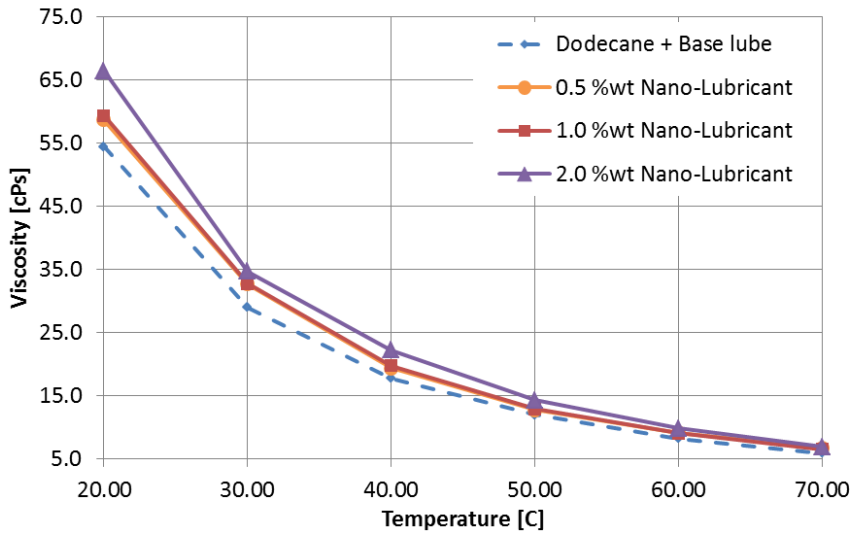

(a)

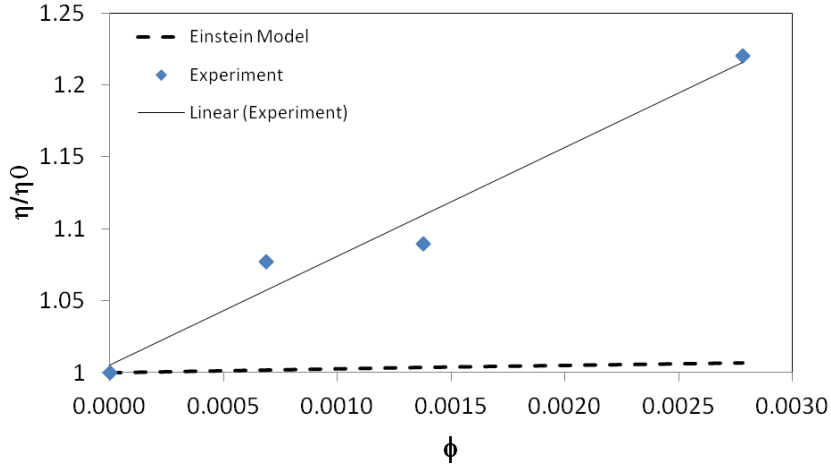

(b)

Figure 6.8: (a) Viscosity versus temperature for different concentrations of nano-lubricants (b) viscosity versus volume fraction for T=20°C.

The data from the friction and viscosity measurements is collapsed into the widely used Stribeck curve [62] in an attempt to develop generalized observations (see Fig. 6.5). The Stribeck curve is able to account for the effect of changes in viscosity due to temperature rise and particle concentration, along with pressure in one combined plot. The change of viscosity versus the steady state temperature is considered in Fig. 6.5 using the data shown in Figs. 6.3(b) and 6.4(a). In the experiments of this paper, the surfaces in the contact undergo severe wear at the higher loads so clearly the system is operating in the boundary lubrication regime (more data is available in the surface analysis section).

In Fig. 6.5, the friction coefficient decreases as more nanoparticles are introduced in the lubricant and as contact pressure increases. As contact pressure increases, more asperities in the contact region yield and undergo plastic deformation. Lower resistance to the applied tangential load is exhibited, causing the overall friction coefficient to drop in accordance with existing friction theories [63-71]. Figure 6.5 shows that CuO nanoparticle additives decrease friction coefficient deep into the boundary lubrication regime (on the far left of the curve).

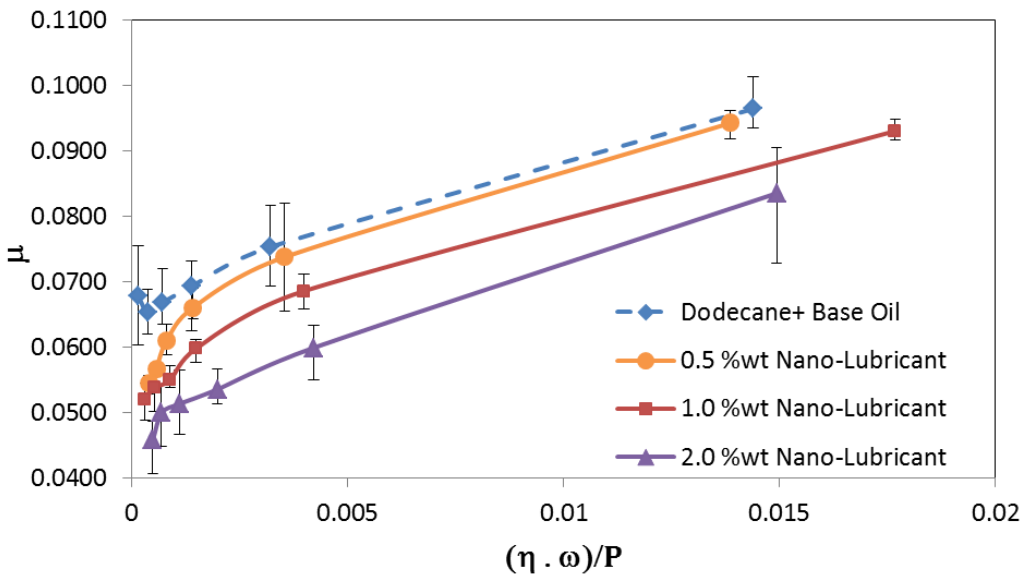

Figure 6.9: Stribeck curve for different weight fractions of nano additives.

After testing, the surfaces are analyzed using a Veeco Dektak 150 stylus profilometer and three dimensional profiles of the surfaces are obtained (see Figs. 6.8-6.10(a)). The 3D surface profiles show clear evidence of surface contact and wear grooves which prove that the system is working in the boundary lubrication regime.

One of the disks used in the friction tests is smaller, resulting in a smaller worn region than the larger washer surface area. Consequently, the unworn surfaces provide a reference plane (baseline) with which to use in a volumetric wear analysis. Figure 6.6 shows a sample cross section profile of a surface after the test. Based on the original surface baseline and the grooves geometry one can integrate the area below the

baseline and find the wear volume. Figure 6.7 presents the predicted volumetric wear rates based on the surface profilometery results discussed. *V* and *s* in this figure represent the wear volume and the sliding distance. Results show an increase in wear up to the 1.0%wt concentration of nanoparticles and a decrease as particle concentration increased up to 2.0%wt (although the inflection point is not defined due to the limited data points). Since wear is larger at the 1.0% weight fraction of nanoparticles and minimum at 2.0%, the results suggest that the addition of nano-lubricants can in some cases increase wear, while in other cases reduce it. Due to the scaling effect on material strength, nanoparticles exhibit higher hardness than bulk materials [1-5, 7, 10] which potentially makes them a source of abrasive wear. The same trend for wear of different nanoparticles has been reported by Hernandez Battez et al. [22]

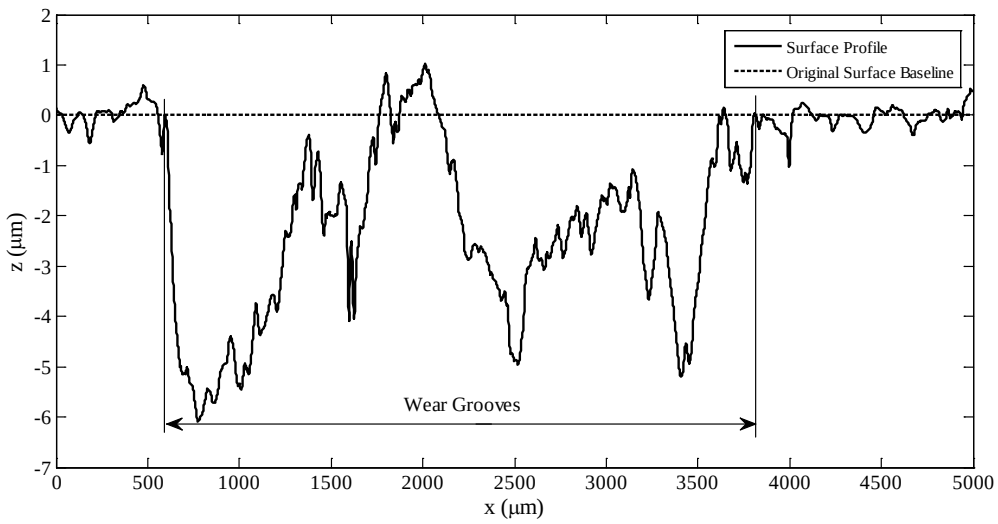

Figure 6.10: Wear analysis schematics.

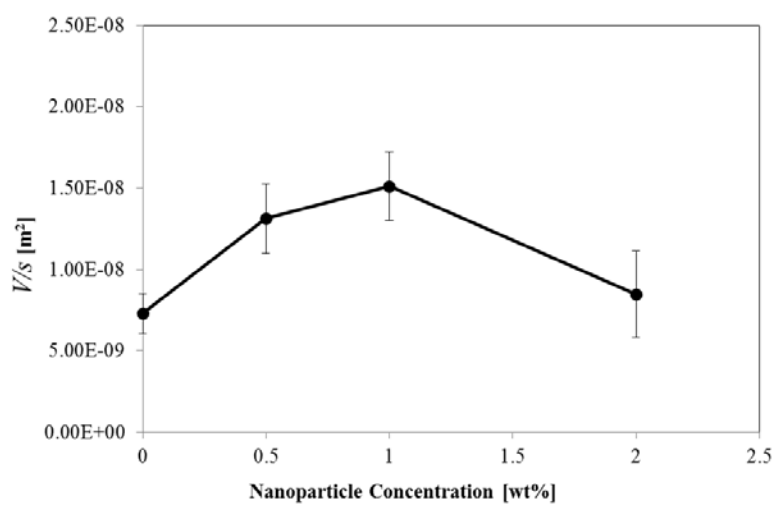

Figure 6.11: Wear per sliding distance as a function of the nanoparticles concentration.

Scanning electron microscopy (SEM) and electron dispersive X-ray spectroscopy (EDS) is also used to investigate the material composition of the surfaces before and after tests. All surfaces were cleaned with acetone before SEM/EDS tests.

Figures 6.8-6.12 present the SEM/EDS microscopy results. SEM/EDS results for surfaces before testing (Fig. 6.8) and for surfaces tested with a base oil only, i.e. no particles, (Fig. 6.9) are reported as control samples. Note that in the second case the wear is severe and results in the coating being worn through. Cases where the coating is not worn away can be compared to the new surfaces, while cases of the severe wear through the coating should be more compatible to the second case. Figure 6.8, presents the SEM image of test surfaces before performing any test and its material composition. As one expects, the majority of the unworn test surfaces are composed of zinc. Whereas, SEM/EDS results show that the majority of the samples worn under a pure base oil are composed of iron inside the wear grooves (Fig. 6.9). It is also evident in Figs. 6.8 and 6.9 that there is no trace of the element copper in or beneath the coating of the surface samples used in this paper, prior to CuO particles being used. Figure 6.10 shows the SEM/EDS analysis for a sample surface tested with a 0.5%wt CuO nano-lubricant. The x-ray analysis indicates that traces of the element copper exists on the surfaces after being exposed to the nano-lubricant during the test. The high concentration of zinc on the surface suggests that the coating at the SEM/EDS analysis is still largely intact on the surface. This is also made more apparent by comparing to the x-ray analysis of the control sample (Fig. 6.8).

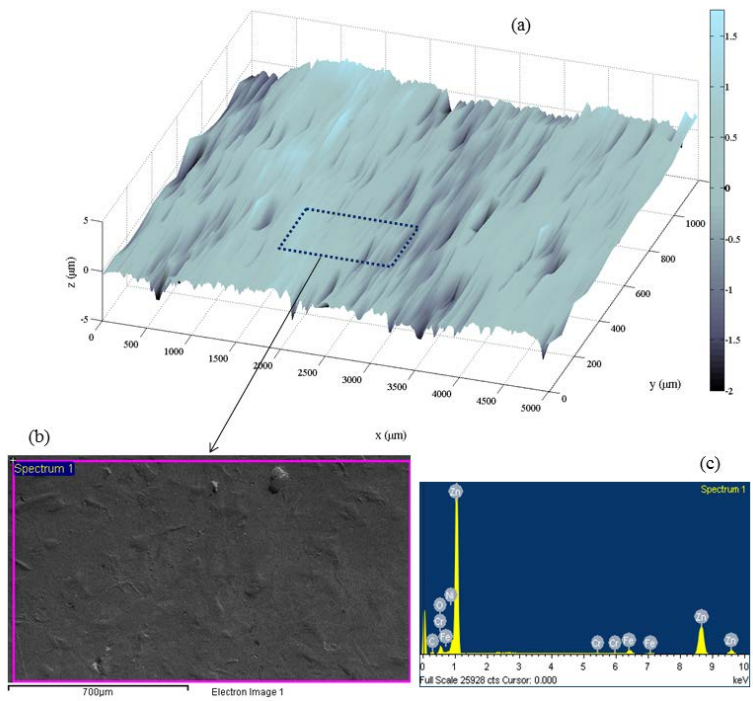

Figure 6.12: The SEM image of the test surfaces as obtained and its material composition using the EDS.

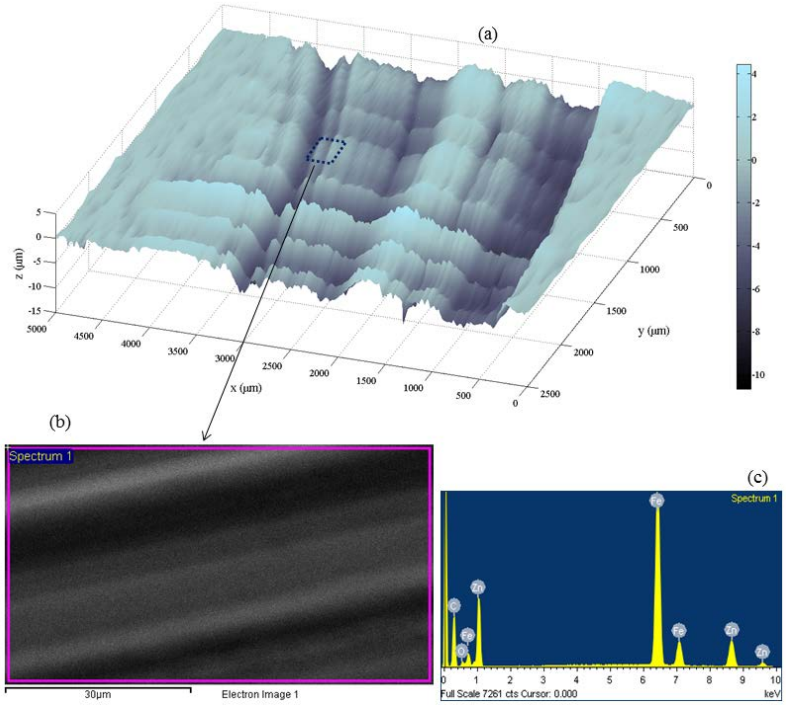

Figure 6.13: The SEM image inside the wear groove for lubricant with no nanoparticles additive and its material composition using the EDS.

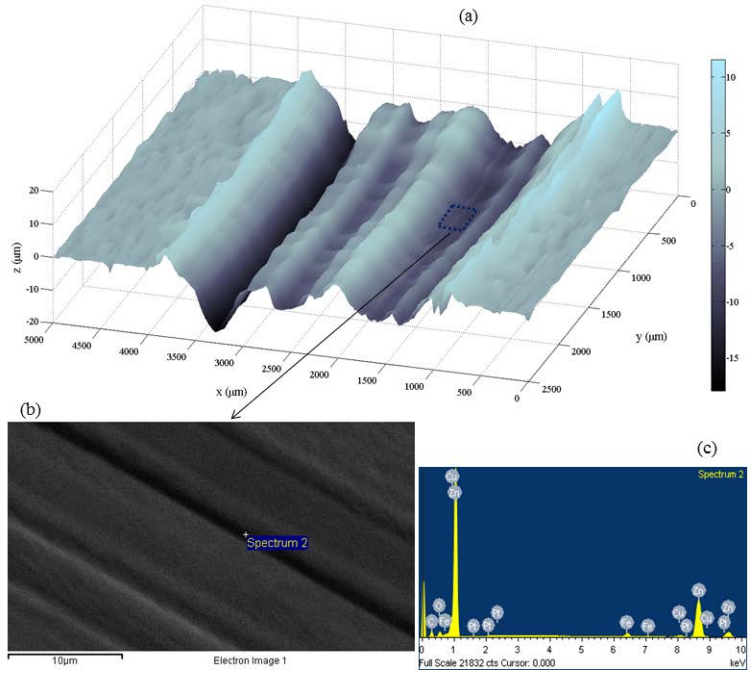

Figure 6.14: The SEM image for the surfaces tested with 0.5%wt CuO nano-lubricant and its material composition using the EDS.

Figures 6.11 and 6.12 present the SEM/EDS result for surfaces tested with 1.0% and 2.0%wt nano-lubricant, respectively. In Fig. 6.11(c), the high traces of iron suggests that the zinc plating has worn through, but the concentrations of copper suggest that the CuO particles could also be deposited on the inside of the wear grooves. This is in contrast to the surfaces worn while submerged in a base lubricant with no CuO particles because they have no signs of copper (see Fig. 6.9). Figure 6.10(d) shows the copper element mapping of the same surface and indicates a well dispersed distribution of nanoparticles adhering to the surface in and outside of the wear grooves. The same arguments stand for Fig. 6.12 and the copper element trace appears to also be randomly distributed. The average weight fraction of copper detected on the surfaces exposed to the nano-lubricant is 1.51%.

The sample surfaces studied in this work are zinc-coated steel disks therefore, a comparative study of the surface composition yields more insight on the particle-surface interaction. That is why the analysis of the original surface (Fig.6.8 (c)) shows that the majority of the surface is made out of zinc with some minor trace of the steel beneath the coating is detected (Fe, C, Cr). Fig. 6.9(c) shows the composition of a surface tested with the base oil. Here higher traces of steel and less traces of zinc are detected which indicates that the coating is partially worn. Fig. 6.10(c) shows the composition of a surface tested with the 0.5 %wt CuO nano-lubricant. High traces of zinc and low traces of steel (Fe, C, Pt) beneath the coating suggest that this is a relatively shallow groove. Fig. 6.11(c) shows the composition of a surface tested with the 1.0 %wt CuO nano-lubricant. High traces of steel (Fe, C) and low traces of zinc suggest that this is a relatively deep groove where the coating is almost worn away. Fig. 6.12(c) shows the composition of a surface tested with the 2.0 %wt CuO nano-lubricant. Mild traces of zinc and steel (Fe, C) suggest that this is a medium groove. Therefore the overall conclusion of Figs 6.10, 6.11, 6.12 is that particles are adhered to the surfaces in all cases regardless of the depth of the grooves. This suggests that the adherence of the particles does not depend on the high pressures within the asperity contacts as is theorized to be the case with many lubricant additives. The minute trace of platinum (Pt) in Fig. 6.10(c) and chromium (Cr) in Fig. 6.8(c) is coming from the additives in the alloy steel and concentrations are marginally detectable in the accuracy of the machine and that is why these elements are not detected in the rest of results.

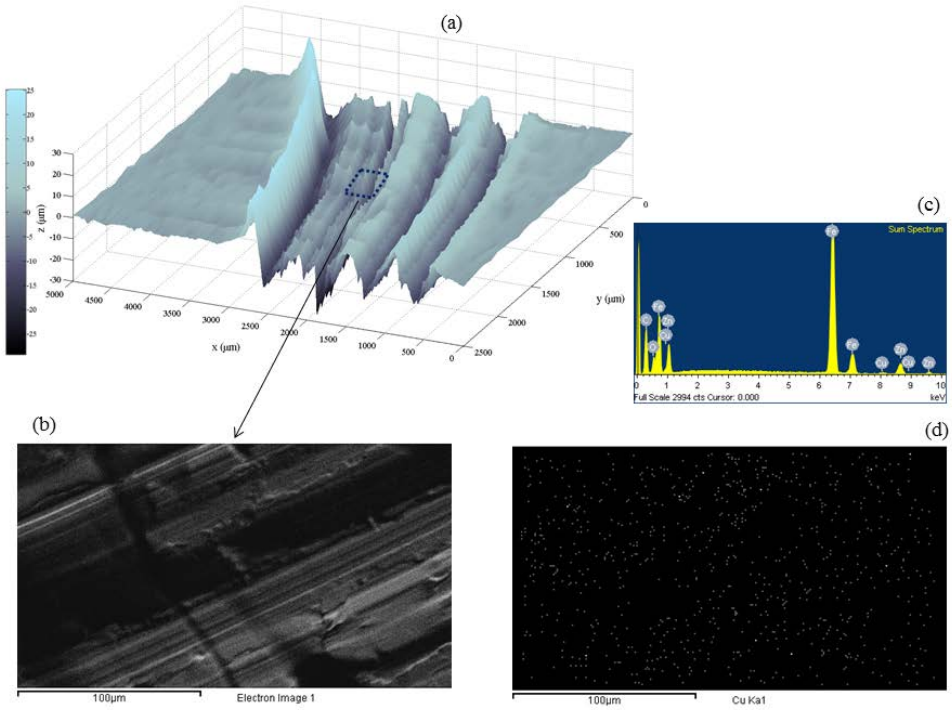

Figure 6.15: The SEM image for the surfaces tested with 1.0%wt CuO nano-lubricant and its material composition using the EDS.

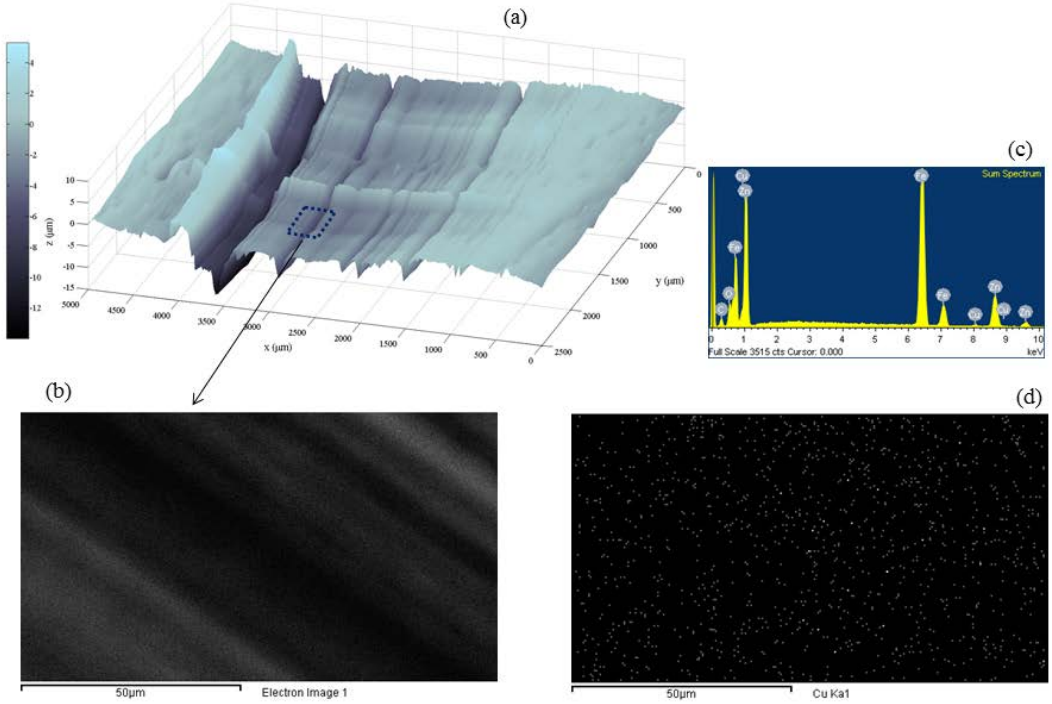

Figure 6.16: The SEM image for the surfaces tested with 2.0%wt CuO nano-lubricant and its material composition using the EDS.

6.2.4 Discussion

Several enhancing and modification mechanisms have been proposed for nanoparticle lubricants in the boundary lubrication regime in the literature, such as: viscosity alteration, thermal stability enhancement, mending worn surfaces and the rolling effect of nanoparticles. Based on the results and discussions presented in this paper, viscosity and thermal properties are affected by the CuO nanoparticles. However, the effect of these two mechanisms is minimal in the boundary lubrication regime where tribology is dominated by the contact of asperities. Particle deposition is evident and the element of copper is present at all the sample surfaces tested with the nano-lubricant. However, the dispersion of particles on the surface is random and is not sufficient to replace a significant portion of the worn material. Therefore, the mending mechanism is not evident in our tests. In contrast, the deposition of nanoparticles happens randomly in the contact zone and the average concentration of CuO deposited on the surface is on the same order as the nanoparticle concentration in the lubricant. The other mechanism, nanoparticles rolling and acting as nano ball bearings implies that the use of a nano-lubricant should result in minimal wear which is not the case in our studies. It is proven that nanoparticles can roll in between surfaces in contact [11], however, based on the extensive wear in our samples it is probably not a dominant mechanism for the current type of particles. Particles of the stable nano-lubricants (such as the one studied in this paper) are able to exist as individual particles and don't form clusters in the suspension. In this paper particles are well coated with the surfactant and several filtration techniques [58] were used to ensure the quality of surfactant in the nano-lubricant. One can use the Kinetic energy theory and Brownian motion to characterize the motion of suspended particles. Calculations show that nanoparticles studied in this paper have an average Brownian velocity of 0.4 m/s which is significant and suggests that particles are dispersed throughout the contact region and are not likely to settle physically in the local valleys. Moreover, Figs 11(d) and 12(d) show a random distribution of particles throughout the contact zone on peaks and in the valleys. Therefore, it is evident that particles are dispersed randomly throughout the contact zone and are able to infiltrate the contact regions. This would disregard the hypothesis that the majority of particles fill up valleys and are not engaged in contact.

Alternatively, the reduction of friction monotonically continues as more nanoparticles are dispersed in the lubricant. Also, wear seems to be a function of nanoparticle concentration. Based on all the discussions and results, we would like to suggest the nanoparticles actually reduce the real area of contact and therefore reduce friction in the boundary lubrication. This theory implies that, particles engaged in contact would keep surfaces apart around the particles which results in the reduction of real area of contact, see Fig. 6.13. Decrease in the real area of contact translates to a reduction of the friction coefficient. As more concentrated nano-lubricants are used, more particles would engage in the contact which explains the monotonic reduction in the friction coefficient versus particle concentration in the tests. In addition these particles would bear high pressures and induce abrasive wear by plowing on the surface. The number of particles in the contact would increase as the nanoparticle concentration increases which is going to decrease both the average particle/surface contact pressure and the plowing abrasive wear. This point should be noted that this work emphasizes the stability of the studied nano-lubricants to disregard any aggregation effects such as

precipitation and clustering. In order to avoid these effects, the concentration of nano-lubricants is limited to 2.0%wt in this study. However, it is reported in the literature [38-40] that the nanoparticle effect on wear and friction would saturate at a certain concentration. The saturation concentration depends on the type and size of the particle, as well as the properties of the base oil.

The mechanism of reduction in the real area of contact needs further investigation and study to be fully proven. One helpful study could be the characterization of the size of nanoparticles prior and after the tests which can prove the abrasive nature of particle-surface contact. It should be added that various nanoparticles behave differently based on their mechanical behavior as governed by chemical and physical properties (As an example, the enhancing mechanism of fullerene-like WS2 (MoS2) nanoparticles is known to be exfoliation and coating the surface) and arguments raised in this chapter are currently limited to the CuO/SOA nanoparticles studied.

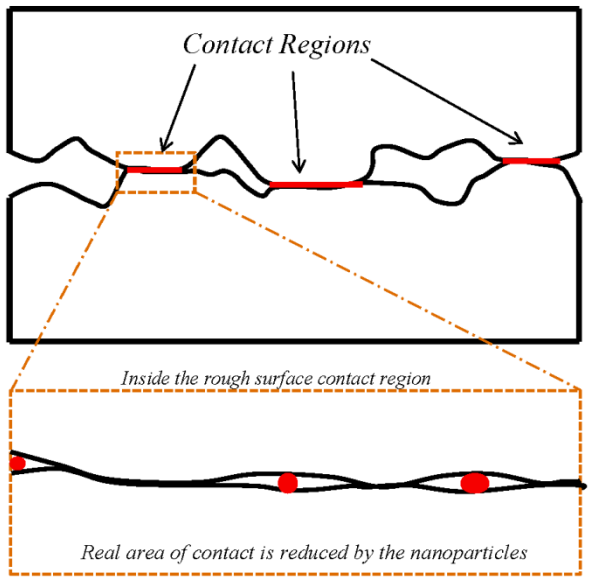

Figure 6.17: Illustration of the proposed mechanism, reduction of the real area of contact by the nanoparticles.

6.3 Analytical multi-scale contact model for nano-lubricants

There is no contact model for nanoparticle lubricants in contact between rough surfaces. The effect of nanoparticles on real area of contact and contact force can be investigated using an analytical model. The goal of this part of the current work is to develop such a contact model and relate the contact parameters to measurable parameters such as friction and wear. This model can also be used to further investigate the proposed reduction in the real area of contact mechanism.

The focus of this study is to investigate the mechanisms governing the wear and friction in the lubrication system of silicon nanoparticles suspended in a lubricant. Silicon nanoparticles are chosen because of the relative wealth of available knowledge compared to other particles. The methodology used in this work uses two sub-models to handle the different scales of contact (i.e. a rough surface contact model and a statistical particle contact model). The rough surface contact model considers the contact of roughness features and provides predictions of the average contact pressure and rough surface contact area. The statistical particle model is used to model particles inside the contact regions of the rough surfaces. This sub-model reports the area of contact of the actual nanoparticles, the void area around the particles, the forces acting on the particles, and the distribution of the deformation mechanisms of the particles [72]. The results from the model are presented and discussed throughout the paper.

The approach taken in this paper tries to identify, quantify and evaluate the most influential contact parameters affecting the system into a model that can illuminate the mechanisms behind the friction and wear behavior of nano-lubricants. This model is based on the extensive available data on the nanoparticles and nanotribology mentioned earlier. However, it is still early to claim that such a model would be quantitatively accurate and includes all the critical details. Rather, its objective is to understand the ‘big picture’ and relationships between the mechanics of particles and surfaces with friction and wear.

6.3.1 Methodology and assumptions

The system of interest in this paper is composed of rough surfaces separated by a stable nano-lubricant, such as those in [58], working in the boundary lubrication regime with no significant hydrodynamic lift (nominally flat surfaces). If surfaces were pushed into contact, the lubricant would squeeze out until asperities initiate contact resulting in contact regions between peaks or asperities. Once the surface separation is lower than the particle diameter particles are entrapped into contact within these contact spots. Particles in contact would separate surfaces locally, resulting in the formation of void areas in the vicinity of particles (see Fig. 6.14). The change in the real area of contact induced by the voids as well as the particles reaction force would alter the contact mechanics.

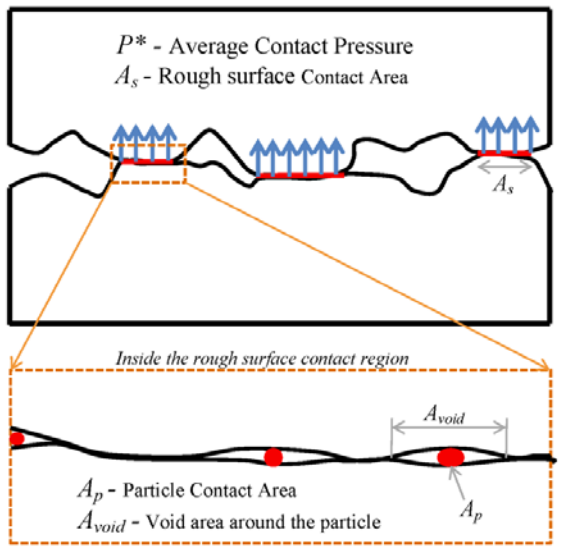

Figure 6.18: Illustration of stacked rough surface and statistical model.

Therefore, the system of interest in this paper includes two distinct ranges of scale which dominate the mechanics. Contact between rough surfaces which depend on the roughness features that are known to be in the scale of microns (for most engineering surfaces), and at smaller scales there are the nano-sized particles. The methodology in this work utilizes two well-known contact sub-models to handle these different scales. A multi-scale rough surface contact model solves the contact between surface asperities. The model reports the real area of contact between surfaces (A_s) and average contact pressure (P^*). A statistical (Greenwood Williamson type[73]) contact sub-model considers the effect of particles inside A_s and also includes the scale dependent properties of particles. This sub-model reports force (F_p), contact area (A_p) and the void area (A_{void}) created by particles. Before discussing more details on the afore-mentioned sub-models, certain assumptions need to be discussed. One assumption associated with the statistical particle sub-model is that the surfaces inside the contact region are effectively flat compared to the dimensions of the particles. The goal is to show that the surface dimples at the nano-scale can't accommodate a nanoparticle and are in fact much wider compared to the geometry of the spherical nanoparticles. In order to show this, a fast Fourier transform is used to decompose the surface into different scales. Each scale is defined by a sine wave which is also defined by an amplitude ($\square$) and wavelength ($\square$). Measurement on different engineering surfaces shows that the ratio of amplitude to wavelength ($B=$ $\square/\square$) is usually in the range of 10^{-4} to 10^{-3} regardless of the scale [74]. The dimples on the surface at the nano-scale can be regarded as the valleys of the sine waves at that scale which has a B value of about 10^{-4} to 10^{-3}. The aspect ratio of spherical particles is *one* which means that if a particle of size $\square$ is placed into the valley of a sine wave with an amplitude that is equal to the particle diameter ($\square$), the wave length of that sine wave is 10^4 to 10^3 times the value of $\square$ The difference in the aspect ratio of decomposed sine waves and nanoparticles at the same $\square/\square$ value suggests that surfaces around the particles are effectively flat comparing to the geometry of the particles.

The effect of fluid pressure also needs to be examined. The fluid pressure around a particle could alter the deformation and fracture of the nanoparticle. In order to evaluate the importance of this effect one can compare the fluid pressure to the failure strength of silicon nanoparticles considered in this paper. The maximum fluid pressure should be less than the surface contact pressure. Therefore, for the sake of evaluating the assumption and considering the worst case scenario, the maximum fluid pressure is deliberately overestimated using a dry contact model. In addition, the lubricant pressure would result in a rise in the hydrostatic stress of the particle which would not cause yielding, but may cause brittle failure. Calculation for three different actual surfaces assumed in this paper has been done according to the multi-scale contact model [74]. Results show that the maximum fluid pressure corresponds to the roughest surface (σ_q*=0.18* μm) and is *0.41 GPa* whereas the minimum failure strength of the nanoparticles considered in this paper is measured to be *10 GPa* [3, 33]. So the overall effect of pressure on the failure of particles is less than 5.0% and for the sake of simplicity in the current work the effect of fluid pressure on the particle deformation and failure is ignored. Nevertheless, the fluid pressure would resist the compression of the particles and delay the fracture of the particle. Therefore it would promote the effectiveness of the particles inside the contact region. However due to the presence of non-continuum and size effects in the particle/surface/lubricant system (especially under tangential motion) further investigation of the system is necessary.

6.3.2 Modeling

This section elaborately discusses and describes the details of the full model. Firstly the contact sub-models, namely the multi-scale rough surface contact model and statistical nanoparticle model, are discussed. Secondly, the algorithm to solve the overall solution is presented. Lastly, the fundamental models for friction and wear are presented.

6.3.2.1 Rough surface sub-model

A multi-scale rough surface model [74] was chosen to solve the contact between rough surfaces. The model uses fast Fourier transform to decompose the rough surface into stacked sine waves. Using superposition the model finds the average contact pressure required to overcome all the scales of roughness and predicts the real area of contact. Equations (6.1-6.4) present the model, where B is the ratio of σ/β for different scales of roughness, E' is the effective elastic modulus (contact modulus), S_y is the yield strength, ν is the Poisson ratio, P^* is the average contact pressure, and F_s and A_s are the contact force and real area of contact between surfaces. The model predicts the contact pressure based on the maximum value of B represented by B_{max} and distinguishes between the elastic and elastic-plastic regimes by the critical value of B_c (see Eq.(6.3)).

$$P^* = \sqrt{2}\pi E' B_{\max} \qquad \text{for } B_{max}<B_c \qquad (6.1)$$

$$P^* = \sqrt{2}\pi E' B_{\max}\left[\left(\frac{12\pi E' B_{\max}}{\sqrt{2}S_y e^{2\nu/3}} + 7\right)\Big/ 11\right]^{-3/5} \qquad \text{for } B_{max}>B_c \qquad (6.2)$$

$$B_c = \frac{\sqrt{2}}{3\pi}\frac{S_y}{E'}e^{2\nu/3} \tag{6.3}$$

$$A_s = \frac{F_s}{P^*} \tag{6.4}$$

The average rough surface contact radius (a_{rs}) can also be found using this model. According to Jackson et al [75] a_{rs} is found to be given by Eq. (5) where λ_{max} is the asperity wavelength corresponding to B_{max}.

$$a_{rs} = \frac{\lambda_{\max}}{\sqrt{2\pi}} \tag{6.5}$$

6.3.2.2 Statistical nanoparticle contact sub-model

Greenwood and Williamson (GW) [73] originally developed their model to consider rough surfaces in contact. However, a similar statistical approach can be re-engineered to model nanoparticles in contact between two flat surfaces. The height distribution and the asperity density considered in the original GW model can be reinterpreted as the particle size distribution and nanoparticle density between surfaces, respectively. The nanoparticle density (η) and density of the nano-lubricant (ρ_{sol}) need to be modeled based on practical and measurable parameters. The density of the nano-lubricant can be found from Eq. (6.6)

$$\begin{aligned} \rho_{sol} &= 100\left(\frac{wt\%}{\rho_{NP}} + \frac{100 - wt\%}{\rho_{\text{lub}}}\right)^{-1} \\ vol\% &= \left[0.01 - \frac{\rho_{NP}}{\rho_{\text{lub}}}\left(0.01 - wt\%^{-1}\right)\right]^{-1} \end{aligned} \tag{6.6}$$

where ρ_{sol} and *wt%* are the density and weight percent of nanoparticles in the final solutions. Subscripts "*NP*", "lub" and "sol" refer to nanoparticle, lubricant and solution. The relation between vol% and wt% is also given in Eq. (6.6) based on simplistic proportionalities.

Nanoparticle density (η) is considered to be the number of nanoparticles (N_{NP}) in contact per nominal area (A_n). Considering d as the separation of two surfaces, the total volume of nano-lubricant in between surfaces is $v_{sol} = A_n d$. The total nanoparticle volume is presented in Eq. (6.7) where v_{NP} is the total volume of nanoparticles in the lubricant.

$$v_{NP} = \frac{\rho_{sol}\ wt\%\ A_n d}{\rho_{NP}} \tag{6.7}$$

Assuming spherically shaped nanoparticles with the distribution of $\eta(D)$ which is a function of nanoparticle size (*D*), one can formulate v_{NP} as a function of the distribution.

$$v_{NP} = \frac{\pi}{6} N_{NP} \int_0^{\infty} \phi(D) \; D^3 dD \tag{6.8}$$

Using Eqs. (6.7) and (6.8) the number of nanoparticles per nominal area of contact could be found from,

$$\eta(d) = \frac{N_{NP}}{A_n} = \frac{\rho_{sol} \; wt\% \; d}{100 \rho_{NP} \left(\frac{\pi}{6} \int_0^{\infty} \phi(D) \; D^3 dD \right)} \tag{6.9}$$

Note that η is a function of surface separation (d) and as surfaces get closer this formulation automatically accounts for the change in the nano-lubricant volume and number of nanoparticles between the surfaces. In this work, the nanoparticle distribution (ϕ) is assumed to be a normal Gaussian function which is characterized by the average particle size and standard deviation (σ).

The statistical model also requires a single nanoparticle indentation model that accounts for nanoparticle deformation and failure. Close observation and in-situ experiments on single spherical silicon nanoparticles have been reported in the literature [2, 3, 33, 35]. Spherical silicon nanoparticles of size 30 to 150 nm were observed to act as brittle materials. The Particles do not exhibit much hardening beyond failure and smaller particles show higher failure strength. Failure strain and failure strength of different size particles is reported. Based on the availability of data on the silicon nanoparticles, this type of nanoparticle was chosen for this work. A single nanoparticle indentation model is also needed to be employed in the statistical model. As reported [3], on average particles deform 45% prior to fracture. Therefore an already developed model [76] for heavily deformed spheres was modified to fit nanoparticle deformation data, see cited papers for more details. The model solves for single particle area of contact and particle force.

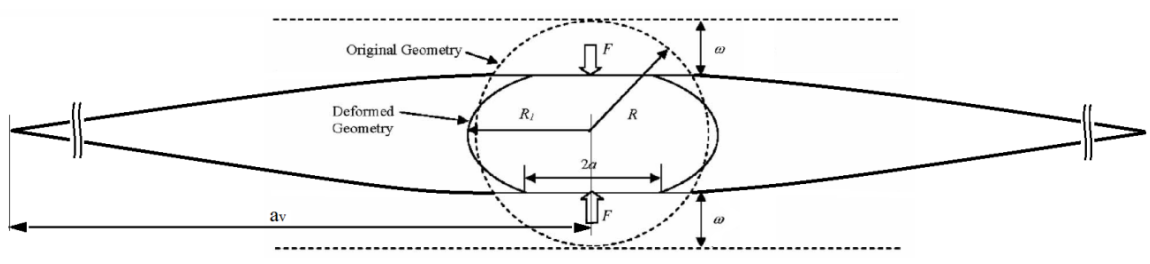

Figure 6.19: Schematic of the spherical particle contact mechanics.

As mentioned in the methodology section, particles separate surfaces resulting in void areas in the vicinity of particles (see Fig.6.15). Each nanoparticle in contact acts as a nano-indenter deforming the surfaces. However, the surfaces possess scale dependent properties as well (e.g. an experiment [76] on steel reports the nano-hardness to be around 10 GPa). Therefore for an accurate modeling of particle/surface interaction further investigation is required. In order to approximate the radius of the void area in this paper a half space elastic model [77] was used. Half the deformed particle diameter R-η was assumed as the indentation on the surface and the surface profile equations

were solved to find where the surfaces meet again and find the void radius per particle (a_v) and void area (A_{void}= πa_v^2) as shown in Fig. 6.15. R is the particle original radius and δ is the particle indentation depth as shown on the Fig. 6.15. The void radius is limited to the average rough surface contact radius (a_{rs}) (Eq.(6.5)). When the load on the particle exceeds the failure strength, the particle fails and the void is assumed to close. Note that in reality, particles are trapped and the voids could not completely close even if the particles fracture. This assumption would underestimate the void area and hence underrates the effectiveness for fractured particles. Therefore it is a conservative assumption which can be further improved once a better understanding of the surface/nanoparticle interaction in the lubricant medium has been achieved. So far three single nanoparticle parameters have been discussed; particle area of contact (A_{NP}), particle force (F_{NP}) and the void area (A_{void}). Also, nanoparticle density (η) and size distribution (ϕ) was introduced and formulated. Rearranging and substituting all these parameters in a GW type model [73] yields the final form of the statistical nanoparticle model, given by

$$\begin{aligned}
\frac{A_p(d)}{A_n} &= \int_d^{\infty} \eta(y)\ \phi(y)\ A_{NP}(\omega, D)\ dy \\
\frac{F_p(d)}{E' A_n} &= \int_d^{\infty} \eta(y)\ \phi(y)\ \frac{F_{NP}(\omega, D)}{E'}\ dy \\
\frac{A_v(d)}{A_n} &= \int_d^{\infty} \eta(y)\ \phi(y)\ A_{void}(\omega, D, a, F)\ dy
\end{aligned} \tag{6.11}$$

A_p, F_p and A_v are the total contact area, force and void area of particles. In Eq. (6.11) particle interference δ is defined as $\delta=(y-d)/2$. Also note that in this set of equations ϕ is a function of y and particles come into contact once the surface separation is smaller than the particle diameter. Also, ϕ is a function of y to account for particles of different sizes. The composite Simpson's method is used to solve the integrals of Eq. (6.11) in this paper.

6.3.2.3 Algorithm

As discussed, the rough surface model uses the surface profile to find the average contact pressure (P^*) and the rough surface real area of contact (A_s). The statistical model solves for contact between two surfaces with the particles in-between and finds the real area of contact for particles (A_p), force carried by particles (F_p) and the void area induced by particles (A_v), see Fig. 6.16 (Note that A_v also includes A_p).

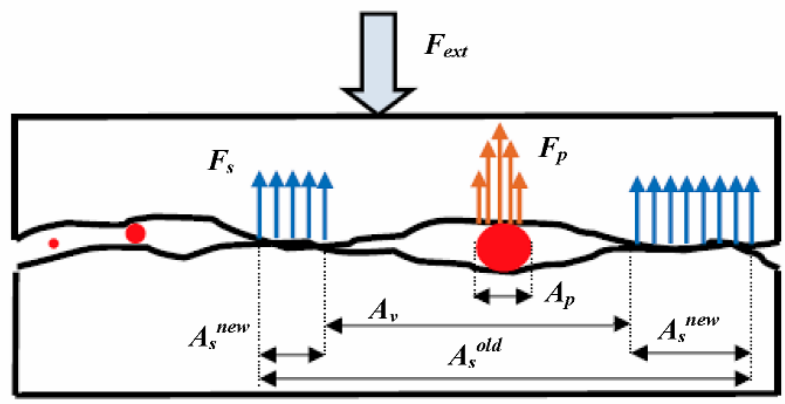

Figure 6.20: Schematic of the overall contact problem.

An algorithm was developed to solve the overall contact problem by balancing the forces between the two sub-models. The goal is to determine how much of the external load (F_{ext}) is carried by the surface (F_s) and how much is carried by the particles (F_p) and to check the force balance equation $F_{ext}=F_s+F_p$. Firstly, an external force of F_{ext} is assumed to be acting on the system and assuming all the load is being carried by the surface, the multi-scale model is used to find the P^* and A_s. Then assuming that the same average pressure is exerted on the particles F_p is found to be

$$F_p = A_s P^* \tag{6.12}$$

Note that particles are assumed to be in contact where surfaces are in contact and this means that A_s should be regarded as the nominal area of contact for the statistical model. Based on the value of F_p the corresponding surface separation is found and A_p and A_v are found (using Eqs. (6.11)). Then the surface area of contact is updated as follows

$$A_s^{new} = A_s^{old} - A_v \tag{6.13}$$

The new surface force is then found based on the updated surface area $F_s=A_s P^*$. The force carried by particles is then updated based on $F_p=F_{ext}-F_s$ and the statistical model is used to find the new values of A_p and A_v. The next solution is found by going back to Eq. (6.13), updating the surface area and iterating through the steps again. The convergence is checked in each iteration according to $\left|\left(F_s^{new}-F_s^{old}\right)/F_s^{old}\right|<10^{-3}$. The final solution is found by iterating through the loop and checking for the convergence criterion. In order to get a faster convergence the statistical model was solved first for various values of d and the solution was determined from a table and using interpolation through the overall algorithm.

6.3.2.4 Friction and Wear Models

The final solution of the contact problem reports A_s, F_s, A_p, F_p and A_v along with the statistical information on the nanoparticles in contact. Validating the direct result from

the model is practically impossible. However, fundamental and simplistic friction and wear models can be utilized to translate the change in the contact force, real contact area and the statistical data on nanoparticles into measurable parameters. The accuracy of the friction and wear models will influence the quantitative accuracy of the final results but validation over general trends of the enhancement is made possible using fundamental models. The friction of the surfaces in contact is governed by the real area of contact and forces acting in the normal and tangential directions. Equation (6.14) can be used to find the coefficient of friction.

$$\mu = \frac{A_s \tau_s + A_p \tau_p}{F_{ext}} \tag{6.14}$$

τ_s and τ_p are shear stresses working on the surface/surface and particle/surface interfaces during sliding, respectively. There have been experimental and theoretical efforts to shed light on the behavior of nanoparticles in dynamic contact [11, 78, 79]. However, in this paper τ_s and τ_p are evaluated as the shear strength between lubricated surfaces in contact.

Combining the effect of particles and surfaces to find an overall model for wear in the system is a challenging task. However, based on the statistical data on particles one can find the particle induced wear using plowing abrasive wear models [77] (see Fig. 6.17).

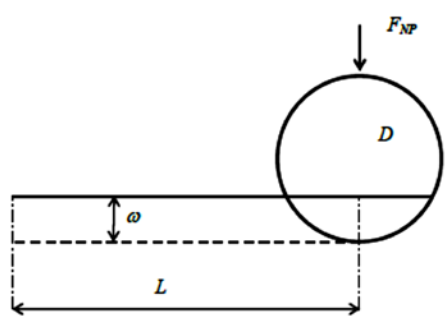

Figure 6.21: Schematic of the particle abrasive wear.

Spherical particles plowing on the surface can induce abrasive wear that is proportional to the cross section of particle to surface interference, see Eq. (6.15) and Fig. 6.17.

$$\begin{aligned} \frac{V_{NP}}{L} &= \int_d^{\infty} \eta(y)\ \phi(y)\ A_{CS}(\omega, D)\ dy \\ A_{CS} &= \frac{D^2}{8}\left\{ Sin^{-1}\left[\frac{8\omega(D-\omega)(D-2\omega)}{D^3}\right] - \frac{8\omega(D-\omega)(D-2\omega)}{D^3}\right\} \end{aligned} \tag{6.15}$$

Where V_{NP}, L and A_{CS} are wear volume (induced by particles), sliding distance and interference cross sectional area between the particle and surface.

6.3.3 Results

This section presents the results of the discussed model for various case studies. The effects of particle concentration, distribution, size and surface roughness on the real area of contact and contact pressure have been studied. Consequently, the change in the real area of contact and pressure at the particle-surface interface is translated to an alteration in friction force and particle induced wear and is also presented. See Appendix II for numerical values used in the model and other complimentary data on the simulations.

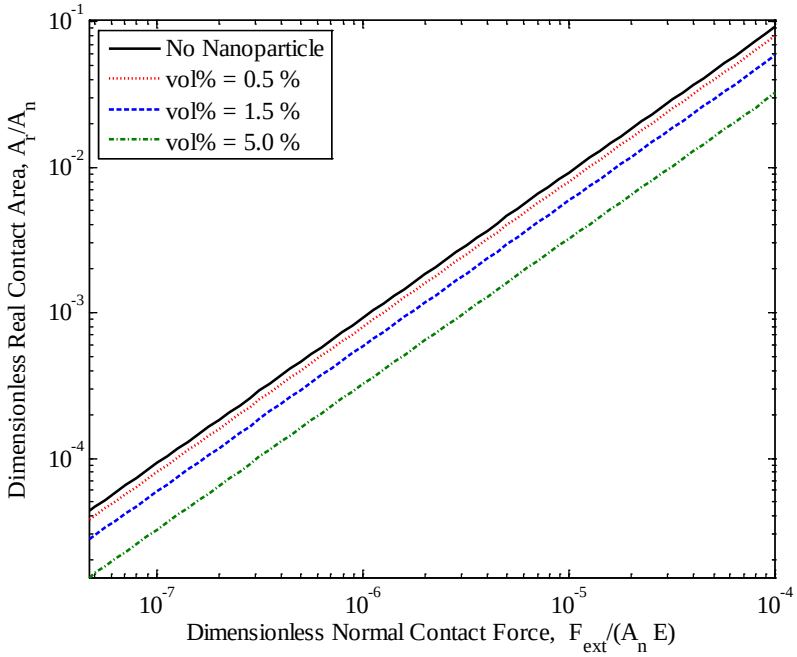

(a)

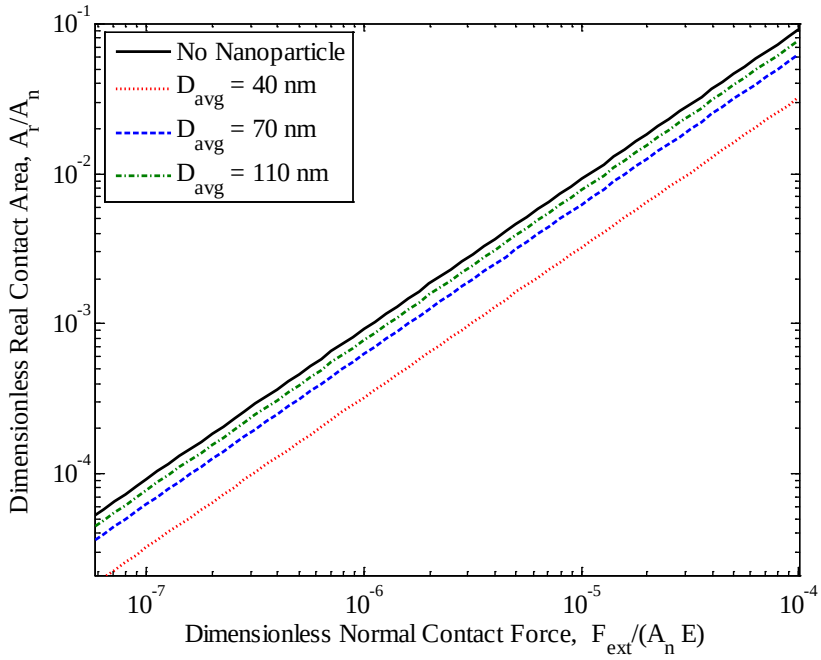

(b)

Figure 6.22: The effect of particle concentration (a) and particle average size (b) on the real contact area versus contact force.

The effect of nanoparticle concentration and average particle size is shown in Figure 6.18. In this study the surface roughness is 0.05 □m and the particle distribution is □g=1.5nm. A_r in this figure is the total real area of contact which is the combined particle and surface contact area, $A_r=A_s+A_p$. Figure 6.18(a) represents the effect of particle concentration for an average particle diameter of 40 nm. As the volume percent increases, the number of particles engaged in the contact escalates. This increases the void area induced in the vicinity of particles and reduces the real area of contact. The effect of various particle sizes for a volume concentration of 5.0% is presented in the Fig. 6.18(b). A decrease in the particle size results in a raise in the number of particles (given that volume concentration is held constant), which would consequently reduce the real area of contact. In this case, smaller particles also exhibit tougher which amplifies the accumulative effect. In either case shown in Fig 6.18, the particles bear high pressures at the particle-surface interface and keep the surfaces apart in the vicinity of particles. This decreases the real area of contact and causes high pressure spikes in the particle-surface interface.

The effect of particle distribution on the real contact area is shown in Fig. 6.19. Figure 6.19(a) shows the dimensionless real area of contact versus dimensionless normal contact force for different distributions of particles all having the same average size (vol% = 5 and Rq=0.05 □m). The distribution of particles versus size is displayed in the Fig 6.19(b). Results suggest that, a sharper distribution of particles results in more reduction in the real area of contact between surfaces. Particles with a wider distribution engage in contact gradually which results in an enormous force on each

particle and consequently particles tend to fracture in a cascading fashion. Whereas particles with a narrower distribution engage in contact simultaneously which results in a stiffer contact (in other words, particles withstand the contact force in large numbers). Figure 6.20, presents the number of fractured particles as a function of the surface separation that shows the cascading fracture of particles with a wider distribution.

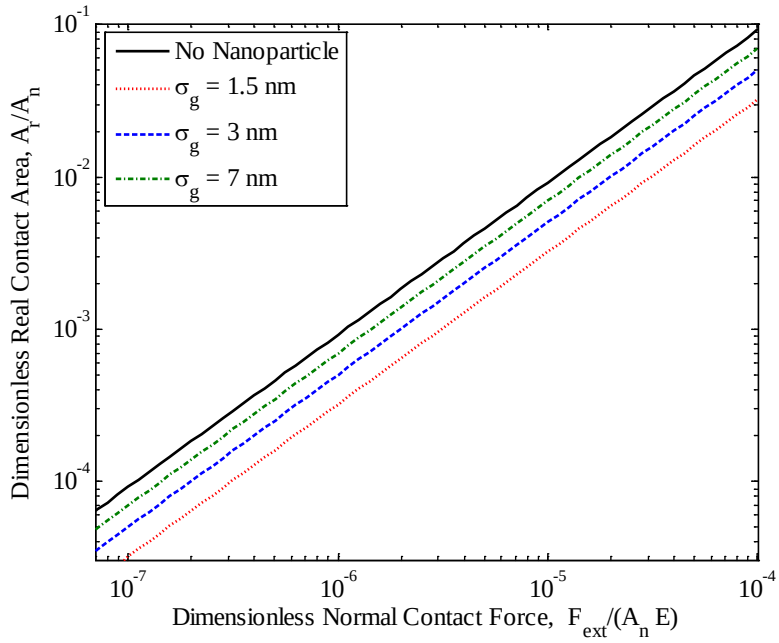

(a)

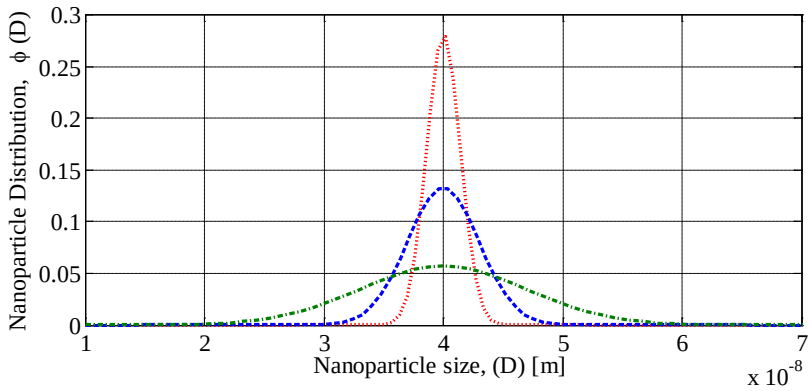

(b)

Figure 6.23: The effect of particle distribution on the real area of contact.

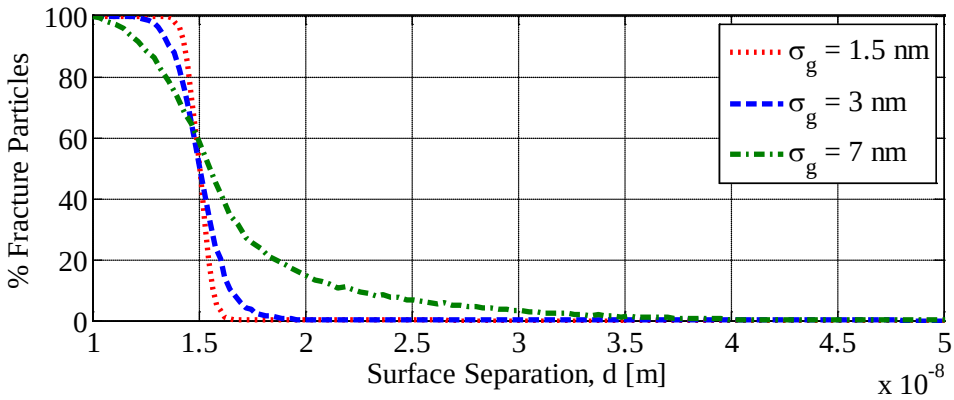

Figure 6.24: Fractured particles as a function of surface separation.

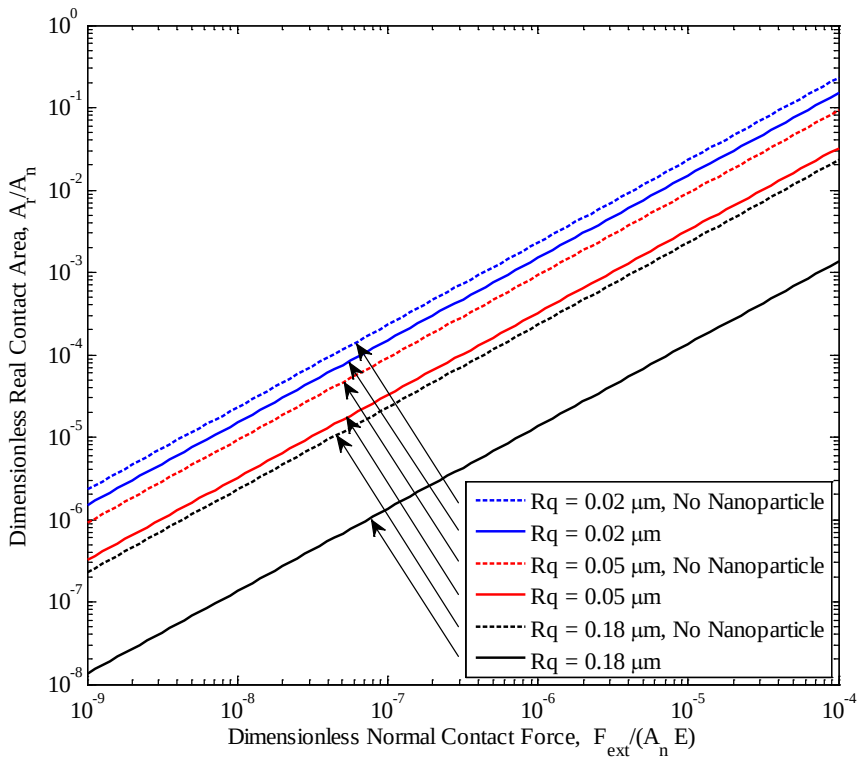

(a)

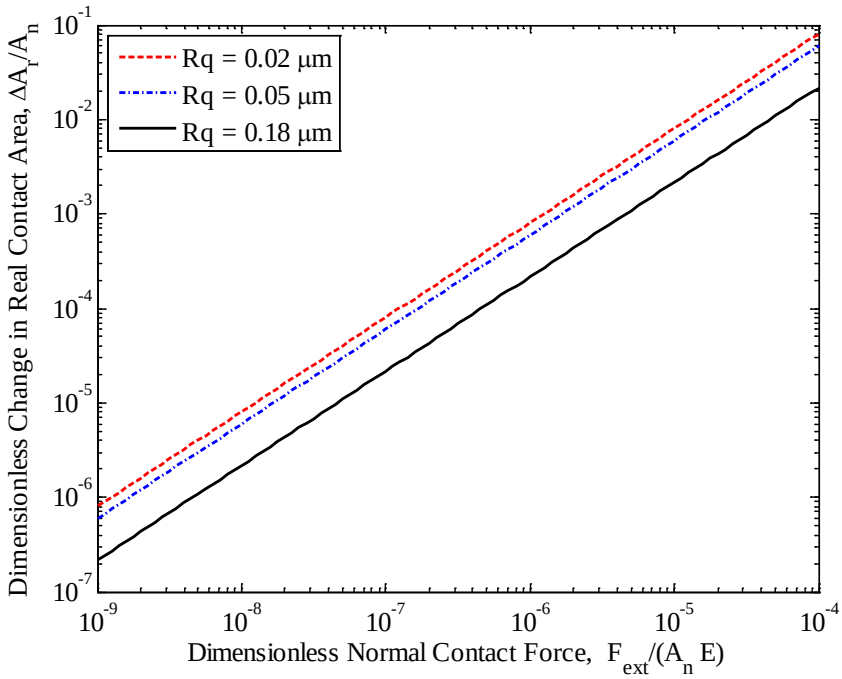

(b)

Figure 6.25: The effect of surface roughness on (a) the real area of contact versus contact force, (b) change in the real area of contact as the result of nanoparticles.

The effect of roughness on the contact characteristics is presented in Fig. 6.21(a). In this study the particle content is vol%=5 and the average size of the particles is 40 nm with the distribution of 1.5nm. Particles stiffen the contact for different values of roughness. As would be expected the reduction in the real area of contact (Fig. 6.21(b)) is more as the surface roughness decreases which suggests that particles are more influential in the contact of smoother surfaces.

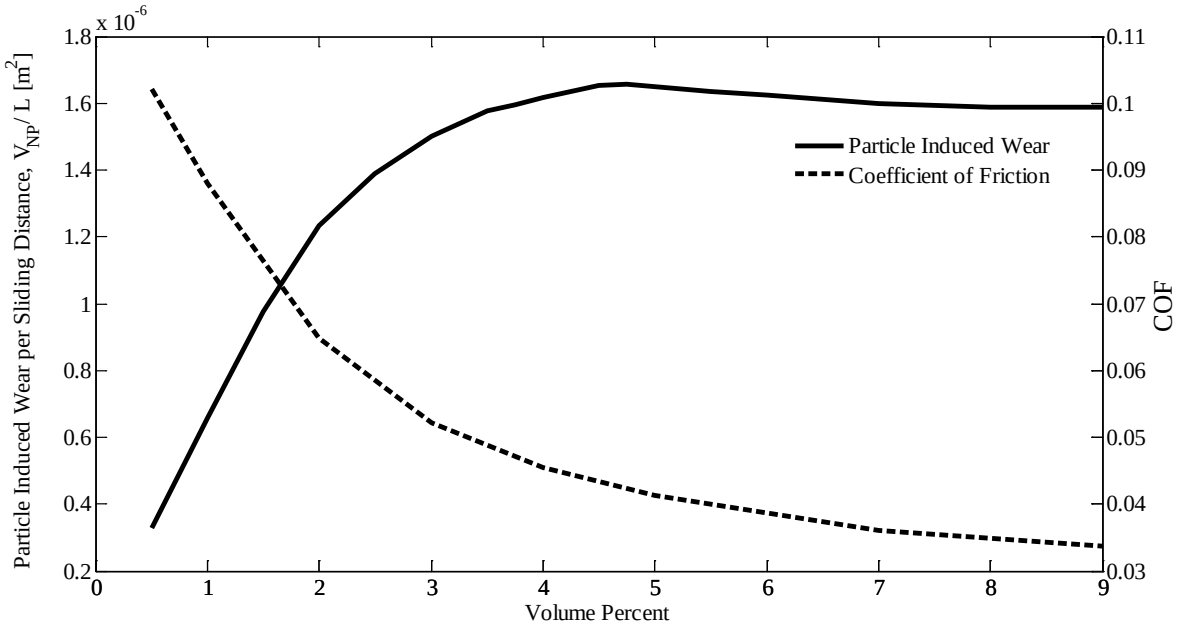

Figure 6.26: Coefficient of friction and particle induced wear versus nanoparticle content.

Figure 6.22 shows the variation of coefficient of friction (COF) and particle induced volumetric wear per sliding distance versus nanoparticle volume percent for Rq=0.05 □m, ⌰=1.5 nm and average particle size of 40 nm. An increase in the content of nanoparticles reduces the friction and lowers the COF and increases wear induced by particles. The decrease in friction is caused by the reduction in the real area of contact. As the particle concentration increases and more particles engage in contact, the average particle force decreases which will cease the increase in wear at a certain particle concentration. Note that the particle induced wear shown on Fig. 6.22 drops to zero as nanoparticle concentration approaches zero which is due to the fact that conventional surface wear has not been included here.

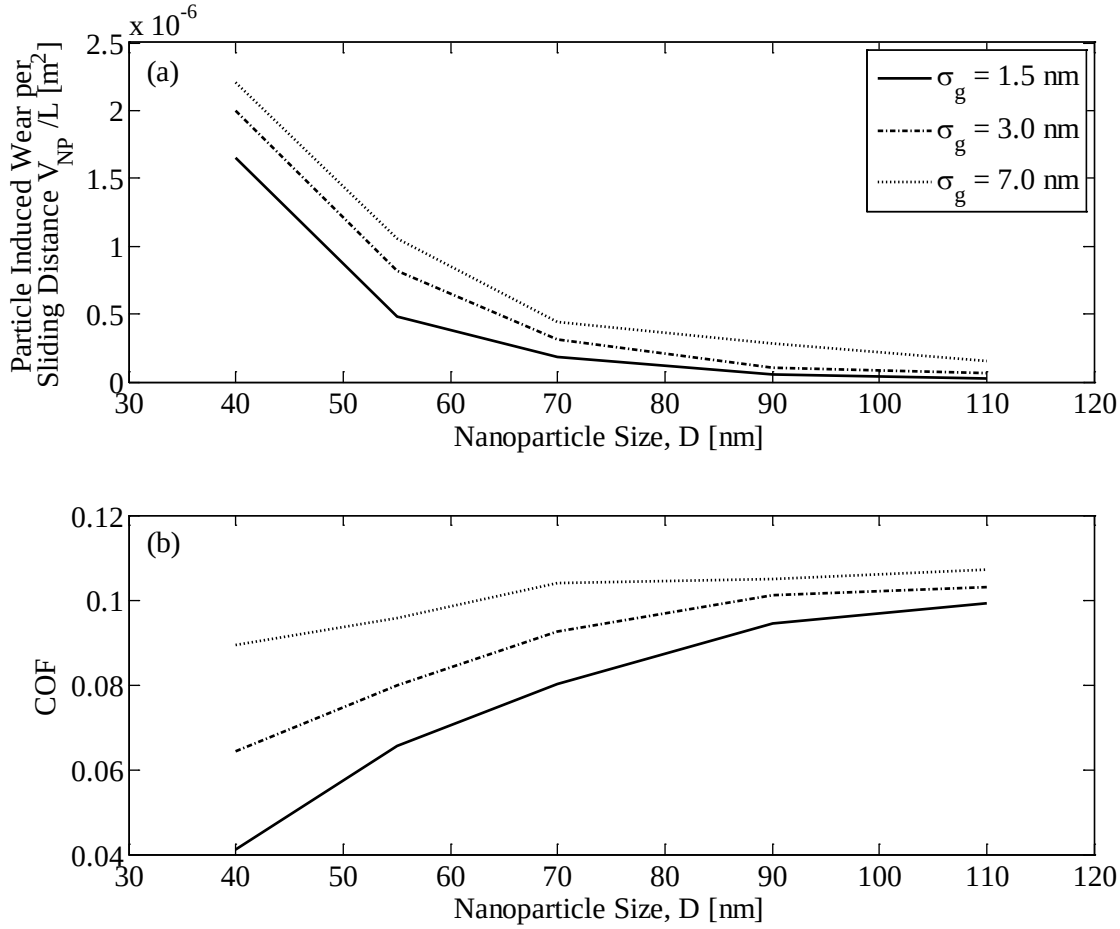

Figure 6.27: Particle induced wear (a) and coefficient of friction (b) changing with particle average size and distribution.

The effect of nanoparticle size and distribution on the particle induced wear and COF is presented in Fig. 6.23 for Rq=0.05 and vol%=5. Figure 6.23(a) suggests that smaller particles and particles with wider distributions of size, induce more wear. Here is a simple sequence to show this: 1. Wear is related to the number of particle times the cross section or $wear \propto N_{NP} \times A_{CS}$. 2. According to Eq.(6.9), $N_{NP} \propto vol\% / v_{avg,NP} \propto 1/D^3$ where $v_{avg,NP}$ is the average particle volume and vol% is constant. 3. $A_{CS} \propto D^2$ according to Eq. (6.15). Thus combining the equations yields $wear \propto 1/D$ which suggests that wear is higher for smaller particles. Figure 6.23(b) shows that smaller particles and the particles with sharper distributions are more effective in reducing friction. This behavior is partially because of the size dependent properties of particles and partially controlled by the number of particles in contact. For instance, when the concentration of particles in a solution is held fixed the total number of the particles is also dependent on the average particle size.

6.3.4 Discussion

The third body nanoparticle multi-scale contact model presented in this paper models the nanoparticles in contact and reports the change in the real area of contact and contact force. Even though silicon nanoparticles were studied, for the sake of available data, the general observations may stand for other kinds of particles as well. This is because nano-structures, including nanoparticles in general, exhibit an elevated strength [1-5, 33-35, 80] which is the source of the mechanisms modeled in this paper. Therefore, unless for particles with special physical or chemical characters e.g. particles capable of bonding with the surface, the general mechanism of reducing the real area of contact is in action. This makes the model applicable for qualitative comparison as long as the size of particles is substantially smaller than the average rough surface radius of contact, $D \ll a_{rs}$.

The developed model suggests that particles reduce the friction in the system by keeping surfaces out of contact locally, resulting in a reduction in the real area of contact. Even though the force carried by the particles is small comparing to the force carried by the surfaces (For example on average $F_p/F_{ext} = 0.083$ for a lubricant with 3.0 %wt particles), the overall effect of particles on the contact area is found to be consequential. Figure 6.22 shows that friction further reduces if more particles are introduced in the lubricant yet eventually this effect saturates. This behavior has been observed experimentally and reported throughout the literature, repeatedly [37, 39, 41, 42] but never theoretically confirmed.

One of the key observations of the nanoparticle contact model is the effect of particle size distribution ($\square_g$) on the nano-lubricant effectiveness. $\square_g$ controls the number of nanoparticles in contact ($\square$ Eq. (6.9)) and also a wider distribution of particles could result in the gradual engagement of nanoparticles in contact and reduce effectiveness (Figs. 6.19-6.20). Particle induced wear and the friction coefficient also changes with $\square_g$, (see Fig 6.23), which makes $\square_g$ an important parameter in nano-lubricant optimization and design. Despite this, the particles size distribution is not always a control parameter in the studies which could be one of the reasons that comparison between different nano-lubricants investigations is sometimes inconclusive.

In this paper only the particle induced abrasive wear was modeled and the effect of different parameters was studied. The accumulative effect of surfaces and particles on the overall wear of the system is very complicated and needs further investigation and study. However, based on the developed model, very helpful observations and predictions can be made that helps better selection of nano-lubricants for further studies. In this work it is assumed that the particles are harder than the surface and abrade the surface. Therefore, soft particles and fullerene like particles[11, 78] (that can deposit layers on the surface) would not induce abrasive wear. Furthermore, these particles reduce the real area of contact which would reduce surface to surface wear and the overall effect of particles is a decrease in the system's wear. Harder particles, such as the silicon nanoparticles studied in this work, would induce wear. One can compare the particle induced wear (approximated by the model) to the lubricated surface wear (without particles) and decide if particles can practically promote wear.

For instance, if particle induced wear is greater than the lubricated surface wear then the nanoparticles would increase wear. If the particle induced wear is predominantly lower than the lubricated surfaces wear then the addition of particles would not change the wear practically. However, if particle induced wear is on the same order as the lubricated surface wear, the competing effects of particle induced wear and reduction in the real area of contact would determine the overall effect of particles on the system. Therefore, particle induced wear, as modeled in this paper, can provide some guidelines for the better selection of particles for a lubricating system. Moreover, this argument suggests that particles could increase or decrease wear based on the lubricant and the surfaces in contact. Thus, particles should be carefully selected for different lubricating systems. Wear of different combinations of surfaces and particles have been studied and the results seem to agree with the general observations from the model and the arguments raised in this paragraph [22, 38, 40].

6.4 The effect of nanoparticles in thin film elasto-hydrodynamic lubrication

Elasto-hydrodynamic lubrication (EHL) has been the topic of extensive studies in the past sixty years. It was originally explored to provide an explanation for the behavior of line and point contact between gears and bearings with a focus on predicting the minimum film thickness [81]. The EHL is interestingly proven to be a very effective lubrication regime especially in the case of thin lubricant films. Various experimental and analytical studies have explored the problems associated with the EHL in different systems [82]. The results suggested that the classical EHL models[83-85] are accurate down to the gaps as small as 10 to 20 nm [86, 87]. For very thin films, by using experimental[88], numerical[89] and analytical methods[90], it has been shown that the surface forces promote layering of the lubricant's molecules, which in turn leads to a considerable reduction in the coefficient of friction (COF). This work explores the effect of nanoparticle additives in the thin film EHL regime.

In the context of nano-lubricants, it has been recently reported by different groups of researchers that nanoparticle additives can improve the lubricity of lubricants [37, 38, 41, 91, 92]. However, most of the studies were aimed at the performance of the nanoparticles in the boundary lubrication regime in which substantial contact occurs between the surfaces. Hence, most of the proposed friction reduction mechanisms for nanopaticles such as rolling [11, 93], transfer films [39, 94], formation of tribofilms [92, 95] and reducing the real area of contact [91, 96] require particles/surface interactions. This paper focuses on the performance of nanoparticle additives on thin film elasto-hydrodynamic lubrication in which no significant contact occurs between the lubricated surfaces and the pressure in the lubrication film is high (0.7~1.5 GPa). The hypothesis of the current work is that nano-sized particles can infiltrate into the small gaps between surfaces in the EHL regime and when the size of the gap is comparable to the particle's size and the film pressure is high, particles may affect the friction properties of the contact pairs. In this paper, we have conducted careful experiments using a sphere (pin) on flat (disk) friction tester to demonstrate the effect of nanoparticles on reducing friction in the EHL regime. Moreover, surface analysis and molecular-level simulations have been utilized to investigate the possible interaction between the nanoparticles and the surfaces or lubricant in order to determine the potential enhancing mechanism. The

results propose a new friction reducing mechanism induced by the nanoparticles in the EHL lubrication regime.

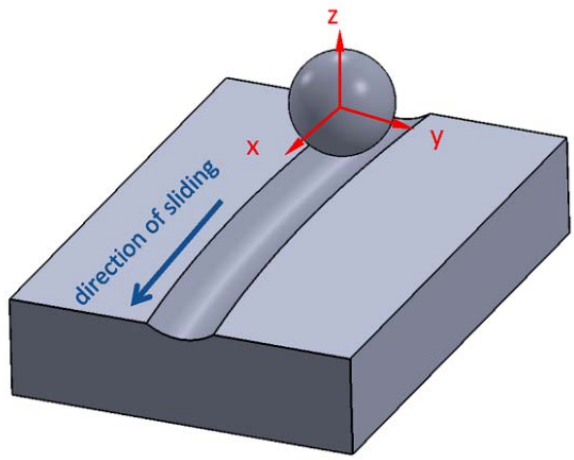

Figure 6.28. Schematic of the contact pair.

6.4.1 Nano-lubricant and experiments

The nano-lubricant used in the experiments contains silver nanoparticles with an average size of 7 nm suspended in polyethylene glycol (PEG). The molecular weight of the PEG is 600 g/mol. polyvinylpyrollidone (PVP) with a molecular weight of 10 Kg/mol is used as the coating agent to stabilize the suspension. The nano-lubricant has 3 mM silver nanoparticles and 1.5 mM PVP suspended in PEG and the control lubricant consists of 1.5 mM of PVP in PEG. The viscosities of the nano-lubricant and the control lubricant are measured to be 170.8 and 166.4 mPa.s, respectively. Also, the nano-lubricant and the sample are observed to behave as Newtonian fluids in shear rates higher than 10 s^{-1} (data is not given here). The stability of the suspension was studied and the nano-lubricant was observed to be stable for a six month period.

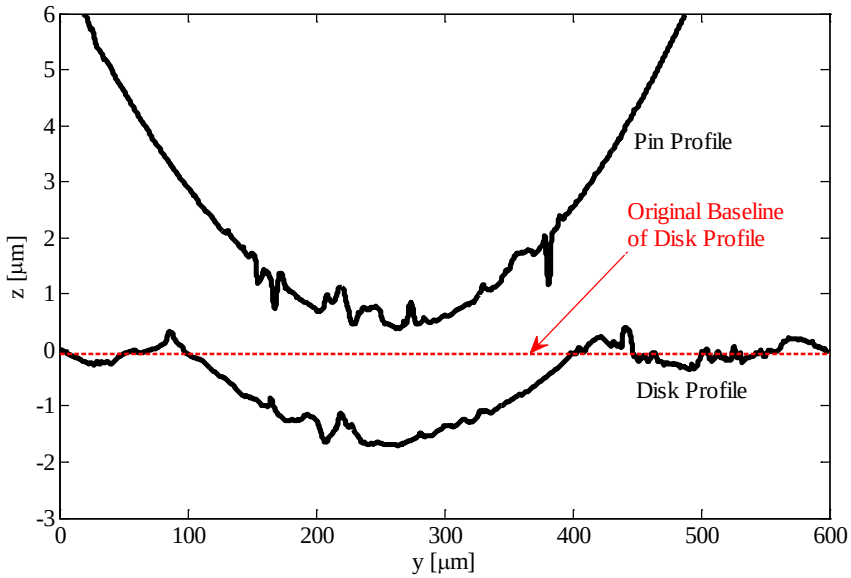

Figure 6.29. Pin and disk profiles after the friction tests for one of the contact pairs.

Friction tests were performed with a pin-on-disk friction test setup that consists of a spherical pin (10 mm diameter) in contact with a rotating disk. This configuration provides a concentrated point contact between surfaces. The disk part is made of AISI 1080 carbon steel and the pin is made of AISI 52100 chromium steel. The contact is submerged under the lubricant using a reservoir. The sphere and disk are brought into contact by changing the normal force while the lubricant exists between the surfaces. An electrical contact resistant sensor (ECR) is used to detect contact between the solid conductive surfaces.

The test procedure has two steps, first the run-in step during which the surfaces are brought into contact. In this step, the contact pressure (maximum Hertzian contact pressure) is held at 0.97 GPa for 15 min and then increased to 1.40 GPa for another 15 min. During this step the surfaces develop and a shallow groove forms on the disk. Figure 6.24 shows the schematic of the contact pair and the groove. During the next step of the friction test the force is changed from 2.0 N to 50.0 N in nine increments over three minute intervals and the friction data is collected. This step tries to collect the data in short intervals so that the change in the geometry of the surfaces is minimal.

Upon completion of the tests, the profiles of the pins and the disks are measured in order to accurately estimate the contact pressures. The profiles of a contact pair are shown in Figure 6.25. The profiles are used to calculate the actual curvature of the pins and the grooves in the contact region during the data collecting step. The overall effective contact radius in the *y*-direction is $R_{y,e}^{-1} = R_{y,p}^{-1} + R_{y,d}^{-1}$ and in the *x*-direction is $R_{x,e} = R_{y,p}$ where subscripts *x, y, e, p* and *d* stand for *x*-direction, *y*-direction, effective, pin and disk (see Fig. 6.24 for definition of coordinates). $R_{y,p}$, $R_{x,p}$ and $R_{y,d}$ have been measured based on the actual surface profiles. Due to the difference in effective contact radius in the *x*- and *y*-directions the contact region is of elliptical shape. Hence, the

contact pressure for elliptical point contact is calculated using the general Hertzian contact solution[97].

The results are plotted in Figure 6.26 in terms of the COF versus the contact pressure (the maximum Hertzian contact pressure). As the contact pressure increases, the COF first decreases and then increases, which is a typical behavior of lubricating pairs in the EHL regime. The plateaus at the far right of the curves correspond to initiation of contact between surfaces. The results indicate that the nanoparticle additives enhance friction in the EHL regime which is associated with the contact pressures ≅ 0.8 to 1.6 GPa. This observation confirms that the supplement of nanoparticles improves friction when contact pairs are separated by a film of lubricant. As mentioned earlier, the viscosity of the nano-lubricant is higher than the viscosity of the control lubricant and therefore the enhancement does not originate from the bulk lubricant properties that are effective in the hydrodynamic lubrication regime. In addition, the ECR sensor shows that there is no contact between surfaces, and the pressure is high, showing that the regime is not boundary lubrication either. These observations lead to the conclusion that the nanoparticles reduce friction in the EHL regime.

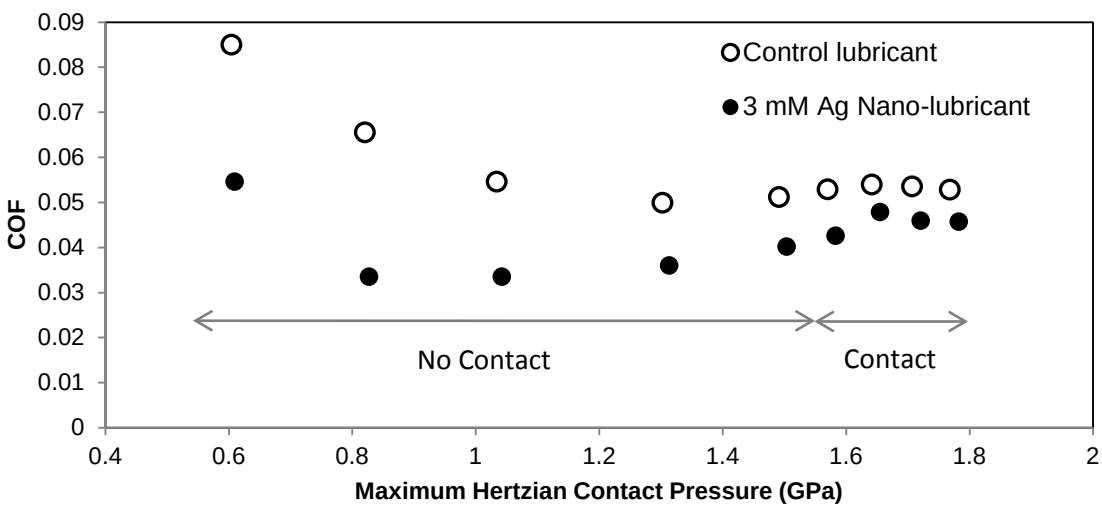

Figure 6.30. Coefficient of friction versus contact pressure.

The contact system consists of three components, particles, surfaces and the lubricant. Therefore, we need to investigate the interaction between any pair of these components to find the dominant effective mechanism of nanoparticles in the EHL regime. The interaction between the lubricant and the surfaces is the common factor for the nano-lubricant and the control lubricant. Hence, the mechanism should have roots in the interaction between the nanoparticles and the surfaces or the nanoparticles and the lubricant. Possible phenomena that arise from the particle/surface interactions can be either the particles forming nano-structures on the surface or filling up the valleys of the surface, leading to a change in the nano-texture of the surface and therefore affecting the EHL. Particle/lubricant interaction at the thin film EHL may also result in the reduction of the COF. For instance, the nanoparticles can affect the flow pattern or glass transition of the lubricant at high pressures. The rest of this work studies the

nanoparticles/surface and the nanoparticles/lubricant interactions in order to find the dominant mechanism responsible for reducing friction.

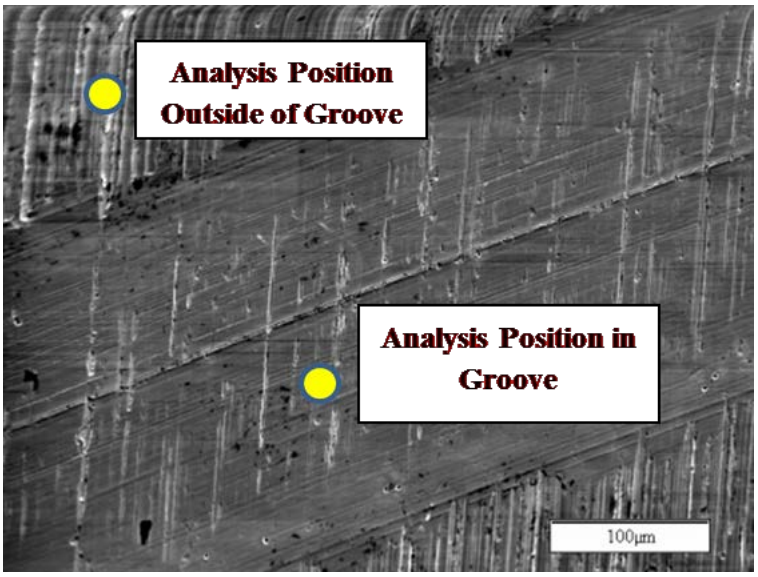

(a)

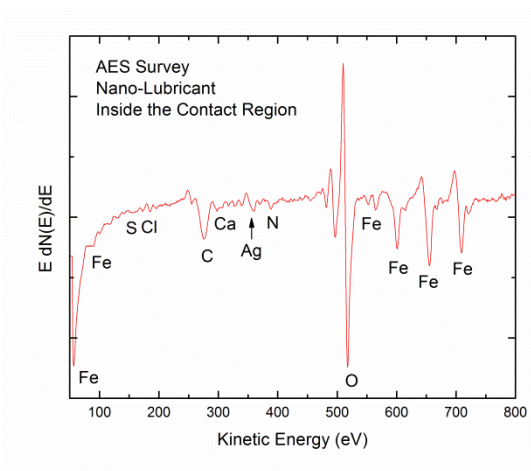

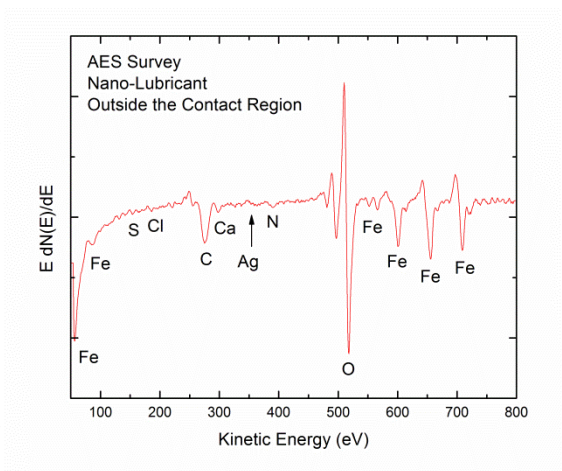

(b) (c)

Figure 6.31. Picture of contact region obtained with scanning electron microscope, (a) AES spectra inside (b) and outside (c) the contact region.

6.4.2 Surface analysis

In order to investigate possible particle/surface interactions, various surface analyses were performed on the disk surfaces after the tests. A scanning electron microscope (SEM) image of one of the contact regions is shown in Figure 6.27 (a). As shown in the figure, Auger electron spectroscopy (AES) spectra were recorded both inside and outside the contact groove. Results shown in Figure 6.27 (b) and (c) indicate that there is slightly more Ag inside the wear groove than outside the groove. Surface stoichiometry measurements both outside and inside the contact groove were obtained

by X-ray photoelectron spectroscopy (XPS), yielding the average amount of surface Ag to be 0.06 and 0.1 at% for the regions outside and inside the groove, respectively. XPS was used for the stoichiometric measurement rather than AES due to the higher accuracy of XPS in stoichiometric determinations. The analysis on the surfaces tested with the control lubricant showed no evidence of Ag on the surfaces. The next step is to study the configuration of the particles on the surface and detect possible chemical bonding between the nanoparticles and the surfaces. Ar sputter etching was used to drill ~ 12.5 nm into the surface (slightly over the average size of a particle). AES results before and after the drilling shows that the Ag signal completely vanished after drilling (see Figure 6.28). Moreover, XPS analysis inside the contact region showed that Fe on the surface is largely in oxide form (Fe_2O_3), with no bonding between Ag and other surface elements. This shows there is no strong bonding between the Ag nanoparticles and the surface. Figure 6.29 illustrates the possible scenarios that may happen in regard to the nanoparticles/surface interaction and schematically shows the possible effects of drilling for each scenario. In the first scenario (see Figure 6.29 (a)), it is assumed that the nanoparticles either (1) deposit in the valleys, (2) coalesce to form nano-structures or (3) bond to the surface. In this scenario, drilling does not remove all of the nanoparticles. In contrast, in the second scenario in which individual nanoparticles are loosely adhered to the surface (see Figure 6.29 (b)), drilling removes the Ag nanoparticles, which is the phenomenon observed in our tests. Considering that the information depth for both AES/XPS is ~ 5 nm, this analysis along with the surface stoichiometry using XPS suggests that Ag resides strictly on the surface in the form of individual nanoparticles loosely adhered to the surface. We conclude that no influential interaction is taking place between the nanoparticles and the surfaces that can be considered to be the mechanism behind the observed friction reduction.

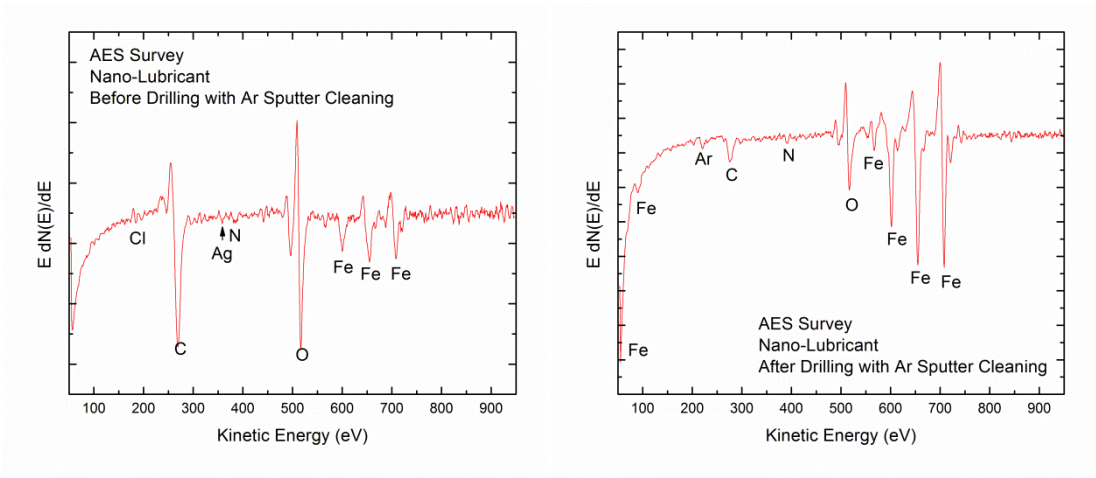

(a) (b)

Figure 6.32. AES analysis on the surfaces before (a) and after (b) drilling with Ar sputter cleaning.

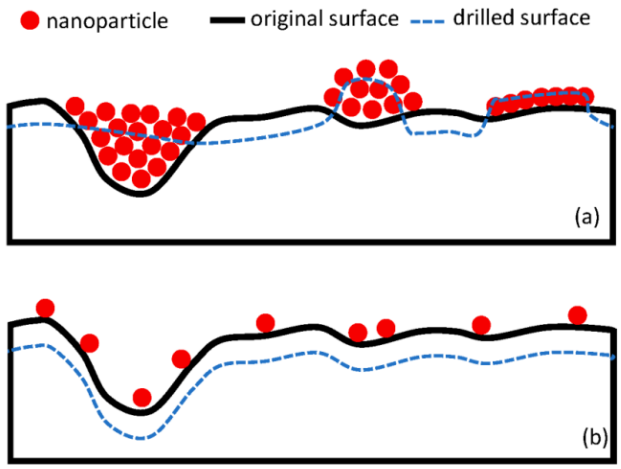

Figure 6.33. Schematic of possible particle/surface interaction: (a) particles deposit on the surface and inside the valleys (b) scattered loosely adhered particles on the surface.

6.4.3 Molecular dynamics simulations

Next, molecular dynamics (MD) simulations are utilized to study the underlying mechanisms in relation to the interactions between the nanoparticles, the surfaces and the lubricant in the thin film EHL. In order to simplify our MD simulations, the lubricant is chosen to be n-dodecane. Since the MD simulations are designed to study the mechanistic interactions between the nanoparticles and the lubricant, this choice of lubricant does not affect our overall purpose for performing MD simulation. The minimum film thickness in the friction tests was estimated by theoretical calculations [84, 85] to be 90 nm and the combined roughness in the sliding direction (*x*-direction) was measured to be 70 nm. This means that the gaps between the surfaces are on average around 20 nm. Therefore, the geometries in MD simulations were chosen to have the similar ratio of particle size over gap size.

Simulations were performed on a smaller system containing a nanoparticle with a diameter ~24 or 37 Å suspended within the gap of 54 Å filled with n-dodecane molecules confined between two rigid walls (see Figure 6.30). The Ag atoms included in the nanoparticle are located on a faced-centered cubic (FCC) lattice with a lattice constant of 4.09 Å [98]. The walls are made of iron atoms located on a body-centered cubic (BCC) lattice with a lattice constant of 2.87 Å [98]. The walls include three layers of atoms with a cross-sectional area of ~60×60 $Å^2$.

The Lennard-Jones (LJ) potential is utilized for interactions among Ag and Fe atoms [98]. The Nath, Escobedo, and de Pablo-revised (NERD) force field [99] is used to describe interactions between dodecane molecules. For the cross-interaction potential between different elements, the Lorentz-Berthelot mixing rule [100] is used for determining the LJ potential parameters. A time step of 1 fs is used in all simulations. All simulations were performed with the large-scale atomic/molecular massively parallel simulator (LAMMPS) molecular dynamics package [101].

The steps of the MD simulations are as follows. Pure fluid (control lubricant) or nano-lubricant (the term that is used for systems containing nanoparticles) systems were initially equilibrated under isobaric-isothermal (NPT) ensembles at T=300 K and atmospheric pressure without the walls. At this stage, the periodic boundary conditions were applied on all directions of simulation boxes. Then, these systems were brought into contact with the two walls and subjected to compression by moving the walls toward each other. In this step, the periodic boundary conditions were applied on the directions parallel to the walls' surfaces, whereas for the normal direction, the fixed non-periodic boundary condition was utilized. A schematic diagram of a nano-lubricant system after compression is exhibited in Figure 6.30.

The density curves (not given here) for different gap distances during compression simulations show that by compressing the fluid within the gap, planar layers of the lubricant's molecules are formed. This phenomenon is in agreement with the results of other MD works [102-105] on thin films between two walls. However, in our study, upon shearing the walls, the layered structure midway between the walls vanishes, leaving only a few ordered layers in the vicinity of the walls. In this scenario, the pressure and gap distance between the walls change simultaneously. To overcome this problem and to find the dependency of the COF on the pressure independently from the gap distance, simulations were carried out on systems containing different numbers of lubricant molecules (i.e. densities). In other words, the gap distance is kept constant while the pressure changes due to the number of molecules. After the compression step, the systems were equilibrated for 1,000,000 time steps under the isothermal-constant volume (NVT) conditions. Then, the walls were sheared in opposite directions for 4,000,000 to 6,000,000 time steps until the systems reached the steady-state condition. Upon attaining the steady-state condition, the normal and shear stresses on the walls were obtained by dividing the average forces imposed on the walls from the lubricant's molecules by the cross-sectional area of the walls. Figure 6.31 exhibits the calculated COF versus pressure for the pure and nano-lubricant cases. The results show that for all cases, the COF decreases with increasing pressure. In addition, the presence of the nanoparticles leads to a decrease in the COF. The general trend of the friction results from the MD simulations (Figure 6.31) and the experiments (Figure 6.26) corroborate each other on the fact that the presence of the nanoparticle in the contact system results in a decrease in the COF. This also supports the idea that the nanoparticles/lubricant interaction is responsible for improved performance in thin film EHL.

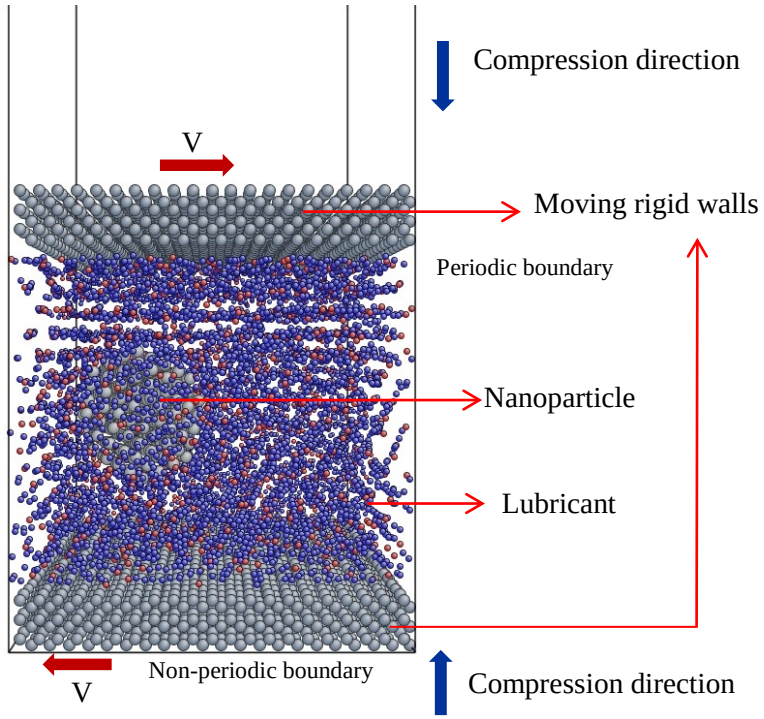

Figure 6.34. Schematic diagram of the simulation system and boundary conditions.

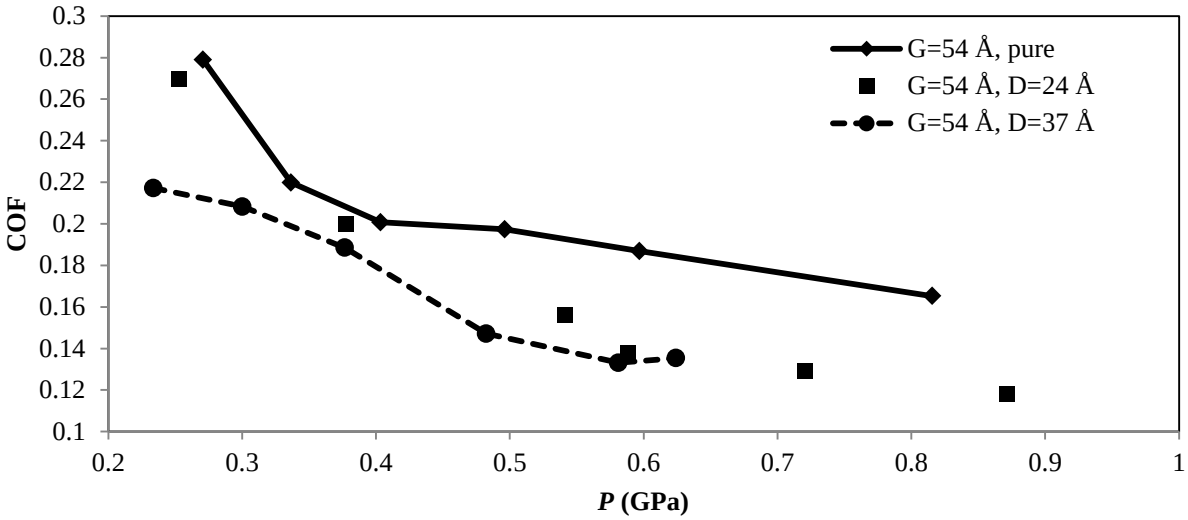

Figure 6.35. COF versus pressure at *G*=54 Å for pure system and two nanofluid systems containing nanoparticles with *D*=24 and 37 Å.

By monitoring the motion of lubricant molecules and tracing them when the walls are sheared, we found that the lubricant's molecules move with each nanoparticle (in a translating motion). This is most likely the key mechanism behind the reduction in the COF when a nanoparticle is present. The presence of a nanoparticle forces the lubricant's molecules to move along with the nanoparticle, promoting an obstructed flow (please refer to movies of molecular dynamics simulations available in supporting

information section). This is clearly observed in the velocity profile for the nano-lubricant cases given in Figure 6.32. For obtaining the velocity profiles, the region between the walls is divided into a sufficient number of slabs normal to the *z*-direction. Then, the time-averaged velocity of all particles within those slabs was calculated. For nano-lubricant cases, there is a flat region in the velocity profiles which indicates that shearing occurs over a few layers of lubricant adjacent to the walls. While for the pure case, the velocity profile includes both a linear region and a jump which shows that shear is distributed through all regions of the gap. The proposed mechanism is further verified by modeling a pure fluid system containing a less number of the lubricant's molecules and a smaller gap. Similar simulation steps were carried out for a gap size of *G*=18 Å and having a pressure of 0.7 GPa. Despite the aforementioned simulations, in this case, shearing does not destroy the planar structure of the layered molecules and dodecane molecules slip on each other on the sliding layers (see Figure 6.32). The calculated COF for this case is 0.12, which is closer to the COF for the nano-lubricant systems rather than COF for the pure fluid with *G*=54 Å and having the same pressure. The similar values of COF suggest that in both cases, the case with a few layers of pure fluid and the nano-lubricant case, the same mechanism occurs. Consequently, this directs us to the conclusion that the mechanism for nanoparticles in the thin film EHL regime is the occurrence of obstructed flow caused by nanoparticles promoting the shearing action over a few layers of the lubricant.

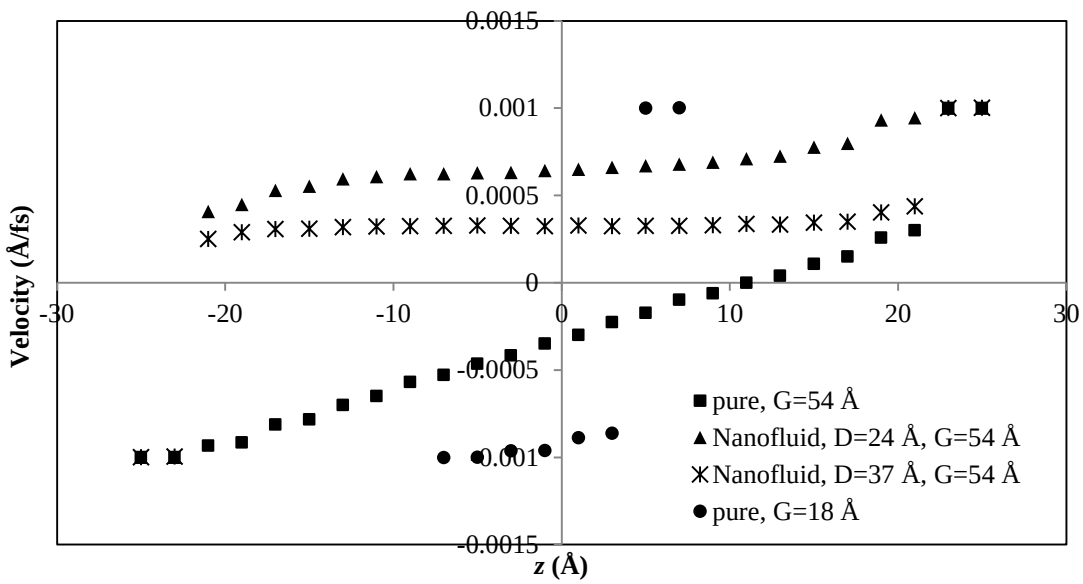

Figure 6.36. Examples of the velocity profiles for the pure and the nano-lubricant cases with *G*=54 Å and a pure case with *G*=18 Å.

6.5 References

[1] Greer, J. R., and Nix, W. D., 2005, "Size Dependence of Mechanical Properties of Gold at the Sub-Micron Scale," Applied Physics A: Materials Science & Processing, 80(8), pp. 1625-1629.

[2] Deneen Nowak, J., Mook, W. M., Minor, A. M., Gerberich, W. W., and Carter, C. B., 2007, "Fracturing a Nanoparticle," Philisophical Magazine, 87(1), pp. 29-37.

[3] Mook, W. M., Nowak, J. D., Perrey, C. R., Carter, C. B., Mukherjee, R., Girshick, S. L., Mcmurry, P. H., and Gerberich, W. W., 2007, "Compressive Stress Effects on Nanoparticle Modulus and Fracture," Physical Review B, 75(21), pp. 10.

[4] Shan, Z. W., Adesso, G., Cabot, A., Sherburne, M. P., Syed Asif, S. A., Warren, O. L., Chrzan, D. C., Minor, A. M., and Alivisatos, A. P., 2008, "Ultrahigh Stress and Strain in Hierarchically Structured Hollow Nanoparticles," Nat Mater, 7(12), pp. 947-952.

[5] Shan, Z. W., Mishra, R. K., Syed Asif, S. A., Warren, O. L., and Minor, A. M., 2008, "Mechanical Annealing and Source-Limited Deformation in Submicrometre-Diameter Ni Crystals," Nat Mater, 7(2), pp. 115-119.

[6] Deng, C., and Sansoz, F., 2009, "Fundamental Differences in the Plasticity of Periodically Twinned Nanowires in Au, Ag, Al, Cu, Pb and Ni," Acta Materialia, 57(20), pp. 6090-6101.

[7] Gerberich, W. W., Michler, J., Mook, W. M., Ghisleni, R., Östlund, F., Stauffer, D. D., and Ballarini, R., 2009, "Scale Effects for Strength, Ductility, and Toughness in "Brittle" Materials," Journal of Materials Research, 24(3), pp. 898-906.

[8] Lockwood, A. J., and Inkson, B. J., 2009, "In Situ Tem Nanoindentation and Deformation of Si-Nanoparticle Clusters," Journal of Physics D: Applied Physics, 42(3), pp. 5.

[9] Kedzierski, M. A., Venerus, D., Buongiorno, J., Christianson, R., Townsend, J., Bang, I., Chen, G., Chung, S., Chyu, M., Chen, H., Ding, Y., Dubois, F., Dzido, G., Funfschilling, D., Galand, Q., Gao, J., Hong, H., Horton, M., Hu, L., Iorio, C., Jarzebski, A., Jiang, Y., Kabelac, S., Kim, C., Kim, J., Kim, S., Mckrell, T., Ni, R., Philip, J., Prabhat, N., Song, P., Vaerenbergh, S., Wen, D., Witharana, S., Zhao, X., and Zhou, S., 2010, "Viscosity Measurements on Colloidal Dispersions (Nanofluids) for Heat Transfer Applications," Applied Rheology Journal, 20(4), pp. 7.

[10] Mook, W. M., Niederberger, C., Bechelany, M., Philippe, L., and Michler, J., 2010, "Compression of Freestanding Gold Nanostructures: From Stochastic Yield to Predictable Flow," Nanotechnology, 21(5), pp. 9.

[11] Lahouij, I., Dassenoy, F., De Knoop, L., Martin, J.-M., and Vacher, B., 2011, "In Situ Tem Observation of the Behavior of an Individual Fullerene-Like Mos2 Nanoparticle in a Dynamic Contact," Tribology Letters, 42(2), pp. 133-140.

[12] Ohmae, N., Martin, J. M., and Mori, S., 2005, *Micro and Nanotribology*, ASME,

[13] Xu, T., Jiazheng, Z., and Kang, X., 1996, "The Ball-Bearing Effect of Diamond Nanoparticles as an Oil Additive," Journal of Physics D: Applied Physics, 29(11), pp. 2932-2937.

[14] Zhou, J., Wu, Z., Zhang, Z., Liu, W., and Xue, Q., 2000, "Tribological Behavior and Lubricating Mechanism of Cu Nanoparticles in Oil," Tribology Letters, 8(4), pp. 213-218.

[15] Rapoport, L., Leshchinsky, V., Lapsker, I., Volovik, Y., Nepomnyashchy, O., Lvovsky, M., Popovitz-Biro, R., Feldman, Y., and Tenne, R., 2003, "Tribological

Properties of Ws2 Nanoparticles under Mixed Lubrication," Wear, 255(7-12), pp. 785-793.
[16] Sajith, V., Mohiddeen, M., Sajanish, M. B., and Sobhan, C. B., 2007, "An Investigation of the Effect of Addition of Nanoparticles on the Properties of Lubricating Oil," ASME Conference Proceedings, 2(pp. 329-335.
[17] Gu, C. X., Zhu, G. J., Li, L., Tian, X. Y., and Zhu, G. Y., 2009, "Tribological Effects of Oxide Based Nanoparticles in Lubricating Oils," Journal of marine science application, 8(1), pp. 71-76.
[18] Lee, C. G., Hwang, Y. J., Choi, Y. M., Lee, J. K., Choi, C., and Oh, J. M., 2009, "A Study on the Tribological Characteristics of Graphite Nano Lubricants," International Journal of Precision Engineering and Manufacturing, 10(1), pp. 85-90.
[19] Zhang, M., Wang, X., Fu, X., and Xia, Y., 2009, "Performance and Anti-Wear Mechanism of Caco3 Nanoparticles as a Green Additive in Poly-Alpha-Olefin," Tribology International, 42(7), pp. 1029-1039.
[20] Zhang, M., Wang, X., Liu, W., and Fu, X., 2009, "Performance and Anti-Wear Mechanism of Cu Nanoparticles as Lubricating Oil Additives," Industrial Lubrication and Tribology, 61(6), pp. 311 - 318.
[21] Gu, C. X., Zhu, G. J., Tian, X. Y., Shi, J. F., and Feng, Y. Y., 2010, "Tribological Effects of Nano-Copper with Different Diameters in Lubricants," Advanced Materials Research, 123 - 125(pp. 1059-1062.
[22] Hernández Battez, A., González, R., Viesca, J. L., Fernández, J. E., Díaz Fernández, J. M., Machado, A., Chou, R., and Riba, J., 2008, "Cuo, Zro2 and Zno Nanoparticles as Antiwear Additive in Oil Lubricants," Wear, 265(3-4), pp. 422-428.
[23] Lee, K., Hwang, Y., Cheong, S., Kwon, L., Kim, S., and Lee, J., 2009, "Performance Evaluation of Nano-Lubricants of Fullerene Nanoparticles in Refrigeration Mineral Oil," Current Applied Physics, 9(2, Supplement 1), pp. e128-e131.
[24] Hernández Battez, A., Viesca, J. L., González, R., Blanco, D., Asedegbega, E., and Osorio, A., 2010, "Friction Reduction Properties of a Cuo Nanolubricant Used as Lubricant for a Nicrbsi Coating," Wear, 268(1-2), pp. 325-328.
[25] Wu, Y. Y., Tsui, W. C., and Liu, T. C., 2007, "Experimental Analysis of Tribological Properties of Lubricating Oils with Nanoparticle Additives," Wear, 262(pp. 819-825.
[26] Hwang, Y., Park, H. S., Lee, J. K., and Jung, W. H., 2006, "Thermal Conductivity and Lubrication Characteristics of Nanofluids," Current Applied Physics, 6(1), pp. e67-e71.
[27] Szlufarska, I., Chandross, M., and Carpick, R., W. , 2008, "Recent Advances in Single-Asperity Nanotribology," Journal of Physics D: Applied Physics, 41(12), pp. 123001.
[28] Bhushan, B., Israelachvili, J. N., and Landman, U., 1995, "Nanotribology: Friction, Wear and Lubrication at the Atomic Scale," Nature, 374(6523), pp. 607-616.
[29] Harrison, J. A., Colton, R. J., White, C. T., and Brenner, D. W., 1993, "Effect of Atomic-Scale Surface Roughness on Friction: A Molecular Dynamics Study of Diamond Surfaces," Wear, 168(1-2), pp. 127-133.
[30] Zhang, L., and Tanaka, H., 1998, "Atomic Scale Deformation in Silicon Monocrystals Induced by Two-Body and Three-Body Contact Sliding," Tribology International, 31(8), pp. 425-433.

[31] Chantrenne, P., Raynaud, M., Clapp, P. C., Rifkin, J., and Becquart, C. S., 2000, "Molecular Dynamics Simulations of Friction," Heat and Technology, 18(SUPPL 1), pp. 49-56.
[32] Landman, U., Luedtke, W. D., and Ringer, E. M., 1992, "Atomistic Mechanisms of Adhesive Contact Formation and Interfacial Processes," Wear, 153(1), pp. 3-30.
[33] Nowak, J. D., Beaber, A. R., Ugurlu, O., Girshick, S. L., and Gerberich, W. W., 2010, "Small Size Strength Dependence on Dislocation Nucleation," Scripta Materialia, 62(11), pp. 819-822.
[34] Zhang, N., Deng, Q. A., Hong, Y., Xiong, L. M., Li, S., Strasberg, M., Yin, W. Q., Zou, Y. J., Taylor, C. R., Sawyer, G., and Chen, Y. P., 2011, "Deformation Mechanisms in Silicon Nanoparticles," Journal of Applied Physics, 109(6), pp.
[35] Deneen, J., Mook, W. M., Minor, A., Gerberich, W. W., and Barry Carter, C., 2006, "In Situ Deformation of Silicon Nanospheres," Journal of materials science, 41(14), pp. 4477-4483.
[36] Wu, Y. Y., Tsui, W. C., and Liu, T. C., 2007, "Experimental Analysis of Tribological Properties of Lubricating Oils with Nanoparticle Additives," Wear, 262(7-8), pp. 819-825.
[37] Tarasov, S., Kolubaev, A., Belyaev, S., Lerner, M., and Tepper, F., 2002, "Study of Friction Reduction by Nanocopper Additives to Motor Oil," Wear, 252(1–2), pp. 63-69.
[38] Zhao, Y., Zhang, Z., and Dang, H., 2003, "A Novel Solution Route for Preparing Indium Nanoparticles," The Journal of Physical Chemistry B, 107(31), pp. 7574-7576.
[39] Greenberg, R., Halperin, G., Etsion, I., and Tenne, R., 2004, "The Effect of Ws 2 Nanoparticles on Friction Reduction in Various Lubrication Regimes," Tribology Letters, 17(2), pp. 179-186.
[40] Zhao, Y., Zhang, Z., and Dang, H., 2004, "Synthesis of in–Sn Alloy Nanoparticles by a Solution Dispersion Method," Journal of Materials Chemistry, 14(3), pp. 299-302.
[41] Martin, J. M., and Ohmae, N., 2008, *Nanolubricants*, *Tribology Series*, John Wiley & Sons Ltd, England.
[42] Ghaednia, H., Jackson, R. L., and Khodadadi, J. M., 2013, "Experimental Analysis of Stable Cuo Nanoparticle Enhanced Lubricants," Journal of Experimental Nanoscience, In Print(pp.
[43] Fan, L., and Khodadadi, J. M., 2012, "An Experimental Investigation of Enhanced Thermal Conductivity and Expedited Unidirectional Freezing of Cyclohexane-Based Nanoparticle Suspensions Utilized as Nano-Enhanced Phase Change Materials," Int. J. Thermal Sciences, In Print(pp.
[44] Liu, G., Li, X., Qin, B., Xing, D., Guo, Y., and Fan, R., 2004, "Investigation of the Mending Effect and Mechanism of Copper Nanoparticles on a Tribologically Stressed Surface," Tribology Letters, 17(4), pp. 961-966.
[45] Poon, C. Y., and Bhushan, B., 1996, "Nano-Asperity Contact Analysis and Surface Optimization for Magnetic Head Slider/Disk Contact," Wear, 202(1), pp. 83-98.
[46] Adams, G. G., Müftü, S., Azhar, N. M., 2003, "A Scale-Dependant Model for Multi-Asperity Contact and Friction," ASME J. Tribol., 125(pp. 700-708.
[47] Adams, G. G., and Muftu, S., 2005, "Improvements to a Scale-Dependent Model for Contact and Friction," J. of Physics D: Applied Physics, 38(9), pp. 1402-1409.
[48] Almeida, L., Ramadoss, R., Jackson, R., Ishikawa, K., and Yu, Q., 2007, "Laterally Actuated Multicontact Mems Relay Fabricated Using Metalmumps Process:

Experimental Characterization and Multiscale Contact Modeling," J. Micro/Nanolith. MEMS MOEMS, 6(2), pp. 023009.
[49] Bhushan, B., Nosonovsky, M., 2003, "Scale Effects in Friction Using Strain Gradient Plasticity and Dislocation-Assisted Sliding (Microslip)," Acta Materialia, 51(pp. 4331-4345.
[50] Jackson, R. L., 2006, "The Effect of Scale Dependant Hardness on Elasto-Plastic Asperity Contact between Rough Surfaces," STLE Trib. Trans., 49(2), pp. 135-150.
[51] Jackson, R. L., Bhavnani, S. H., and Ferguson, T. P., 2008, "A Multi-Scale Model of Thermal Contact Resistance between Rough Surfaces," ASME J. Heat Transfer, 130(pp. 081301.
[52] Polonsky, I. A., Keer, L. M., 1996, "Scale Effects of Elastic-Plastic Behavior of Microscopic Asperity Contacts," ASME J. Tribol., 118(pp. pp.335-340.
[53] Dareing, D. W., and Khonsari, M., 1995, "Liquid Transported Powder Lubricant Study," Technical Report No. DTIC Document,
[54] Hua, D. Y., and Khonsari, M. M., 1996, "Elastohydrodynamic Lubrication by Powder Slurries," Journal of tribology, 118(1), pp. 67-73.
[55] Khonsari, M. M., 1997, "On the Modeling of Multi-Body Interaction Problems in Tribology," Wear, 207(1–2), pp. 55-62.
[56] Trezona, R. I., Allsopp, D. N., and Hutchings, I. M., 1999, "Transitions between Two-Body and Three-Body Abrasive Wear: Influence of Test Conditions in the Microscale Abrasive Wear Test," Wear, 225–229, Part 1(0), pp. 205-214.
[57] Adachi, K., and Hutchings, I. M., 2003, "Wear-Mode Mapping for the Micro-Scale Abrasion Test," Wear, 255(1–6), pp. 23-29.
[58] Clary, D. R., and Mills, G., 2011, "Preparation and Thermal Properties of Cuo Particles," The Journal of Physical Chemistry C, 115(5), pp. 1767-1775.
[59] Jackson, R. L., Green, I. , 2001, "Study of the Tribological Behavior of a Thrust Washer Bearing," Trib. Trans., 44(3), pp. 504-508.
[60] Venerus, D., Buongiorno, J., Christianson, R., Townsend, J., Bang, I., Chen, G., Chung, S., Chyu, M., Chen, H., Ding, Y., Dubois, F., Dzido, G., Funfschilling, D., Galand, Q., Gao, J., Hong, H., Horton, M., Hu, L., Iorio, C., Jarzebski, A., Jiang, Y., Kabelac, S., Kim, C., Kim, J., Kim, S., Mckrell, T., Ni, R., Philip, J., Prabhat, N., Song, P., Vaerenbergh, S., Wen, D., Witharana, S., Zhao, X., and Zhou, S., 2010, "Viscosity Measurements on Colloidal Dispersions (Nanofluids) for Heat Transfer Applications," Appl. Rheol., 20(pp. 7 pages.
[61] Einstein, A., 1906, "Eine Neue Bestimmung Der Molekuldimensionen," Ann. Phys., 19(pp. 289.
[62] Williams, J. A., 2000, *Engineering Tribology*, Oxford, New York.
[63] Jackson, R. L., and Green, I., 2006, "The Behavior of Thrust Washer Bearings Considering Mixed Lubrication and Asperity Contact," Tribology Transactions, 49(pp. 233-247.
[64] Chang, W. R., Etsion, I., Bogy, D., B., 1988, "Static Friction Coefficient Model for Metallic Rough Surfaces," ASME J. Tribol., 110(1), pp. 57-63.
[65] Cohen, D., Kligerman, Y., and Etsion, I., 2008, "A Model for Contact and Static Friction of Nominally Flat Rough Surfaces under Full Stick Contact Condition," ASME J. Tribol., 130(3), pp. 031401.

[66] Etsion, I., Levinson, O., Halperin, G., and Varenberg, M., 2005, "Experimental Investigation of the Elastic-Plastic Contact Area and Static Friction of a Sphere on Flat," ASME J. of Tribology, 127(1), pp. 47-50.
[67] Kogut, L., and Etsion, I., 2004, "A Static Friction Model for Elastic-Plastic Contacting Rough Surfaces," 126(1), pp. 34.
[68] Dickey, R. D. I., Jackson, R. L., and Flowers, G. T., 2011, "Measurements of the Static Friction Coefficient between Tin Surfaces and Comparison to a Theoretical Model," Journal of Tribology, 133(3), pp. 031408-7.
[69] Polycarpou, A. A., and Etsion, I., 1998, "Comparison of the Static Friction Subboundary Lubrication Model with Experimental Measurements on Thin-Film Disks," Tribology Transactions, 41(2), pp. 217-224.
[70] Lee, C.-H., Eriten, M., and Polycarpou, A. A., 2010, "Application of Elastic-Plastic Static Friction Models to Rough Surfaces with Asymmetric Asperity Distribution," Journal of Tribology, 132(3), pp. 031602-11.
[71] Lee, C.-H., and Polycarpou, A. A., 2007, "Static Friction Experiments and Verification of an Improved Elastic-Plastic Model Including Roughness Effects," Journal of Tribology, 129(4), pp. 754-760.
[72] Stempfle, P., Pantale, O., Djilali, T., Njiwa, R. K., Bourrat, X., and Takadoum, J., 2010, "Evaluation of the Real Contact Area in Three-Body Dry Friction by Micro-Thermal Analysis," Tribology International, 43(10), pp. 1794-1805.
[73] Greenwood, J., and Williamson, J., 1966, "Contact of Nominally Flat Surfaces," Proceedings of the Royal Society of London. Series A. Mathematical and Physical Sciences, 295(1442), pp. 300-319.
[74] Jackson, R. L., 2010, "An Analytical Solution to an Archard-Type Fractal Rough Surface Contact Model," Tribology Transactions, 53(4), pp. 543-553.
[75] Jackson, R. L., Malucci, R. D., Angadi, S., and Polchow, J. R., 2009, "A Simplified Model of Multiscale Electrical Contact Resistance and Comparison to Existing Closed Form Models," eds., pp. 28-35.
[76] Ohmura, T., Tsuzaki, K., and Matsuoka, S., 2001, "Nanohardness Measurement of High-Purity Fe–C Martensite," Scripta Materialia, 45(8), pp. 889-894.
[77] Williams, J., 2005, *Engineering Tribology*, Cambridge University Press,
[78] Lahouij, I., Dassenoy, F., Vacher, B., and Martin, J. M., 2011, "Real Time Tem Imaging of Compression and Shear of Single Fullerene-Like Mos 2 Nanoparticle," Tribology Letters, pp. 1-11.
[79] Mishra, M., and Szlufarska, I., 2012, "Analytical Model for Plowing Friction at Nanoscale," Tribology Letters, pp. 1-10.
[80] Greer, J. R., Oliver, W. C., and Nix, W. D., 2005, "Size Dependence of Mechanical Properties of Gold at the Micron Scale in the Absence of Strain Gradients," Acta Materialia, 53(6), pp. 1821-1830.
[81] Greenwood, J., 1988, "Film Thicknesses in Circular Elastohydrodynamic Contacts," Proceedings of the Institution of Mechanical Engineers, Part C: Journal of Mechanical Engineering Science, 202(1), pp. 11-17.
[82] Dowson, D., 1995, "Elastohydrodynamic and Micro-Elastohydrodynamic Lubrication," Wear, 190(2), pp. 125-138.
[83] Dowson, D., and Higginson, G., 1959, "A Numerical Solution to the Elasto-Hydrodynamic Problem," Journal of Mechanical Engineering Science, 1(1), pp. 6-15.

[84] Hamrock, B., and Dowson, D., 1976, "Isothermal Elastohydrodynamic Lubrication of Point Contacts: Part Ii—Ellipticity Parameter Results," Journal of Lubrication Technology, 98(pp. 375.
[85] Hamrock, B. J., and Dowson, D., 1976, "Isothermal Elastohydrodynamic Lubrication of Point Contacts: Part 1—Theoretical Formulation," Journal of Lubrication Technology, 98(pp. 223.
[86] Johnston, G., Wayte, R., and Spikes, H., 1991, "The Measurement and Study of Very Thin Lubricant Films in Concentrated Contacts," Tribology Transactions, 34(2), pp. 187-194.
[87] Cooper, D., and Moore, A., 1994, "Application of the Ultra-Thin Elastohydrodynamic Oil Film Thickness Technique to the Study of Automotive Engine Oils," Wear, 175(1), pp. 93-105.
[88] Zhang, C., 2005, "Research on Thin Film Lubrication: State of the Art," Tribology International, 38(4), pp. 443-448.
[89] Gao, J., Luedtke, W., and Lman, U., 1995, "Nano-Elastohydrodynamics: Structure, Dynamics, and Flow in Nonuniform Lubricated Junctions," Science, 270(5236), pp. 605-608.
[90] Abd-Alsamieh, M., and Rahnejat, H., 2001, "Nano-Lubricant Film Formation Due to Combined Elastohydrodynamic and Surface Force Action under Isothermal Conditions," Proceedings of the Institution of Mechanical Engineers, Part C: Journal of Mechanical Engineering Science, 215(9), pp. 1019-1029.
[91] Ghaednia, H., Jackson, R. L., and Khodadadi, J. M., 2013, "Experimental Analysis of Stable Cuo Nanoparticle Enhanced Lubricants," Journal of Experimental Nanoscience, pp. 1-18.
[92] Kalin, M., Kogovšek, J., and Remškar, M., 2012, "Mechanisms and Improvements in the Friction and Wear Behavior Using Mos< Sub> 2</Sub> Nanotubes as Potential Oil Additives," Wear, 280(pp. 36-45.
[93] Tao, X., Jiazheng, Z., and Kang, X., 1996, "The Ball-Bearing Effect of Diamond Nanoparticles as an Oil Additive," Journal of Physics D: Applied Physics, 29(11), pp. 2932.
[94] Tannous, J., Dassenoy, F., Lahouij, I., Le Mogne, T., Vacher, B., Bruhács, A., and Tremel, W., 2011, "Understanding the Tribochemical Mechanisms of If-Mos 2 Nanoparticles under Boundary Lubrication," Tribology Letters, 41(1), pp. 55-64.
[95] Li, B., Wang, X., Liu, W., and Xue, Q., 2006, "Tribochemistry and Antiwear Mechanism of Organic–Inorganic Nanoparticles as Lubricant Additives," Tribology Letters, 22(1), pp. 79-84.
[96] Ghaednia, H., and Jackson, R. L., 2013, "The Effect of Nano-Particles on the Real Area of Contact, Friction and Wear," J. of Tribology pp.
[97] Johnson, K. L., 1987, *Contact Mechanics*, Cambridge university press,
[98] Zhen, S., and Davies, G., 1983, "Calculation of the Lennard-Jones N–M Potential Energy Parameters for Metals," physica status solidi (a), 78(2), pp. 595-605.
[99] Nath, S. K., Escobedo, F. A., and De Pablo, J. J., 1998, "On the Simulation of Vapor–Liquid Equilibria for Alkanes," The Journal of Chemical Physics, 108(pp. 9905.
[100] Allen, M. P., and Tildesley, D. J., 1989, *Computer Simulation of Liquids*, Oxford university press,

[101] Plimpton, S., 1995, "Fast Parallel Algorithms for Short-Range Molecular Dynamics," Journal of Computational Physics, 117(1), pp. 1-19.
[102] Gao, J., Luedtke, W., and Landman, U., 1997, "Layering Transitions and Dynamics of Confined Liquid Films," Physical review letters, 79(4), pp. 705-708.
[103] Gao, J., Luedtke, W. D., and Landman, U., 1997, "Origins of Solvation Forces in Confined Films," 5647(pp. 4013-4023.
[104] Dijkstra, M., 1997, "Confined Thin Films of Linear and Branched Alkanes," Journal of Chemical Physics, 107(8), pp. 3277-3288.
[105] Zhang, L., Balasundaram, R., Gehrke, S. H., and Jiang, S., 2001, "Nonequilibrium Molecular Dynamics Simulations of Confined Fluids in Contact with the Bulk," The Journal of Chemical Physics, 114(pp. 6869.
[106] Wadwalkar, S., Jackson, R., and Kogut, L., 2010, "A Study of the Elastic—Plastic Deformation of Heavily Deformed Spherical Contacts," Proceedings of the Institution of Mechanical Engineers, Part J: Journal of Engineering Tribology, 224(10), pp. 1091-1102.
[107] Jackson, R. L., and Green, I., 2005, "A Finite Element Study of Elasto-Plastic Hemispherical Contact," ASME J. Tribol., 127(2), pp. 343-354.

7. Thermal Conductivity and Heat Dispersion Effect
(Dr. Kuang-Ting Hsiao, Mechanical Engineering, University of South Alabama)

Summary

Under the project, the USA group has been working on synthesis and thermal conductivity characterization of several types of NEPCMs including CNF/paraffin wax NEPCMs and the high temperature HHTCNF/$ZnCl_2$ NEPCMs. The paraffin matrix NEPCM study shows that the thermal conductivity enhancements due to 8 wt% HHTCNF doping were 126.3% and 210.8% while being in the liquid phase and in the solid phase, respectively. The LHT grade CNF, however, provided much less thermal conductivity enhancement to the NEPCM. Therefore, it has been concluded the thermal conductivity enhancement of a CNF/paraffin NEPCM substantially depends on the phase of the PCM, the loading of CNF, and the type of CNF used. For the high temperature HHTCNF/$ZnCl_2$ NEPCM study, the 8wt% HHTCNF/$ZnCl_2$ NEPCM improved the thermal conductivity by almost 200%.

The thermal conductivity enhancement of NEPCM also provides a significant improvement in the thermal energy charging and discharging speed when using NEPCM as the energy storage material. Compared with the base paraffin wax PCM, the 8wt% HHTCNF/paraffin wax NePCM significantly accelerated the discharging speed and the charging speed to 3 times (340%) and 2 times (200%) respectively.
A numerical study about the heat dispersion of the liquid-phase NEPCM was performed. Heat dispersion is an enhanced heat transfer due to local-level heat convection deviation from the macro-scale heat convection within a representative unit cell of either a porous medium or a solid-liquid mixture. Through the unit cell non-isothermal computational fluid dynamics (CFD) simulations, it was concluded that the heat dispersion effect can be approximated by an analytical function of Peclet number, Reynolds number, and nanoparticle volume fraction. For a simulated micro-channel flow study of a liquid-phase NEPCM consisting of 5% volume-fraction CuO-Paraffin, the heat dispersion was found to increase the total heat transfer by about 8%.

A parallel plate device was developed for measuring the thermal conductivity of PCM and NEPCM through their phase-changing period. The thermal conductivity measurement during the phase-changing period cannot be measured by traditional the transient hot wire method due to the latent heat involved during the phase-changing process. This in-house developed parallel plate device is a steady-state method and can measure the thermal conductivity within the phase-changing temperature zone. The eicosane and CuO/eicosane NEPCM were tested by the parallel plate device; reasonable results and trendlines were found. As being heated near the melting point, rapidly decreasing trends of thermal conductivity can be found in both the eicosane and the CuO/eicosane NEPCM cases.

Under this research project, three master students were graduated with quality master theses and one continues his thesis work. An invention disclosure was filed in early 2013. The PI has been in contact with the recently graduated master students to prepare manuscripts based on their research results.

7.1. TECHNICAL CONTENTS:

7.1.1. Topic 1: Thermal conductivity measurement and synthesis of CNF/Paraffin matrix NePCM

This work is mainly based on our work reported in [1, 2, 3]. The USA group began by mixing Carbon Nanofibers (CNF) into paraffin matrices. Two different grades of CNFs and two different paraffin matrices were used. Substantial improvement in the thermal conductivity was found. Also, the thermal conductivity significantly depends on the phase of the NEPCM and the type of CNF used.

A household paraffin wax (from Gulf Wax) along with Light-Heat-Treated (LHT) CNF (PR-24, from Applied Science, Inc.) was used for the first set of experimental study. The PR-24 CNF has a diameter about 100 nm and length about 50-200 μm according to the manufacturer. The PCM was placed in an oven and melted into a liquid. Then, CNF was mixed into it. The PCM was mixed by hand for approximately 5 minutes and then sonicated for 50 minutes. The sonication process allows for better CNF dispersion in the PCM. As shown in Figure 7.1, the microscope picture indicates throrough dispersion of CNFs within the paraffin wax matrix.

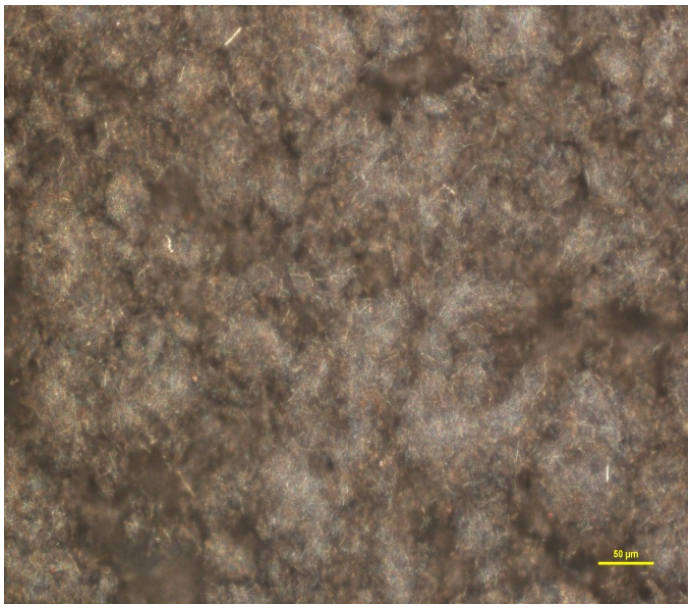

Figure 7.1: Microscope pictures of NEPCM with 4 wt% LHT-CNF at 200x magnification.

The PCM was placed back into the oven to maintain its liquid form in order to create two different test samples, one with 4 weight percent (4 wt%) CNF enhanced paraffin wax and one with the pristine paraffin wax. The PCM was poured into a wax paper mold to achieve a cylindrical shape and cooled to the room temperature. A KD2 Pro thermal analyzer manufactured by Decagon Devices, Inc. was used to measure the thermal conductivity of the PCM and NEPCM samples. Figure 7.2 shows the measurement

setup of the device. The KD2 Pro measurement device is fast and simple to use. A TR-1 needle sensor was placed into the specimen and the device measured the thermal conductivity within ± 5% of the actual value. Each test took approximately five minutes.

Figure 7.2: Picture of the KD2 Pro measurement device used to measure the thermal conductivity of each specimen.

The KD2 Pro was used to take five thermal conductivity measurements of the pristine PCM and five measurements of the NEPCM with CNF. Table 7.1 lists the results of the KD2 Pro device. The KD2 Pro measurement device found that the thermal conductivity of the PCM was enhanced by the inclusion of 4 wt% CNF for about 38.6%.

Table 7.1: Thermal conductivity results from the KD2 Pro measurement device for the 4 wt% CNF enhanced paraffin wax sample and the pristine paraffin wax sample.

Test Run	*Pristine Paraffin Wax [W/m·K]*	*4 wt% CNF/Paraffin Wax [W/m·K]*
Run 1	0.264	0.375
Run 2	0.268	0.379
Run 3	0.267	0.363
Run 4	0.266	0.377

Run 5	0.268	0.364
AVERAGE	**0.267**	**0.372**
% improvement	**-**	**39.4%**

After the success of the 4 wt% LHT grade CNF/Paraffin Wax NEPCM. A more systematic study was conducted. The paraffin was changed to industrial grade paraffin wax provided by Sigma-Aldrich Inc. (St. Louis, Missouri) with a melting temperature range of (53-57°C) and a thermal conductivity of 0.151 and 0.242 W/m•K for liquid and solid respectively. Two types of heat treated PR-24 CNFs were purchased from Applied Sciences, Inc. (Cedarville, OH) with an average diameter and length of 100 nm and 50-200 μm respectively. High heat-treated carbon nanofibers (HHTCNFs) and low heat-treated carbon nanofibers (LHTCNFs) are produced from heat treating the as-produced PR-24 vapor grown carbon nanofibers (VGCNFs) to different temperature levels. HHTCNFs are produced from heating VGCNFs to 3000°C, which creates a fully graphitic fiber with miniscule iron levels, while LHTCNFs are produced from a heat treatment of 1500°C and have much greater iron content than that of HHTCNFs [4]. According to [4], the LHTCNFs have higher electrical conductivity values, while the HHTCNFs have higher thermal conductivity values. The exact thermal conductivity of CNF is largely unknown, but Al-Saleh et al. estimated that the thermal conductivity of CNF is approximately 1950 W/m•K [5], while S. Agarwal et al. stated that the thermal conductivity value of CNF should be compared to that of graphite (600 W/m•K) [6]. The thermal conductivity of each NePCM sample was measured at its solid phase and liquid phase. The thermal conductivity tests were recorded by using KD2-Pro Thermal Properties Analyzer (Decagon Devices Inc. Pullman, Washington). The KD2-Pro has two detachable probes for thermal conductivity testing (KS-1 sensor for liquids (accuracy: ±5%) and TR-1 sensor for solids (accuracy: ±10%)).

Thermal conductivity testing in the liquid phase of 2, 4, 6, and 8 wt% HHTCNF/paraffin NePCM samples compared to that of base paraffin wax (0.151W/m K ±5%) increased 36.7, 65.4, 103.5, and 126.3% respectively at a temperature range of 57-59°C, while the LHTCNF/paraffin NePCM samples increased 19.7, 26.9, 42.4, and 50.2% for the same respective weight fractions. These results are clearly shown in Figure 7.3. The liquid phase thermal conductivity for both LHTCNF and HHTCNF NePCM increases at an almost linear rate as the CNF weight fraction increases.

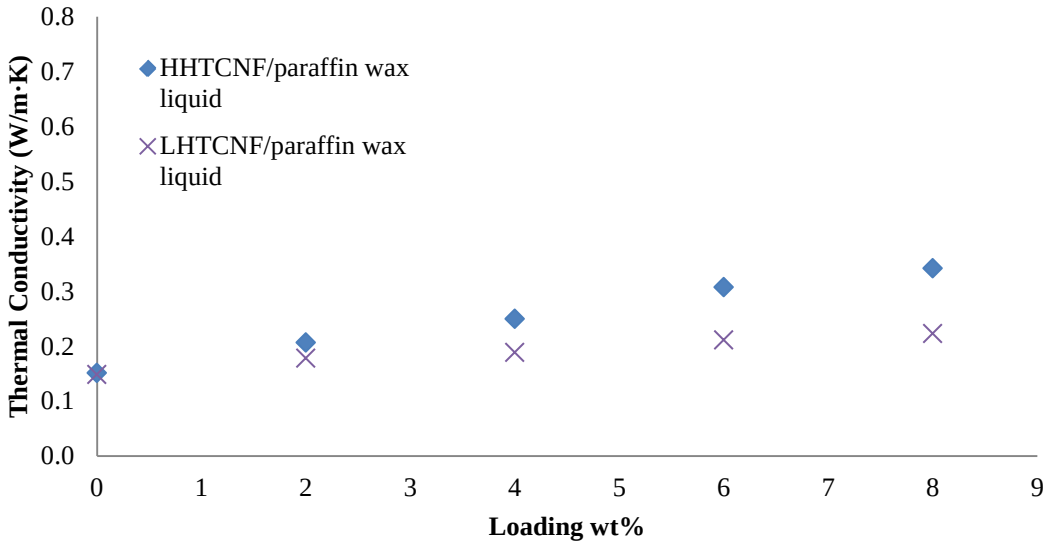

Figure 7.3: Liquid thermal conductivity of LHTCNF/paraffin and HHTCNF/paraffin NePCMs vs. the CNF weight fractions.

Similarly, Figure 7.4 shows the results of thermal conductivity tests in the solid phase with 2, 4, 6, and 8 wt% CNF enhanced NePCM samples compared to that of base solid paraffin wax (0.242 W/m K ±10%). Increases of 63.8, 123.2, 177.3, 210.8% for HHTCNF/paraffin NePCM samples and 22.6, 38.2, 41.4, and 59.7% for LHTCNF/paraffin NePCM samples were observed respectively at room temperature (22-24 °C). The solid phase thermal conductivity also increases at an almost linear rate as the CNF weight fraction increases.

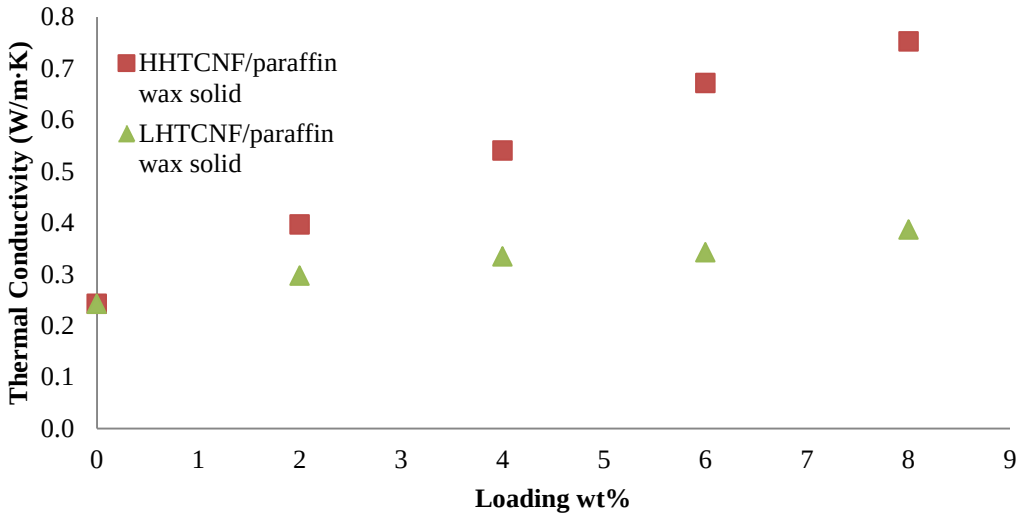

Figure 7.4: Solid thermal conductivity of LHTCNF/paraffin and HHTCNF/paraffin NePCMs vs. the CNF weight fractions.

From the results shown in Figure 7.3 and Figure 7.4, it is found that HHT grade CNF is much more effective than the LHT grade CNF for enhancing the thermal conductivity of NEPCM. Furthermore, the solid state NEPCM has much higher thermal conductivity as well as the relative improvement than the liquid state NEPCM. A more detailed comparison is shown in Table 7.2. The phase-induced relative % increase of the thermal conductivity is raised from 60.23% to 120.00% when the HHT-CNF loading is increased from 0 wt% to 8 wt%. Such phase-induced thermal conductivity improvement is believed to be due to the solidification of the PCM, thus reducing the thermal resistance between the highly conductive CNFs in the NePCM.

In conclusion, CNF can substantially enhance the thermal conductivity of paraffin wax based NePCM. It is proved that the thermal conductivity enhancement is a function of (1) CNF grade, (2) CNF loading, and (3) phase of the PCM. With an 8 wt% HHTCNF loading in a paraffin was-based NePCM, the thermal conductivity can be increased by 201.8% as shown in Table 7.2.

Table 7.2: HHTCNF/paraffin thermal conductivity (k) data, the relative percent increase against the base paraffin, and the relative percent increase due to phase change from liquid to solid.

HHTCNF loading	**0wt%** (Base paraffin)	**2wt%**		**4wt%**		**6wt%**		**8wt%**	
	k (W/m·K)	k (W/m·K)	Relative % Increase Against the base paraffin of the same phase	k (W/m·K)	Relative % Increase Against the base paraffin of the same phase	k (W/m·K)	Relative % Increase Against the base paraffin of the same phase	k (W/m·K)	Relative % Increase Against the base paraffin of the same phase
Liquid Phase	0.1511	0.2065	36.7%	0.2499	65.4%	0.3075	103.5%	0.3420	126.3%
Solid Phase	0.2421	0.3965	63.8%	0.5404	123.2%	0.6714	177.3%	0.7524	210.8%
Relative % Increase from liquid phase to solid phase	60.23%	92.00%		116.25%		118.34%		120.00%	

7.1.2. Topic 2: Thermal charging and discharging tests of NEPCM

An important purpose of NePCM is to increase the energy discharging and charging speeds. Such charging and discharging behaviors occur at the melting point (zone) when the conversion between the PCM's latent heat and the environmental energy is in the process. The USA group has performed the discharging and charging test of a HHTCNF/paraffin wax sample (see Figure 7.5a) by alternatively placing the sample into boiling water and an ice/water mixture and recording the center temperature (see Figure 7.5b). Table 7.3 further shows the speeds and times for discharging and charging processes through the phase-transition zone. Compared with the base PCM, the 8 wt% HHTCNF/paraffin wax NePCM significantly accelerated the discharging speed and the charging speed to 3 times (340%) and 2 times (200%) respectively.

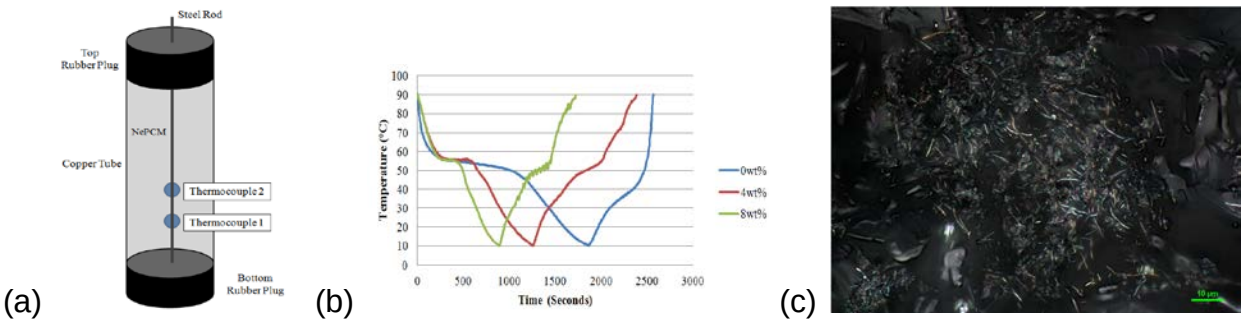

Figure 7.5: (a) NePCM being placing inside the copper tube container for discharging and charging test. (b) Center temperature (thermocouple 2) vs. time for the discharging and charging test for 0wt%, 4%, and 8 wt% HHTCNF/paraffin wax NePCM. (c) Microscope picture of 8 wt% HHTCNF/paraffin wax NePCM [2].

Table 7.3: Comparison of the times and speeds for discharging and charging processes through the phase-transition. 8 wt% HHTCNF/Paraffin wax NePCM achieved a significant improvement in the discharging and charging performance. [2]

	Discharge Through the Phase Change			Charge Through the Phase Change		
Specimen	Time (seconds)	Relative Speed	Relative Time	Time (seconds)	Relative Speed	Relative Time
Paraffin Wax	1070	100%	100%	435	100%	100%
4wt% HHTCNF/Paraffin Wax	635	169%	59%	317	137%	73%
8wt% HHTCNF/Paraffin Wax	315	340%	29%	217	200%	50%

7.1.3. Topic 3: Thermal conductivity measurement for CNF/Salt matrix NEPCM

Based on the heat engine model in thermodynamics, the same amount of heat stored at a higher temperature has a higher exergy, which is the capability to produce work when the thermal energy being released to the atmospheric environment at the room temperature. Thus, although paraffin waxes are high capacity PCMs, the thermal energy stored in the paraffin waxes, however, contains low level exergy due to the paraffin waxes' low melting points. To create a NEPCM with the capability to store thermal energy that has a high exergy level, the USA group has been looking for the high temperature salt-matrix NEPCM. An example is the table salt (NaCl), which has a very high melting point of 801°C that is much higher the melting point of industrial grade paraffin wax at 57-59°C. However, due to difficulty to handle the salt-induced corrosive environment at such high temperature, the USA Group tried to use a salt with a much lower melting point that could be handled by many metals. The zinc chloride ($ZnCl_2$, melting point of 292°C) was selected for this study. The zinc chloride powder was mixed the HHTCNF and then melted in an oven then allowed to be cooled in the oven. The thermal conductivity of the NEPCM was only measured at its solid phase at the

room temperature by KD2-Pro due to the temperature limit the KD2-Pro can handled. The thermal conductivity of the solid-phase HHTCNF/$ZnCl_2$ NEPCM has a strong and positive dependence on the HHTCNF's loading as shown in Figure 7.6. The pure $ZnCl_2$ has a thermal conductivity of 0.64 W-m/°C and the 8 wt% HHTCNF/$ZnCl_2$ NEPCM improved the thermal conductivity by almost a 200% increment. Figure 7.7 shows the microscope pictures of the NEPCM with different HHTCNF loadings. Note that there is no successful liquid phase thermal conductivity measurement and charging and discharging testing results due to the difficulty to handle the molten $ZnCl_2$ salt at the high temperature (above 292°C) that many sealants and metals would fail. Nevertheless, the effectiveness of HHTCNF in enhancing the thermal conductivity of salt-based NEPCM has been proven by the experiments.

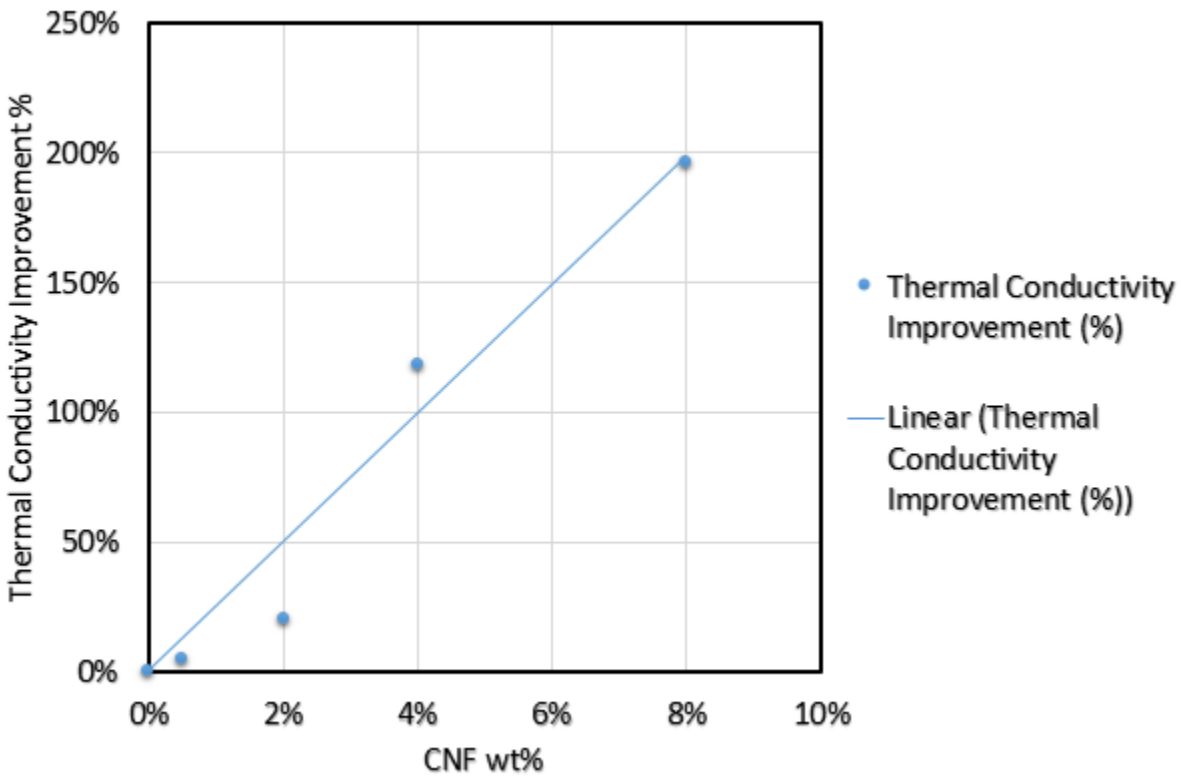

Figure 7.6: Thermal conductivity improvement of solid-phase HHTCNF/ZnCl2 NEPCM of various CNF weight fractions.

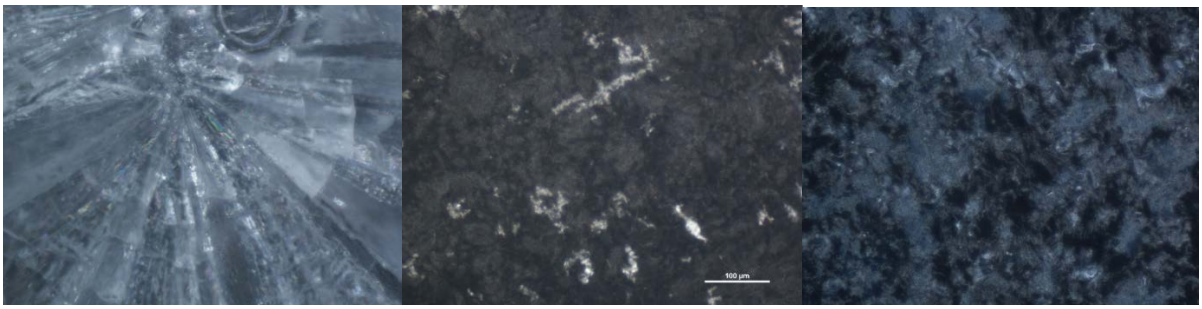

(a)Neat $ZnCl_2$ (b)0.5wt% HHTCNF/$ZnCl_2$ (c) 2.0wt% HHTCNF/$ZnCl_2$

Figure 7.7: Microscope pictures for different weight fractions of HHTCNF/$ZnCl_2$ NEPCMs.

7.1.4. Topic 4: Numerical Modeling of Heat Dispersion in NEPCM

One interesting topic of the NEPCM is the possible heat dispersion effect of the liquid-phase NEPCM. Heat dispersion is the enhanced heat transfer due to local-level heat convection deviation from the macro-scale heat convection in a representative unit cell of a porous medium or a solid-liquid mixture. The goal of this work is to understand the potential impact of heat dispersion phenomenon on a nanofluid (i.e., nanoparticles suspending in a liquid matrix) such as a liquid NEPCM. The representative unit cell approach has been used to study the velocity distribution and the temperature distribution when a shear flow condition is applied to a nanofluid consisting of sphere conductive nanoparticles [7]. The geometry of the representative unit cell is given in Figure 7.8. The simulated velocity results show that there are circulation zones in the unit cell caused by the nanoparticle and the shear flow (see Figure 7.9). If one applies a temperature drop in the vertical direction of the unit cell, these circulation zones will enhance the overall heat transfer in the vertical direction (see Figure 7.10). The temperature contours shown in Figure 7.10 clearly indicate the dependence to the Reynolds Number and the Peclet Number. Note that the Reynolds number and Peclet number are based on the shear rate applied to the unit cell and the unit cell length. As there is no net-flow in the vertical direction, such heat transfer is associated with heat dispersion instead of macro-scale convection (which is zero since the net velocity of the unit cell in the vertical direction is zero). To quantitatively describe the heat dispersion, the dimensionless heat dispersion coefficient is defined as:

$$k_{disp}^{*} = \frac{k_{disp}}{k_f} = \frac{k_{total} - k_{stag}}{k_f} \tag{7.1}$$

where k_f, k_{total}, and k_{stag} are the fluid thermal conductivity, total thermal conductivity of the unit cell, and the thermal conductivity of the unit cell when the flow is stagnant, respectively.

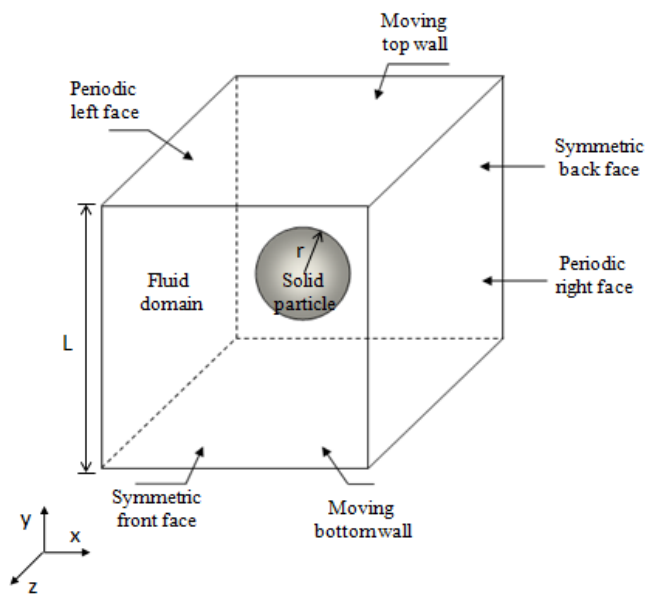

Figure 7.8: A representative unit cell of a nanofluid and its boundaries.

(a)

(b)

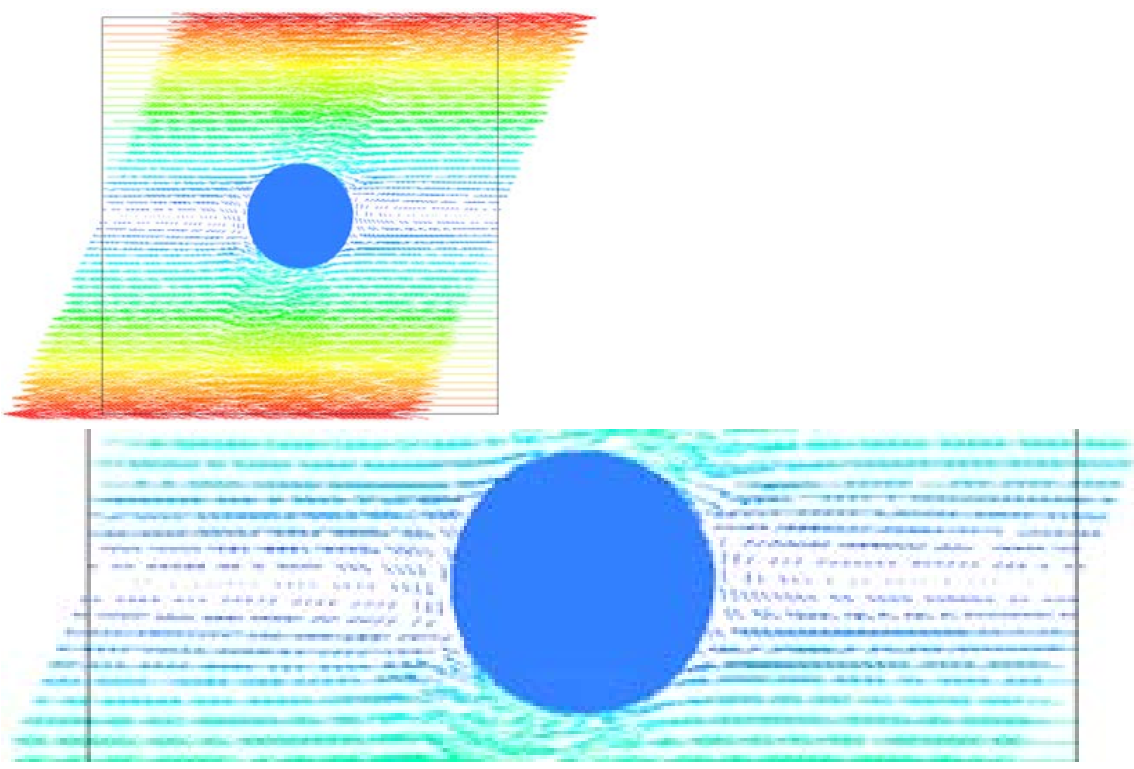

Figure 7.9: Example of velocity distribution (a) unit cell results (b) circulation zones.

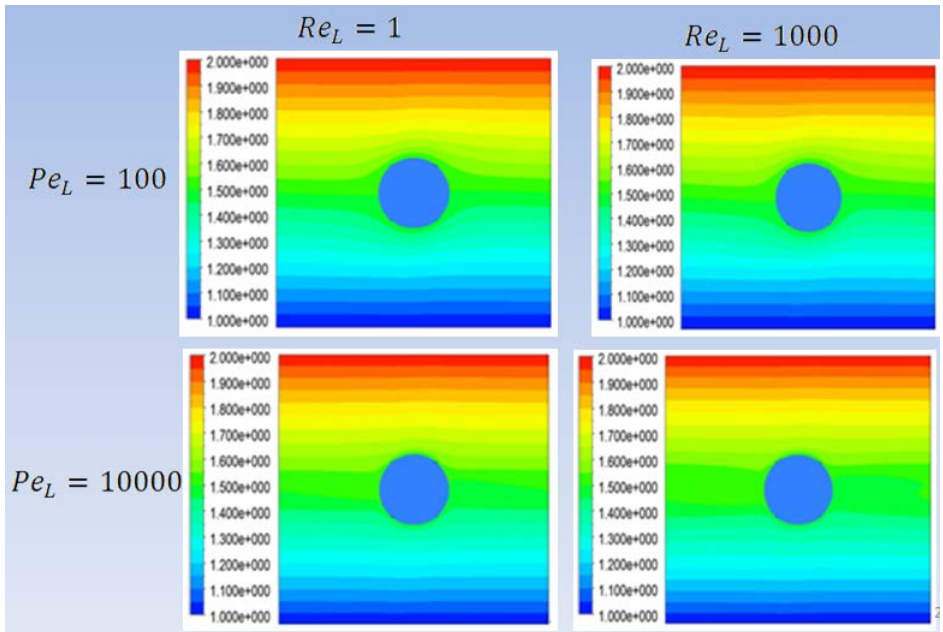

Figure 7.10: Temperature contours of the unit cell simulations with different Peclet numbers and Reynolds numbers.

By using the numerical simulation with zero flow velocity (i.e., stagnant), it was validated that the k_{stag} agrees with the Maxwell's model nicely as shown in Figure 7.11. Note the Maxwell's model [8] is given as:

$$\frac{k_{E,maxwell}}{k_f} = \frac{k_s + 2.k_f + 2.(k_s - k_f).\varphi_s}{k_s + 2.k_f - (k_s - k_f).\varphi_s} \tag{7.2}$$

where k_E, k_f, and k_s are the thermal conductivity of the nanofluid, base fluid and nanoparticles, respectively and φ_s is the volume fraction of the nanoparticles. Hence, one can assume:

$$k^*_{stag} = \frac{k_{stag}}{k_f} = \frac{k_{E,maxwell}}{k_f} = \frac{k_s + 2.k_f + 2.(k_s - k_f).\varphi_s}{k_s + 2.k_f - (k_s - k_f).\varphi_s} \tag{7.3}$$

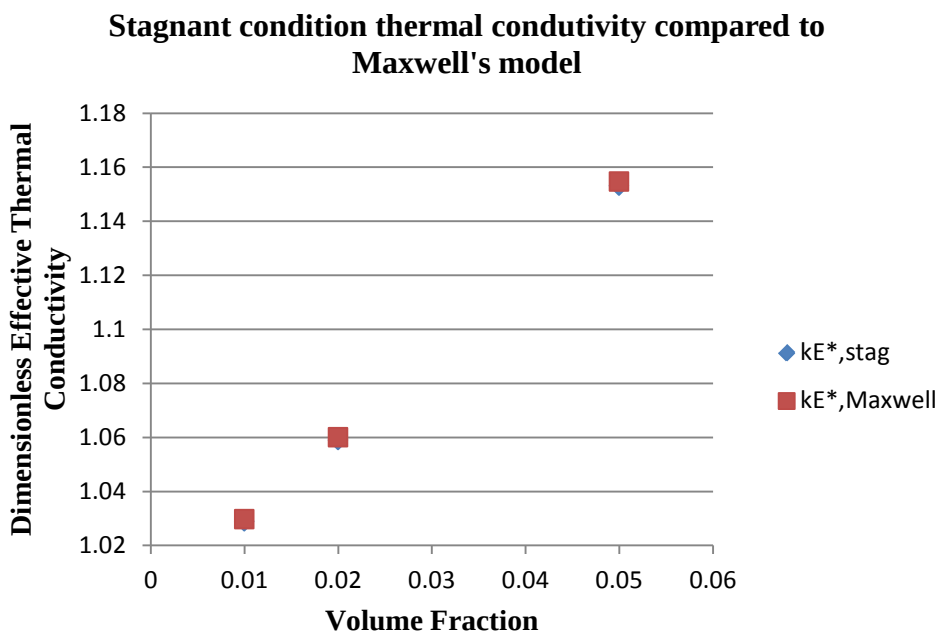

Figure 7.11: The Numerical Results of Dimensionless Stagnant Thermal Conductivity and Maxwell's Model.

By conducting many unit cell simulations with different Peclet numbers, Reynolds numbers, volume fractions, and thermal conductivity ratio between solid nanoparticle and fluid matrix, we obtained many data points. An interesting correlation of the data points against the diameter based Reynolds number (Re_d), diameter based Peclet number (Pe_d), and volume fraction (φ) has been found as:

$$k_{disp}^{*} = 0.00784 Re_d^{0.0352} \varphi_s^{0.988} \left(Pe_d \left(\frac{6\varphi_s}{\pi} \right)^{-\frac{1}{3}} \right)^{\left(0.9 - \left(\left(-1.3*10^{-6} Re_d^2 \varphi_s^{-\frac{2}{3}} + 1.6*10^{-5} Re_d \varphi_s^{-\frac{1}{3}} + 1.43 \right) \varphi_s \right) \right)} \tag{7.4}$$

Note that the thermal conductivity ratio between the solid nanoparticle and the fluid matrix has no much less influence to the heat dispersion. The strongest influence is from the diameter-based Peclet number. The dependence on the diameter-based Peclet number indicates that the heat dispersion phenomenon will be less significant if we decrease the diameter of the nanoparticle or reduce the shear rate of the nanofluid.

For practical reasons, it is important to know the total effective thermal conductivity. From the modeling analysis, the total effective thermal conductivity can be approximated as:

$$k_{total} = k_f k^*_{total} = k_f\left(k^*_{stag} + k^*_{disp}\right) =$$

$$k_f\left(\frac{k_s+2.k_f+2.(k_s-k_f).\varphi_s}{k_s+2.k_f-(k_s-k_f).\varphi_s} + 0.00784 Re_d^{0.0352}\varphi_s^{0.988}\left(Pe_d\left(\frac{6\varphi_s}{\pi}\right)^{-\frac{1}{3}}\right)^{\left(0.9-\left(\left(-1.3*10^{-6}Re_d^2\varphi_s^{-\frac{2}{3}}+1.6*10^{-5}Re_d\varphi_s^{-\frac{1}{3}}+1.43\right)\varphi_s\right)\right)}\right) \quad (7.5)$$

This equation approximation provides about less than 3% deviation from the non-isothermal CFD simulation results for an assumed case study of micro-channel flow consisting of a 5% volume-fraction CuO-Paraffin NEPCM [8]. For this simulated micro-channel flow study, the heat dispersion was found to increase the heat transfer by 8%.

7.1.5. Topic 5: Parallel Plate Thermal Conductivity Measurement Device

For measuring the thermal conductivity of a PCM or a NEPCM, the KD2-Pro sensor, which is based on transient hot wire method, can be used for measuring the PCM or NEPCM in either liquid phase or solid phase. However, if the temperature is very close to the melting point, the transient hot wire method will not work since it cannot handle the scenario if the latent heat is involved during the measurement. Hence, it is necessary to have a method for measuring the thermal conductivity of a PCM or a NEPCM from the solid phase to the liquid phase. The parallel plate method developed by the USA group is a steady state method and can achieve this objective (see Figure 7.12) [2]. The thermal conductivity data of eicosane and 8 wt% CuO/eicosane NEPCM were collected from the solid-phase to the liquid-phase by the parallel plate device and is shown in Figure 7.13 [2]. For both materials, the thermal conductivity smoothly decreased when the temperature increased. However, as shown in Figure 7.3, there is a steeper thermal conductivity decrease trend when the temperature increases close to the melting point.

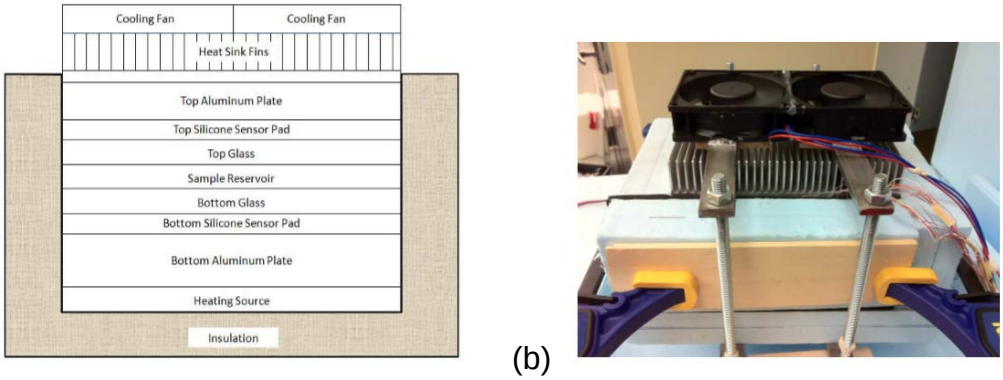

(a) (b)

Figure 7.12: Parallel plate device for thermal conductivty measurment [2]. (a) schematic, (b) assembed system ready to use.

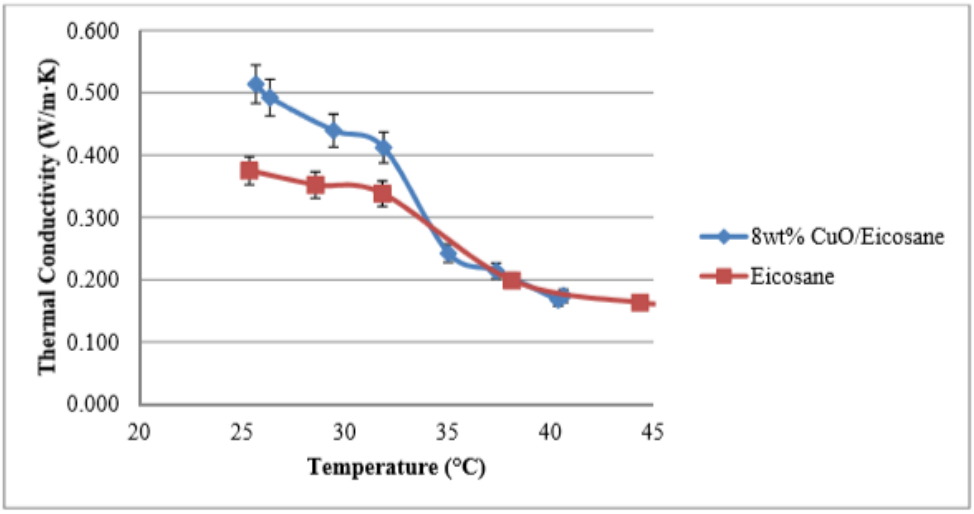

Figure 7.13: Thermal conductivity measurements with the parallel plate device through the phase change of 8wt% CuO/Eicosane NePCM compared to base eicosane. [2]

7.2. GRADUATE STUDENTS INVOLVED IN NEPCM RESEARCH

One of the important missions of the project is education and workforce development. The USA group has graduated three master (i.e., Master of Science degree in Mechanical Engineering) students funded by this project and currently still have one graduate student working on his master's thesis. Table 7.4 summarized the graduate student education activities. The graduated students have been either working or pursuing Ph.D. study after leaving the group. The USA-PI will work with the already graduated master students to continue publishing journal papers based on their thesis work.

Table 7.4: Summary of graduate students supported by this project.

Name	Inst.	Degree Pursued/ Awarded (date)	Duration of Involvement with Project	Published/Submitted Papers on NePCM		Invention Disclosure
				Journal	Conf.	
Mr. Peter Sakalaukus	USA	MS / Aug. 2011	12/09-8/11	0	1	0
Mr. Andrew Mosley	USA	MS / Dec. 2012	8/10-12/12	0 *	1	1 [3]
Ms. Anusha Rudraraju	USA	MS / May 2013	1/11-12/12	0 *	0	0
Mr. Nathan Brock	USA	MS / (exp. 5/14)	8/11 - now	0 *	0	0

**Note: We will continue to prepare journal paper manuscripts based on the master students' thesis results as shown in the aforementioned topics.*

7.3. REFERENCES

1. Sakalaukus Jr. P.J., Mosley A., Farah B.I., Hsiao K.-T. "Thermal conductivity characterization of nano-enhanced paraffin wax." Proceedings of the ASME 2011 International Mechanical Engineering Congress & Exposition (IMECE2011), November 11-17, 2011, Denver, Colorado, USA. (paper number: IMECE2011-65070)
2. Mosley A.W, "An experimental study of the thermal properties of a nano enhanced paraffin wax," **Master Thesis**, Department of Mechanical Engineering, University of South Alabama, December 2012.
3. Mosley A.W. and Hsiao K.-T. "Method and Processing of Nanofiber Enhanced Phase Change Materials", Invention Disclosure filed to University of South Alabama, Tech Transfer Office.
4. "Pyrograf III Carbon Nanofiber," Pyrograf Products Inc, [Online]. Available: http://pyrografproducts.com/Merchant5/merchant.mvc?Screen=cp_nanofiber. [Accessed 18 February 2013].

5. Y. Zhong, Q. Guo, S. Li, J. Shi and L. Liu, "Heat transfer enhancement of paraffin wax using graphite foam for thermal energy storage," Solar Energy Materials and Solar Cells, vol. 94, pp. 1011-1014, 2010.
6. M. H. Al-Saleh and U. Sundararaj, "A review of vapor grown carbon nanofiber/polymer conductive composites," Carbon, vol. 47, pp. 2-22, 2009.
7. Rudraraju A., “Numerical investigation of the enhanced thermal conductivity due to heat dispersion of a nanofluid,” **Master Thesis**, Department of Mechanical Engineering, University of South Alabama, May 2013.
8. J. C. Maxwell, *A treatise on electricity and magnetism*. Oxford : Clarendon Press, 1873.

Training of Students: The following PhD, MS, BS and HS students have been associated with the NePCM projects at five (5) Alabama institutions:

Name	*Inst.*	*Degree Pursued/ Awarded or Expected Date*	*Duration of Involvement with Project*	*Published/Submitted Papers on NePCM*	
				Journal	*Conf.*
Dr. Dan CLARY	AU	PhD / Dec. 2011	8/07 - 12/11	4	1
Mr. Sharif HOSSAIN	AU	PhD / (exp. 8/14)	8/11 - now	0	1
Mr. Jason DARVIN	AU	BS / May 2013	8/11 - now	0	0
Dr. Liwu FAN	AU	PhD / Aug. 2011	8/07 - 8/11	4	6
Mr. Mahdi NABIL	AU	MS / Aug. 2013	8/11 – 8/13	1	3
Mr. Hasan BABAEI	AU	PhD / (exp. 8/14)	8/09 - now	6	6
Mr. Yousef EL HASADI	AU	PhD / Aug. 2013	8/08 – 8/13	2	6
Mr. M. MOEINI SEDEH	AU	PhD / (exp. 8/14)	8/09 - now	2	8
Mr. Rouzbeh RASTGAR	AU	PhD (exp. 8/16)	8/12 - now	0	0
Ms. Tatyana BODRIKOVA	AU	BS / May 2011	8/09 - 5/11	0	0
Mr. Alex SCAMMELL	AU	BS / May 2011	1/10 - 5/11	0	0
Mr. Matthew PERRELLA	AU	BS / May 2012	1/11 - 5/12	0	1
Mr. Chad ROSE	AU	BS / May 2012	1/11 - 5/12	0	0
Mr. Devin KALAFUT	AU	BS / May 2012	1/11 - 5/12	0	0
Mr. Md. Haroon SHEIKH	UA	MS / Aug. 2013	12/09 - now	0	2
Ms. Julaunica TIGNER	TU	MS / Aug. 2012 PhD / (exp. 8/15)	12/09 - now	1	1
Ms. Trena SHARPE	TU	BS / (exp. 5/14)	8/11 - now	0	0
Ms. Alexandria BUFFORD	TU	H.S. student	6/11 - 8/11	0	0
Mr. Mark GUEST	AUM	BS / May 2011	9/09 - 5/12	0	1
Mr. Vincent HENINGBURG	AUM	BS / Dec. 2010	9/09 - 5/12	0	0
Ms. Jessica MORRIS	AUM	BS / May 2011	8/10 - 5/12	0	1
Mr. Tim HORNSBY	AUM	Pre-Eng	5/11 - 8/11	0	1
Mr. A. BERTAGNOLLI	AUM	BS / (exp. 12/13)	5/12 - now	0	1
Mr. Derek LATHAN	AUM	BS / (exp. 12/13)	5/12 - now	0	0
Mr. Chris DIGGS	AUM	BS / (exp. 05/14)	1/13 - now	0	0
Mr. Peter SAKALAUKUS	USA	MS / Aug. 2011	12/09 - 8/11	0	1
Mr. Andrew MOSLEY	USA	MS / Dec. 2012	8/10 - 12/12	1	1
Ms. Anusha RUDRARAJU	USA	MS / May 2013	1/11 - now	0	1
Mr. Nathan BROCK	USA	MS / May 2013	8/11 - now	0	0
Mr. Hamed GHAEDNIA	AU	PhD / (exp. 8/14)	8/10 - now	3	6
Mr. Robert WILLIAMS	AU	BS / Aug. 2012	5/11 - 12/11	0	0
Mr. Stephen BRANDON	AU	BS / Dec. 2012	2/12 - 9/12	0	0
Mr. Tyler SMITH	AU	BS / Aug. 2013	2/12 - 9/12	0	0
Ms. Hannah NEUFFER	AU	BS / (exp. 8/14)	10/12 - now	0	0

In cases of multiple-authorships of the published/submitted journal/conference articles by the students, credit is only given to the lead student with the greatest contribution to the publication.

The number of published/submitted journal papers by the PhD students who have been associated with the NePCM project range between 2 and 6, that is a very good publication record for doctoral students. Many MS-level students have also submitted one (1) journal paper or are at the preparation stages of their manuscript.

The following table summarizes the numbers of awarded and in-progress graduate degrees:

PhD		**MS**	
Awarded	In Progress	Awarded	In Progress
3	6	4	3

Leveraged non-DOE Academic Support: Given their involvement with the Alabama EPSCoR projects and based on their outstanding record of graduate studies, four (4) graduate students at Auburn and the University of South Alabama have been awarded competitive AL EPSCoR Graduate Research Scholars Program (GRSP) Fellowships ($25k/year) on six (6) occasions. The graduate students in the Samuel Ginn College of Engineering have also received extra stipends since August 2009 under the Dean's graduate research initiative directed at attracting and retaining high-quality graduate students. Moreover, four (4) undergraduate Mechanical Engineering students at Auburn have been awarded competitive Auburn University Undergraduate Research Fellowships ($4.4k stipend and $1.4k materials). These students are:

Name	*Inst.*	*Fellowship*	*Duration*	*Amount*
Dr. Liwu FAN	AU	AL EPSCoR GRSP	8/09 – 8/10; 8/10 – 8/11	$50,000
Mr. Yousef EL HASADI	AU	Mechanical Eng.	8/10 – 8/12	$16,000
Mr. Hasan BABAEI	AU AU	AL EPSCoR GRSP College of Eng.	8/10 – 8/11; 8/12 – 8/14 8/09 – 8/12	$75,000 $35,000
Mr. Hamed GHAEDNIA	AU AU	AL EPSCoR GRSP College of Eng.	8/12 – 8/13 8/10 – 8/12	$25,000 $16,000
Mr. M. MOEINI SEDEH	AU	College of Eng.	8/09 – 8/13	$38,000
Mr. Mahdi NABIL	AU	College of Eng.	8/11 – 8/13	$12,000
Mr. Rouzbeh RASTGAR	AU	College of Eng.	8/12 – 8/13	$4,000
Mr. Nathan BROCK	USA	AL EPSCoR GRSP	8/12 – 8/13	$25,000
Mr. Alex SCAMMELL	AU	AU UG Fellowship	5/10 – 5/11	$5,800
Mr. Matthew PERRELLA	AU	AU UG Fellowship	5/11 – 5/12	$5,800
Mr. Chad ROSE	AU	AU UG Fellowship	5/11 – 5/12	$5,800
Mr. Devin KALAFUT	AU	AU UG Fellowship	5/11 – 5/12	$5,800